

# **Studies of the signatures of magnetospheric substorms in coherent backscatter radars**

Thesis submitted for the degree of  
Doctor of Philosophy at the  
University of Leicester

By

Jonathan Kenneth Gauld

Radio and Space Plasma Physics Group  
Department of Physics and Astronomy  
University of Leicester

December 2000

UMI Number: U138358

All rights reserved

INFORMATION TO ALL USERS

The quality of this reproduction is dependent upon the quality of the copy submitted.

In the unlikely event that the author did not send a complete manuscript and there are missing pages, these will be noted. Also, if material had to be removed, a note will indicate the deletion.



UMI U138358

Published by ProQuest LLC 2013. Copyright in the Dissertation held by the Author.  
Microform Edition © ProQuest LLC.

All rights reserved. This work is protected against  
unauthorized copying under Title 17, United States Code.



ProQuest LLC  
789 East Eisenhower Parkway  
P.O. Box 1346  
Ann Arbor, MI 48106-1346

# **Studies of the signatures of magnetospheric substorms in coherent backscatter radars**

**Jonathan Gauld**

## **Abstract**

Ground-based coherent backscatter radar systems are used extensively to investigate small-scale dynamics of the ionosphere and related geophysical processes in the magnetosphere. At high-latitudes, HF coherent backscatter radars are especially effective, as radio waves in the HF band undergo sufficient refraction to bring about the required magnetic field orthogonal configuration that enables backscatter. Much of the work in this thesis uses data from HF radars, looking in particular at effects in the data which can be detected during magnetospheric substorms. Typically, a total or partial loss of radar data occurs during substorm intervals, with a duration of some tens of minutes for an isolated event. This phenomenon lends itself to several possible explanations, for instance the radar propagation conditions may have altered, or the radar reception may have been affected by enhanced D-region absorption, or the scattering structure itself could become depleted by the substorm. Several examples of this phenomenon are considered in relation to these geophysical mechanisms, in order to determine which of these mechanisms might be the most significant in each case. For two events, there was electron density data available from an incoherent scatter radar, which was used to produce a model of the D-region absorption. This was compared with cosmic radio noise absorption data from an appropriately located imaging riometer, and then used to model the absorption of the HF radar as a function of elevation angle. The electron density profiles were also used in conjunction with a mathematical ray tracing program, to model the HF radar propagation, and this has been compared with measured HF radar elevation angle data. The remaining events, for which electron density profiles were not available, have been examined in relation to absorption data and magnetometer data, and are explained by analogy with features seen in the detailed cases.

## **Acknowledgements**

I would like to thank everyone in the Radio and Space Plasma Physics Group at the University of Leicester. Special thanks are due to Dr Tim Yeoman, my supervisor, for his encouragement and positive approach. Also to Dr Jackie Davies, Dr Steve Milan and Dr Darren Wright for their various efforts on my behalf.

I would like to thank the Ionosphere and Radio Propagation Group at Lancaster University for supplying the IRIS data, the IMAGE magnetometer institution for magnetic data and the EISCAT institution.

# Contents

<b>Chapter 1</b>	<b>The solar-terrestrial environment</b>	<b>Page</b>
1.1	Introduction	1
1.2	The solar-terrestrial environment	1
	1.2.1 The solar environment	1
	1.2.2 The solar wind	1
	1.2.3 The Earth's magnetosphere	2
	1.2.4 The Earth's ionosphere	3
1.3	Introduction to the area of research	6
	1.3.1 The magnetospheric substorm	6
	1.3.2 Aims of the current research	7
<b>Chapter 2</b>	<b>Charged particle motion and structure formation in the ionosphere</b>	
2.1	Introduction	9
2.2	The motion of charged particles in the upper atmosphere	9
2.3	The generation of electric fields	12
2.4	High-latitude E region plasma irregularities	13
2.5	Plasma waves in the high-latitude F region	15
2.6	Summary	17
<b>Chapter 3</b>	<b>Instrumentation and techniques</b>	
3.1	Introduction	19
3.2	Principles of HF radar detection	19
	3.2.1 The CUTLASS HF radar facility	19
	3.2.2 The principle of coherent backscatter	19
	3.2.3 The detection of coherent backscatter	19
	3.2.4 Extracting Doppler spectra	22
3.3	The EISCAT radar facility	23
3.4	The IRIS riometer	24
3.5	The IMAGE magnetometer array	25
<b>Chapter 4</b>	<b>HF ray propagation in a magnetoplasma</b>	
4.1	Introduction	26
	4.2.1 HF radio wave propagation	26
	4.2.2 The refractive index of a magnetoplasma	26
	4.2.3 Negligible magnetic field and negligible collision frequency	27
	4.2.4 Transverse propagation with field and collisions	28
	4.2.5 A collisional plasma with insignificant magnetic field	28
	4.2.6 Attenuation of HF radiowaves	29
	4.2.7 The absorption of radio waves	29
	4.2.8 The absorption along a ray path	30
	4.2.9 Non-deviative absorption	30
	4.2.10 Deviative absorption	31
	4.2.11 Signal fading	

4.3.1	Ray theory	32
4.3.2	The Jones3D ray tracing program	32

## **Chapter 5 Mechanisms by which substorms affect CUTLASS data and an initial case study**

5.1	Introduction	34
5.2.1	Signatures of energetic particle precipitation	34
5.2.2	Particle precipitation as an operational constraint on CUTLASS	35
5.3.1	A case study of a radar signal drop out: 18/06/96	37
5.3.2	Data from CUTLASS and IMAGE	37
5.3.3	IRIS data	38
5.4.1	Modelling the absorption measured by IRIS	38
5.5.1	Modelling the absorption experienced by CUTLASS	41
5.5.2	Ray tracing applied to CUTLASS propagation paths	42
5.6	Analysis of the CUTLASS data loss	43
5.6.1	Assumptions upon which the analysis is based	43
5.6.2	Implications of the absorption calculations	43
5.6.3	Analysis of the ray tracing with regard to CUTLASS operation	44
5.7	Summary	45

## **Chapter 6 A multiple instrument study of a substorm interval – 21/08/98**

6.1	Introduction	47
6.2	The data set from the substorm period	47
6.2.1	CUTLASS and IMAGE data	47
6.2.2	IRIS data	47
6.2.3	EISCAT data	48
6.3	Examining the role of absorption in producing the signal loss	48
6.3.1	Modelling IRIS absorption	48
6.3.2	The absorption experienced by CUTLASS	49
6.4	Examining alterations in radar propagation during the substorm	50
6.4.1	Ray tracing through EISCAT profiles	50
6.4.2	supporting evidence from interferometry	51
6.5	Loss of irregularities by electric field shorting	52
6.6	Summary	53

## **Chapter 7 An overview of substorm signatures in CUTLASS data**

7.1	Introduction	55
7.2	Further CUTLASS case studies	55
7.2.1	Case study – 07/05/96	56
7.2.2	Case study – 24/08/97	56
7.2.3	Case study – 15/04/98	57
7.2.4	Case study – 29/04/98	58
7.2.5	Case study – 10/05/96	59
7.3	General features and statistics	60
7.3.1	Typical features of events and related statistics	60
7.3.2	CUTLASS elevation angle data	61
7.3.3	CUTLASS velocity data	62

7.4	Summary	63
<b>Chapter 8 Summary and Conclusions</b>		
8.1	Introduction	64
8.2	Summary of the events which are examined in detail	65
8.3	General features associated with CUTLASS data loss events	66
8.4	Future work	67
<b>References</b>		69

# Chapter 1

## The solar-terrestrial environment

### 1.1 Introduction

The work presented in this thesis relates to the region of the earth's atmosphere between approximately 60 and 1000 km in altitude, known as the ionosphere. The primary instrument from which data is used, is the CUTLASS Finland HF radar (chapter 3), which maps plasma convection velocities in the ionosphere, thereby enabling the electric field to be inferred (Chapter 2). The dynamics of the ionosphere are strongly coupled with processes in the solar atmosphere, not only due to the radiation emitted, but also due to the solar wind. The aim of this chapter is to provide an overview of the solar terrestrial environment and some of the processes involved in their coupling, and also to provide an outline of the geophysical phenomena being investigated in this thesis.

### 1.2 The solar terrestrial environment

#### 1.2.1 The solar environment

The Sun continuously emits electromagnetic radiation over a broad spectrum, with the total radiated flux varying by less than 0.1% over an 11 year solar cycle. The hard and soft X-rays and extreme ultraviolet (EUV) parts of the spectrum are especially significant in relation to the terrestrial environment as this 'solar ionising' radiation is largely responsible for the formation of the ionosphere (Section 1.2.4). Although the total radiated electromagnetic flux remains almost constant over a solar cycle, the flux in EUV and X-ray varies considerably, from a factor of two in the case of EUV to almost five for X-ray.

#### 1.2.2 The solar wind

This solar corpuscular radiation originates in the plasma of the solar atmosphere, the corona, and is constantly expanding outwards into interplanetary space, driven by a thermal pressure gradient. The solar wind particles are predominantly protons and electrons, and at 1 AU are supersonic, have typical speeds of 300 to 600 km/s (Gosling et al., 1976), but which may be as high as 1000 km/s during disturbed periods (Davies, 1990). The solar wind carries with it the 'frozen in' interplanetary magnetic field (IMF) (Section 1.3.1), which causes compression of the earth's dayside magnetic field, whilst extending its nightside field into a tail like configuration, the geomagnetotail (Section 1.2.3). The rotation of the sun together with the

magnetic field carrying properties of a collisionless plasma, result in the twisting of the IMF into a spiralled configuration, known as the Parker spiral (Fig.1.1).

### 1.2.3 The Earth's Magnetosphere

The magnetosphere (Fig.1.2) is a magnetic cavity in the interplanetary magnetic field (IMF), first predicted by Chapman and Ferraro in the nineteen thirties. In their model, the earth starts off with a dipole field, and the solar wind is then switched on. The magnetised plasma flows radially away from the sun, distorting the dipole field until an equilibrium configuration is reached. The magnetopause defines the boundary between the magnetosphere and the IMF, where the magnetic and solar wind dynamic pressure are in equilibrium and a current sheet exists. The resulting magnetic cavity is then closed to the IMF, and shielded from the solar wind. One consequence of this model is that the solar wind plasma could not cross the magnetopause, so that solar wind and magnetospheric plasma would be distinct.

In reality the magnetosphere is not always, or even often, closed to the IMF, probably being opened at times to the IMF by a topology such as that proposed by Dungey (1961), in his theory of magnetic reconnection (Fig.1.3a). Magnetic reconnection describes the process by which magnetic field lines change from open to closed configuration and vice-versa; this is believed to occur in regions with adjacent anti-parallel magnetic fields - these regions commonly occurring at the magnetopause boundary on the dayside, and at the neutral X point on the nightside (Fig.1.3a), and must be separated by a current, as a consequence of Ampère's law. The open magnetic field lines allow the exchange of particles and energy between the solar wind and the terrestrial environment, and ensure that their dynamics are strongly coupled. Three main factors compete electrostatically for the control of plasma convection in the magnetosphere. On high L shells, the flow is antisunward, and is controlled by the solar wind, either due to open field lines associated with magnetic reconnection at the magnetopause, or by momentum transfer across the magnetopause boundary by a viscous interaction (Axford and Hines, 1961). On lower L shells, the flow is a superposition of sunward return flows driven by reconnection in the tail, and corotation with the earth, the relative importance of these processes being dependent upon geomagnetic latitude.

On the dayside, the magnetopause is usually located some  $10 R_E$  above the equator ( $R_E$  = earth radius = 6400km). On the nightside a detectable magnetic tail or 'wake' may be found as far as  $1000 R_E$  downstream (Intriligator et al., 1969). Since the speed of magnetohydrodynamic (MHD) waves in the solar wind is the Alfvén speed, typically 50 km/s at 1AU, and the solar wind speed is about 400km/s, the earth is travelling through the solar

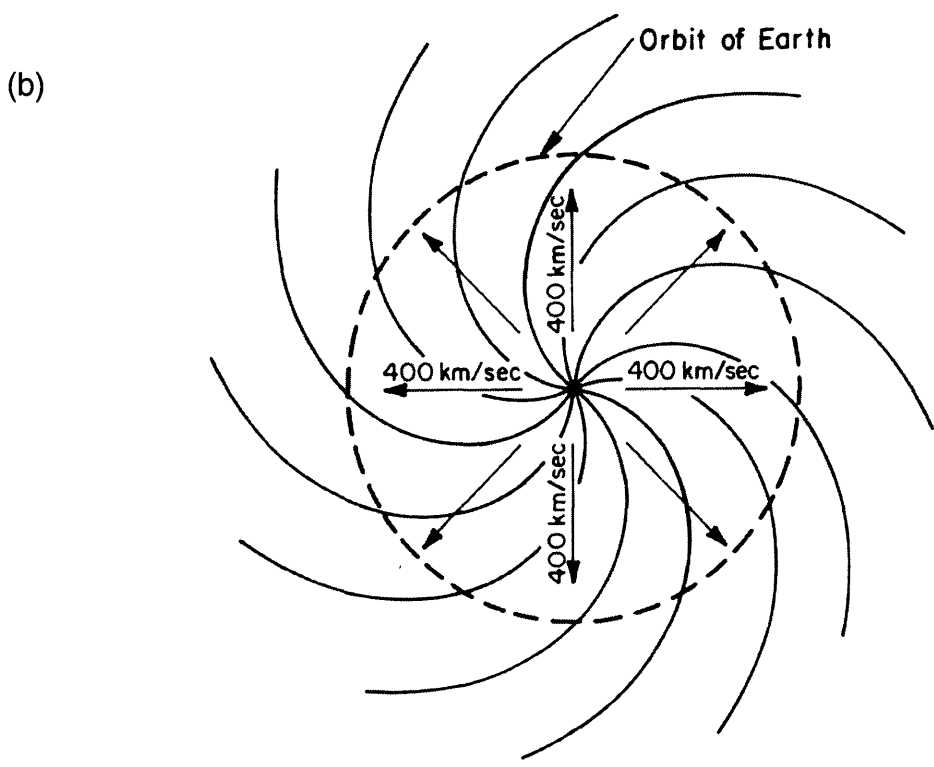
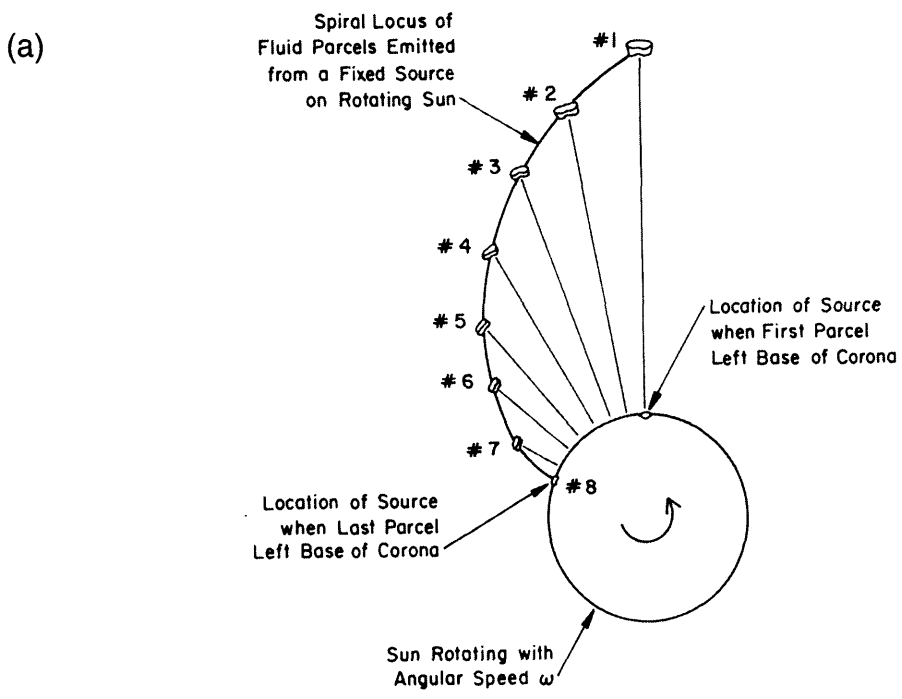


**Fig.1.1.** The Parker spiral. (a) schematic showing how the solar magnetic field develops into an Archimedean spiral due to rotation. (b) the overall configuration of the solar magnetic field in the ecliptic plane [adapted from *Parker, 1963*].

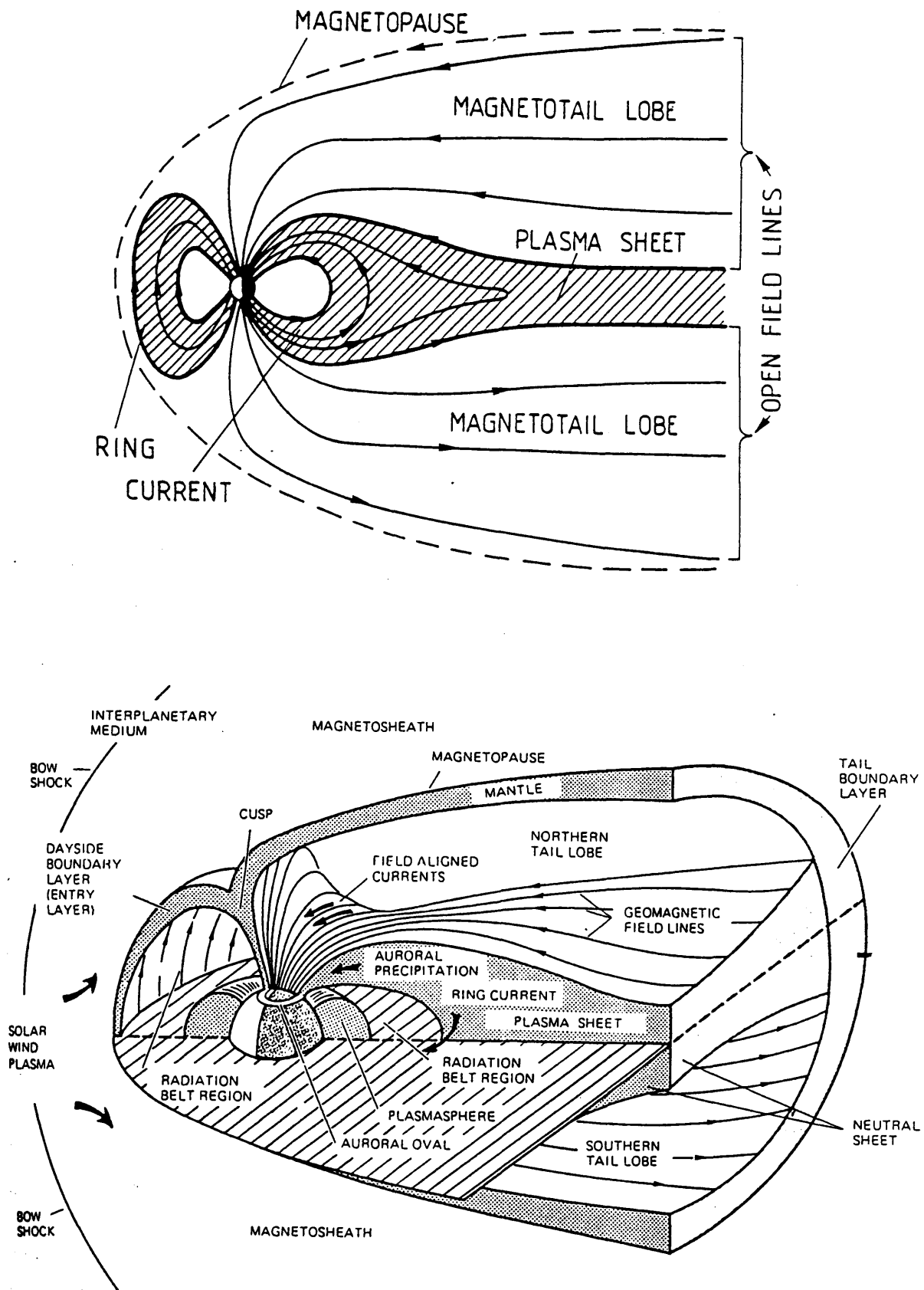
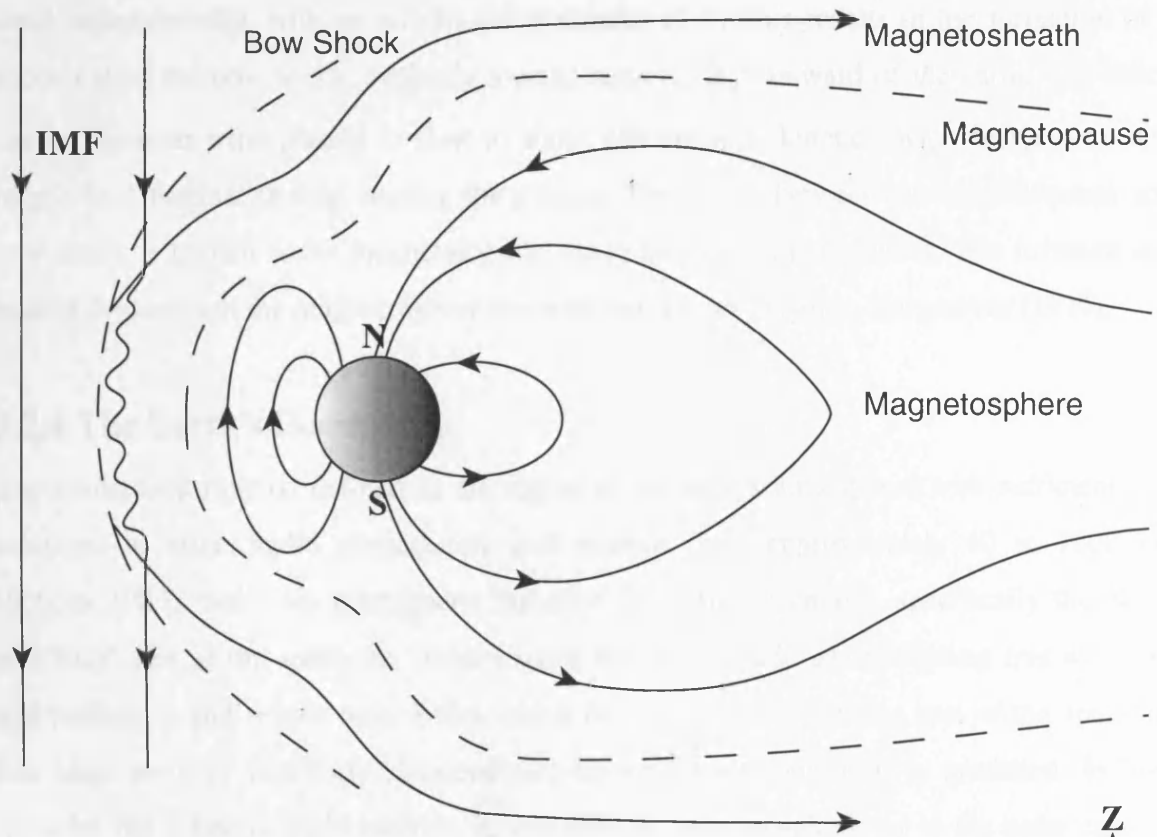
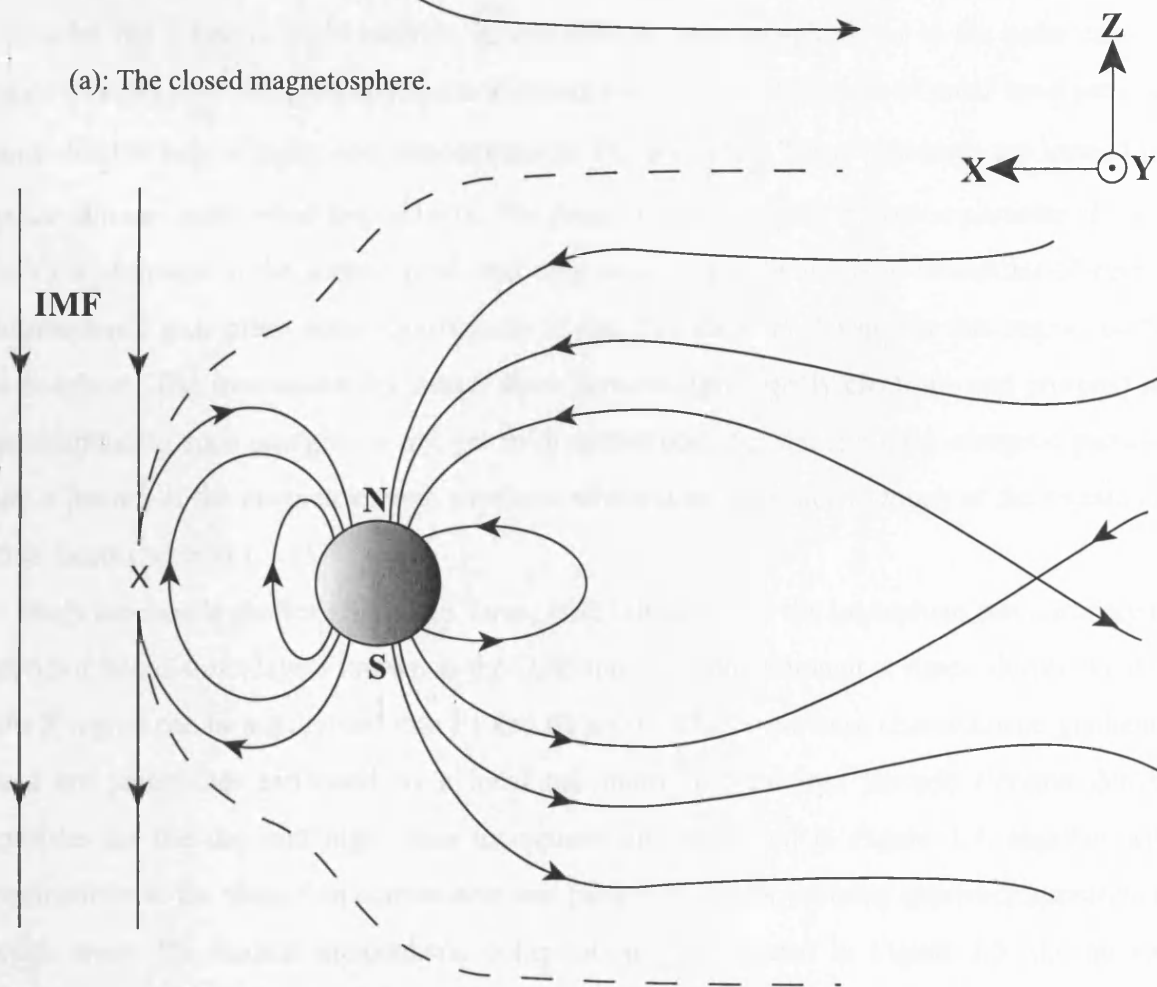


**Fig.1.2.** Two and three dimensional schematic representations of the geomagnetic field and the locations of various plasma populations and current systems (Milan, 1994).



(a): The closed magnetosphere.



(b): Dungey's Open magnetosphere.

**Fig.1.3.** The topology of the closed magnetosphere (a), together with Dungey's configuration for an open magnetosphere (b), in which the process of magnetic reconnection occurs at the neutral X points (From Storey, 2000).

wind supersonically, with an Alfvén mach number of 8. This results in the formation of a shock called the bow shock, typically located some  $13 R_E$  sunward of the earth. The shock causes the solar wind plasma to slow to about 250 km/s, its kinetic energy being converted largely into thermal energy, heating the plasma. The region between the magnetopause and bow shock is known as the magnetosheath, where the plasma is turbulent. The structure and related dynamics of the magnetosphere are reviewed by, for instance, Hargreaves (1979).

#### **1.2.4 The Earth's Ionosphere**

The ionosphere may be defined as the region of the earth's atmosphere with sufficient free electrons to affect radio propagation, and extends from approximately 60 to 1000 km (Schunk, 1983). Solar electromagnetic radiation of sufficient energy, specifically the X-ray and EUV part of the spectrum, photo-ionises the atmospheric gas producing free electrons and molecular and atomic ions. Below about 60 km, the solar ionising part of the spectrum has been more or less fully absorbed and no significant ionisation is produced. In high latitudes the magnetic field extends far out into the magnetosphere, or in the polar cap can open directly into interplanetary space allowing entry to the ionosphere of solar wind particles and also the loss of light ions, predominantly  $H^+$  and  $He^+$ . These processes are termed the polar rain and polar wind respectively. The precipitation of highly energetic particles (1 - 100 keV) is common in the auroral oval, and their collisions with atoms or molecules of neutral atmospheric gas, often adds significantly to the free electron density in this region of the ionosphere. The mechanism by which these particles (principally electrons and protons) are accelerated to such energies is not yet fully understood, but the resultant energetic particles are a feature of the magnetospheric substorm which is of relevance to much of the research in this thesis (Section 1.3.1).

Early ionosonde studies (Breit and Tuve, 1926) showed that the ionosphere can normally be divided into distinct layers known as the D, E and F region, although at times, during the day, the F region can be subdivided into F1 and F2 layers. The layers have characteristic gradients, and are sometimes separated by a local minimum. Typical mid latitude electron density profiles for the day and night time ionosphere are illustrated in Figure 1.4, together with indications of the major ion constituents and parts of the solar ionising spectrum important in each layer. The neutral atmospheric composition is illustrated in Figure 1.5; the number density of neutrals is at least 2 orders of magnitude greater than the ions at any given height, however the presence of charged particles has a profound effect upon atmospheric convection. The presence of these charged particles results in a degree of coupling between

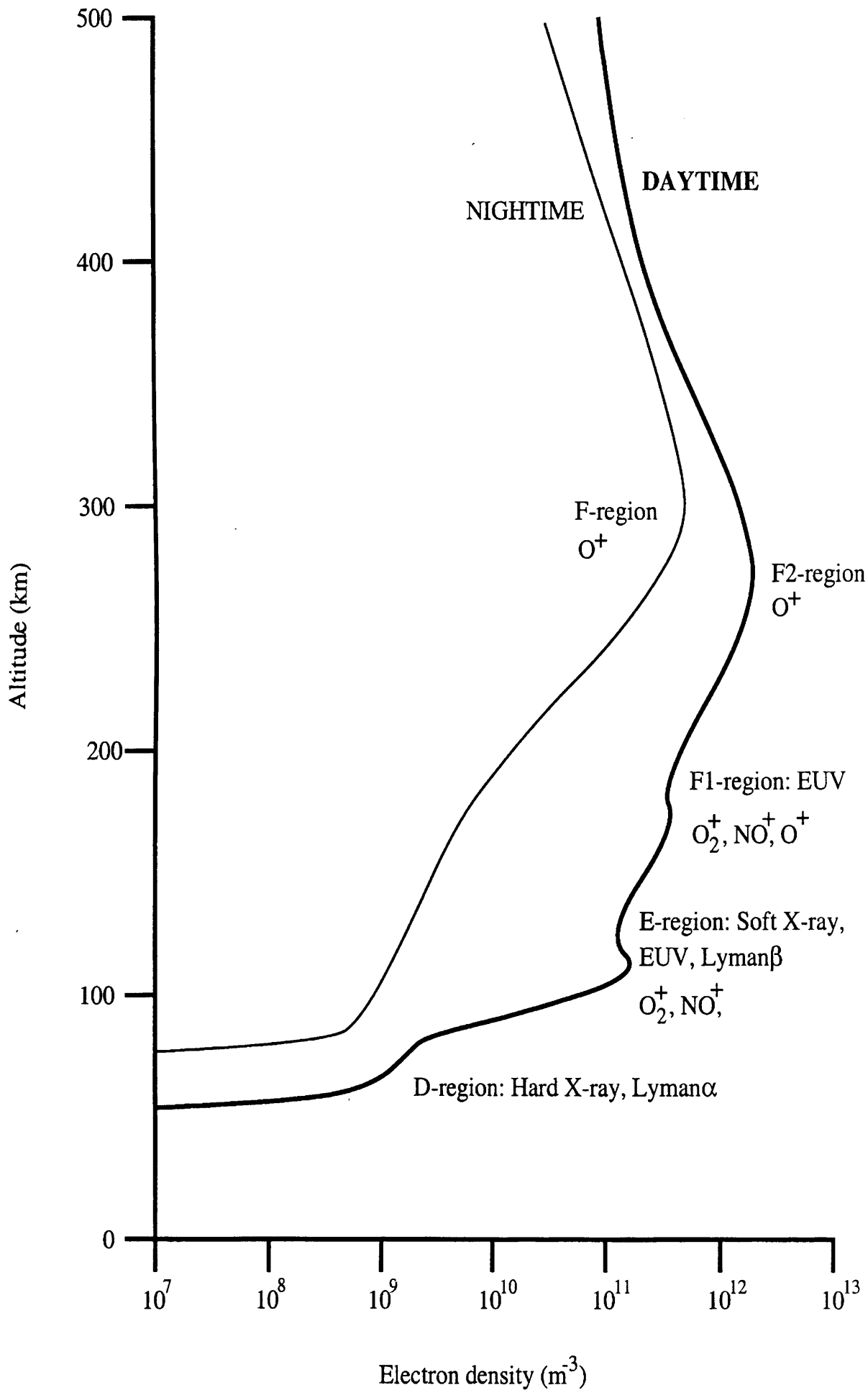


**Fig.1.4.** Typical mid-latitude electron density profiles for moderate solar activity (from Davies, 1996).

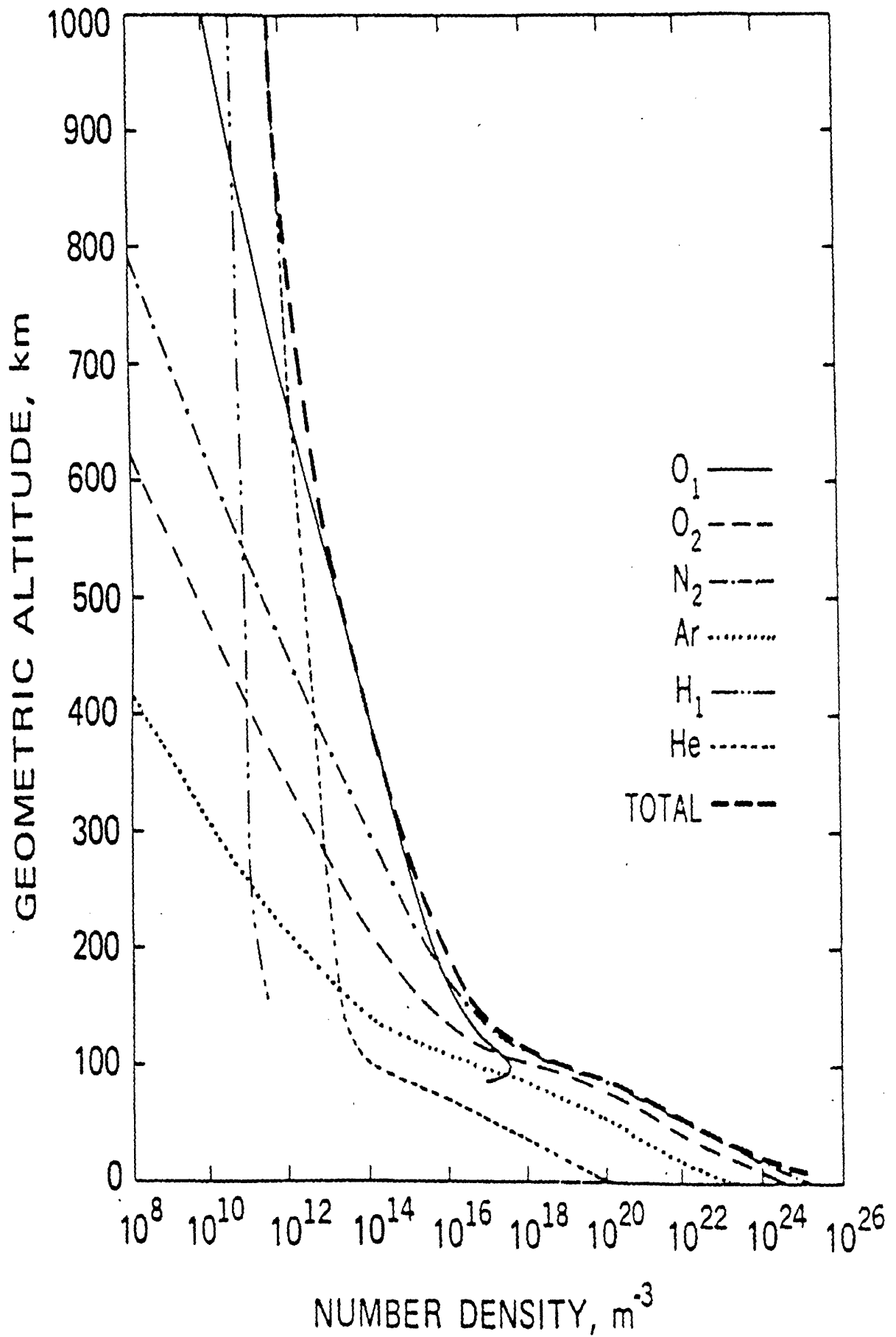


**Fig.1.5.** Density and composition of the neutral atmosphere as a function of altitude (Richmond, 1982)

distant convection regimes throughout the ionosphere and the magnetosphere. This is a consequence of electric fields being mapped over great distances along the magnetic field, meaning that the electrodynamics of one region can be imposed on a distant region, resulting in a coupling of the plasma convection regimes (Chapter 2), and sometimes also the neutral atoms convection. Several commonly occurring high latitude plasma convection patterns are illustrated in Figure 1.6. Global scale flow patterns can evolve between one state and another on a time scale of tens of minutes (Cowley & Lockwood, 1992), often being controlled by a flipping of the z and y components of the interplanetary magnetic field.

A simplistic model of the formation of the ionosphere by photoionisation is provided by Chapman theory (Kivelson and Russell, 1995). The theory assumes that the ion production rate  $Q$ , is directly proportional to the flux of solar ionising radiation and to the density of neutral particles, whilst the flux of solar ionising radiation reduces spatially at a rate proportional to  $Q$ . The neutral particle density is assumed to be governed by a hydrostatic equation. These assumptions can be formulated as differential equations whose solution will give the ion production rate as a function of altitude. For a fixed solar Zenith angle

$$Q = Q_m \exp[1 - y - \exp(-y)] \quad (1.1)$$

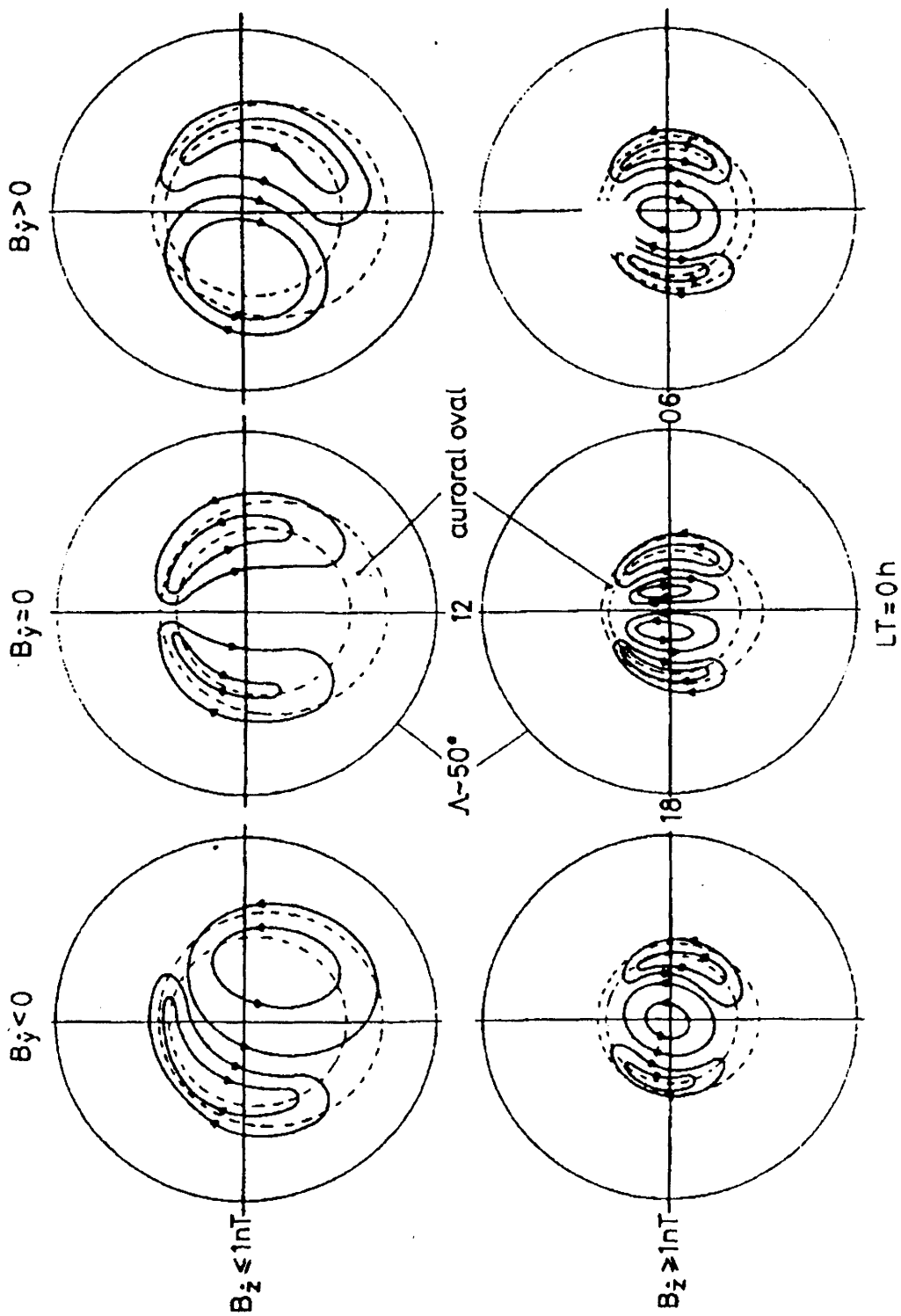
where,

$y = (h - h_m) / H_n$ ,  $h$  is the height,  $h_m$  is the height at which the peak ion production rate occurs,  $H_n$  is the neutral density scale height, and  $Q_m$  is the peak ion production rate.

Mechanisms which cause electron losses will now be considered. Electrons are lost either to chemical reactions or to transport processes. There are two dominant chemical reactions which need to be considered, the recombination reaction and the attachment reaction. Recombination involves an electron recombining with a positive ion to form a neutral, whereas attachment involves an electron attaching to a neutral to form a negative ion, which can then recombine with positive ions. These loss mechanisms give rise to the following forms for electron loss rate

$$L(N) = \alpha N^2 \quad \text{Recombination dominant} \quad (1.2)$$

$$L(N) = \beta N \quad \text{Attachment dominant} \quad (1.3)$$



The patterns are given in invariant magnetic latitude ( $\lambda$ ) — magnetic local time (MLT) frames with the magnetic pole at the centre and noon at the top  
 $\odot$   $B_r$  = northward  
 $\dashv$   $B_r$  = dawn-to-dusk component of IMF

**Fig.1.6** Inferred steady state convective flow patterns in the Northern hemisphere for various orientations of the IMF, as seen by an observer corotating with the Earth (Lockwood, 1993).

where the electron density is  $N$ , the coefficient of recombination  $\alpha$  and coefficient of attachment  $\beta$ .

The local rate of change of electron density is given by the following electron continuity equation, which is the sum of electron sources, sinks and transport by a plasma velocity field  $\mathbf{V}$ .

$$\partial N / \partial t = Q - L(N) - \nabla \cdot (N\mathbf{V}) \quad (1.4)$$

If quasi equilibrium is assumed and the usually less important transport term neglected, then the resulting continuity equation can be solved for electron density to give the following expressions for the Chapman alpha and beta layers

$$N_\alpha = \sqrt{Q_m / \alpha} [\exp \frac{1}{2} [1 - y - \exp(-y)]] \quad \text{Chapman } \alpha \text{ layer} \quad (1.5)$$

$$N_\beta = Q_m / \beta [\exp[1 - y - \exp(-y)]] \quad \text{Chapman } \beta \text{ layer} \quad (1.6)$$

The D region is best fitted by a  $\beta$  Chapman layer and the predominant loss mechanism is therefore the attachment reaction. In the E region recombination is the more important electron loss process so that an  $\alpha$  Chapman layer gives the best fit. At F region altitudes, transport processes become more important and a single Chapman layer may not give a particularly good fit. However, adding together several Chapman layers and thereby increasing the number of free parameters in the model can result in much better fits being obtained. This is the approach which has been used (Chapter 5) when fitting a model ionosphere to measurements to enable ray tracing analysis.

The foregoing Chapman layer analysis assumes a constant solar zenith angle. The analysis can however be related to the peak ion production rate for all Zenith angles (i.e. for overhead sun), and to the height of this peak, and an extra dimension 'zenith angle' introduced, thereby increasing the extent of the model from an area to a volume (Rishbeth and Garriott, 1969). The ionosphere is reviewed in detail by, for instance, Schunk(1983).

## **1.3 introduction to the area of this research**

### **1.3.1 The magnetospheric Substorm**

It first became clear to researchers in 1957 with the introduction of a global array of all sky cameras that the type of aurora observed at a particular location was dependent on universal time (UT) as well as local time (LT), which implies the presence of global auroral effects. The temporal and spatial development of these effects were first described by Akasofu (1964), which he called the 'auroral substorm'. Three distinct phases of the substorm can be identified, termed the growth, expansion and recovery phases.

During the growth phase there is increased erosion of magnetic flux from the dayside magnetosphere. This flux is eroded by the magnetic reconnection process (Section 1.2.3) and is convected with the flow of plasma across the polar cap, the flux and particles moving together such that the magnetic field is 'frozen in' to the flow (Kelley,1989). This magnetic flux then arrives on the nightside as an increase in open flux, causing an equatorial motion of the auroral oval. The process of magnetic reconnection, as well as being an energy transfer process, is a process which opens and closes magnetic field lines; the substorm growth phase is effectively a consequence of non steady state reconnection processes on the dayside and the nightside. There is also an associated thinning of the plasma sheet and stretching of the magnetotail, becoming more 'tail-like'. Primarily the growth phase is a period when solar wind kinetic energy is converted into and stored as magnetic energy in the earth's magnetosphere.

The expansion phase, which follows the growth phase, is a period in which the width of the auroral oval increases, showing a poleward expansion. Magnetic energy, stored in the tail during the growth phase, is explosively released, and the magnetotail geometry is reconfigured, becoming more dipole like (known as 'dipolarisation'). Reorientation of the magnetic field on the nightside, progresses in a slightly different way to that on the dayside, in that, it is bursty and apparently somewhat chaotic in nature. It is considered very likely that a second neutral X line forms in the magnetotail at some point in the expansion phase, and at this point magnetic flux is essentially being squeezed together until it snaps and reconfigures; a schematic of the suggested development of the magnetotail configuration during the expansion phase, known as the near earth neutral line model, is displayed in Figure 1.7. Newly reconfigured magnetic field lines will ring at their natural resonant frequency and launch a magnetohydrodynamic (MHD) wave, the passage of which may be recorded by

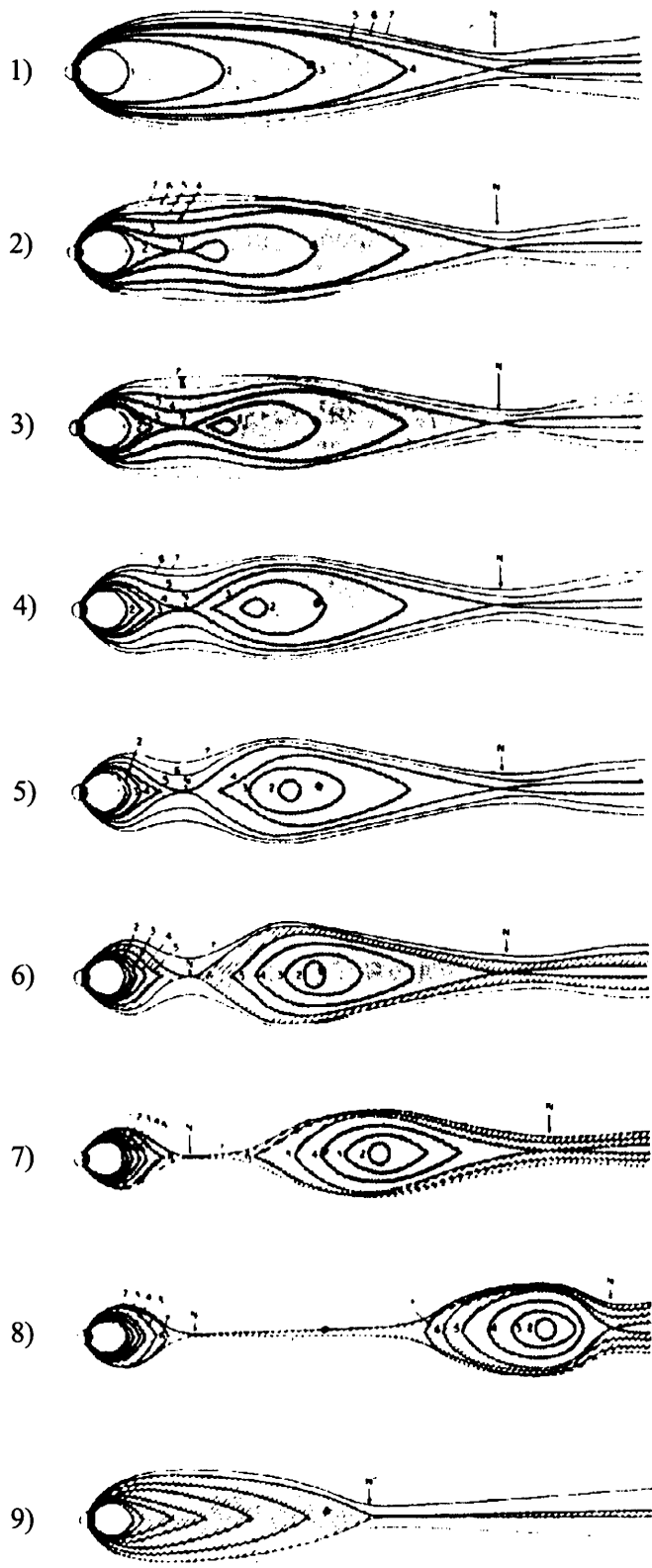


**Fig.1.7.** Schematic of the NENL model in which a reconnection site close to Earth is responsible for expansion phase onset (from *Hones, 1979*).

ground based magnetometers in Pi2 filtered magnetic perturbation data, and which signifies the onset of the substorm expansion phase. The current which flows through the tail's neutral x region is known as the cross tail current; during the substorm expansion phase, part of this current is diverted along magnetic field lines into the auroral ionosphere, forming the so called substorm current wedge (SCW) (Fig.1.8a). Changes of these large scale current systems can be detected by magnetometer networks (Fig.1.8b), which show characteristic perturbations that may be used to infer the geometry and location of the SCW. A process of magnetic field aligned particle acceleration is set in motion at the expansion phase onset, in the vicinity of the newly formed second neutral x line, and is associated with the occurrence of large induced electric fields. Highly energetic charged particles then cascade down the field lines of the auroral oval through the magnetosphere and into the ionosphere, a phenomena known as a 'particle injection'. A further process of field aligned particle acceleration exists closer to the earth in auroral latitudes, although its mechanism is not fully understood.

The end of the expansion phase and the beginning of the recovery phase is marked optically by the cessation of the poleward expansion the auroral oval. The recovery phase is a period of relaxation of the magnetosphere to its pre-growth phase state. There are a number of active phenomena associated with the period, such as the appearance of omega bands.

### **1.3.2 Aims of the current research**

Data used in this thesis is from CUTLASS, IRIS, EISCAT, and IMAGE (Chapter 3), however, the primary instrument will be the CUTLASS HF backscatter radar, with the data from other instruments usually being complimentary to or related to the CUTLASS data. It has been noted that during magnetically active periods such as magnetic storms or substorms, the CUTLASS radar commonly suffers a loss of the signal over all or part of the field of view. The following is a typical example of such a signal loss, seen on a latitude-time-velocity (LTV) plot from CUTLASS beam 9, together with the observed magnetic perturbations (Fig.1.9). CUTLASS beam 9 was operating in a high time resolution mode on this occasion, making a sample every 14 seconds rather than the usual 2 minutes, and the signal loss at 2026 UT appears clearly as a 'bite out' of the data, with a duration of some 18 minutes. Enhanced D region absorption has been cited as a probable explanation for the signal loss (Yeoman & Lühr,1997). The HF radar data loss process, during magnetically active intervals, is the topic of this research; the relative importance of several candidate mechanisms, which might cause the link between the substorm process and the HF radar signal loss phenomenon are examined, concentrating initially on a pair of particularly well

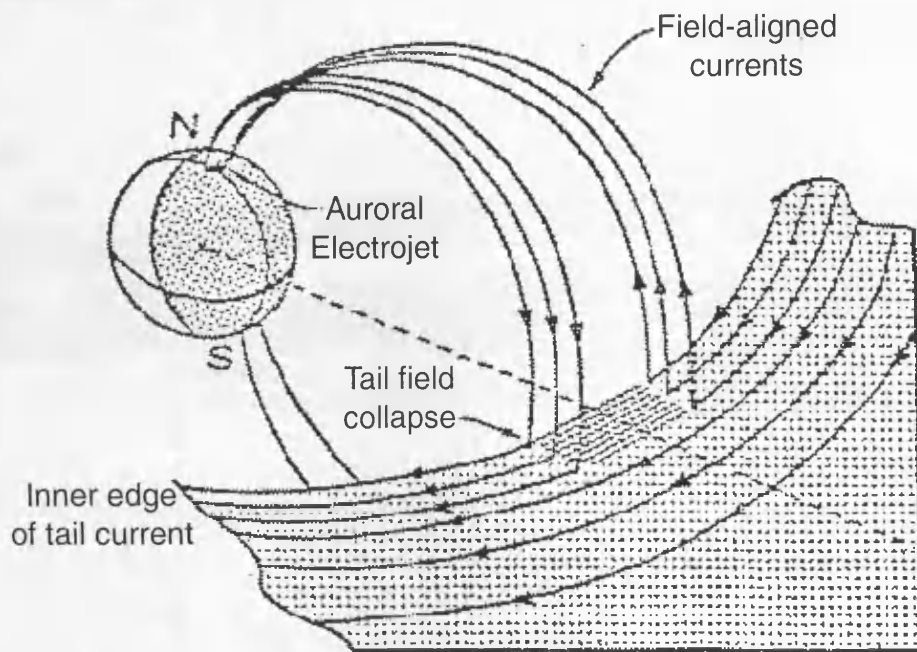


**Fig.1.8 (a)** Schematic of the Substorm Current Wedge [from McPherron et al., 1973].

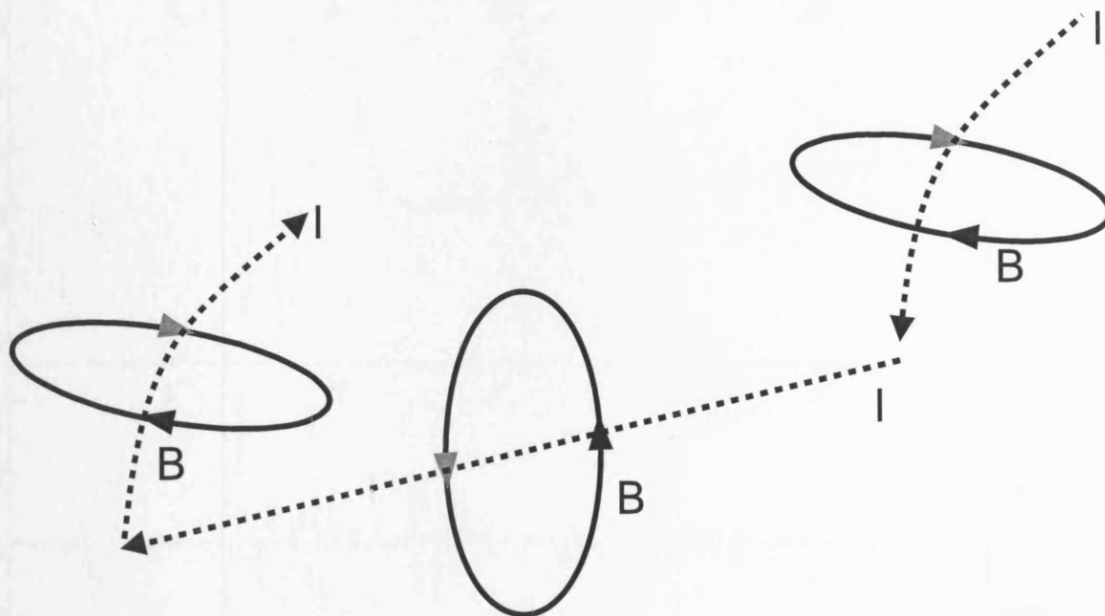


**Fig.1.8 (b)** The magnetic field produced by the substorm current system in the ionosphere (From Storey, 2000).

# SUPERDARN PARAMETER PLOT

## FINLAND: vel

06/08/95

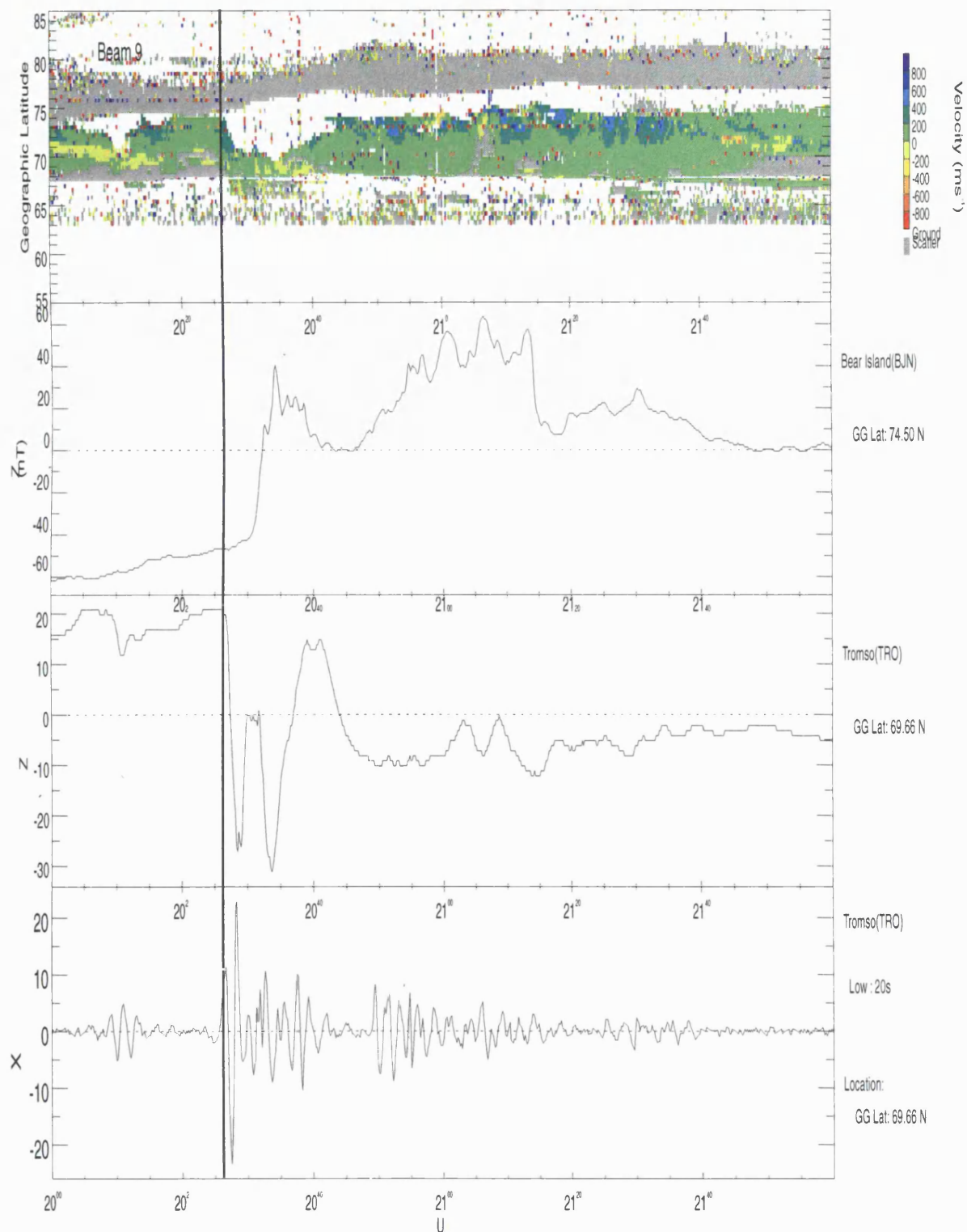


**Fig.1.9.** The start of a substorm expansion phase, marked by Pi2 pulsations and magnetic perturbations, and the start of a CUTLASS data loss event, are virtually simultaneous.

instrumented events (Chapters 5 - 6); these candidate mechanisms are - signal absorption, changes of ray propagation, and the possibility that suitable HF backscatter producing structures might become depleted by the substorm process. The analysis is largely carried out, by comparing the behaviour of various parameters measured by CUTLASS during and prior to a substorm, for instance received power and elevation angle, with models for the likely behaviour of these parameters. An absorption model is developed, based on EISCAT data, and verified by IRIS data, whilst mathematical ray tracing analysis is carried out using the Jones3D program, again supported by data from EISCAT.

## Chapter 2

### Charged particle motion and structure formation in the ionosphere

#### 2.1 Introduction

Much of the work in this thesis concerns the use of HF radars to measure plasma convection in the high latitude ionosphere. It would therefore be helpful to review briefly some of the basic theory of particle dynamics and plasma convection in this region, and its relationship with various instability mechanisms which cause plasma density irregularities. Most of the radar data presented in this thesis relates to occasions when there has been a sudden loss of data, often accompanied by an impulsive event in the magnetic signature. The theory of irregularity growth is of particular importance when examining these impulsive radar loss events, since the loss of irregularity structure is one of the candidate mechanisms for causing the loss of the radar signal. Many of the relevant aspects of theories of irregularity growth are therefore reviewed in this chapter. For more comprehensive reviews of the subject the reader is referred to publications by Fejer (1979), Fejer and Kelley (1980), Keskinen and Ossakow (1983), Farley (1985) and Haldoupis (1988).

#### 2.2 The motion of charged particles in the upper atmosphere

The major gas constituents of the atmosphere at ionospheric heights are atomic oxygen, oxygen and nitrogen together with ions of these molecules, and free electrons; it must be remembered however, that the number density of charged particles present is at least two orders of magnitude smaller than the neutrals throughout the E and F regions (section 1.2.4). The collective or fluid motion of each ionised species may be treated as an individual fluid type, with its own specific momentum equation. The effect of interacting with the other fluid types in the gas is then introduced in the form of a frictional drag term. The resulting equation of motion is altered considerably from the neutral atmospheric form, with the velocity-dependent Coriolis force being omitted due to the introduction of the much larger, velocity-dependent magnetic force.

The other significant body forces which must be included are the electric, gravitational and frictional forces, resulting in the following equation of motion

$$m_j n_j \frac{d\mathbf{V}_j}{dt} = -\nabla p_j + m_j n_j \mathbf{g} + q_j n_j (\mathbf{E} + \mathbf{V}_j \times \mathbf{B}) - \sum_{k(j \neq k)} m_j n_j \nu_{jk} (\mathbf{V}_j - \mathbf{V}_k) \quad (2.1)$$

Where the subscripts indicate particle species number and,

- $q_j$  charge of particle
- $m_j$  mass of particle
- $n_j$  particle number density
- $\mathbf{V}_j$  particle bulk flow (centre of momentum) velocity
- $\nu_{jk}$  collision frequency between particles of given species
- $\mathbf{E}$  electric field (in earth fixed frame)
- $\mathbf{B}$  magnetic field
- $\mathbf{g}$  gravitational acceleration
- $p_j$  The pressure of given particle species

This equation will now be used to look at some of the features of charged particle motion in the atmosphere, with only the ion neutral collisions being considered in the frictional drag term. The pressure field is specified as an equation of state

$$p_j = n_j \kappa_B T_j \quad (2.2)$$

where,

- $T_j$  temperature of the given particle species
- $\kappa_B$  Boltzmann constant

With these assumptions, the steady state momentum equation may be written

$$\mathbf{V}_j - \kappa_j (\mathbf{V}_j \times \hat{\mathbf{B}}) = -D_j (\nabla n_j / n_j) + b_j \mathbf{E} + (D_j / H_j) \hat{\mathbf{g}} + \mathbf{U} \quad (2.3)$$

where,

- $\kappa_j = q_j B / m_j \nu_{jn}$  The ratio of gyrofrequency to collision frequency
- $D_j = \kappa_B T_j / m_j \nu_{jn}$  The diffusion coefficient
- $b_j = q_j / m_j \nu_{jn}$  The mobility
- $H_j = \kappa_B T_j / m_j g$  The scale height
- $\mathbf{U}$  The velocity of the neutral wind
- $\hat{\mathbf{B}}$  Unit vector in direction of magnetic field

$B$	Magnetic field magnitude
$\hat{\mathbf{g}}$	Unit vector in direction of gravitational acceleration
$g$	Magnitude of gravitational acceleration

Firstly consider the situation if the collision frequency is much greater than the gyrofrequency so that  $\kappa_j \ll 1$ . Then the second term on the left hand side of (2.3) can be dropped since the first term will dominate. This has removed any magnetic field dependency from (2.3) and the motion is identical to that which would be produced by these driving forces in the absence of a magnetic field. These particles are then said to be unmagnetised, and the plasma termed 'collisional'. The dominant term on the right hand side of (2.3) is  $\mathbf{U}$  so that the equation reduces approximately to  $\mathbf{V}_j = \mathbf{U}$  which means that the particles are coupled with the neutral wind.

Next consider the case of gyrofrequency much greater than collision frequency so that  $\kappa_j \gg 1$ . The dot product of (2.3) with  $\hat{\mathbf{B}}$  gives the velocity component resolved parallel to the magnetic field

$$(\mathbf{V}_j)_{\text{parallel}} = [b_j \mathbf{E} + (D_j / H_j) \hat{\mathbf{g}} + D_j (\nabla n_j / n_j) + \mathbf{U}] \cdot \hat{\mathbf{B}} \quad (2.4)$$

This is the same as the field parallel velocity in the case  $\kappa_j \ll 1$ , so that the motion parallel to the magnetic field is unaffected by the field.

The cross product of (2.3) with  $\hat{\mathbf{B}}$  gives the component of the fluid velocity normal to the magnetic field. The first term on the left hand side of (2.3) is dropped due to the large value of  $\kappa_j$ . This results in the following expression

$$(\mathbf{V}_j)_{\perp} = (1 / B^2) [\mathbf{E} - (\kappa_B T_j / q_j) \nabla n_j / n_j + (m_j / q_j) \mathbf{g} + (1 / \kappa_j) \mathbf{U}] \times \mathbf{B} \quad (2.5)$$

The first term on the right hand side of (2.5) is usually the most important, so that the expression may be simplified as

$$(\mathbf{V}_j)_{\perp} = (\mathbf{E} \times \mathbf{B}) / B^2 \quad (2.6)$$

The resulting motion is clearly no longer independent of the magnetic field, being perpendicular to both the electric and magnetic field vectors. This ' $\mathbf{E} \times \mathbf{B}$  drift' is therefore associated with a magnetised or 'collisionless' plasma. This discussion has shown that the key factor in determining the response of a plasma to applied forces in the presence of an

external magnetic field is the ratio of the constituent particles' gyro to collision frequencies. In the E region the ratio of gyro to collision frequency for electrons satisfies  $\kappa_e \gg 1$  so that the electrons are magnetised and move with field normal component given by (2.6). By contrast, ions in the E region satisfy  $\kappa_i \ll 1$  so that the motion is collision dominated with the field normal (and field parallel) velocity given by the right hand side of (2.3). This implies that in the E region the ions are more or less dragged along with the neutral wind, whereas the electrons travel through the neutral wind at a velocity of  $\mathbf{E} \times \mathbf{B} / B^2$ . This differential flow between the ions and electrons in the E region produces strong electric currents, termed electrojets. In the F region however, the electrons and ions are both strongly magnetised and flow with very nearly the same field perpendicular velocity component (2.6), so that the field perpendicular current systems are relatively weak here. In the D region where electrons and ions both flow at approximately the neutral wind velocity, the current systems are again relatively weak.

The current density in the ionosphere can in principal be expressed in terms of the ion and electron velocity field solutions of (2.3). If the (generally less important) gravitational and pressure gradient terms are omitted from (2.3), the resulting velocity field solutions give the usual form of the current equation, expressed as a tensor relationship in terms of the electric field magnetic field and neutral wind only

$$\mathbf{J} = \sigma \cdot (\mathbf{E} + \mathbf{U} \times \mathbf{B}) \quad (2.7)$$

where  $\mathbf{J}$  is the current density and  $\sigma$  a conductivity tensor. This relationship is applicable for most ionospheric altitudes, where the plasma remains semi collisional. At magnetospheric heights however, the plasma is collisionless, and the current equation no longer applies. Magnetic field perpendicular currents at these heights are caused by pressure gradients, inertial effects and gravity.

### 2.3 The generation of electric fields

Steady state plasma flows in the high latitude F region are driven by an applied electrostatic field associated with the build up of a space charge. The plasma flow in the E region is dominated by the neutral wind, with the applied electrostatic field causing strong currents to flow through the neutral wind. Space charges are caused when currents flow with a divergence, which can be seen from the current divergence equation, derived from Maxwell's equations

$$\nabla \cdot \mathbf{J} = -\frac{\partial \rho_c}{\partial t} \quad (2.8)$$

where  $\rho_c$  is the space charge density. Any forces which cause ions and electrons to respond differently will cause a current to flow, such as collisions with the neutrals, pressure gradients and gravity. Whenever the resulting currents flow with a divergence, a space charge is produced with an associated electrical energy. However, the electric field produced by a space charge itself modifies the current to limit the build up of charge, forcing the current to become divergence free (Kelley,1989). Except on very short time scales, equation 2.8 becomes  $\nabla \cdot \mathbf{J} = 0$ .

The origin of the electrical energy which drives currents, and to a considerable extent plasma convection in the high latitude ionosphere, is the kinetic energy of the solar wind. The auroral ionosphere forms part of a large scale current system, linking with the outer magnetosphere and solar wind via field aligned currents. The ionosphere is a load in this system so that  $\mathbf{J} \cdot \mathbf{E} > 0$ , and electrical energy is converted into mechanical energy and also released as heat. The solar wind is a generator in this system meaning that  $\mathbf{J}_{sw} \cdot \mathbf{E}_{sw} < 0$ , mechanical energy being converted into electrical energy as the solar wind interacts with the magnetosphere. The electrical energy created, flows through the magnetosphere into the ionosphere as a Poynting flux, being largely dissipated in the ionosphere as Joule heat (Kelley,1989). At lower latitudes, the ionosphere is not connected magnetically to the IMF, and the imposed electric field in the ionosphere is caused by a neutral wind dynamo, with the dynamo effect of the E and F region neutral winds competing for electrodynamic control of the system (Kelley,1989).

## 2.4 High latitude E region Plasma Irregularities

The presence of plasma irregularities in the ionosphere are essential for the operation of coherent scatter radars, such as CUTLASS; Plasma waves of various scales exist in the ionosphere, from the thermal fluctuations right up to global scale. The time scale on which plasma wave structures persist is also variable. The plasma waves which are important for CUTLASS are on a length scale of tens of metres, and decay in a fraction of a second. When CUTLASS receives a backscattered signal from a particular location in the ionosphere, it indicates the presence of a spectrum of plasma irregularities and an associated instability mechanism; plasma instability mechanisms tend to be operative in the auroral zones, meaning that the aurora can often be imaged by HF radar, such as CUTLASS. Both linear and non linear theories of varying complexity have been put forward to explain plasma instability

mechanisms. Perhaps the most important of these are the 'two stream' and 'gradient drift' instabilities, referred to in the literature as type 1 and type 2 respectively, and which are identified in backscatter radar by characteristic power spectra (Fig.2.1).

The two stream (Farley-Buneman) instability, was first derived independently by Farley (1963) using kinetic theory, and Buneman (1963) using the Navier Stokes equations. It is referred to as 'two stream' because it requires a relative velocity between the population of electrons and ions and is therefore an E region phenomenon. The theory suggests that only when the component of this relative velocity in the direction of the irregularity wave vector exceeds the speed of sound in the plasma (approximately 360 m/sec) does the instability have a positive growth rate. For this reason, two stream plasma wave vectors form a 'cone of instability' (Fig.2.2).

Although the Farley-Buneman two stream theory has been successful in explaining many of the radar observations, it was noted that there are occasions when the electric field is not strong enough to excite the two stream mode (Balsley,1969). Under these circumstances radar experiments showed returns, with characteristic spectra of the type 2 or gradient drift mode. The gradient drift instability is so called because it requires the presence of a gradient in the background plasma density. When the orientation of the plasma density gradient is favourable, the wave's perturbation electric field will cause a perturbation  $E \times B$  drift which will drive even lower density plasma into regions already depleted by the wave, and vice versa, thereby increasing the size of the density perturbations (Fig.2.3(a)). Rogister and Dangelo (1970) developed a two fluid collisional model for the electrojet plasma, in which the zero order electric field and density gradient are the primary driving terms. Various developments have since been made to this two fluid linear theory, resulting in the following dispersion relation and growth rate for the combined gradient drift and two stream processes (Haldoupis,1988)

$$\omega_k = \frac{kV_d}{1 + \Psi} \cos \theta \quad (2.9)$$

$$\gamma_k = \frac{\Psi}{(1 + \Psi)} \left[ \frac{\omega_k^2 - k^2 C_s^2}{v_i} + \frac{\Omega_e \omega_k}{v_e k L} \right] \quad (2.10)$$

where,

$$\Psi = \frac{v_e v_i}{\Omega_e \Omega_i} \left[ 1 + \frac{\Omega_e^2}{v_e^2} \sin^2 \alpha \right]$$

$$C_s = \sqrt{\frac{\kappa_B (T_e + T_i)}{m_i}} \quad \text{ion-acoustic speed}$$

$\alpha$  The magnetic aspect angle defined as (smallest) angle between the wave propagation vector  $\mathbf{k}$  and a vector perpendicular to the magnetic field

$\theta = \arccos(\mathbf{k} \cdot \mathbf{V}_d)$  The angle between the wave propagation vector and the relative flow vector

$\mathbf{V}_d = \mathbf{V}_e - \mathbf{V}_i$  velocity of electron stream relative to ions

$V_d = |\mathbf{V}_d|$  speed of electron stream relative to ions

$k, \mathbf{k}$  wave number and propagation vector, respectively

$T_e, T_i$  electron and ion temperatures respectively

$\nu_e, \nu_i$  electron-neutral and ion-neutral collision frequencies

$\Omega_e, \Omega_i$  electron and ion gyrofrequencies, respectively

$L = \frac{n_0}{(dn_0 / dx)}$  electron density gradient scale length along the applied electric field

$n_0$  the zero order electron density

$m_i$  mean ion mass

The second term in the growth rate expression (eqn.2.10) is the gradient drift contribution to the instability, and the first term is the Farley-Bunemann contribution; if the plasma density gradient along the applied electric field is small i.e.  $L$  is large, then the growth rate reduces to the Farley Bunemann form.

## 2.5 Plasma waves in the high latitude F region

In the F region, the relative velocity between electrons and ions is not sufficient to excite the two stream instability and its associated gradient drift process. A slightly different type of gradient drift process operates in the F region termed the  $\mathbf{E} \times \mathbf{B}$  instability. The source of

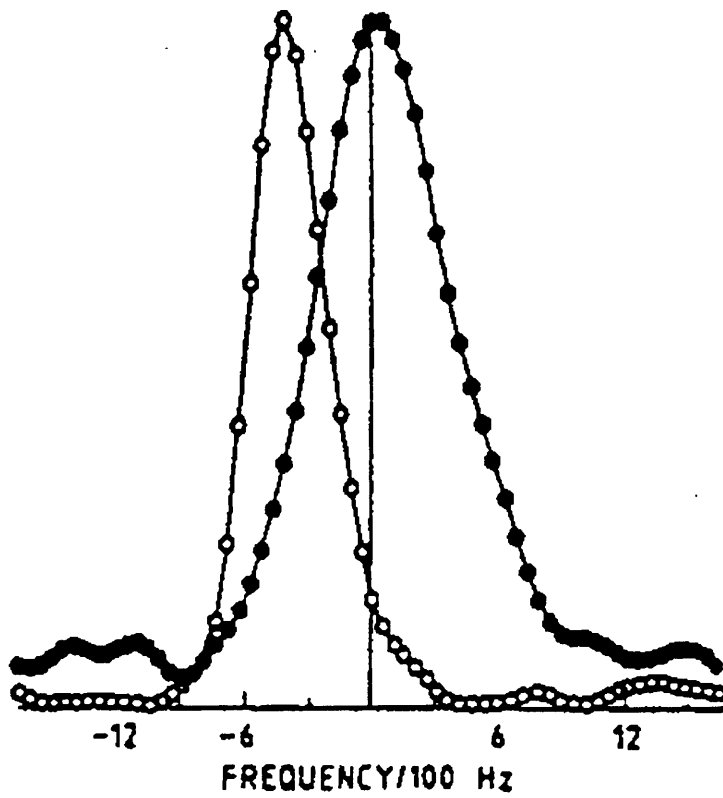


**Fig.2.1.** Typical examples of type 1 (open circles) and type 2 (closed circles) Doppler spectra. The type 1 spectra are narrow, with their spectral peaks located at a Doppler shift equal to, or slightly above the ion acoustic speed. The type 2 spectra are broader, suggesting the existence of strong plasma turbulence (Haldoupis, 1988).

TWO-STREAM

WAVES EXCITED IF:  $v_D \cos \vartheta > (1 + \Psi) C_S$

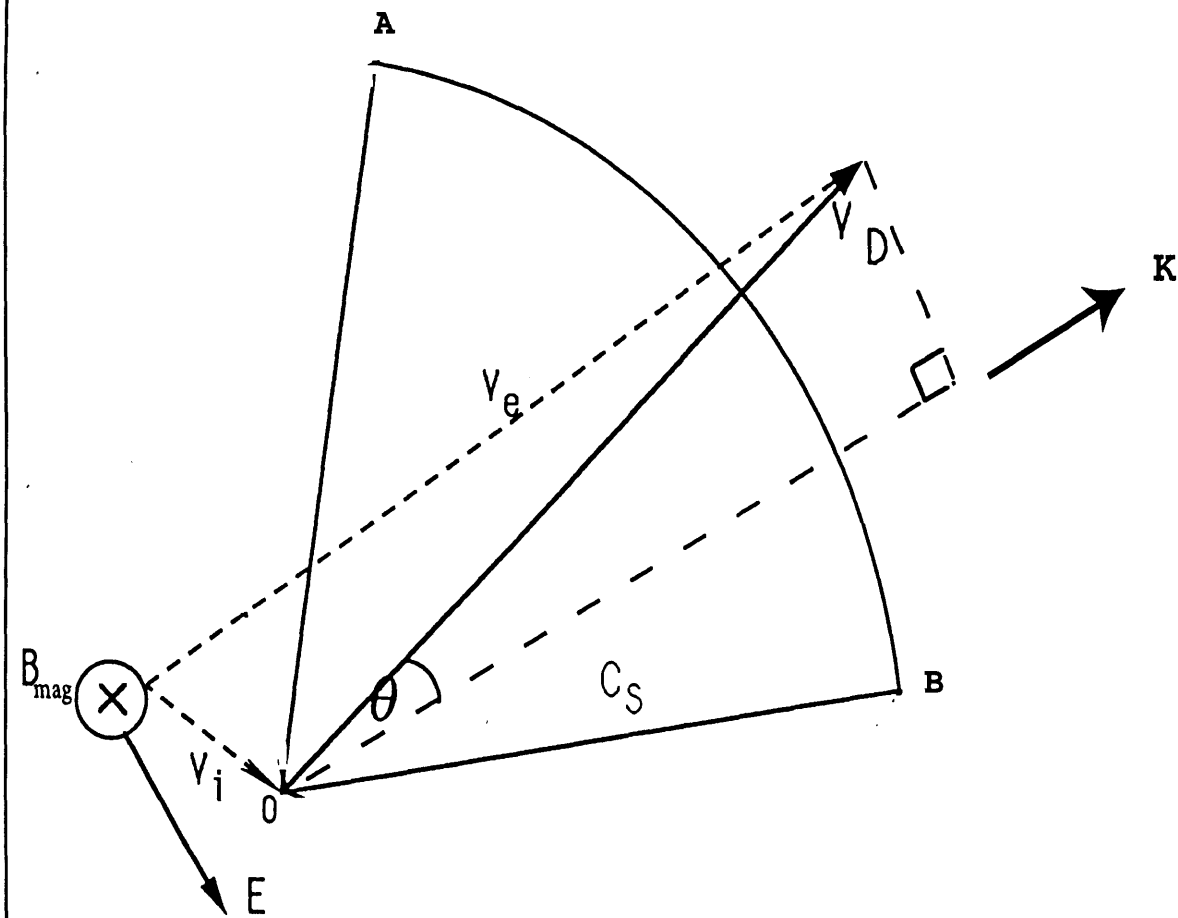


**Fig.2.2.** A cone of instability, drawn in the magnetic field orthogonal plane. Two stream wave propagation vectors  $k$ , lie within the cone  $OAB$ , where distance  $OA = OB = C_S$ . N.B.  $\Psi \sim 0$  in the E region (After Eglitis, 1990).

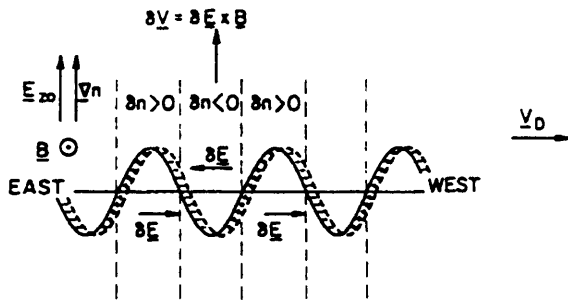


**Fig.2.3(a)** Schematic diagram showing the (E-region) gradient drift process (Kelley, 1989).

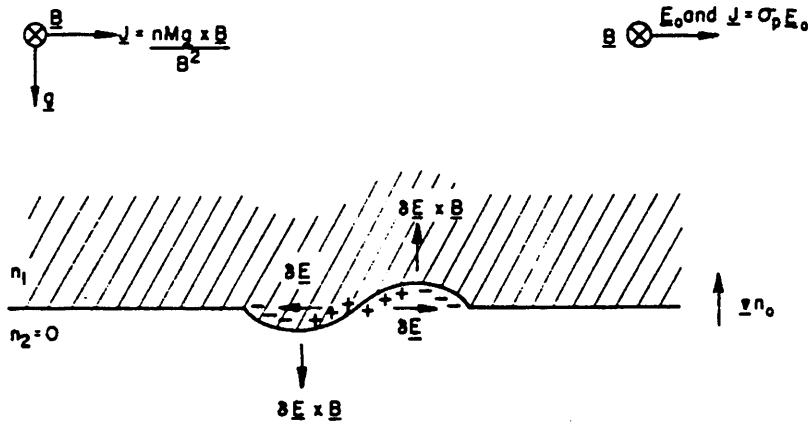


**Fig.2.3(b)** Schematic diagram of the generalised  $\mathbf{E} \times \mathbf{B}$  instability at high-latitudes (or the Rayleigh-Taylor instability at equatorial F-region) (Kelley, 1989).

charge separation producing the wave perturbation field in this case is a Pedersen current rather than the Hall current of the two stream case. Perturbation electric fields  $\delta\mathbf{E}'$  become established due to the application of the zero order field across any initial variations in plasma density and hence conductivity which may be present. The plasma will then become unstable provided that the applied electric field and plasma density gradient  $\nabla n$  have a suitable geometry, the required condition being

$$(\mathbf{E}' \times \mathbf{B}) \cdot \nabla n > 0 \quad (2.11)$$

Where  $\mathbf{E}'$  is the applied electric field in the reference frame of the neutral wind  $\mathbf{U}$ . The reason for the above geometry consideration is that only when this is satisfied will a perturbation field  $\delta\mathbf{E}'$  be oriented correctly in relation to the background density gradient for the plasma motion  $\delta\mathbf{E}' \times \mathbf{B}$  to move regions of lower density plasma up the gradient more quickly than regions of higher density plasma, causing initial density perturbations to grow (Fig.2.3(b))

The following expression (Vickrey and Kelley,1982) for the growth rate  $\gamma$ , includes the electric field shorting effect of a magnetically conjugate conducting E region and is therefore applicable in the auroral Zones

$$\gamma = \frac{E'_0}{BS} \left( \frac{M-1}{M} \right) - k^2 D_{\perp} \quad (2.12)$$

where,

$$\frac{E'_0}{B} = \frac{1}{B^2} (\mathbf{E}' \times \mathbf{B}) \cdot \frac{\nabla n}{|\nabla n|}$$

$$M = 1 + \Sigma_P^F / \Sigma_P^E$$

$\Sigma$  The field line-integrated Pedersen conductivity in the (E) or (F) region

$S$  An inverse density gradient scale length

$D_{\perp}$  The height-averaged diffusion coefficient

If the E region field line-integrated Pedersen conductivity is large relative to that in the F region, then  $M \approx 1$  and the growth rate becomes small due to shorting of the perturbation electric field by current flow along the magnetic field lines and through the E region.

For high latitudes, the effect of field aligned currents should be included in the formulation, and the instability is then referred to in the literature as the current convective instability (Ossakow and Chaturvedi, 1979). The current convective instability introduces a term to the growth rate involving the field aligned drift velocity of electrons relative to ions. The effect of this can be destabilising even when the configuration of applied electric field and background plasma density gradient is stabilising (Kelley,1989) i.e. (eqn.2.11) is not satisfied.

The wave length dependency introduced to the growth rate (eqn.2.12) by the diffusive damping term  $k^2 D_{\perp}$  puts a lower limit on the wavelength of structure formed directly by the E x B instability. wavelengths at 15m, important for CUTLASS backscatter may be too short to be caused directly by the instability, however, it is very likely that some energy would cascade into this wavelength range from larger scales in a manner similar to neutral turbulence (Kelley,1989).

## 2.6 Summary

Equations governing the fluid motion of charged particles in the upper atmosphere were used to look at the differing responses of ions and electrons to sets of applied body forces at various altitudes. It was shown that an applied electrostatic field in the E region is associated with a significant differential flow between ions and electrons, resulting in the electrojet current systems, whereas an applied field in the F region controls the plasma motion, without producing significant field perpendicular currents. A variety of well known plasma instability mechanisms were reviewed, and formulations for their growth rates included. It should be noted, as it will be relevant later in the thesis, that the given instability growth rates are dependent on the magnetic field perpendicular component of the applied electric field, measured in the reference frame of the neutral wind. The generation of the electrostatic field by divergent current flow was covered, as was the standard formulation for the current equation. It can be seen from the current equation that a changing current can be caused by a changing electric field, a changing neutral wind or changing plasma parameters. In the F region, the time scale for neutral wind velocity change by collisional interaction with the ions is several hours (Kelley,1989). It follows that the impulsive changes in current flow which occur in various events presented in this thesis must be associated in the F region with changing plasma parameters (conductivity) and or changing electric fields. In reality, the plasma conductivity and applied electric fields are inextricably linked, so that they would change simultaneously. Therefore, an increased current flow might be associated with

increased conductivity and reduced electric fields. This is the essence of the electric field shorting concept and is a process which may be important in causing the decay of irregularity structure due to the significance of the applied electric field in the growth rate.

## Chapter 3

### Instrumentation and techniques

#### 3.1 Introduction

All the instrumentation directly relevant to this thesis is described in this chapter, and where additional understanding of the measured parameters is of relevance, the basic aspects of the signal processing techniques used, have been examined.

#### 3.2 Principles of HF radar detection

##### 3.2.1 The CUTLASS HF radar facility

CUTLASS, the co-operative UK twin located auroral sounding system, is a bistatic coherent HF backscatter radar system, one radar being located in Iceland, the other in Finland, forming part of the SuperDARN radar network (Greenwald et al., 1995). The radars can operate in the range 8-20 MHz, and consist of 16 antennas with transmit and receive capability, phased to produce 16 beams, separated by 3.24 degrees in azimuth. They measure the line of sight velocity of the scattering structure, which in the F region at least may be taken as equal to the line of sight  $\mathbf{E} \wedge \mathbf{B}$  velocity (Chapter 2). Both radars look north towards the Svalbard Archipelago, viewing a common volume in this vicinity, where the component of the plasma convection velocity normal to the magnetic field can be resolved (Fig.3.1). In addition to line of sight convection velocity, the returned signal power and irregularity spectral width are obtained. Interferometer arrays exist at both radar sites, which enable the backscatter elevation angle to be determined as a function of range (Milan et al., 1997). The radars commonly receive energy scattered back from the ground, rather than from the ionosphere, which at times overpowers the data of interest. Groundscatter is routinely filtered out of the data by the criteria that both the spectral width and l-o-s velocity are less than 50 m/s. Various HF radar propagation modes, and regions from which backscatter is produced (i.e. from the ground, and from regions where the radar vector is orthogonal to the magnetic field) are displayed in Figure 3.2.

##### 3.2.2 The principle of coherent backscatter

Coherent scatter radar will receive a backscattered signal only if the transmitted signal encounters suitable structures from which to scatter, which means in practice, enhanced non-

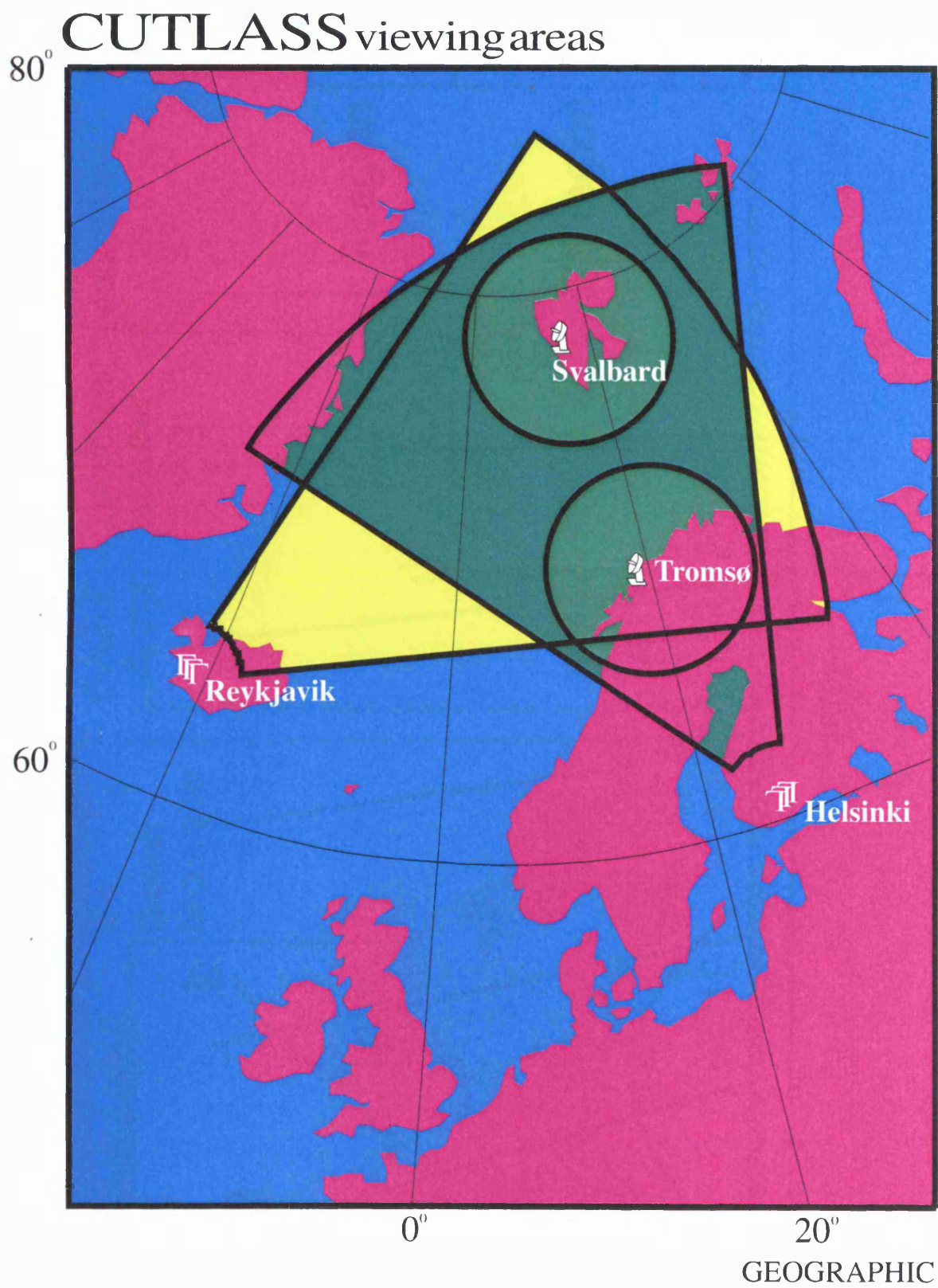
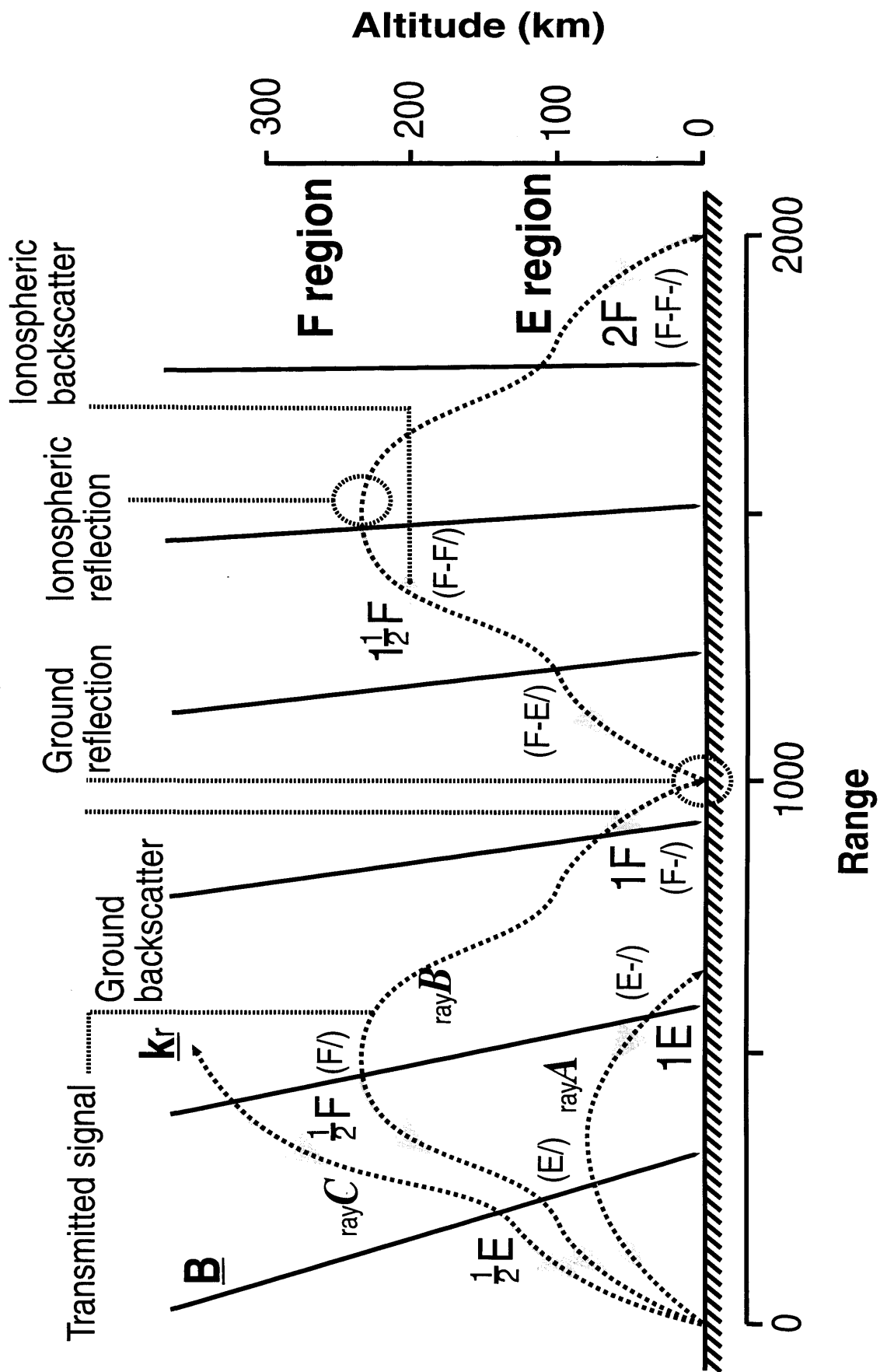


Fig.3.1. The field of view of the CUTLASS radars.



**Fig.3.2.** A schematic diagram, showing various propagation modes of an HF radar, and regions from which backscatter can occur (Milan et al., 1997 (b)).

thermal plasma density fluctuations or ‘irregularities’ such as those described in the previous chapter. The underlying principle of coherent backscatter is identical to the process involved in crystalline Bragg scatter, and occurs because of constructive interference between waves scattered from within a structured medium. The dependency of the intensity of the backscattered signal upon the scattering structure will now be examined. For a plane electromagnetic wave incident upon a scattering volume  $v$ , whose scale length is large compared with the wavelength of the incident signal and small enough to ensure statistical uniformity, the electric field of the scattered wave is given by (Haldoupis, 1988)

$$E_s(t) \propto \int_v \Delta n(\mathbf{r}, t) \exp(-j(\mathbf{k}_i - \mathbf{k}_s) \cdot \mathbf{r}) d^3\mathbf{r} \quad (3.1)$$

where  $\mathbf{k}_i$  and  $\mathbf{k}_s$  are vectors in the direction of the incident and scattered wave,  $n(\mathbf{r}, t)$  is the perturbation electron density relative to the background average. The above integral is a Fourier spatial wave component for electron density perturbations parallel to the vector  $(\mathbf{k}_i - \mathbf{k}_s)$ . If the radar and receiver are co-located, then the relevant spatial wave component corresponds to backscatter, which requires  $\mathbf{k}_s = -\mathbf{k}_i$  and therefore  $(\mathbf{k}_i - \mathbf{k}_s) = 2\mathbf{k}_i$ . In other words, the component of the Fourier spatial spectrum of density structure which controls the intensity of backscatter has a wave number twice the incident wave number and half the incident wave length. The presence of electron density structure at half the transmitted wave length is therefore the requirement for backscatter to occur.

### 3.2.3 The detection of coherent backscatter

Consider first the transmission and subsequent detection of backscatter from a single radar pulse. The received signal will bear some resemblance to the transmitted signal, and this fact is used to extract information about the received signal. The phase of the transmitted signal is preserved in a reference signal, which is compared with the received signal to recover the phase difference between the transmitted and received signals. The received signal amplitude and this phase difference is expressed as a complex number, known as a phasor

$$r(t) = Ae^{i\phi} = A\cos\phi + Ai\sin\phi \quad (3.2)$$

Where the characteristics of the received signal are an amplitude  $A$  and phase change  $\phi$ , relative to the reference signal. The information from each sample of the received signal is then contained in a phasor, and constitutes a data point for use in the auto-correlation function (ACF) analysis.

If the phase change of the received signal could be accurately measured more than once within the lifetime of an irregularity, its phase speed could in principle be calculated, as this is related to the rate of change of phase angle, the 'angular Doppler shift' (See section 3.2.4). However, such measurements using a series of pulses would produce unreliable results, as the pulses would need to be so close together as to result in cross range noise. This is the reception of unwanted return signals from pulses and corresponding ranges other than the one of interest.

The duration of the transmitted pulse imparts a range resolution to the received signal. If the pulse has duration  $\tau$ , then the range resolution is  $c\tau/2$ . Coherent scatter radars therefore measure the plasma flow at distances corresponding to distinct range gates, of which CUTLASS in the standard mode has 75, each of length 45 km.

CUTLASS uses a seven pulse series, the whole pulse sequence being repeated some 80 times or so over seven seconds during each integration. The pulses are sequenced so that the time between pairs of pulses form multiples of a basic lag of  $T=2400\mu s$ , and there are 17 distinct lag times available between the pairs of pulses (Fig.3.3). The objective of a pulse scheme is to maximise the number of distinct lag times without duplicating any lags, as this will cause a range ambiguity. When the integration is complete, there are 80 phase and amplitude measurements (phasors) for each of the 7 pulses in the sequence. The process of irregularity decay is assumed to be stationary during the integration period (i.e. the plasma parameters do not change), therefore the resulting data set of phasors can be used to construct a 17 lag complex autocorrelation function, in which information about the irregularities' phase velocity spectrum is contained. The value assigned to each lag of the autocorrelation function is the 'mean lagged product', and is found as the mean of 80 phasor products of the form  $r^*(t).r(t+nT)$  where  $n = 0,1,2\dots$  corresponds to successive lag numbers. Averaging many estimates of the phasor product is necessary, in order to remove any contributions from noise or cross range noise, the signals from which will be uncorrelated. The analysis outlined in this section is carried out by hardware and software at the radar site, the output from CUTLASS being a 17 point complex autocorrelation function, which contains information about the spectrum of irregularities from which the signal has been scattered.

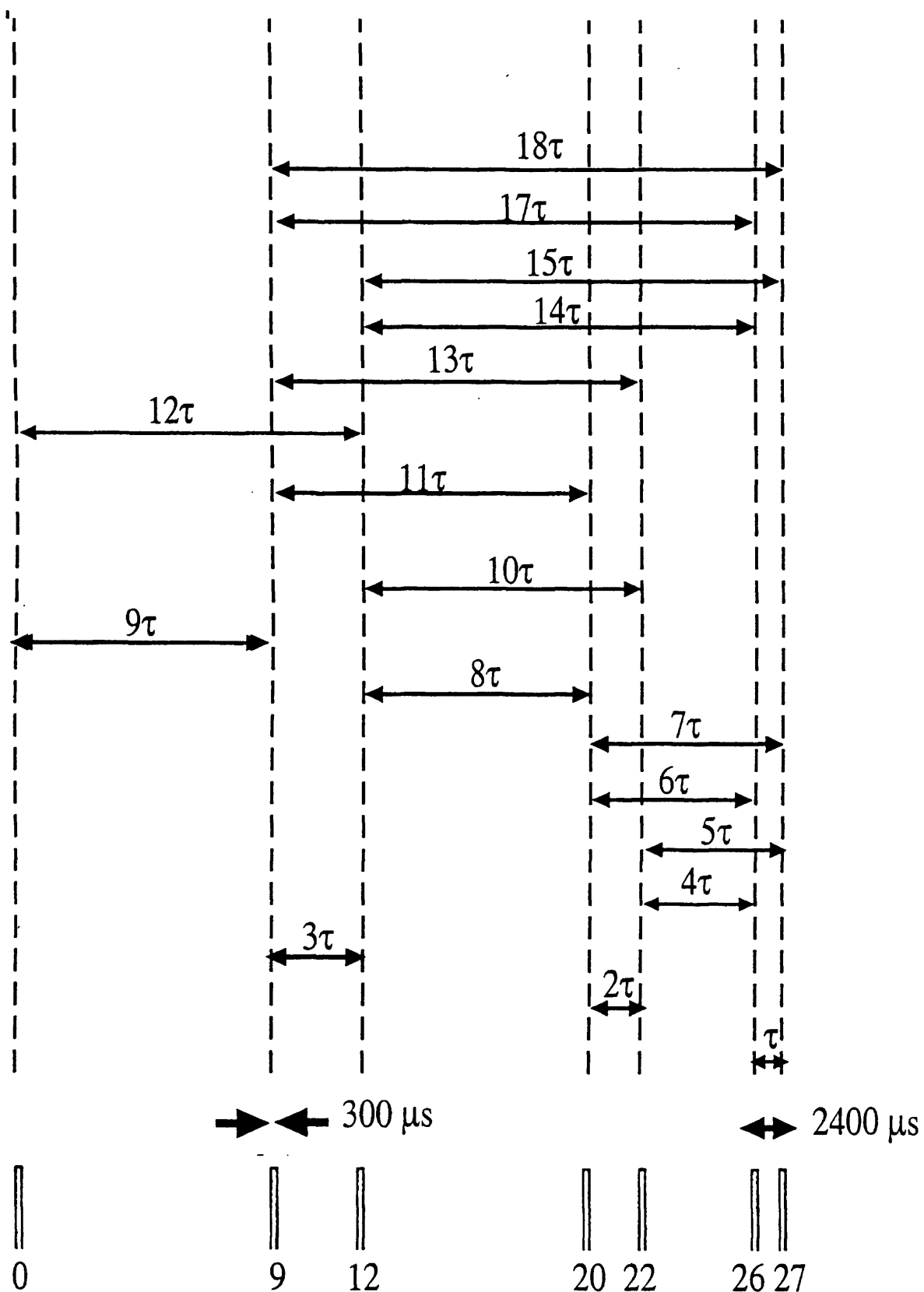


**Fig.3.3.** The normal scan pulse scheme for the CUTLASS radar. There are seven pulses in the sequence, the pulse length is  $300 \mu\text{s}$  and the basic lag separation is  $2400 \mu\text{s}$ . (From Provan,1998).

### 3.2.4 Extracting Doppler spectra

Having obtained a 17 lag autocorrelation function, there are several ways to proceed. One option is to transform the discrete autocorrelation function directly into a 32 point Doppler spectrum by the discrete Fourier transform (Greenwald et al., 1985). This technique has several disadvantages, for instance, it is time consuming, and does not directly result in an estimate of the average Doppler shift over the spectrum. Also, due to the limited number of points for the fast Fourier transform (FFT), the spectral widths tend to be considerably overestimated. On the other hand, features such as the superposition of signals with different Doppler spectra can be identified more easily using the discrete transform approach, as the spectra obtained will reflect directly the fluid motion spectrum of the contributing irregularities (Villain, 1987). An alternative approach, and the technique used in the analysis procedure of CUTLASS is to obtain the irregularity spectral parameters directly from the ACF by assuming an appropriate functional form, and fitting the measured ACF to this functional form. The theory of collective wave scattering from a non-uniform plasma predicts that the measured ACF should have a Lorentzian form, a Gaussian form, or a superposition of these forms, and in fact the Lorentzian (exponential) most commonly produces the best fit (Hanuise, 1993).

The Lorentzian form for the ACF is  $R_\lambda(t) = C_\lambda e^{(i\omega - \lambda)t}$  (3.3)

The Gaussian form for the ACF is  $R_\sigma(t) = C_\sigma e^{i\omega t} e^{-\sigma^2 t^2}$  (3.4)

Where,  $\lambda$  and  $\sigma$  are the temporal decorrelation parameters,  $\omega$  is the Doppler frequency, and  $C_\lambda$  and  $C_\sigma$  are lag zero power.

The real part of the Fourier transform of the ACF is a Doppler power spectrum. For instance the Fourier transform of the Lorentzian ACF gives a Doppler spectrum of the form

$$S_\lambda(\omega') = C_\lambda \frac{2\lambda}{\lambda^2 + (\omega - \omega')^2} \quad (3.5)$$

This spectrum has peak power at  $\omega' = \omega$ , and full half power spectral width of  $2\lambda$  (Fig.3.4). The Doppler spectrum resulting from the Gaussian decorrelation leads to a spectral width of  $3.3\sigma$  (Villain et al., 1987). Therefore, the values inferred for spectral width will depend upon the fit selected for the ACF, although both functional forms commonly produce similar

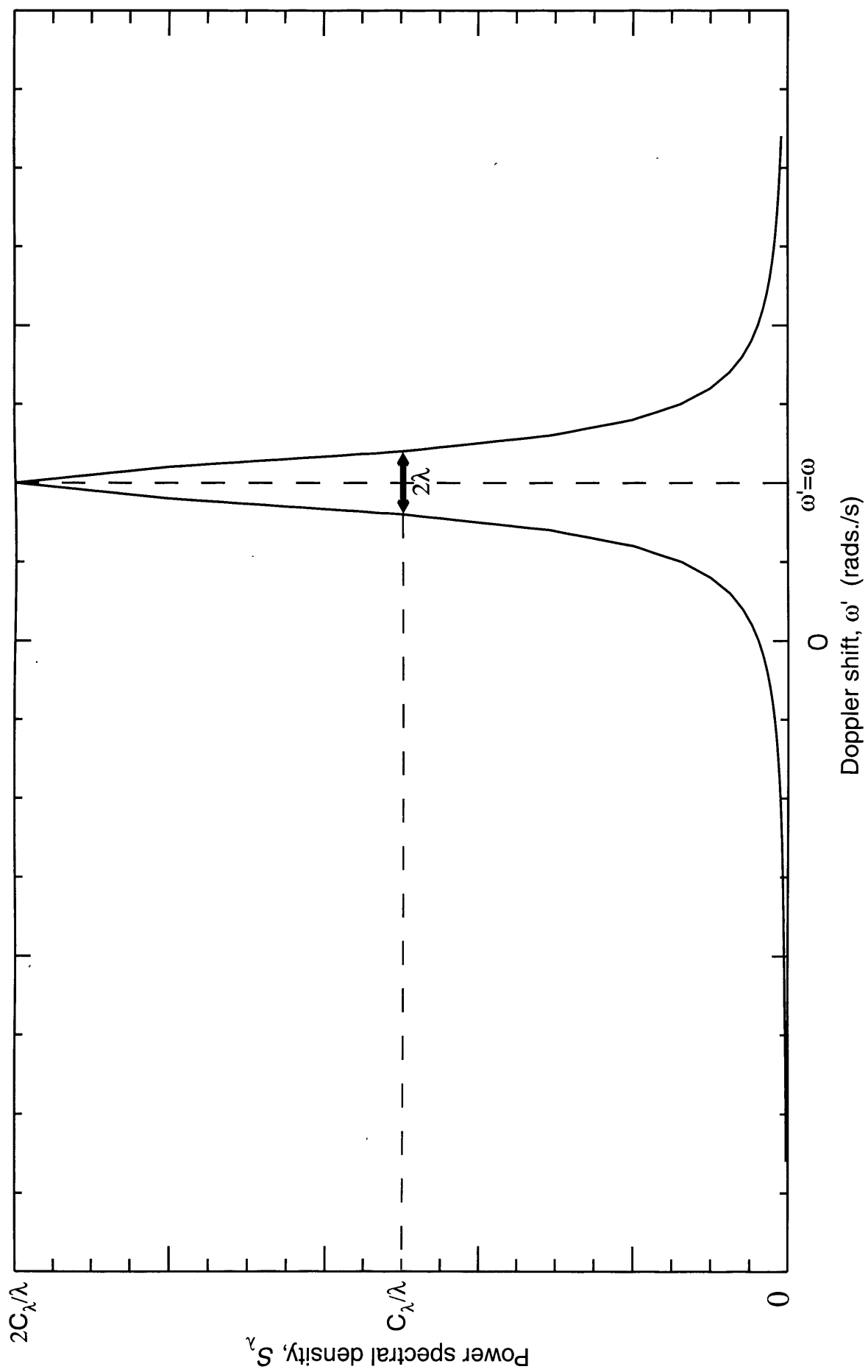


**Fig.3.4.** The power spectrum resulting from the Lorentzian ACF form.

results (Baker et al.,1986). The spectral parameters  $\omega$ ,  $\lambda$ , and  $\sigma$  are obtained directly from the 17 point ACF. The parameters associated with irregularity decay,  $\lambda$  and  $\sigma$ , are found by a linear least squares fit on the logarithm of the ACF magnitude as a function of lag, and the Doppler shift parameter,  $\omega$ , is found by a linear least squares fit on the phase angle  $\tan^{-1}(I/R)$  as a function of lag, where  $R$  and  $I$  are the real and imaginary parts of the ACF respectively. The mean Doppler shift in angular frequency  $\omega$ , is related to the mean spectral phase velocity  $v_0$  and the radar wavelength  $\lambda$  by the following expression

$$\omega = \frac{2\pi v_0}{\lambda} \quad (3.6)$$

One of the main advantages of the ACF fitting routine over the discrete Fourier transform approach is that a much better velocity resolution is obtained, being of the order of 10 m/s instead of 50 m/s. The power received by the radar is defined as lag zero of the ACF, but is actually obtained more efficiently from the lag zero intercept of the least squares fit on the ACF magnitude.

### 3.3 The EISCAT radar facility

The European Incoherent Scatter (EISCAT) facility comprises three radars, a tristatic UHF radar, which commenced full operation in 1982, a monostatic VHF system and the more recently constructed EISCAT Svalbard radar (ESR). The VHF radar, which has been operating since 1985, has both transmitter and receiver co-located at Tromso, northern Norway. The transmitter of the UHF system is located at Tromso, and receivers are sited at Tromso, Kiruna in Sweden and Sodankyla in Finland. The ESR is a monostatic UHF radar sited at Longyearbyen in Spitsbergen, some 1000 km to the north of Norway.

In 1906, J.J. Thomson demonstrated that a single free electron is capable of scattering electromagnetic radiation, and it was proposed by Fabry (1928) that this 'Thomson' scatter might be used to probe the ionospheric plasma. This form of scatter is incoherent as it will occur even if the electron distribution is random, in other words, structure in the electron density, which would result in coherence, is not necessary for backscatter to occur. For wave lengths significantly longer than the Debye length of typically 0.3 cm to 6.0 cm, which includes the wavelength range used by EISCAT, the scatter is in fact quasi-coherent, resulting from the presence of ion-acoustic and electron-acoustic waves which satisfy the Bragg criterion in relation to the investigating radar wavelength. Only over length scales which significantly exceed the Debye length does electrostatic coupling allow organised plasma motions which can support these 'acoustic' or 'pressure wave' modes. The spectral shape

associated with quasi-coherent scatter essentially has four peaks, corresponding with the electron and ion acoustic wave modes, travelling both towards, and away, from the radar. However, the ion lines are sufficiently close together that they often merge, whereas the electron or 'plasma' lines are sharp and distinct (Fig.3.5). The ACF analysis is enabled either by 'long pulse', or by a sophisticated alternating phase coded pulse scheme (Lehtinen and Häggström, 1987), designed to overcome conflicting objectives of high spatial and spectral resolution. A separate 'power profile' pulse is transmitted when using the alternating code, to overcome the problem that lag zero is unavailable, and is used in the determination of the electron density profile.

EISCAT routinely measures profiles of electron density and line of sight plasma velocity along the beam direction. A plasma velocity vector is available at the tristatic point using the UHF system. Other plasma parameters which can be obtained include the ion and electron temperatures, for which an ion composition has to be assumed. By assuming equal ion and electron temperatures, the ion-neutral collision frequency can be determined for altitudes below 120 km, also estimates of electric fields, current densities and conductivities can be obtained by making various additional assumptions. The parameters of relevance to this thesis are electron density, and line of sight and tristatic velocities. The mechanism of incoherent scatter and the derivation of all the parameters which can be either measured directly or derived by making various additional assumptions are extensively reviewed in the literature (e.g. Benyon and Williams,1978).

### **3.4 The IRIS Riometer**

IRIS, imaging riometer for ionospheric studies (Browne et al.1995), is located at Kilpisjarvi in northern Finland, (20.79E,69.05N). It is operated by Lancaster University, and commenced operation in September 1994. The relationship between the field of view of IRIS and the CUTLASS radar is displayed in figure 3.6(a), the IRIS beam pattern is displayed in figure 3.6(b), with the location of the EISCAT radar also indicated. The system samples the level of background cosmic radio noise at 38.2 MHz, which shows a predictable diurnal power variation; any anomalies in this received power result from either changes of HF absorption in the ionosphere, especially the D region, or from scintillation. Scintillation, is a focusing and defocusing of the signal, which occurs if a radio star passes through the field of view, and is analogous to the visible twinkling of a star. The signal from radio stars can therefore be tracked across adjacent beams as the earth rotates, and can mask interesting absorption features which may be present. Beam formation is carried out by an assembly of Butler

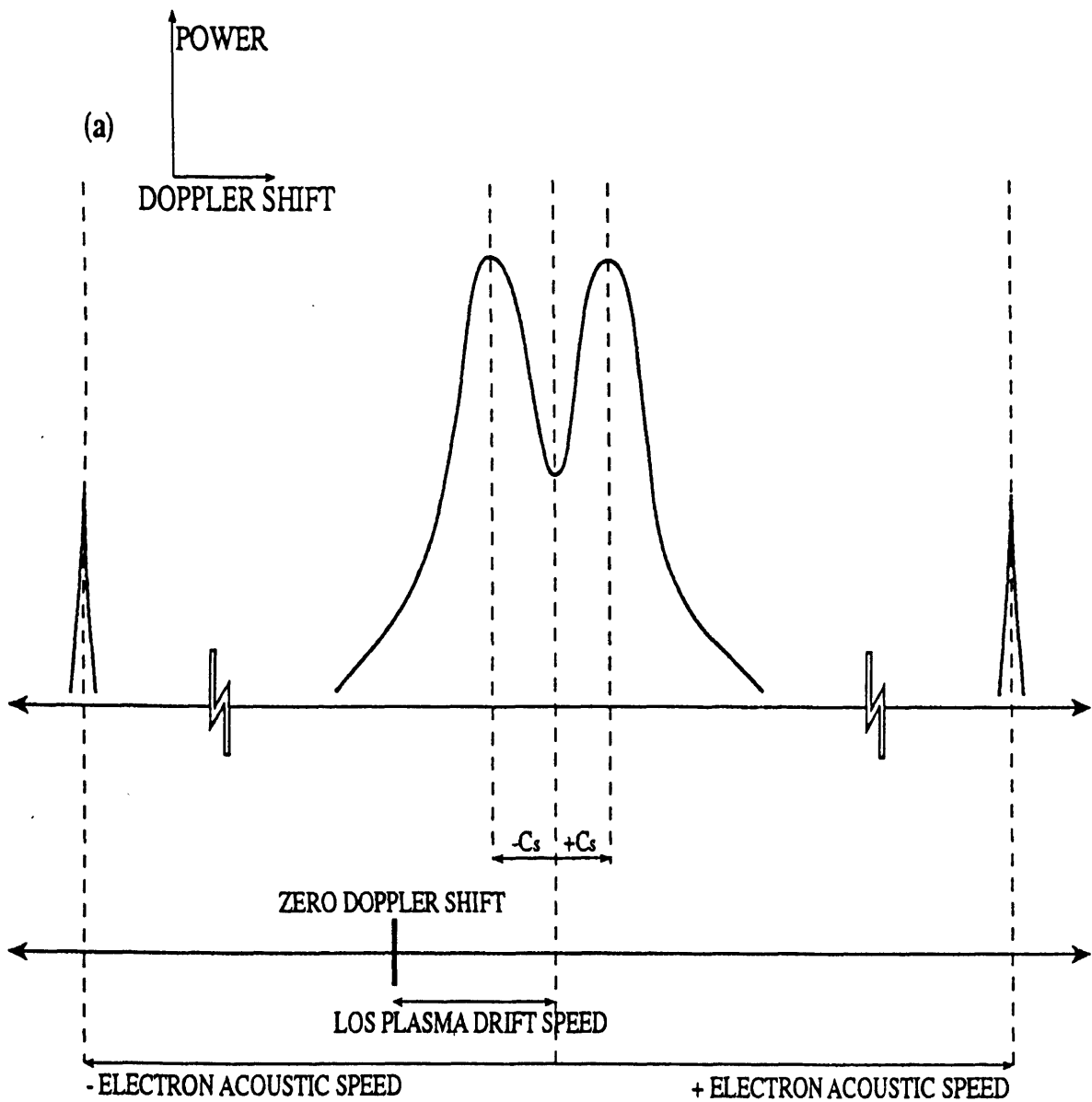


Fig.3.5. Incoherent scatter spectrum (Eglitis, 1994).

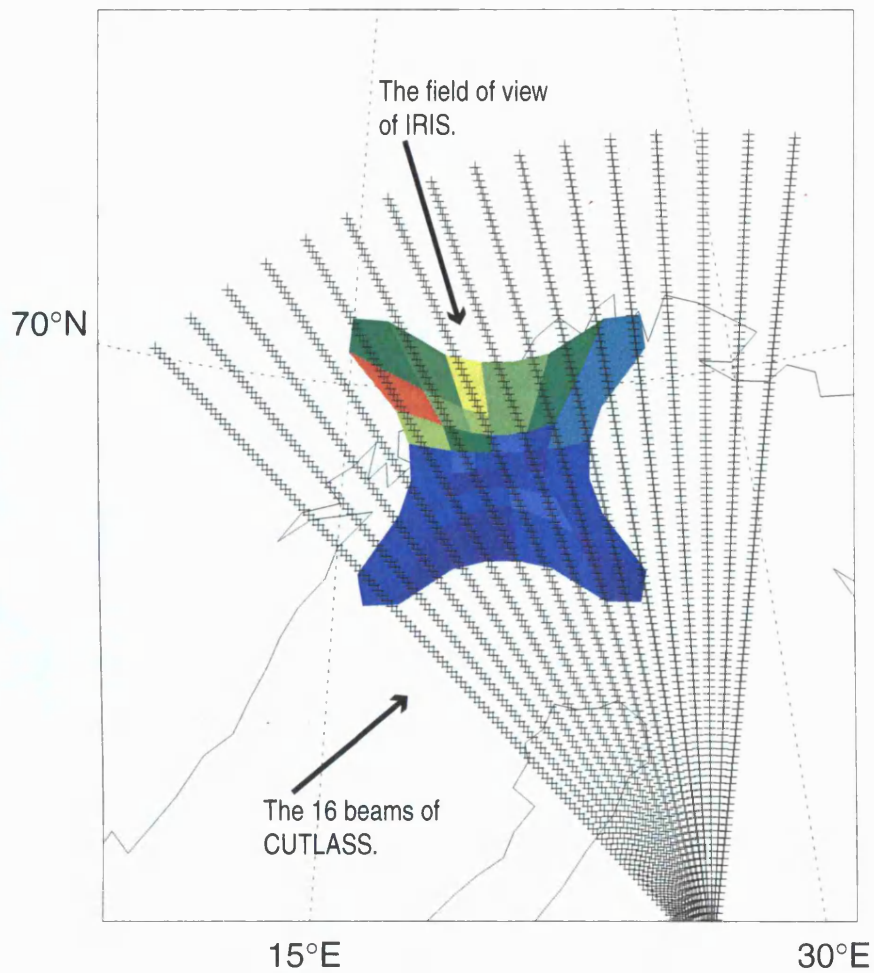


Fig.3.6(a) The relationship between the field of view of CUTLASS and that of IRIS.

### KILPISJÄRVI IRIS BEAMS

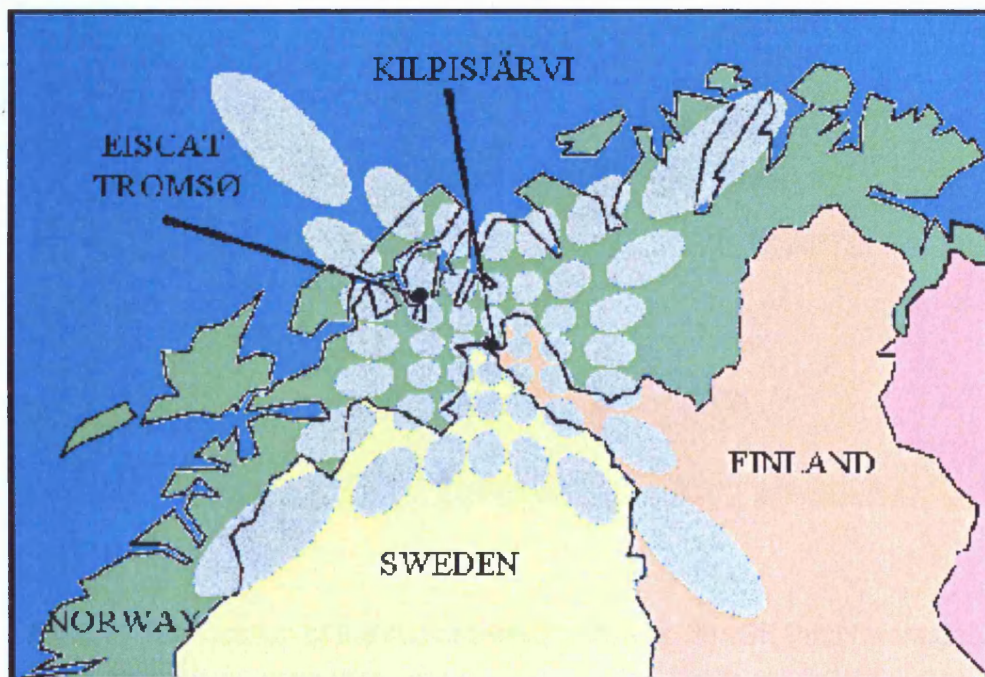


Fig.3.6(b) The beam pattern of IRIS (<http://www.dcs.lancs.ac.uk/iono/iris/>).

# IMAGE Magnetometer Network

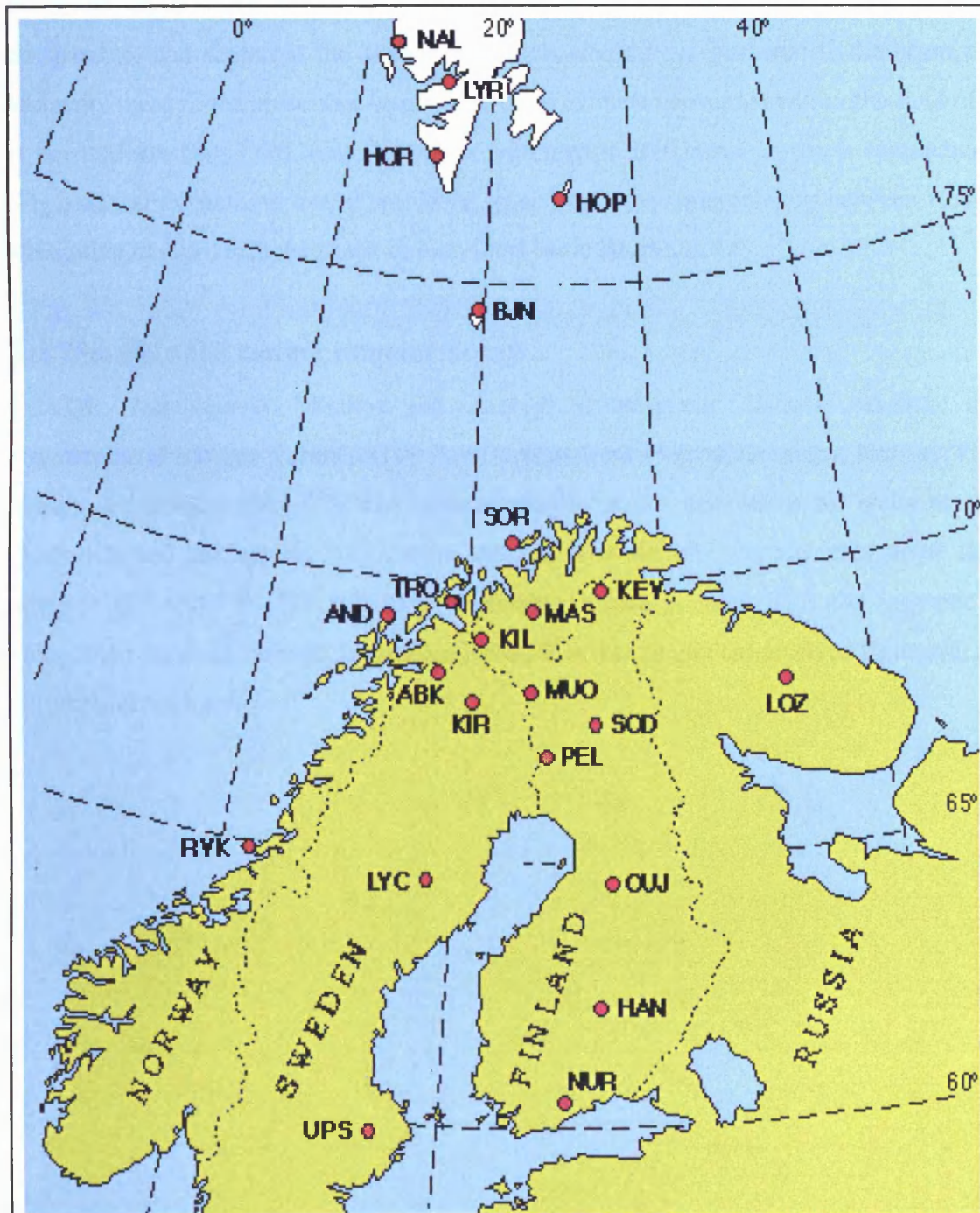


Fig.3.7. The location of the stations which make up IMAGE (<http://www.geo.fmi.fi/image/stations.html>).

matrices (Detrick, 1990), the phasing resulting in 49 narrow beams, of width between 13 and 16 degrees (fig.3.1b). The beam intersections shown are at 90 km, since a large proportion of the total absorption normally occurs at around this altitude (chapter 5). The absorption is calculated by subtracting the received power from a corresponding quiet time power curve (the power curves being expressed in dB), and then multiplying this figure by the cosine of the zenith angle of the beam. The absorption values attributed to the beams are then directly comparable, and represent the absorption which would have occurred if the beam passed vertically through the absorbing layer. Although the beam coverage within the field of view is not uniform (Fig.3.6b), map data plots presented in this thesis are on a continuous grid (Fig.3.6a), since nothing useful would be gained by either interpolating between beams, or attempting to reproduce the shape of individual beam intersections.

### **3.5 The IMAGE magnetometer array**

IMAGE, International Monitor For Auroral Geomagnetic Effects, consists of 23 magnetometer stations maintained by 9 institutions from Finland, Germany, Norway, Poland, Russia and Sweden (Fig.3.7). The prime objective of this network is the study of auroral electrojets and propagating 2-D current systems. The stations range in geographic latitude between 60° and 79°. The following coordinate system is used. **X** is the magnetic field component resolved towards geographic North, **Y** is the component resolved Eastward, and **Z** vertically downward.

# Chapter 4

## HF ray propagation in a magnetoplasma

### 4.1 Introduction

The aim of this chapter is to cover some of the basic features of radio wave propagation in a plasma or magnetoplasma, concerning in particular, wave refraction and attenuation, and ray tracing by computer program. The Appleton-Hartree equation for the refractive index of HF radio waves in a magnetoplasma, is central to the theory of radio wave propagation, and is introduced in section 4.2.2; some of the more straightforward properties of HF propagation which follow from it are examined in the remainder of the chapter.

### 4.2.1 HF radio wave propagation

The first instance of long distance over the horizon radio communication around a substantial curvature of the earth was achieved by Marconi on 31 December 1901, when he succeeded in transmitting a radio signal from Cornwall, England, to Newfoundland, Canada. During a voyage on the liner S.S. "Philadelphia" in 1902, Marconi discovered that radio signals can be received over much greater distances at night than in the day, contrary to theoretical predictions of workers at the time, who based their calculations on the diffraction of radio waves around the protuberance of the earth. It was suggested independently by Kennelly (1902), and Heaviside (1902), that the observations made during Marconi's voyage might be explained by the presence of an electrically conducting layer in the earth's upper atmosphere, capable of reflecting radio waves back towards earth. This conducting layer became known as the Kennelly-Heaviside layer, and is now known as the ionosphere. It was pointed out by Joseph Larmor (1924), that the ionosphere could not be regarded as a conductor for the purposes of modelling radio wave refraction, as this would result in the wave undergoing excessive absorption in the process of refracting sufficiently to return to earth. It was therefore concluded that the plasma should be regarded as a non isotropic dielectric, and is one of the assumptions used in the derivation of the Appleton-Hartree equation.

### 4.2.2 The refractive index of a magnetoplasma

In general, the wave propagation number  $k$  is complex, with a non zero imaginary part implying that the medium is dissipative. An exponentially decaying plane wave solution of the form  $e^{i(\omega t - kx)}$  is considered. The complex refractive index is defined as

$$n = (\mu - i\chi) = \frac{ck}{\omega} \quad (4.1)$$

The Appleton-Hartree dispersion relation for the refractive index of a magnetoplasma may be expressed in the following form, after Ratcliffe (1959)

$$n^2 = (\mu - i\chi)^2 = \frac{c^2 k^2}{\omega^2} = 1 - \frac{X}{1 - iZ - \frac{Y_T^2}{2(1 - X - iZ)} + \left[ \frac{Y_T^4}{4(1 - X - iZ)^2} + Y_L^2 \right]^{\frac{1}{2}}} \quad (4.2)$$

where,

$$X = \frac{\omega_p^2}{\omega^2} = \frac{N_e e^2}{\epsilon_0 m_e \omega^2}, \quad Y = \frac{\omega_H}{\omega} = \frac{eB}{m_e \omega}, \quad Z = \frac{\nu}{\omega}.$$

$\omega_H$  is the electron angular gyrofrequency,  $\omega_p$  is the plasma angular frequency,  $\omega$  is the wave angular frequency,  $e$  is the electric charge of an electron,  $m_e$  is the mass of an electron,  $\epsilon_0$  is the permittivity of free space,  $N_e$  is the plasma electron density,  $B$  is the external magnetic field magnitude,  $\nu$  is the collision frequency between electrons and all other particles,  $Y_L = Y \cos \theta$ ,  $Y_T = Y \sin \theta$ , and  $\theta$  is the angle between the direction of the wave phase propagation and the external magnetic field. The L and T subscripts therefore stand for longitudinal and transverse.

Full details of the derivation of the Appleton-Hartree equation are given by Davies (1969). A number of simplifying cases which will be considered in the next section, in order to gain insight into the nature of propagation in the ionosphere.

### 4.2.3 Magnetic field can be neglected and negligible collision frequency

To illustrate some straightforward features of radio wave propagation, the case of small  $Z$  and small  $Y$  in the Appleton-Hartree equation (4.2) is considered. Small  $Y$  is a physically realistic assumption at all wave frequencies considered in this thesis due to the wave frequency being much larger than the electron angular gyrofrequency. With these assumptions, Equation. 4.2 reduces to the following

$$n^2 = \mu^2 = 1 - X = 1 - \frac{\omega_p^2}{\omega^2} \quad (4.3)$$

It follows from this expression that a wave whose frequency is less than the plasma frequency cannot propagate, the plasma frequency being a lower bound upon waves which

can propagate, and the group velocity  $v_g \rightarrow 0$  as  $\omega \rightarrow \omega_p$ . A wave which can no longer propagate will reflect, and so a wave of angular frequency  $\omega_0$  propagating with vertical incidence through a horizontally stratified layer will reflect if it reaches a plasma frequency  $\omega_v$  such that  $\omega_0^2 = \omega_v^2 = \frac{Ne^2}{\epsilon_0 m_e}$ . The layer whose plasma frequency is  $\omega_v$  and electron density  $N$  is able to reflect a wave propagating with oblique incidence angle  $\phi$ , whose angular frequency  $\omega_{ob}$  is greater than the corresponding frequency  $\omega_0$  of the wave which reflects with vertical incidence (Fig.4.1), and this is summarised by the following relationship, a consequence of Snell's law, and known as the secant law

$$\omega_{ob} = \omega_v \sec \phi. \quad (4.4)$$

This relationship is based on a horizontally stratified ionosphere and a flat earth, but the relationship may also be expressed in a form which applies to a curved earth as follows:  $\omega_{ob} = k\omega_v \sec \phi$ . The additional factor  $k$  is dependant upon the ground range and allows for the curvature of the earth; for short ranges  $k=1$  and the expression reduces to the flat earth form, but for extreme ranges, the curvature of the earth is significant and  $k \approx 1.2$  (Sharp, 1959).

#### 4.2.4 Transverse propagation with field and collisions

The propagation of a wave whose propagation vector is normal to the external magnetic field can be independent of the magnetic field, which can be seen by substituting  $Y_L = 0$  into the Appleton-Hartree equation (4.2) and choosing the positive sign for the square root term; if the negative sign is chosen, the propagation is dependent upon the magnetic field. A characteristic wave is one which can propagate in a medium without change of wave polarisation, and in a magnetoplasma there are two characteristic waves; the wave defined by choosing the positive sign in the Appleton-Hartree equation is called the ordinary (O) wave and the other is the extraordinary (X) wave. In the collisionless case, the ordinary wave with transverse propagation has a real polarisation number, the wave is linearly polarised, and the electrons in the plasma move parallel to the magnetic field. Generally the polarisation number is a complex, indicating a phase difference between the wave field components, so that the waves are elliptically polarised; the ellipses described by the electric field vectors of the O and X modes rotate in the opposite sense from each other.

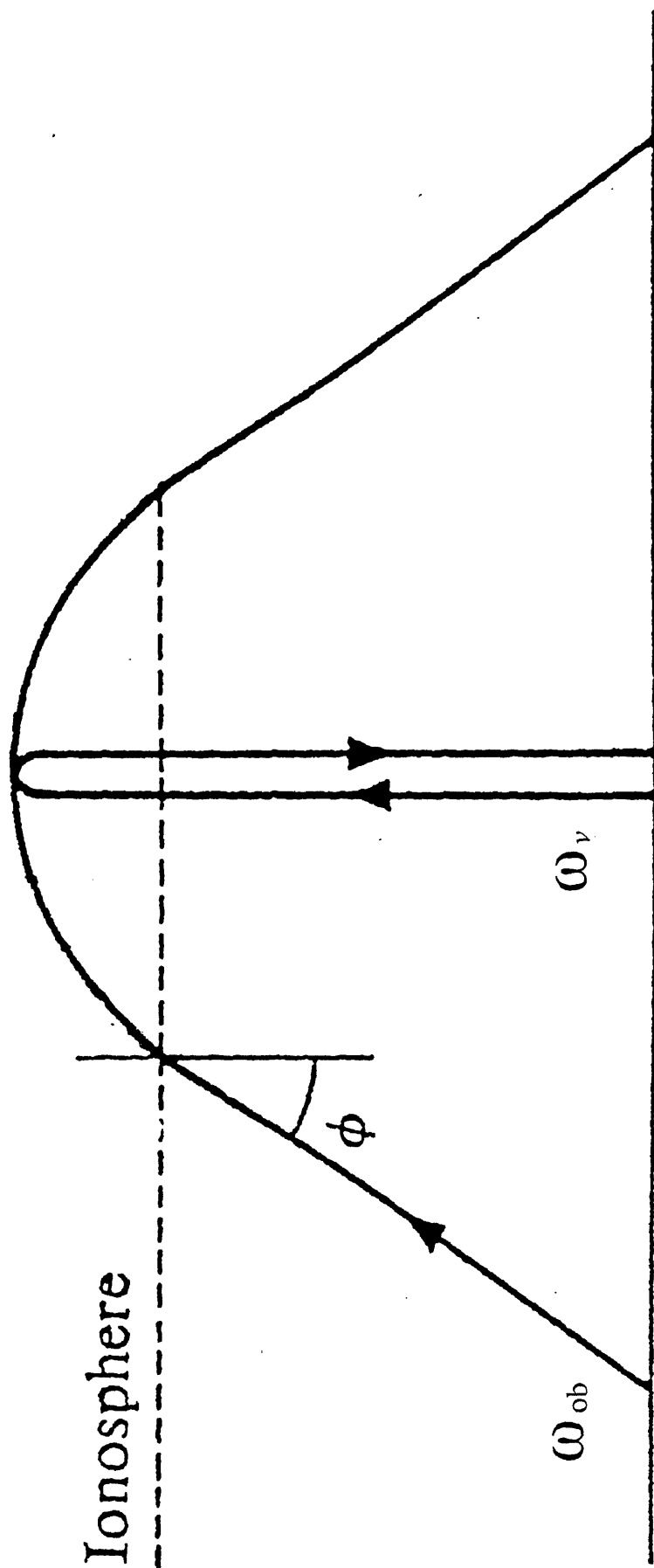


**Fig.4.1.** Schematic illustration of oblique and vertical ray paths in the context of the secant law (Davies, 1969).

### 4.2.5 A collisional plasma and negligible magnetic field

With the (physically appropriate) assumption of small  $Y$  in the Appleton-Hartree formula (4.2), the equation reduces to

$$n^2 = (\mu - i\chi)^2 = 1 - \frac{X}{1 - iZ} \quad (4.5)$$

The effect of collisions is to cause attenuation of the wave, its energy being converted largely into plasma thermal energy; the complex term in the refractive index and the corresponding term in the wave number show that the wave electric field vector decays exponentially with distance. The complex wave propagation number is  $k = (k_{real} - \kappa i)$  where  $\kappa$  is known as the absorption coefficient. It follows from the definition of a complex refractive index (4.2) that  $\kappa = \frac{\omega}{c} \chi$ , and  $\chi$  may be readily obtained from the above equation.

### 4.2.6 Attenuation of HF radiowaves

There are several mechanisms which result in a change of amplitude of a radio wave as the phase front advances, and of these, distance attenuation would usually be the most significant. In an isotropic medium, the power flow per unit area of a wave radiated from a source which is small compared with the propagation distance, will decrease as the square of the distance from the source. Although this inverse square power dependence is very significant for the capacity to receive a broadcast signal, in the case of HF radar, any spreading of the advancing wave is potentially matched by an equal spreading of the scattering cross section, so that the total backscatter from a particular type of scattering medium is independent of where it is placed. The most significant mechanism which can cause radio wave attenuation in the context of HF radar is signal absorption.

### 4.2.7 The absorption of radio waves

It follows immediately by solving for  $\chi$  from 4.5, and substituting this into the definition of the absorption coefficient, that the absorption per unit length  $\kappa$ , is given in the absence of magnetic field by

$$\kappa = \frac{\omega}{2\mu c} \cdot \frac{XZ}{1 + Z^2} = \frac{e^2}{2\varepsilon_0 m_e c} \cdot \frac{N_e \nu}{\mu(\omega^2 + \nu^2)} \quad (4.6)$$

The absorption coefficient becomes large under two circumstances - firstly, for small  $\mu$  : the wave suffers heavy group retardation - effectively, the ray takes a relatively long time to travel unit distance, and therefore dissipates more energy through collisions in travelling unit

distance, whilst undergoing marked curvature of the ray path; the ray theory upon which these equations are based is not strictly valid in the limit  $\mu \rightarrow 0$ , since the wavelength in the medium becomes large, and it is no longer appropriate to assume that the changes in refractive index over a wavelength are negligible (Budden, 1961). Secondly, for large  $N_e \nu$ , with  $\omega \gg \nu$  the absorption coefficient becomes large: the wave angular frequency is much larger than the collision frequency for HF radio waves above about 50 km, and the highest absorption coefficient seen in the ionosphere, apart from that associated with a normal reflection and large real part of the refractive index, occurs in the D region.

#### 4.2.8 The absorption along a ray path

The units in which absorption is measured are usually logarithmic, commonly the Neper or the decibel. Two signal amplitudes  $A_1$  and  $A_2$  are said to differ by  $n$  Nepers when  $n = \ln(A_1/A_2)$ . The bel is based on ratios of signal power rather than signal voltages, and uses a log to base 10. The powers  $P_1$  and  $P_2$  differ by  $B_1$  bels when  $B_1 = \log(P_1/P_2) = 2\log(A_1/A_2)$ . It follows from these definitions that 1 Neper = 8.68 decibels. The total absorption  $L$ (Nepers) which occurs over a particular path is found by integration of the absorption coefficient  $\kappa$ (Nepers/m) along the path  $s$ :-

$$L = \int_s \kappa ds \quad (4.7)$$

#### 4.2.9 Non-deviative absorption

In the D region and much of the lower E region, HF radio waves undergo very little refraction, since  $\mu \approx 1$ ; the wave angular frequency term dominates over the collision frequency, and the absorption coefficient is inversely proportional to the square of the wave frequency, and directly proportional to the product  $N_e \nu$ . Under these circumstances the absorption coefficient may be approximated by the following equation of non-deviative absorption:

$$\kappa \approx \frac{e^2}{8\pi^2 c \epsilon_0 m_e} \cdot \frac{N_e \nu}{f^2} \quad (4.8)$$

Here, the wave angular frequency  $\omega$  has been replaced by the actual wave frequency  $f$ , which is measured in Hertz. It can be seen in Figure 4.2, which shows the typical variation with altitude of the electron density, the collision frequency, and their product, that the coefficient of non-deviative absorption peaks in the D region, at an altitude of about 80 km,

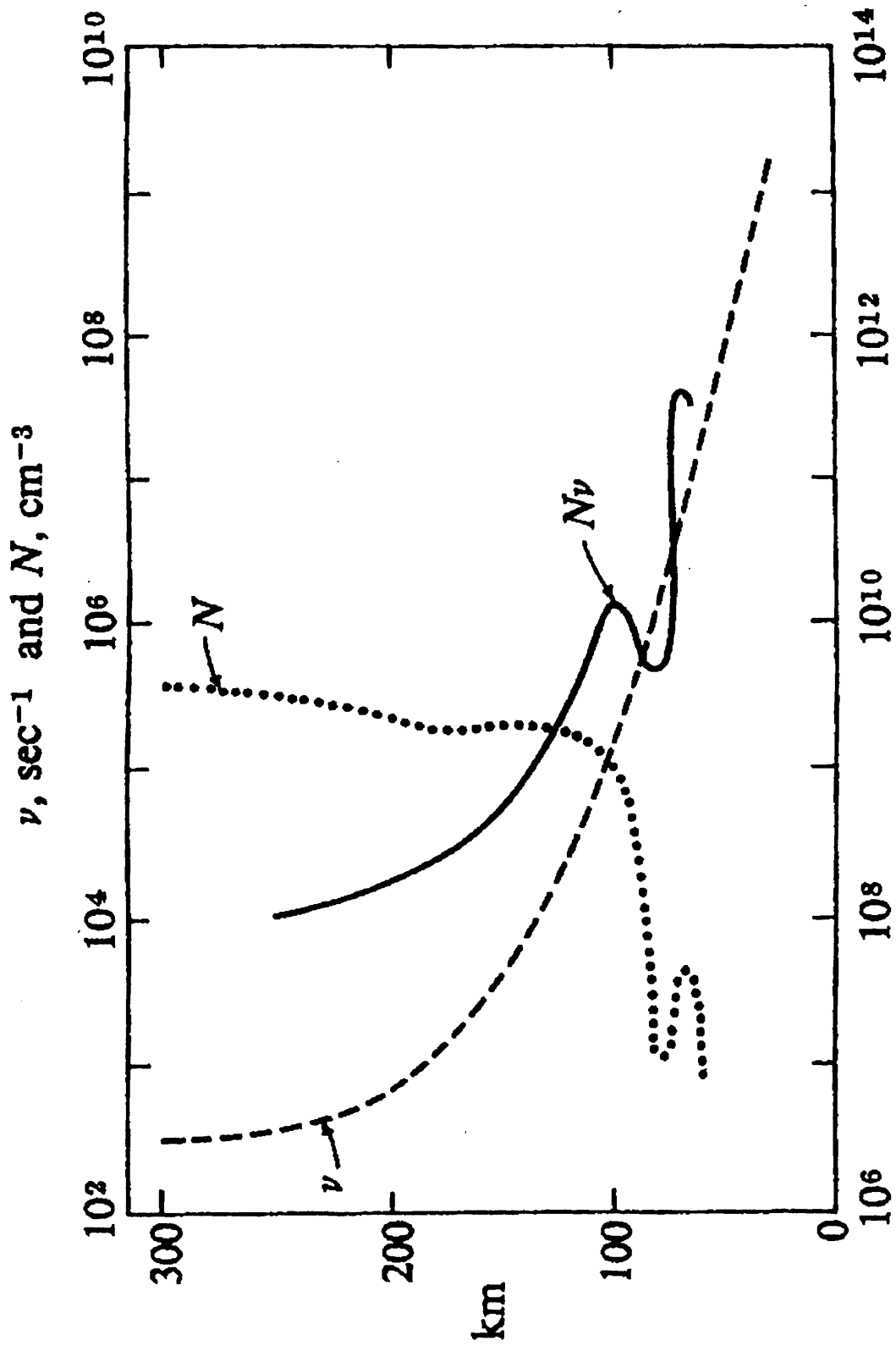


Fig.4.2. Typical profiles of electron density  $N$ , collision frequency  $\nu$ , and their product  $N\nu$ , which controls the rate of nondeviative radio absorption (Davies, 1969).

where it is several orders of magnitude higher than it is in the upper E region and the F region.

#### **4.2.10 Deviative absorption**

For rays incident normally on a horizontally stratified ionosphere, Snell's law shows that the rays will enter a region in which the real part of the refractive index is close to zero; these rays will then undergo considerable deviative absorption. For many of the ray paths considered in the context of HF radar, the propagation is oblique, and the deviative absorption is relatively small or negligible.

#### **4.2.11 Signal fading**

In general, fading refers to any mechanism which can cause a temporal variation in the amplitude of the received signal. Interference between different wave propagation modes, or any temporal variations of plasma density will result in fading. Since the ionosphere is not perfectly homogeneous, any small variations or irregularities in the reflecting surface will cause scattering of a radio wave, so that a received signal does not originate at a point source in the ionosphere; signals scattered from a number of sources, arrive simultaneously at the receiver and interfere with one another to produce fading, a process known as 'interference fading'. There will be a 'beating' between signals whenever different modes arrive simultaneously at a receiver, for instance rays of high and low elevation angles or extraordinary and ordinary rays. Temporal variations in plasma density result in a Doppler shift of the received signal, the size of which will vary for different wave components and propagation modes; this produces spreading of the signal in the frequency domain, and the width of the spread is related to the level of ionospheric disturbance. Doppler spreading of signals on high latitude paths is often much greater than at mid latitudes (Vincent et al., 1968; Hunsucker and Bates, 1969), due to the dynamics processes of the auroral oval.

#### **4.3.1 Ray theory**

In an isotropic, non-dissipative medium, it can be shown by examining the wave field equations that the ray direction is governed by Snell's law (Kelso, 1964), and the refractive index depends only upon the position in the medium. In an anisotropic non dissipative medium however, the situation is more complex, the phase propagation still depends upon Snell's law, but the refractive index depends not only on the position in the medium, but on the phase propagation vector itself; the ray and phase propagation are in general different, and

the calculation of ray paths is much more complex. The ray direction, is defined in ray theory formulations, by either the Poynting vector  $\mathbf{E} \times \mathbf{H}$ , which gives the direction and magnitude of energy flux, or by the direction of group propagation. The group propagation, loosely speaking, is the propagation of points of constant phase in a disturbance formed by the sum of a distribution of waves of slightly different frequencies, centred around the frequency of interest or 'carrier' frequency. It not self evident that rays based on Poynting vector methods should be identical to those based on group propagation, or even that group propagation can always be uniquely defined (Kelso,1964). Comparisons between Poynting vector and wave group methods have been undertaken by Hines (1951(a)) in which he showed that at least in the case of a dispersive and anisotropic, but non-dissipative and homogenous medium, the two approaches are equivalent, whilst in a separate paper Hines (1951(b)) found the Poynting vector approach to be unsatisfactory in a dissipative, anisotropic medium. Great delicacy and attention to detail is required in dealing with the complicated and subtle theoretical and mathematical concepts required to understand ray theory, and is beyond the scope of this thesis, however, a comprehensive treatise of the subject can be found in Kelso (1964) or Budden (1985).

### **4.3.2 The Jones 3D ray tracing program**

The Jones3D programme is one of the most widely used ray tracing computer programmes for radio waves in the ionosphere. For example, it has been used to trace HF rays at high latitudes using meridional electron density distributions (Villain et al., 1984), to locate the SAFARI (Scandinavian and French auroral radar investigation, Villain et al., 1985) HF radar echoes, to simulate the effect of atmospheric gravity waves on the Goose bay HF radar observations (Samson et al., 1990) and to investigate over the horizon equatorial spread doppler clutter problems (Anderson et al., 1996). The program was developed by Jones in 1968, and is described by Jones and Stephenson (1975). The ray tracing method employed, was first developed by Hazelgrove (1955) out of Hamiltonian optics; it is a Poynting vector method, and invokes Fermat's 'principle of least time', which says that a ray between two points is a curve for which the time of transmission is stationary, in the sense implied by the theory of the calculus of variations (Kelso, 1964). This elegant theory reduces the problem of ray path calculation to numerically integrating a set of differential equations, Hamilton's equations, involving only the ray coordinates, the phase index of refraction and its derivatives, the wave propagation vector, and a parameter of integration, the group path.

Hazelgrove's general results are obtained in a formal derivation given by Brandstatter (1959) in a report on the work.

The Jones3D program is able to calculate, as well as the ray path, other useful ray parameters, such as absorption, phase path, group path, and in case of a time varying ionosphere, the doppler shift. The program is controlled through an array of input parameters, which as well as allowing one to initialise the necessary ray and ionospheric parameters, allows one to select from a variety of electron density models, magnetic field models, collision frequency models, perturbations and tilts; the program is structured in such a way as to enable the user, if necessary, to write compatible routines of their own to replace any of these models.

## **Chapter 5**

# **Mechanisms by which substorms affect CUTLASS data and an initial case study**

### **5.1 Introduction**

This chapter is aimed at achieving several objectives in the context of the thesis as a whole; firstly, mechanisms which, from a theoretical standpoint, would be expected to result in there being an association between the extent of the returns seen by the CUTLASS radar, and the precipitation into the ionosphere of energetic particles, are examined. It will then be taken as implicit, that energetic particle precipitation is the essential feature of magnetically active periods and substorms, which links their occurrence with the CUTLASS data loss phenomenon. The second objective is to develop, through the careful analysis of an interval of CUTLASS data loss, a strategy for using to best effect the available supporting data from EISCAT, IRIS and IMAGE. The interval under consideration is from 2200 UT on 18/06/96 until 0500 UT on 19/06/96, during which a period of intense and sustained substorm activity occurred, and nearly all the CUTLASS data were lost. The disappearance of this data is analysed in the context of the suggested mechanisms of data loss (Section 5.2.2), with the aid of ray tracing techniques, and an absorption model based upon EISCAT data, which is applied firstly to IRIS, and then to CUTLASS. The interval being considered in this chapter is a subinterval of a slightly longer interval examined in a study by Milan et al. (1999); his findings are therefore compared and contrasted with those presented in this chapter (Section 5.7).

#### **5.2.1 Signatures of energetic particle precipitation**

Energetic particle precipitation in the auroral zones is associated with magnetically active periods, and enhancements in this precipitation are to be expected during magnetospheric substorms. Energetic particles travel down magnetic field lines and will eventually reflect, unless they have enough energy to reach the more dense regions of the upper atmosphere, where their energy can be dissipated via collisional interactions, resulting in the production of free electrons in the ionosphere. This ionisation provides a signature of the energetic particle precipitation, which may be detected in various ways. An incoherent scatter radar, such as EISCAT, can be used to provide measurements of electron density against altitude, since this is proportional to the returned power; it will therefore detect the size and location of any change in ionisation resulting from energetic particle precipitation. An imaging riometer, such

as IRIS, cannot be used directly to derive an electron density profile, but is still able to detect the ionisation associated with energetic particle precipitation, due to the increased absorption of background cosmic radio noise. Evidence of electron density enhancements are provided by IRIS, but no altitude resolution is available, at least, not from a single riometer, as the measured absorption is an integral value along the entire ray path. A third method for detecting ionisation, and the most commonly used, is the ionosonde. There are several ionosondes in operation in northern Scandinavia, however, they are of only limited use in this thesis, due to the fact that, during the active periods of interest, their signals tend to be absorbed beyond the threshold for detection, and also, the time resolution is often poor.

EISCAT is operational for only a small percentage of the year, and for a yet smaller percentage in the CP-1 mode, in which the UHF beam at Tromsø is aligned along the local magnetic field direction in the F region, an elevation of  $77^\circ$  and azimuth of  $182^\circ$ . However, IRIS is operational continuously, barring any technical difficulties, and is therefore used frequently in this thesis to provide evidence of increased ionisation due to particle precipitation. The data to be presented in this chapter is unusual in that CUTLASS, IRIS and EISCAT were all operating during a period of high magnetic activity, with EISCAT using the CP-1- K mode (Davies et al., 2000).

### **5.2.2 Particle precipitation as an operational constraint on CUTLASS**

Particle precipitation of the type associated with the auroral zones, when present at a certain intensity, is likely to be favourable for the production of ionospheric irregularities, being associated with enhanced E region electrojets and large scale field aligned currents. This is evidenced by the fact that the CUTLASS Finland radar regularly starts to receive ionospheric returns in the midnight sector as Northern Scandinavia effectively rotates underneath the auroral oval (Milan et al., 1997). However, the response of CUTLASS to the higher levels of energetic particle precipitation associated with substorm activity tends to be a drop out or complete loss of received ionospheric backscatter (Yeoman & Lühr, 1997).

For the purposes of this thesis, a radar signal drop out event may be defined as being any occasion on which the radar return signal shows an obvious disappearance, or reduction in received power, over the whole or part of the radar field of view, occurring on a time scale of at least minutes. Clearly the temporal and spatial requirements of this definition could be specified, but these events have been selected from the data set by eye, and therefore stand out as being 'obvious to the naked eye'. All of the radar drop out events found in this way, have a

duration of at least ten minutes, and involve the latitudinal extent of the data being reduced by at least two degrees.

There are three distinct classes of process within the ionosphere which will influence the power of the received signal of an HF radar, possibly resulting in its loss, and all three are related to the plasma electron density and in turn, to energetic particle precipitation.

- Firstly, the signal could suffer absorption. The power of the signal is largely controlled by the electron density in the D region and lower E region (Section 4.4.9), so that an increase in electron density, especially in these regions, will cause the signal to be attenuated.
- Secondly, as previously noted, ionospheric irregularities are field aligned, and produce strong backscatter when the ray's propagation vector is close to being magnetic field orthogonal, the so called 'orthogonality condition'. Any change in the electron density along the ray path will result in a change in the propagation conditions and the ray path will be altered. This will in turn change the power density of suitably field orthogonal ray propagation at any point, thereby causing the radar returns to be redistributed, or even to be lost altogether. It will be demonstrated by ray tracing analysis (Section 5.5.2), that increases in plasma frequency of the order seen during substorm activity, would be likely to alter the radar propagation conditions sufficiently to cause at least a partial signal loss.
- Thirdly, if the scattering structures (the ionospheric irregularities), were to disappear for any reason, then so would the backscattered signal. As noted earlier, the E region in the auroral zones is a particularly good conductor due to ionising precipitation. During periods of intense substorm associated particle precipitation, the conductivity in the E region is increased, so that, initially steady state currents flow with a divergence, implying a charge redistribution which tends to short out electrostatic fields in the E region; this shorting can map along the magnetic field to the F region and beyond (Kelley, 1989). The shorting process is significant in relation to the production of ionospheric instabilities, since viable plasma instability mechanisms will have electric field dependence. For example, the two-stream instability in the E region is predicted to switch off completely when the electric field falls beneath a threshold value (Chapter 2), whilst the growth rate of the generalised  $\mathbf{E} \wedge \mathbf{B}$  instability in the F region, may become small during precipitation, due to E region shorting effects (Vickrey and Kelley, 1982). It seems likely therefore, that both E and F region plasma irregularities might be affected by substorm activity, perhaps being depleted sufficiently to cause a radar drop out event.

Each of the three processes outlined above might in principle lead to a radar drop out event when taken in isolation; however, since each process depends upon an increase in electron

density, it seems plausible, indeed probable, that several of the above processes could act together to produce a radar drop out event. It is straightforward to think of D, E and F region electron density profiles that would effectively isolate each process, and conversely, if it were possible to show that one process was working in isolation, this would convey information about the likely electron density profile over the ray path.

It has already been noted that a radar drop out commonly occurs during a magnetospheric storm or substorm, and the next section comprises a 1<sup>st</sup> study into the underlying physical mechanisms which have resulted in a radar signal loss. Gaining an understanding of these processes is important both as a radar operational constraint, and as a diagnostic of the electrodynamics of the auroral zone ionosphere and its overlying magnetosphere.

### **5.3.1 A case study of a radar signal drop out: 18<sup>th</sup> - 19<sup>th</sup> June 1996**

During an interval from shortly after 2300 UT on 18/06/96 until shortly before 0400 UT on 19/06/96, there was a period of sustained magnetic activity measured throughout the IMAGE magnetometer chain. The CUTLASS (Finland) radar, which was operating in the standard mode, showed an extensive data loss, EISCAT measured substantial increase in electron density and IRIS witnessed a strong cosmic radio noise absorption event.

### **5.3.2 Data from CUTLASS and IMAGE**

Magnetic field perturbations in the X component (positive towards the north) have been plotted for the station at Tromsø together with Pi2 pulsations and a CUTLASS latitude-time-velocity (LTV) plot from 2100 UT on 18/06/96 until 0600 on 19/06/96, using a common time axis for the three plots (Fig.5.1). It is immediately clear when viewing the plots in this way that the radar drop out and the period of enhanced magnetic activity correspond very closely in time. The Pi2 pulsations are quasi-continuous, the magnetic activity having resulted in a succession of substorms. An electron density-time profile from EISCAT (Tromsø) has also been plotted alongside a CUTLASS PTV plot (Fig.5.2), and shows a clear enhancement during the period of the CUTLASS signal loss. The simultaneous nature of the enhanced magnetic activity, the (precipitation induced) enhancement in electron density, and the CUTLASS data loss, strongly suggests that these events are related. The LTV plots presented in this chapter concentrate on beam 5, since this looks over Tromsø (the main EISCAT site), but the spatial time series in velocity (Fig.5.3) demonstrates that all the beams had lost their ionospheric backscatter data by 2322 UT on 18/06/96, and this remained the situation until

# SUPERDARN PARAMETER PLOT

18 Jun 1996<sup>(170)</sup>

to

19 Jun 1996<sup>(171)</sup>

Finland: vel

normal (ccw) scan mode (127)

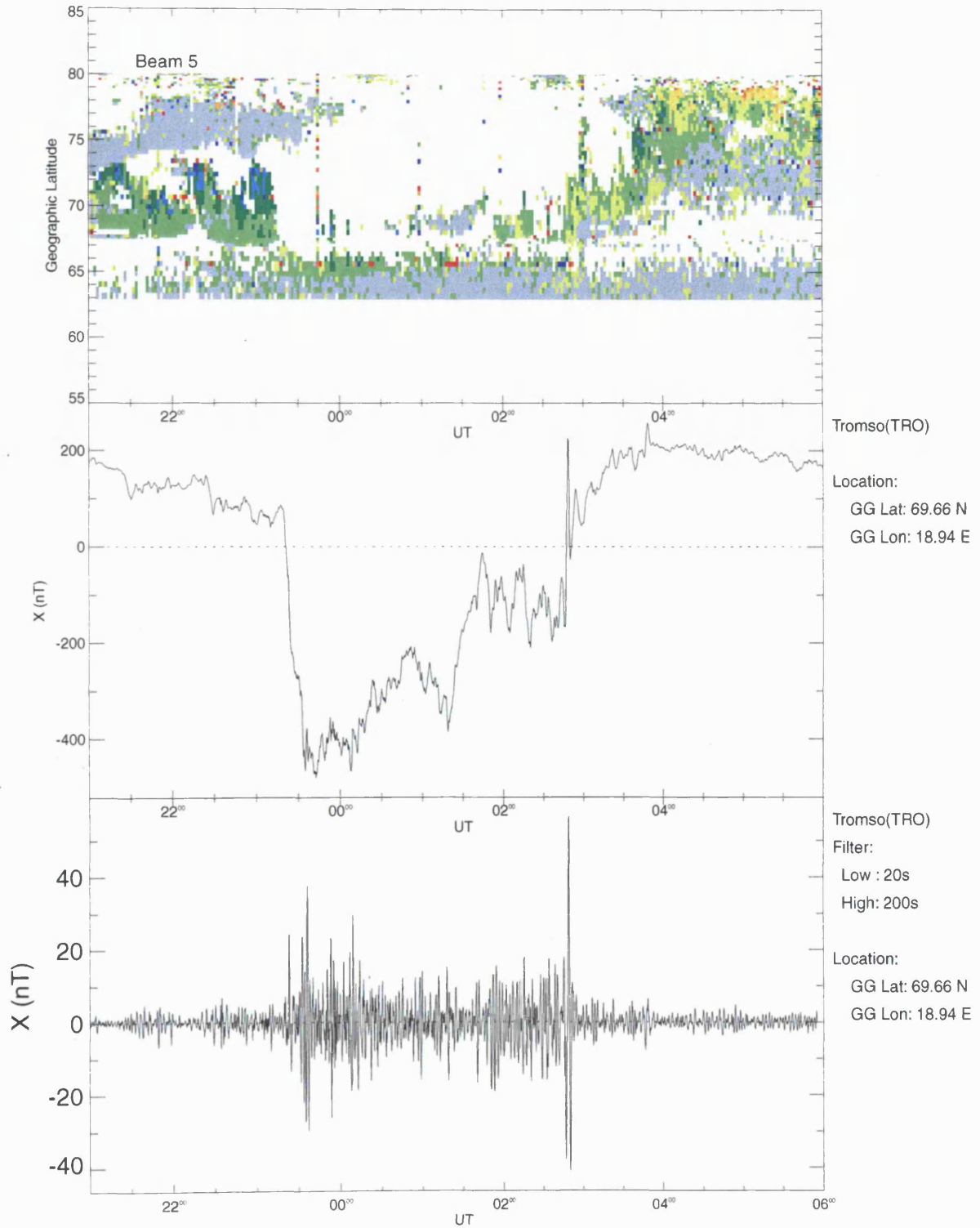


**Fig.5.1.** CUTLASS data together with magnetic X component and Pi2 filtered data from the station at Tromso, showing the correspondence between increasing magnetic activity and the disappearance of CUTLASS data.

# CUTLASS Power / EISCAT CP1 Power Profile

18/19 June 1996

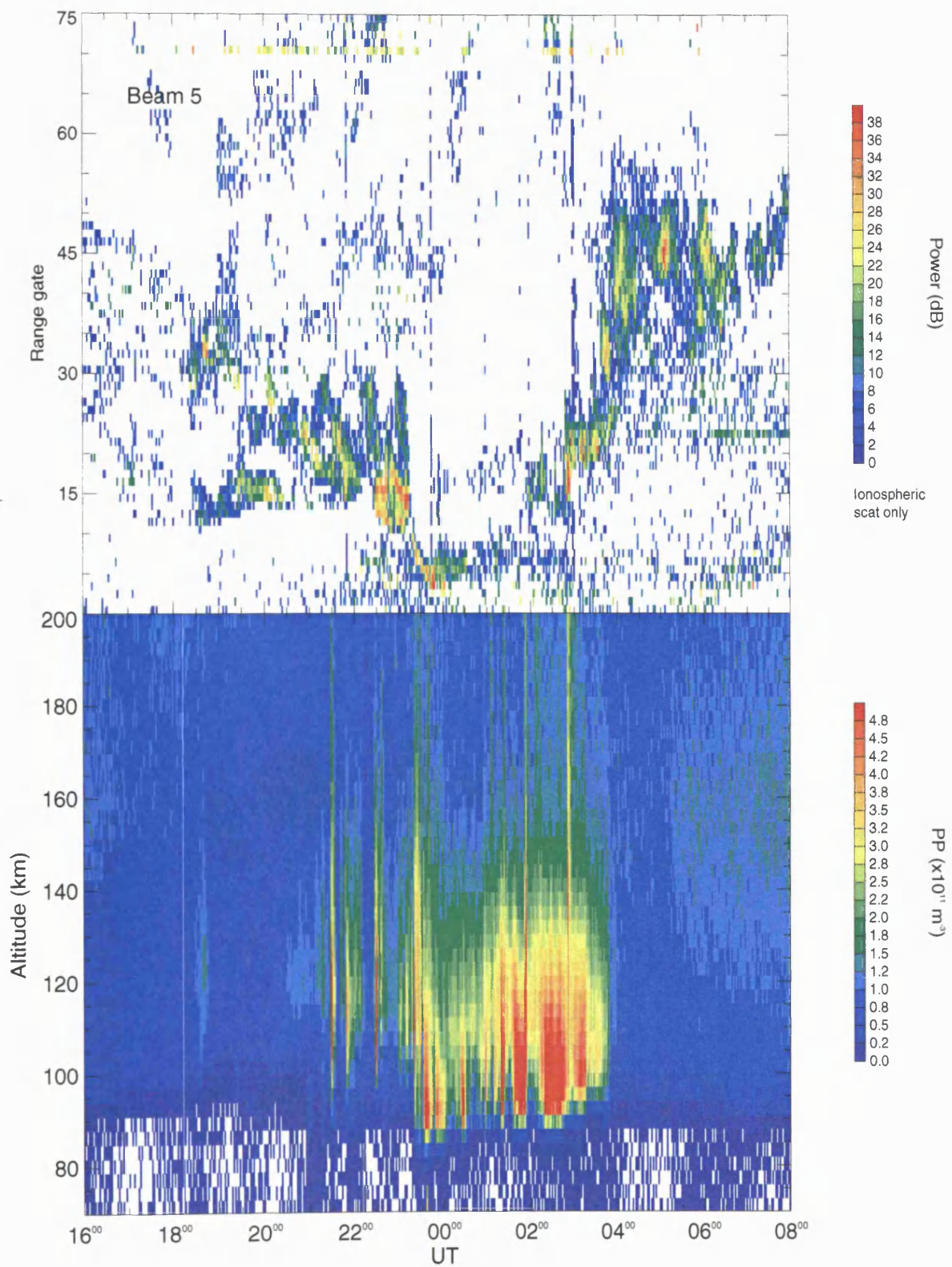


**Fig.5.2.** CUTLASS power data and EISCAT electron density data, showing the correspondence between a period of CUTLASS data loss and a period of electron density enhancement.

# SUPERDARN PARAMETER PLOT

## Finland: vel

18 Jun 1996 <sup>(170)</sup>  
 normal (ccw) scan mode (127)

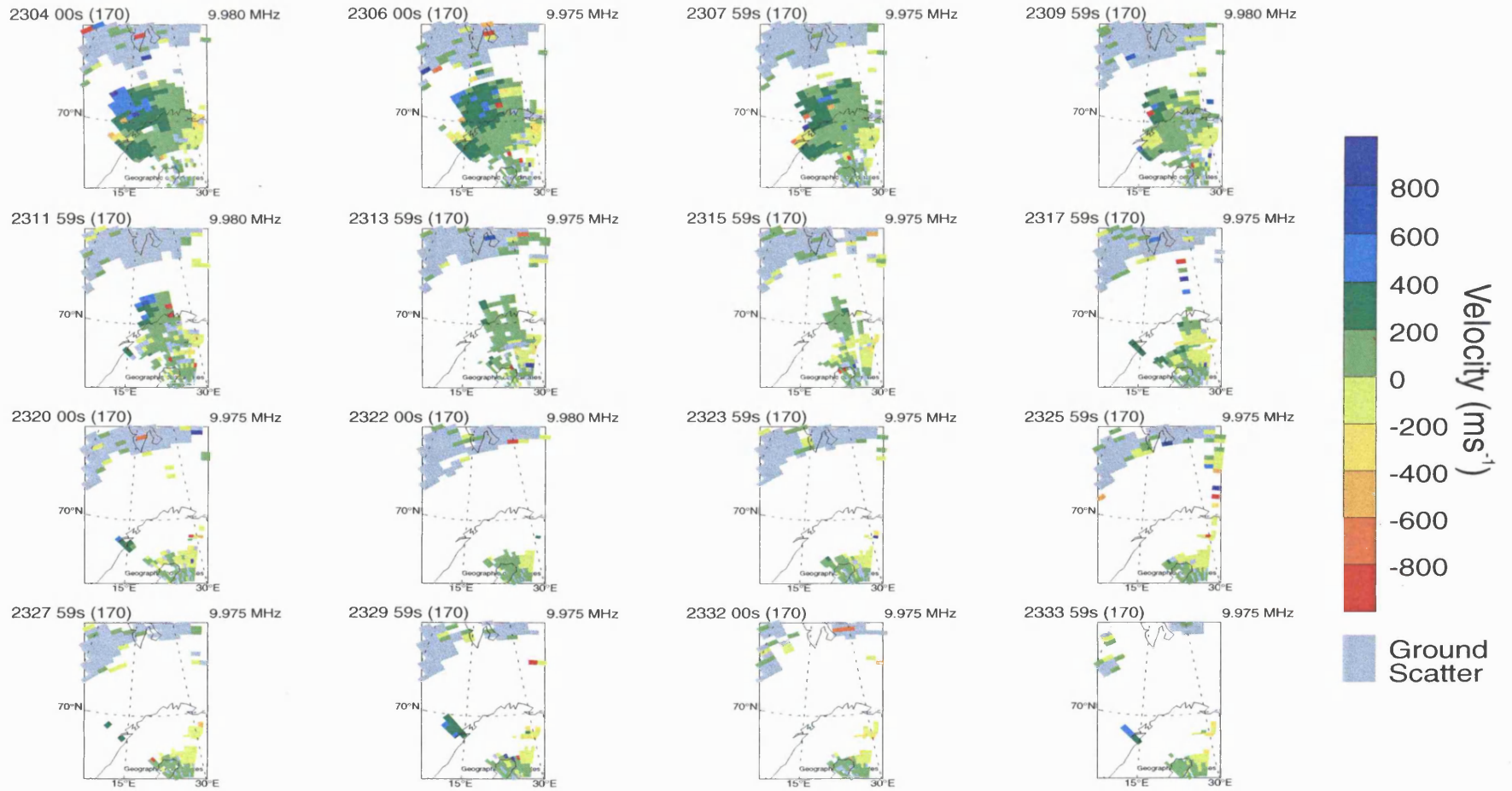


Fig.5.3. Time series of CUTLASS velocity data, leading into the period of sustained substorm activity, showing the loss of CUTLASS data to be widespread.

approximately 0245 UT on 19/06/96. It is noticeable that the ground scatter return evident at about 75 degrees north (geographic) is not affected until some time after the initial disappearance of the ionospheric backscatter return; the reason for this is believed to be that this backscatter originates behind the radar, a point which is discussed further in section 5.6.1.

### **5.3.3 IRIS data**

The 49 beams of IRIS are numbered from 1 to 49, going from the top left to the bottom right, and counting from West to East. With this numbering system, the field aligned CP-1 EISCAT beam direction intersects beam 16 of Iris in the upper D region and lower E region, where radio wave absorption is at a peak (Section 4.4.9). The beam width of EISCAT is however far smaller than that of IRIS, so that EISCAT was looking through a portion of beam 16 of IRIS throughout the interval. The general enhancement in electron density measured by EISCAT at 2320 UT implies that an enhancement in the absorption measured by IRIS is to be expected, at least the vicinity of beam 16, and indeed, an enhancement occurs across the entire field of view, which lasts for several hours (Fig.5.4). The fact that the entire field of view sees enhanced absorption suggests that the active region may be considerably larger than the field of view of IRIS, perhaps covering the greater part of the field of view of CUTLASS (Section 5.6.1).

### **5.4.1 Modelling the absorption measured by IRIS**

Since the interval being studied in this chapter has both an interesting period of enhanced absorption measured by IRIS, and electron density profiles are available from EISCAT (at a location which intersects beam 16 of IRIS in the D region), it has been possible to use the EISCAT electron density profiles together with an empirical atmospheric composition and temperature model (MSIS 90), to model the absorption measured by beam 16 of IRIS during the interval. Theoretical radio wave absorption calculations are later carried out for a frequency of 10 MHz (Section 5.5.2), the frequency used by CUTLASS during the interval, and the implications of these calculations with regard to CUTLASS are discussed (Section 5.6.2).

The EISCAT CP-1-K (Davies et. al., 2000) mode uses a pulse length of 350  $\mu$ s, which provide the long pulse measurements over 21 range gates extending from 140 km to 600 km in altitude; high altitude resolution measurements are obtained in the E- and lower F-region by means of a 16 baud, strong condition, alternating code, with pulse length of 21  $\mu$ s, providing altitude resolution of 3.1 km. In addition, both a 21  $\mu$ s and a 40  $\mu$ s power profile

# IRIS Riometer time\_series

18 Jun 1996 - 19 Jun 1996

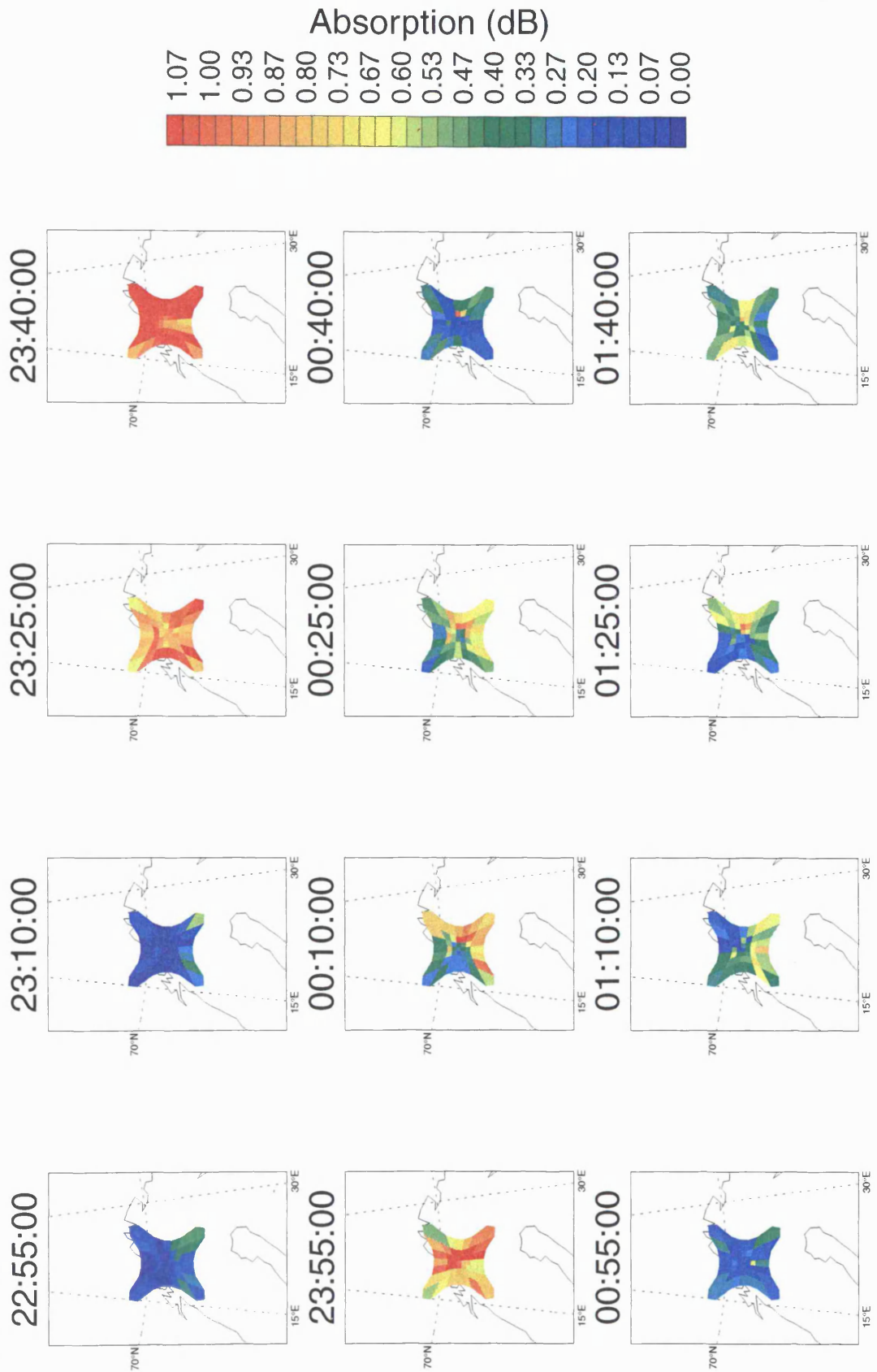


**Fig.5.4.** Time series of cosmic radio noise absorption measured by IRIS, showing that there was a widespread increase in absorption, which corresponded with the loss of CUTLASS data, and persisted for several hours.

pulse is transmitted, the former of which provides the lag zero of the alternating code autocorrelation function, and also provides the basis of the electron density profile used in the forthcoming analysis.

The absorption calculation uses the following equation for the absorption coefficient (Davies,1969), appropriate for a slowly varying plasma and non deviative propagation.

$$\kappa = 4.6 \times 10^{-2} \left[ \frac{N\nu}{\omega^2 + \nu^2} \right] \quad (5.1)$$

Where  $\kappa$ , the absorption coefficient is measured in dB/km,  $N$  is the plasma electron density,  $\omega$  is the wave angular frequency and  $\nu$  an effective collision frequency between electrons and all other particles. For radio wave absorption in the HF or VHF range, the appropriate effective collision frequencies are identical to the standard collision frequencies for momentum transfer (Banks, 1966). The following electron neutral collision frequencies (Schunk and Nagy, 1978) and electron ion collision frequency (Banks,1966) have been used in the absorption calculation

$$\langle \nu_e, N_2 \rangle = 2.33 \times 10^{-11} N(N_2) [1 - 1.21 \times 10^{-4} T_e] T_e \quad (5.2)$$

$$\langle \nu_e, O_2 \rangle = 1.82 \times 10^{-10} N(O_2) [1 + 3.6 \times 10^{-2} T_e^{1/2}] T_e^{1/2} \quad (5.3)$$

$$\langle \nu_e, O \rangle = 8.9 \times 10^{-11} N(O) [1 + 5.7 \times 10^{-4} T_e] T_e^{1/2} \quad (5.4)$$

$$\langle \nu_e, H \rangle = 4.5 \times 10^{-9} N(H) [1 - 1.35 \times 10^{-4} T_e] T_e^{1/2} \quad (5.5)$$

$$\langle \nu_e, He \rangle = 4.6 \times 10^{-10} N(He) T_e^{1/2} \quad (5.6)$$

$$\langle \nu_{ei} \rangle = 54 N_i T_e^{-3/2} \quad (5.7)$$

where  $\langle \nu_e, \text{molecule} \rangle$  is the electron-neutral collision frequency with the specified molecule (units of  $s^{-1}$ ),  $\nu_{ei}$  is the electron-ion collision frequency,  $N(\text{molecule})$  is the number density of the specified molecule (units  $m^{-3}$ ),  $N_i$  is the ion number density (units  $m^{-3}$ ), and  $T_e$  is the electron temperature (Kelvin).

The values of molecular density and temperature used in the collision frequency equations are obtained from the MSIS 90 model (Hedin, 1991).

The absorption coefficient gives the spatial rate change of absorption, and the total absorption is therefore found by integrating the absorption coefficient through distance. In this case it is appropriate to integrate through height, as the absorption measured by IRIS has

been normalised by dividing by the relative path length of the beam. EISCAT makes one sample every 2 minutes, and successive altitude gates are separated by 3.1 km. The total absorption has been calculated in the most straightforward way, by assuming that the absorption coefficients are constant between each EISCAT range gate; the calculation also insists that data exists in at least 40 of the first 50 range gates, otherwise no point is plotted. The calculation is completed at range gate 50 of EISCAT or an altitude of 210 km, any contributions to the total absorption above this height being negligible. Although in this case, the absorption calculation is applied to a vertical path, the following absorption integral allows a ray to propagate at a general angle  $\theta$  to the vertical

$$A(t) = 4.6 \times 10^{-2} \sum_{g=1}^{g=50} (h(g+1) - h(g)) (\sec \theta(h, \text{lat}, \text{lon})) \left( \frac{N(g, t)_{\text{EISCAT}} \nu(h, \text{lat}, \text{lon}, t)_{\text{MSIS}}}{\omega^2 + \nu^2(h, \text{lat}, \text{lon}, t)_{\text{MSIS}}} \right) \quad (5.8)$$

where,

$A$  = the total absorption ( a function of time and units dB)

$g$  = the range gate number of EISCAT

$t$  = time (the start of an EISCAT integration period)

$h$  = the altitude at the start of each range gate (a function of gate)

lat = latitude of a point on the path

lon = longitude of a point on the path

$N$  = electron density measured by EISCAT (a function of gate and time)

$\nu$  = the collision frequency between electrons and all other particles (this is the sum of the collision frequencies given by equation 4.2 - 4.6. The molecular temperature and density values come from MSIS and are themselves functions of altitude, latitude, longitude and time.

$\omega$  = the angular wave frequency of interest

The absorption calculated in this way has been plotted (black), together with the measured values from IRIS beam 16 (red) for the interval from 2100 UT on 18/06/96 to 0400 UT on 19/06/96 (Fig.5.5). The modelled and measured values are clearly in reasonably good agreement, especially when one considers the number of possible sources of error in the values which have been input to the model, i.e. EISCAT electron density profiles, and an MSIS empirical model. Another factor, which will tend in general to cause the modelled values to be an overestimation of the IRIS data is the following – The IRIS quiet power curve

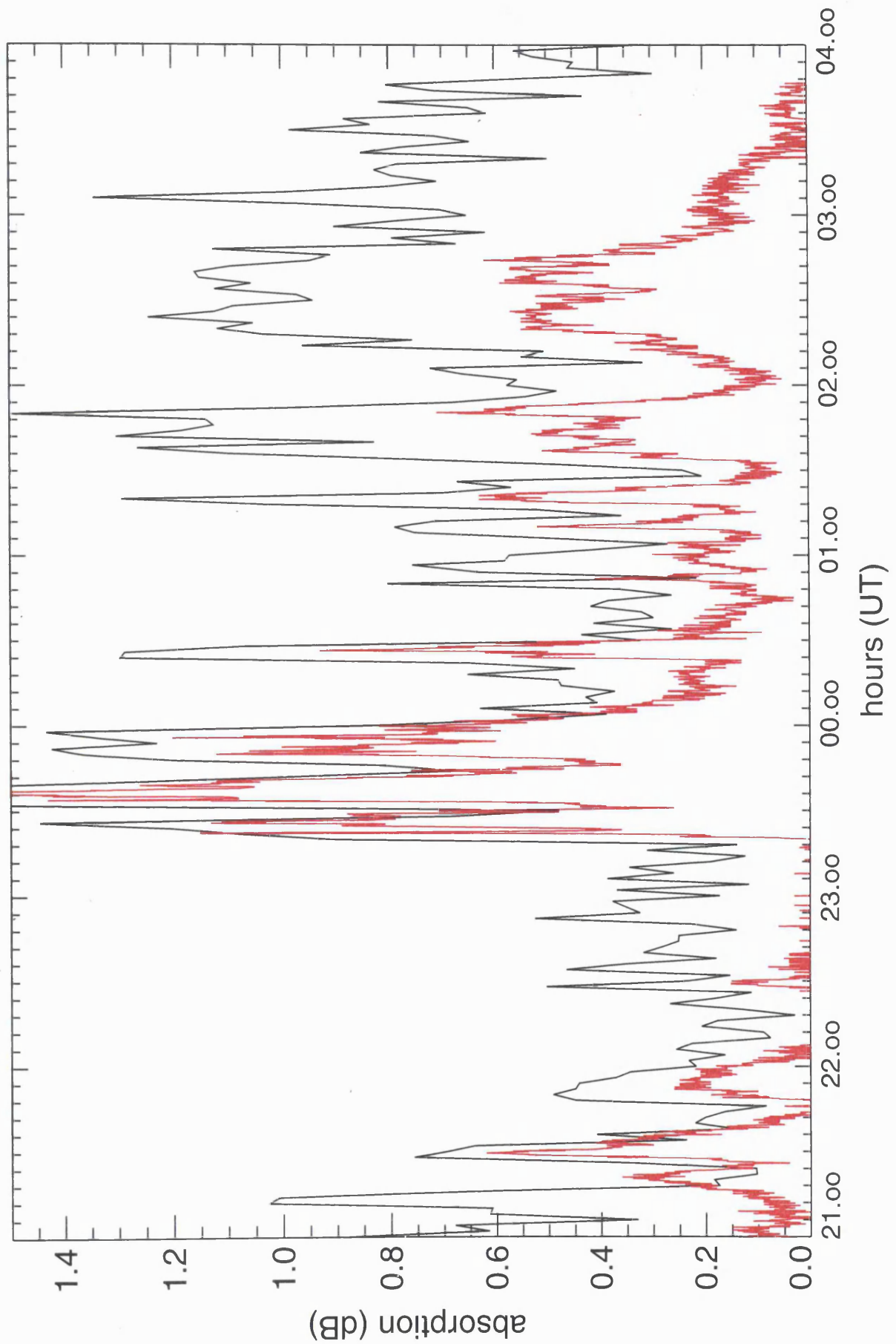


**Fig.5.5.** Absorption data from beam 16 of IRIS (red), together with modelled absorption (Black) for the interval between 2100 UT on 18/06/96 and 0400 UT on 19/06/96.

is a lower power level than would be the case if there were no ionosphere, and hence no absorption at all. This means that derived IRIS absorption, found by subtracting the received power from the quiet time power, is not quite the same thing as our absorption model has calculated since we have not accounted in our model for the fact that the quiet time power is itself already reduced by an unknown level of 'quiet time' absorption. The fact that our model values are in reasonable agreement with the IRIS data suggests that the necessary theoretical offset needed in our model is slight.

### **5.5.1 Modelling the absorption experienced by CUTLASS**

Having modelled the absorption of IRIS and found a very good correspondence between modelled and measured values, the question of applying this model, or at least a slightly modified version of it, to the absorption experienced by CUTLASS will now be addressed. Rather than modelling the total absorption for each available point in time, along a fixed elevation angle, it is now desirable to model the total absorption against elevation angle, using electron density profiles from fixed points in time, representing the conditions before and during the interval of CUTLASS data loss. Examination of EISCAT electron density profiles in a time series leading up to the active period (Fig.5.6) suggests that it would be reasonable to use the profile from 2318 UT on 18/06/96 as representative of the profiles from before the substorm induced enhancement, and the next profile in the time series from 2320 UT, at which point the enhancement initially occurred, as representative of the active period, during which the CUTLASS data was lost. Notional straight line propagation is assumed, at a range of elevation angles, using the CUTLASS operating frequency of 10 MHz. The assumption of straight line propagation is appropriate, since the vast majority of the total absorption occurs in the D region and lower E region, where the plasma frequency is not high enough to result in a great deal of refraction when considering propagation at 10 MHz. This assumption will also enable the separation of the effects of absorption and propagation when analysing data in respect to CUTLASS operation. Although the calculated absorption assumes straight line propagation, this does not mean to say that the rays penetrate the layer at a fixed angle; the earth's curvature continually changes the effective angle at which the straight line path passes through an assumed horizontally stratified layer, and this has been included in the formulation. The absorption calculation is again based upon Equation 5.8, however, the IRIS operating frequency is now replaced by the CUTLASS operating frequency, and a correction factor is applied to each term in the summation, which accounts for the angle at which the ray is passing through the layer at that point on the ray path. The correction factor is calculated

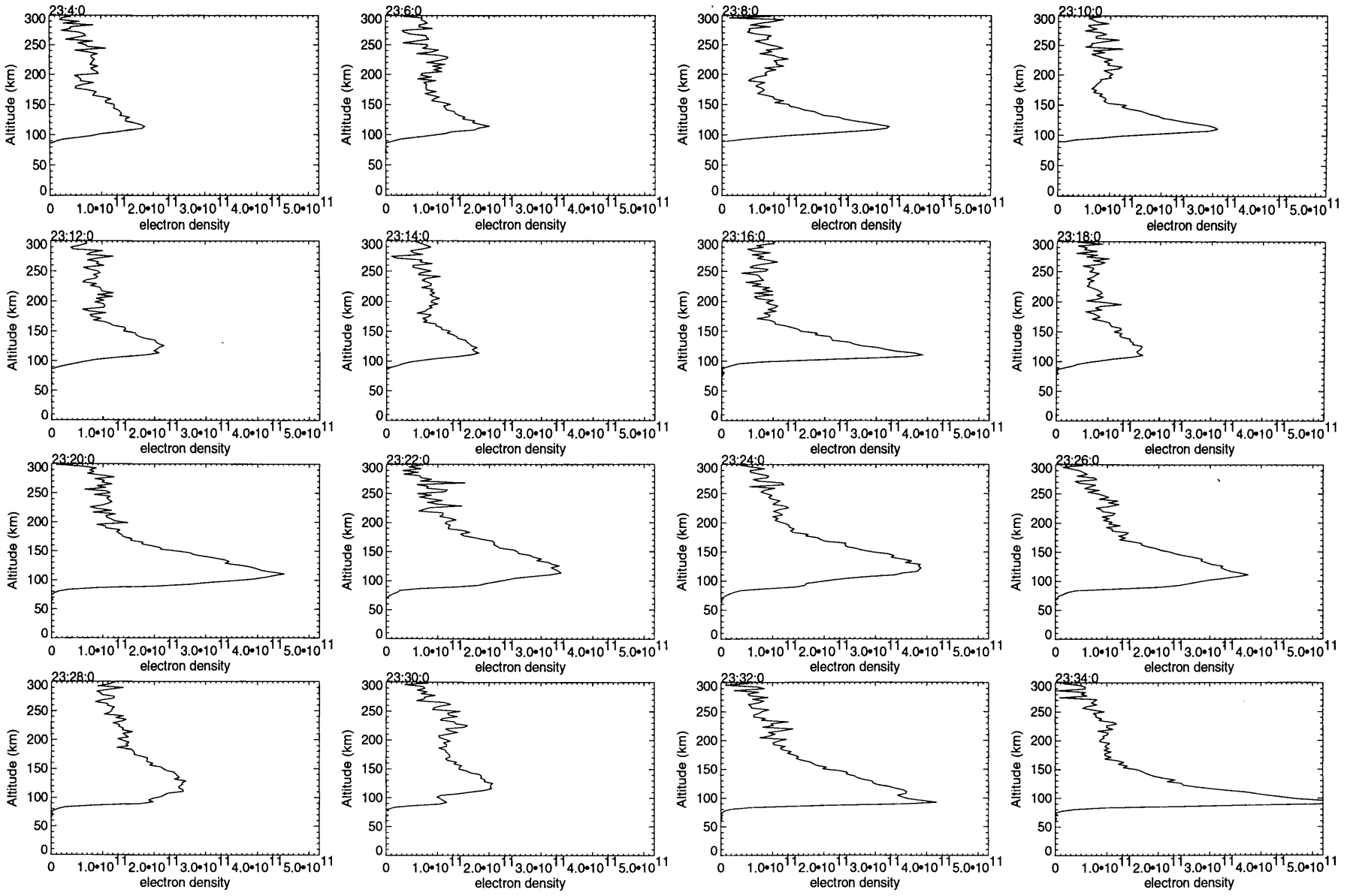


**Fig.5.6.** Time series of EISCAT electron density profiles, leading into the magnetically active period which commenced shortly after 2300 UT on 18/06/96. The profiles from 2318 UT and 2320 UT were chosen as representative profiles from before and after respectively, the onset of the active period.

for each point in the summation, by taking the altitude associated with the point, then working out the great circle range at which a ray of the given elevation angle will reach the given altitude, and converting this range into a great circle angle, which is equal to the appropriate angular offset to be applied to the initial elevation angle, which is used to work out the path length through the layer at that point in the sum. The absorption calculation has been terminated when the ray reaches the ground range of Tromsø at  $69.6^{\circ}$  geographic latitude, since this is a typical range from which backscatter is received during the event. Finally, the total calculated absorption is doubled, since the backscattered radiation has passed through the absorbing layer twice (i.e. out and back). The absorption calculated from the two profiles is depicted in Figure 5.7, and is discussed in detail in section 5.6. For elevation angles above about  $5^{\circ}$ , the absorbing layer is completely penetrated, but below this angle the absorbing layer is only partially penetrated so that absorption starts to reduce. The absorption profile representative of prior to the active period (Fig.5.7a) has a peak absorption of 11 dB at an elevation angle of  $5^{\circ}$ , and the absorption profile representative of during the active period (Fig.5.7b) has a peak absorption of 75 dB at an elevation angle of  $4^{\circ}$ . For the lowest elevation angles, the considerable reduction in absorption from the peak might go some way towards negating the lower power radiating and receiving capacity of the antennae at these angles, and indeed, interferometer measurements indicate that low elevation angles are not uncommon (Chapter 7).

### **5.5.2 Ray tracing applied to propagation paths of CUTLASS**

The EISCAT profile from 2318 UT will again be regarded as being a representative plasma frequency profile prior to the precipitation enhancement, and the profile from 2320 UT as representative of the period covering the precipitation enhancement. The Jones3D ray tracing program has been used to model radio wave propagation at 10 MHz, the operating frequency of CUTLASS, through plasma frequency profiles provided by functional fits found for the profiles at 2318 UT and 2320 UT (Fig.5.8). The form used for the fitting is the sum of two Chapman layers (Equation 1.6), since this form is compatible with the code used by Jones3D, and the fitting was achieved manually by adjusting the six model parameters. With the assumption that the active region of precipitation gradually covered the whole ray path, the implication is, that the mode of propagation of CUTLASS might have evolved from something resembling the ray trace through first profile (Fig.5.9), into something resembling the ray trace through the second profile (Fig.5.10). The ray paths, which include relevant annotations, will be used in the forthcoming analysis of the CUTLASS data loss (Section

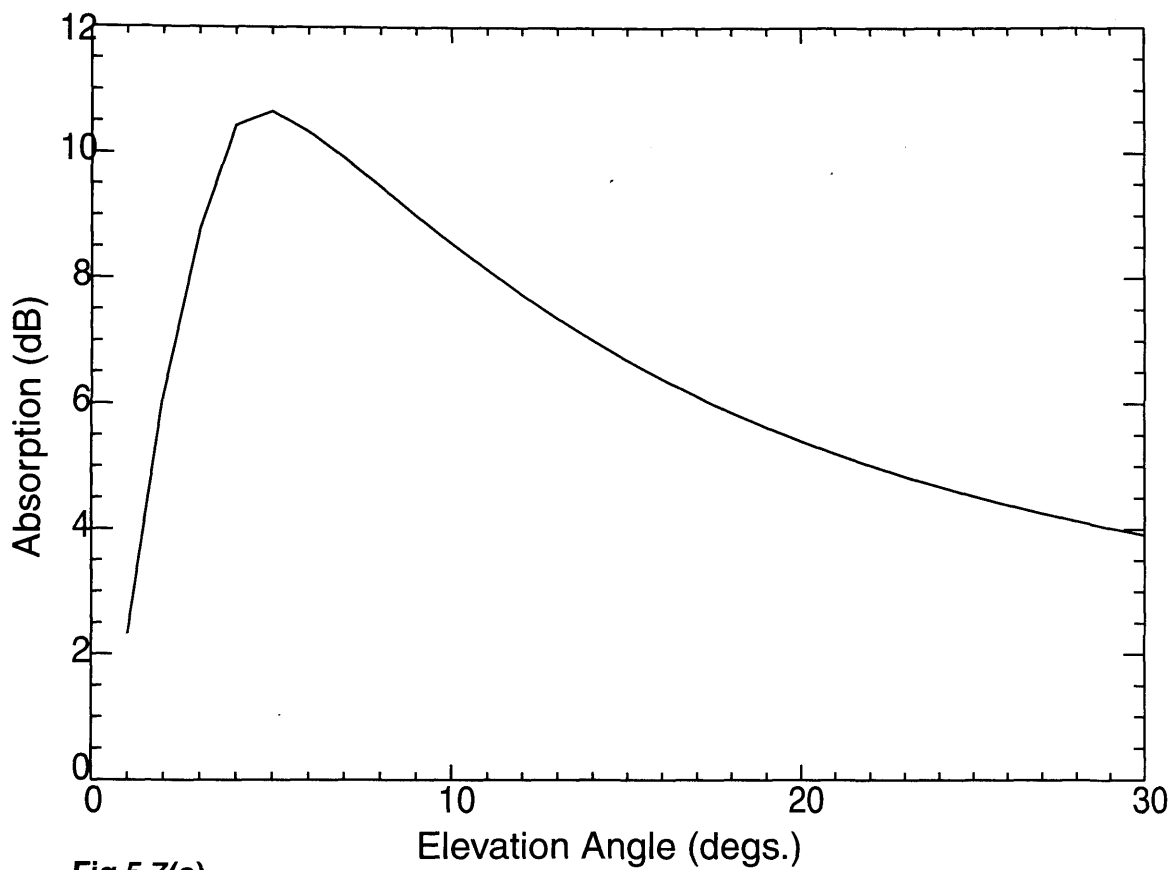


Fig.5.7(a)

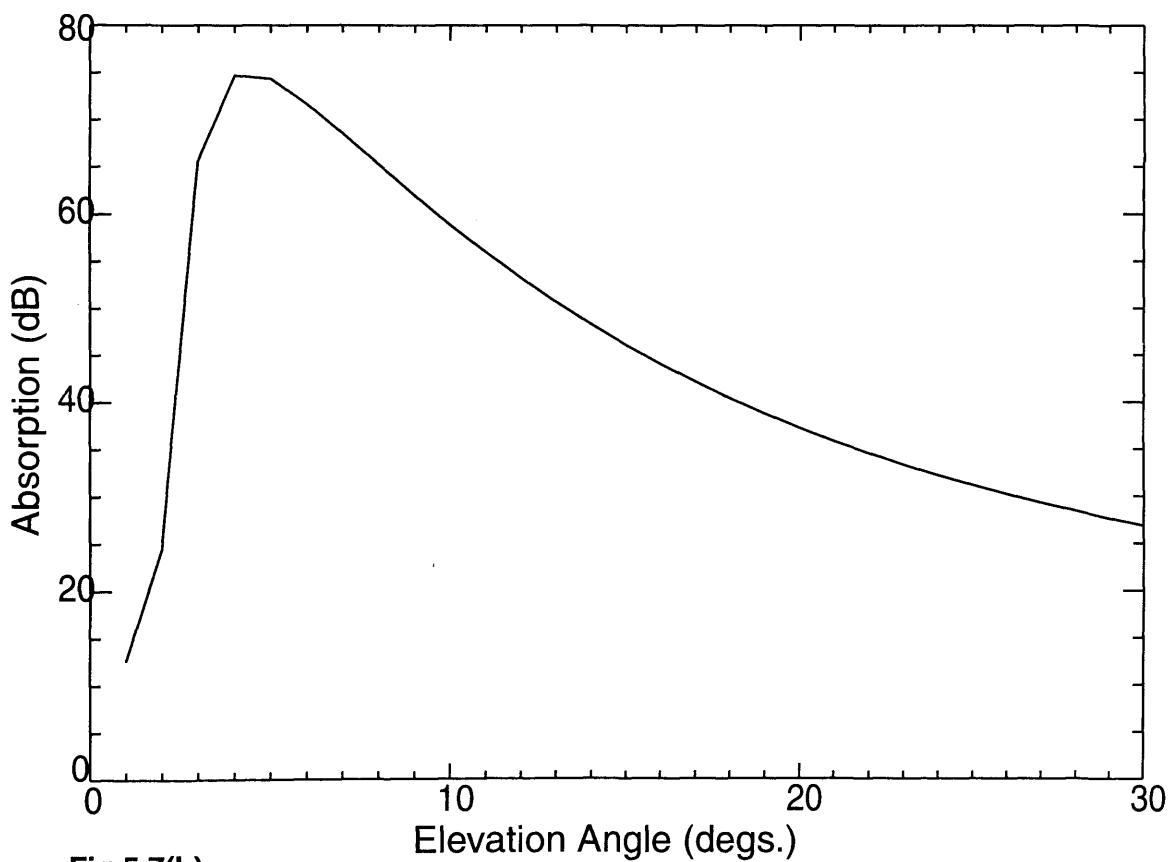
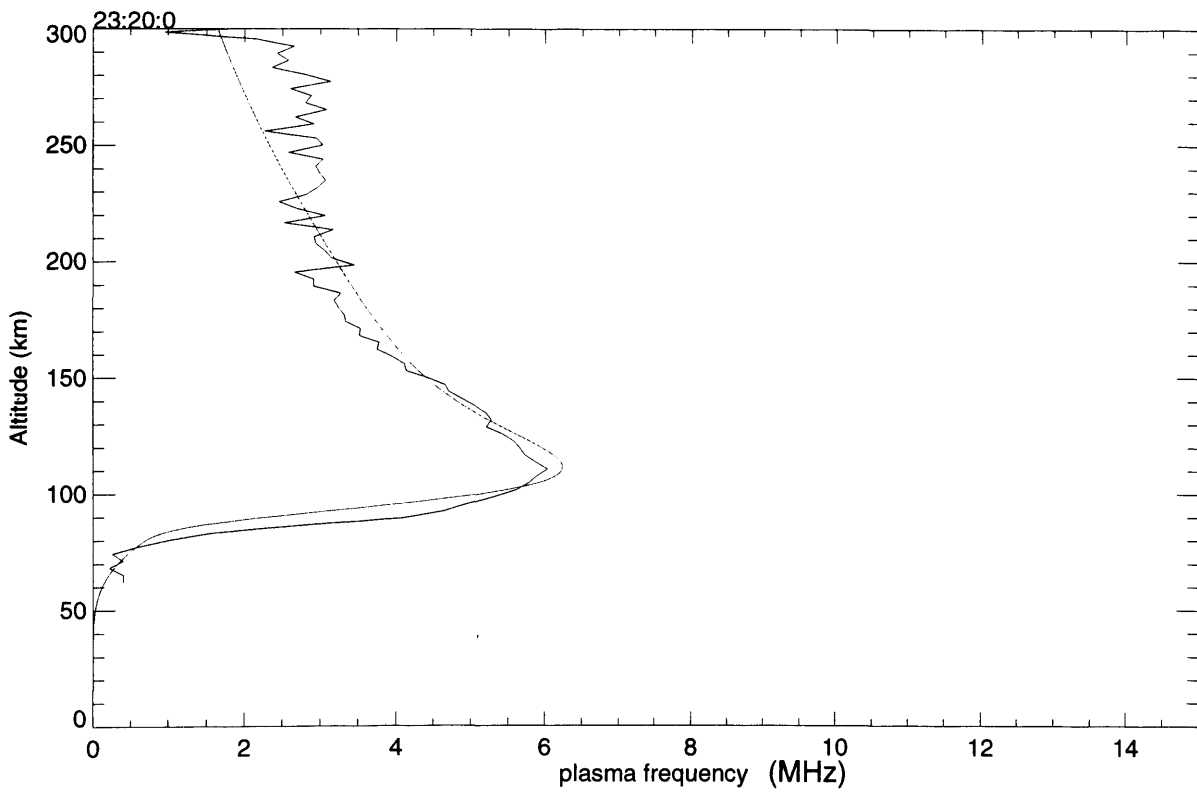
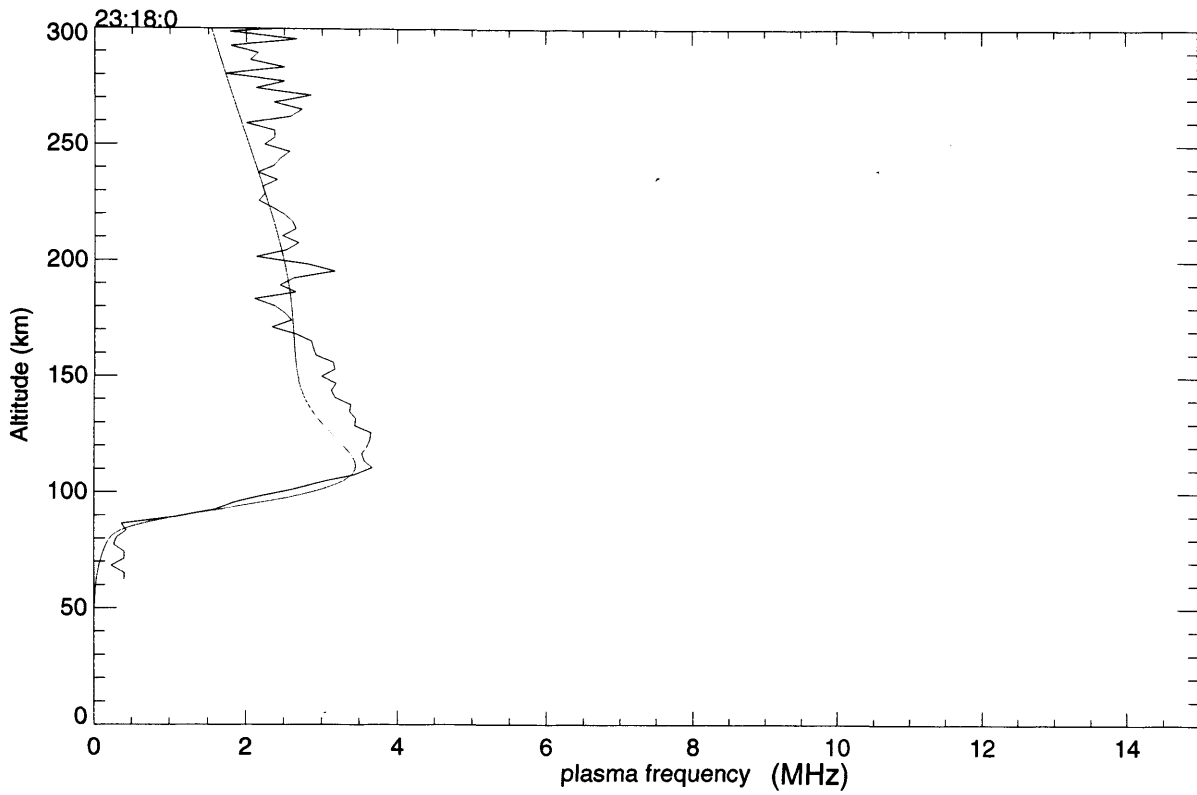


Fig.5.7(b)

Absorption in the ionosphere of the rays of CUTLASS, plotted against elevation angle of transmission. Based on the electron density profiles from EISCAT of 2318 UT on 18/06/96 (fig.5.7a), and 2320 UT on 18/06/96 (fig.5.7b).



**Fig.5.8.** Plasma frequency profiles, based on EISCAT electron density data, together with double Chapman layer fits to these profiles. The upper panel is based on the electron density profile from 2318 UT on 18/06/96, and the lower panel is based on the electron density profile from 2320 UT on 18/06/96.

Jones3d ray-trace

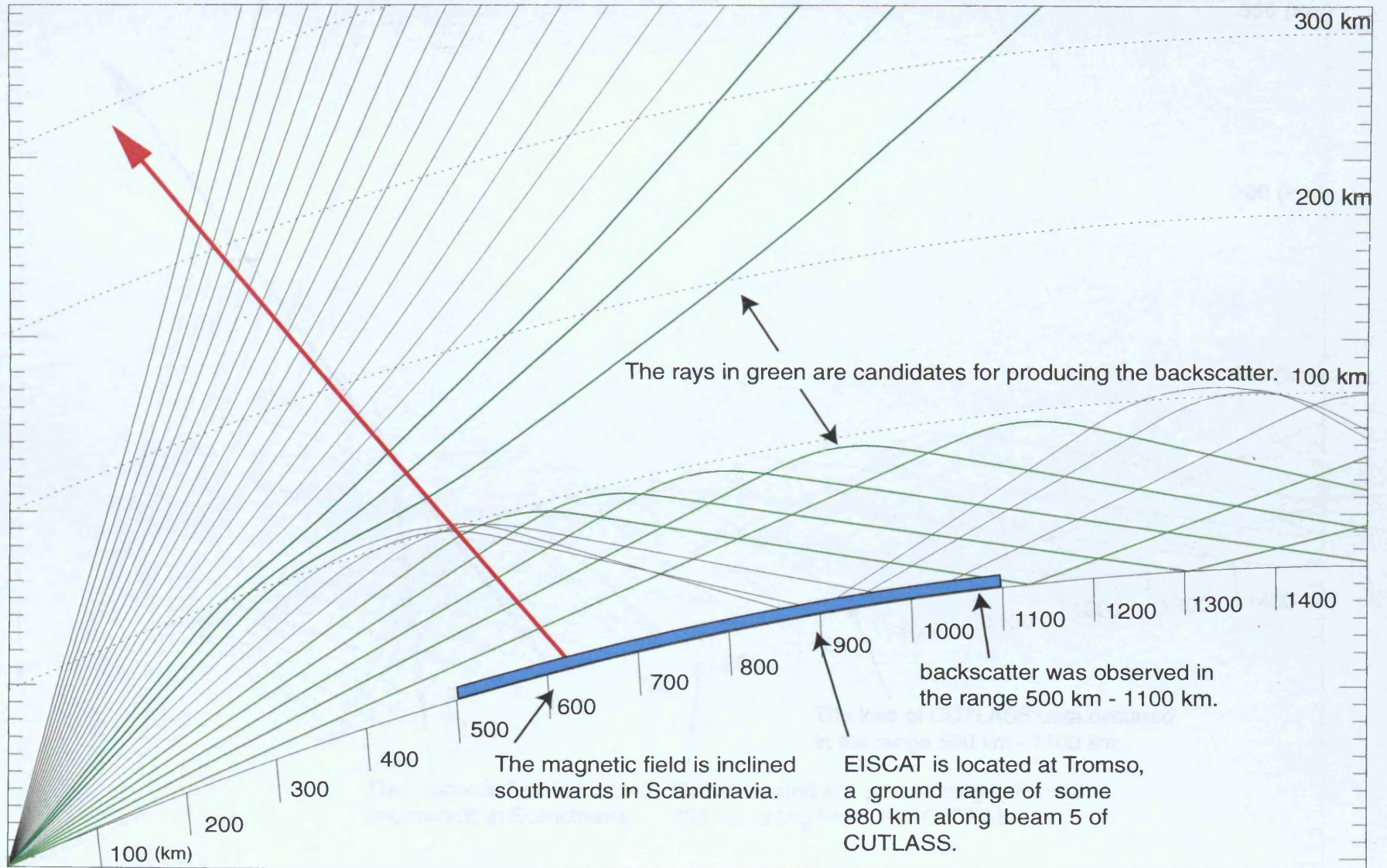


**Fig.5.9.** Ray trace through EISCAT plasma frequency profile of 2318 UT on 18/06/96. This ray trace is representative of CUTLASS propagation paths prior to the active period, and is aimed specifically at CUTLASS beam 5, since this is the beam which contains the field of view of EISCAT.

Jones3d ray-trace

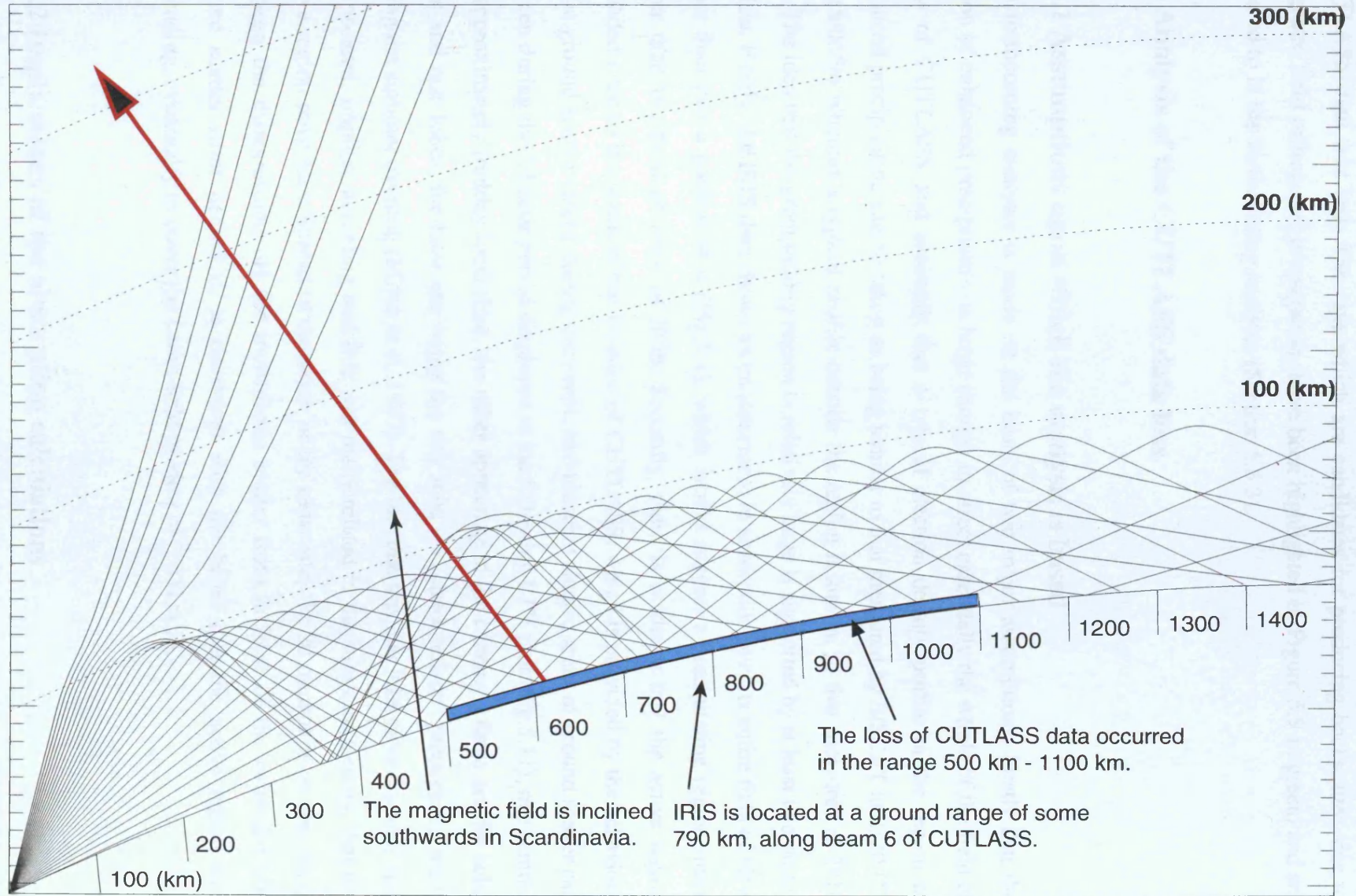


**Fig.5.10.** Ray trace through EISCAT plasma frequency profile of 2320 UT on 18/06/96. This ray trace is representative of CUTLASS propagation paths during the active period.

5.6), as being representative of the radar propagation, before, and during, the period in which CUTLASS data was lost. The rays which are candidates for producing backscatter, due to magnetic field orthogonal propagation, have been highlighted in Figure 5.9 in green, and are referred to in the forthcoming analysis (Section 5.6.3).

## **5.6 Analysis of the CUTLASS data loss**

### **5.6.1 Assumptions upon which the analysis is based**

The forthcoming analysis is made on the basis of two major assumptions. Firstly that the region of enhanced precipitation is large enough to affect essentially the whole of the field of view of CUTLASS and secondly that a typical electron density profile in the region of enhanced precipitation can be taken as being similar to that measured by EISCAT at 2320 UT on 18/06/96 whereas a typical profile outside the region is similar to that measured at 2318 UT. The idea that the precipitating region is relatively large is supported by at least two pieces of data. Firstly, the IRIS data shows an enhancement in absorption over its entire field of view rather than just a portion of it (Fig.5.4), which would suggest a precipitating region much larger than the field of view of IRIS. Secondly, there is evidence that the active region extended even to the south of the location of CUTLASS, which is provided by the behaviour of the ground scatter return during the event; two crescent shaped areas of ground scatter can be seen during the 24 hour period displayed in the following LTV plot (Fig.5.11), one centred on approximately midday local time, the other appearing in the evening - these are the radar front and rear lobes, the later one being the rear lobe - a characteristic propagation mode during the summer evening (Milan et al.,1997). The fact that this rear lobe ground scatter also disappeared, implies, assuming that this was really related to the substorm activity, that the active region must have spread to the south of the radar site; the 20 minute or so time delay between the disappearance of the ionospheric scatter from in front of the radar and this ground scatter from behind it, is consistent with the belief that the active region was expanding, eventually to cover the entire field of view of CUTLASS.

### **5.6.2 Implications of the absorption calculations**

The dependency of absorption against elevation angle of the transmitted rays of CUTLASS was investigated in Section 5.5.2. It can be seen that absorption varies between 2 dB and 11 dB when the representative electron density profile from 2318 UT is used (Fig.5.7a), whereas,

# SUPERDARN PARAMETER PLOT

Finland: vel

18 Jun 1996<sup>(170)</sup>  
normal (ccw) scan mode (127)

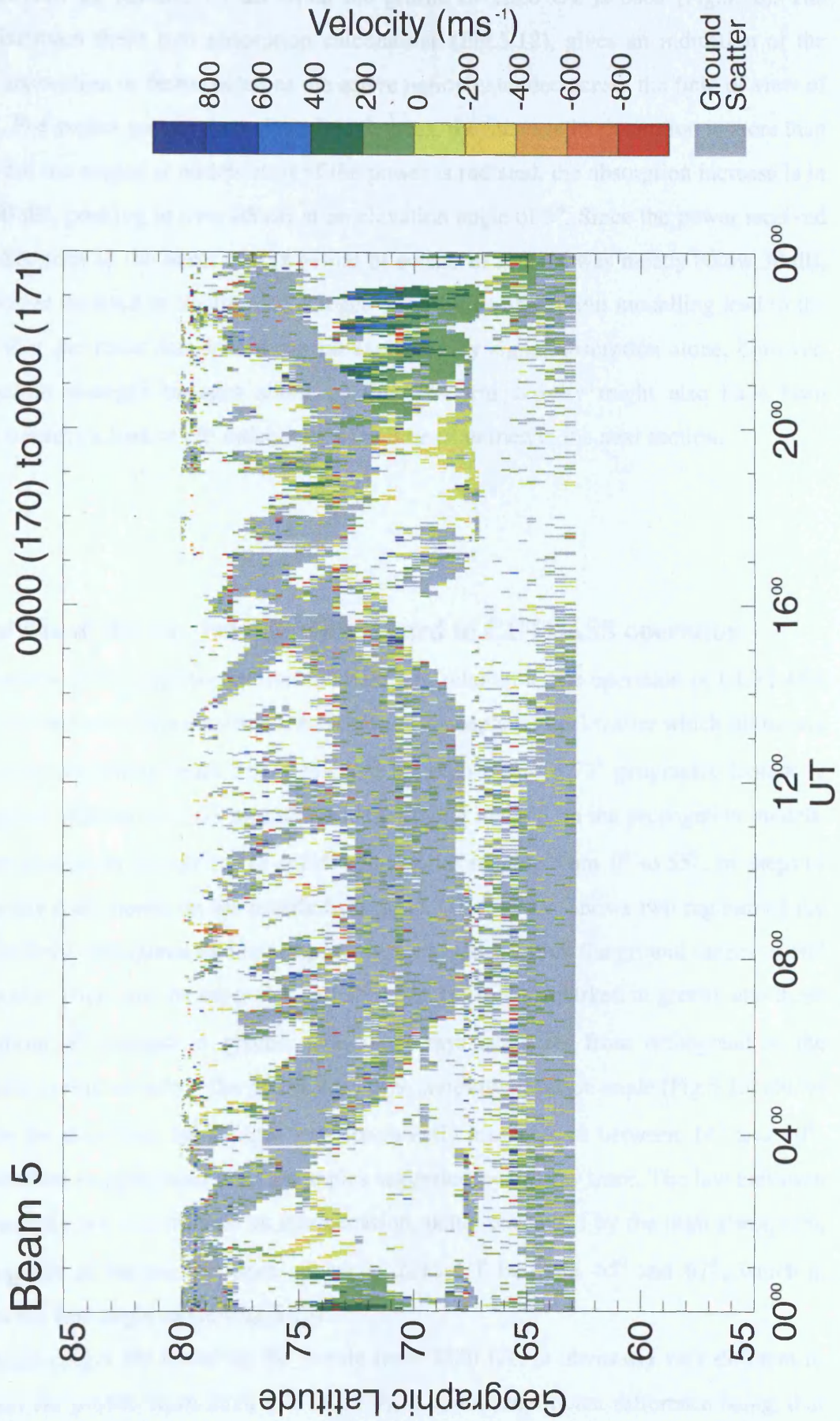


**Fig.5.11.** LTV plot of CUTLASS data covering the full twenty four hours of 18/06/96. The double crescent effect seen in the ground scatter is typical at this time of year, with the smaller crescent being from the radar rear lobe.

it varies between 12 dB and 75 dB when the profile of 2320 UT is used (Fig.5.7b). The difference between these two absorption calculations (Fig.5.12), gives an indication of the increase in absorption to be expected as the active region extended across the field of view of CUTLASS. For angles greater than about two degrees, the increase in absorption is more than 15 dB, and for the angles at which most of the power is radiated, the absorption increase is in excess of 30 dB, peaking at over 65 dB at an elevation angle of 5°. Since the power received by CUTLASS prior to the onset of this period of substorm activity was mostly below 30 dB, the assumptions detailed in Section 5.6.1 together with this absorption modelling lead to the conclusion that the radar data losses can be explained by signal absorption alone, however, the propagation changes brought about by the substorm activity might also have been effective in causing a loss of HF radar data, as will be examined in the next section.

### **5.6.3 Analysis of the ray tracing with regard to CUTLASS operation**

The implications of the ray propagation modelling in relation to the operation of CUTLASS (Section 5.5.1) will now be examined. The region of ionospheric backscatter which ultimately disappears is located along beam 5 of CUTLASS between 67° and 73° geographic latitude (a ground range of 500 km to 1100 km), these ranges being marked on the propagation models. The rays are plotted on the ray traces at elevation angles ranging from 0° to 55°, in steps of size 2°. The ray trace based on the profile from 2318 UT (Fig.5.9) shows two regimes of ray which can be field orthogonal and hence produce backscatter within the ground ranges of 500 km to 1100 km. There are the rays with elevations of 16° to 20° (marked in green), and those less than about 8° (marked in green), with other rays being far from orthogonal to the magnetic field in this vicinity. The CUTLASS time series in elevation angle (Fig.5.13) shows that prior to the data loss, backscatter was consistently measured at between 14° and 20°, which is therefore in agreement with the angles suggested by this ray trace. The low elevation mode is generally not in evidence on this occasion, being weakened by the high absorption, although a patch of backscatter does appear at 2315 UT between 65° and 67°, which is measured as the low angle mode (Fig.5.13).

The ray trace (Fig.5.10) based on the profile from 2320 UT, is obviously very different to that based on the profile from 2318 UT (Fig.5.9), the most significant difference being, that rays with elevation angles in the ranges 14° to 20° no longer penetrate the peak of the layer, but are instead reflected back towards the surface of the earth, on a path that would not be

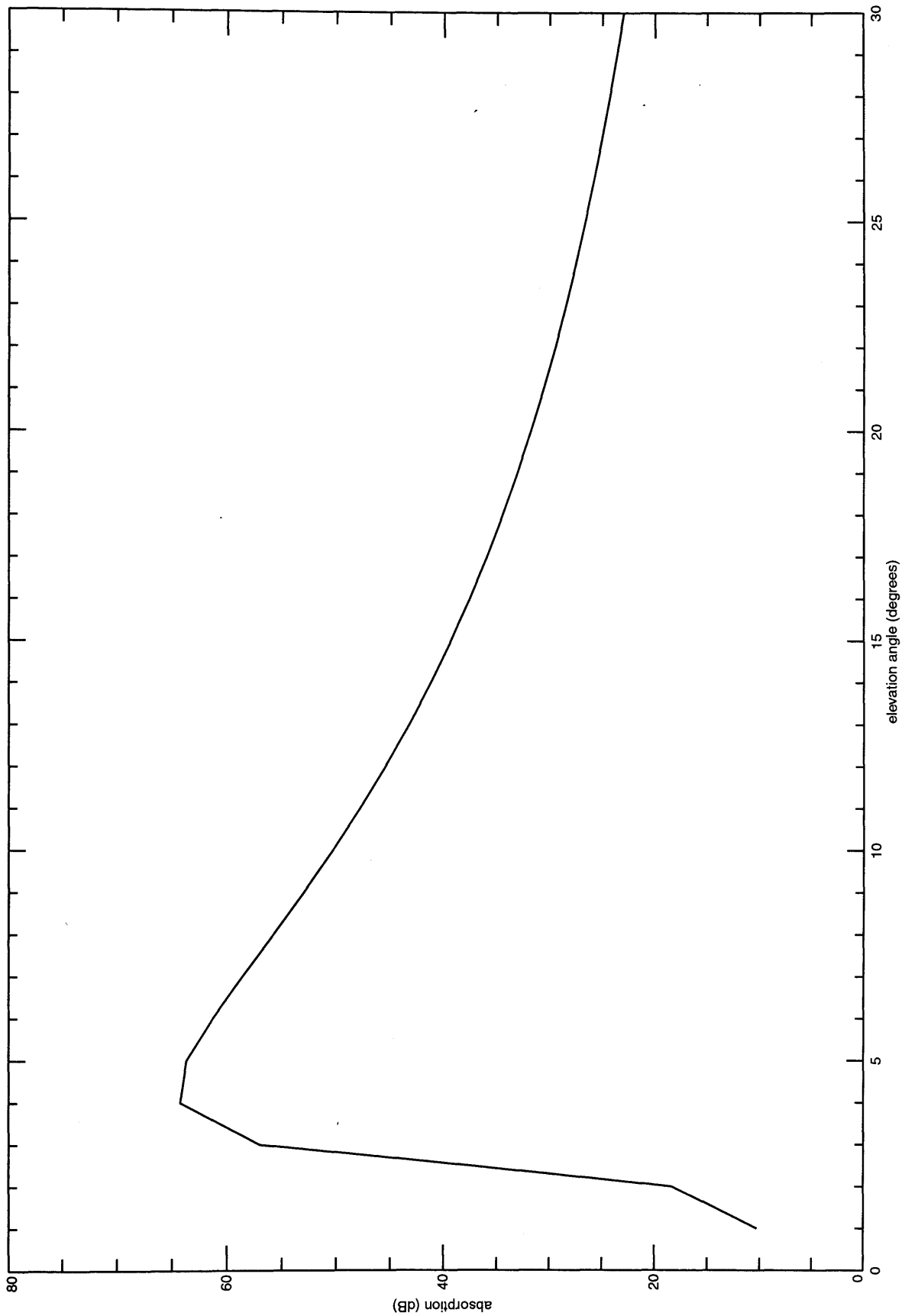


**Fig.5.12.** The increase in absorption of CUTLASS' rays brought about by basing the absorption calculation upon the EISCAT electron density profile from 2320 UT on 18/06/96 (fig.5.7b) instead of the profile from 2318 UT on 18/06/96 (fig.5.7a).

# SUPERDARN PARAMETER PLOT

Finland: elev (phi0)

18 Jun 1996 <sup>(170)</sup>  
normal (ccw) scan mode (127)

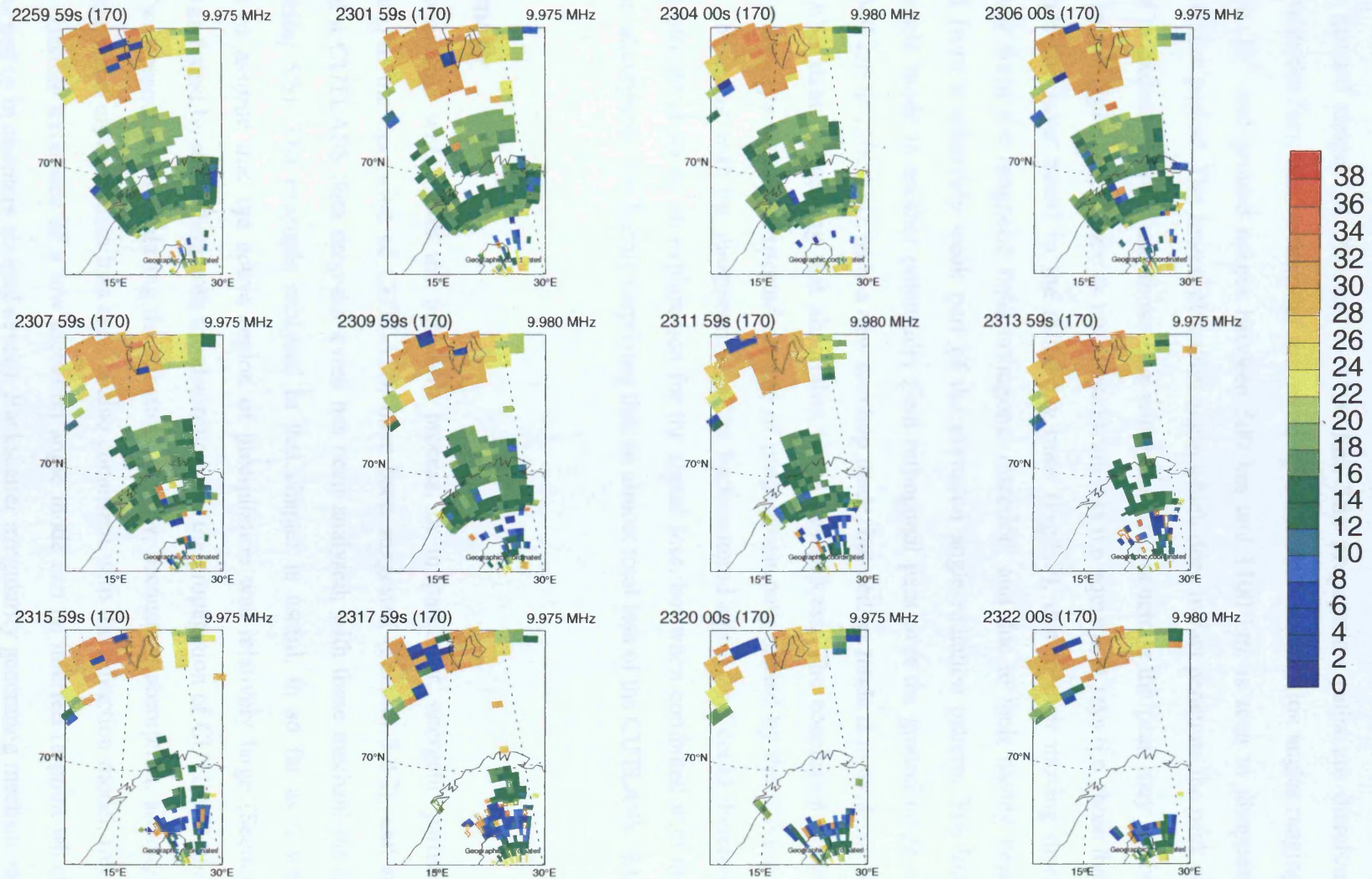


Fig.5.13. Time series of CUTLASS data in 'elevation angle of receipt', leading into the magnetically active period.

expected to result in the production of backscatter, due to the ray direction (and its associated propagation vector) not being close to the magnetic field orthogonal direction anywhere within the ground ranges of 500 km to 1100 km. The propagation paths are therefore consistent with the fact, that backscatter measured by CUTLASS at elevation angles ranging from  $14^{\circ}$  to  $20^{\circ}$  and ground ranges between 500 km and 1100 km, is seen to disappear during the active period. The lowest elevation angle which does in fact penetrate the peak of the layer is in excess of  $40^{\circ}$ , and those rays which can still penetrate the peak may not be able, even in principle, to produce as much backscatter as the equivalent rays (i.e. those that just penetrate the layer peak) in the initial ray trace (Fig.5.9), due to their moving more quickly away from the magnetic field orthogonal direction, and due to their having been transmitted from a relatively weak part of the elevation angle radiation pattern. The low elevation angle mode is another potentially field orthogonal path over the ground range in question (500 km to 1100 km), as is a new two hop mode, but neither mode is in evidence in the CUTLASS data, suggesting that absorption is the key process. The conclusion drawn from this analysis is that the expected change of propagation path caused by the substorm activity, is consistent with the disappearing of the backscattered signal, and could therefore perhaps be offered alone as an explanation for the signal loss, but when combined with the evidence for absorption, it is hardly surprising that an almost total loss of the CUTLASS data occurred.

## 5.7 Summary

Three mechanisms which link the substorm process, or in particular, energetic particle precipitation, to the operation of CUTLASS, have been suggested (Section 5.2.2), and an example of a CUTLASS data drop out event has been analysed, with these mechanisms in mind (Section 5.6). The example analysed in this chapter is useful, in so far as it was reasonable to assume that the active region of precipitation was relatively large (Section 5.6.1). It was found by modelling both the absorption and the propagation of CUTLASS, that the signal was essentially lost during the substorm activity, because of absorption, although the large scale and uniform data loss seen is also consistent with the refraction model, from which the possible existence of a low elevation angle mode can be inferred (a point which will be returned to in chapters six and seven). Backscatter irregularity generating mechanisms are also likely to have been significantly affected during the event, a point considered by Milan et al.(1999); this study of the interval, which is also supported by EISCAT data, does not use the assumption of a spatially uniform ionosphere as we have done here (Section

5.6.1), but never the less concludes that absorption was likely to have been a major contributory factor in causing the radar signal loss; the EISCAT data was used by Milan and co-workers to look at conductances in the E-region and F-region, in the context of the model of the  $\mathbf{E} \wedge \mathbf{B}$  instability proposed by Vickrey and Kelley (1982) (Section 2.5) which includes the effects of E-region shorting upon the perturbation electric field; the results suggest that irregularity growth rates (in the region from which backscatter was lost) were probably reduced during the interval of radar data loss; the study also provides evidence by analysing elevation angle-range data from near range scatter, that transmitted rays were not being reflected straight back from the lower E region to ground (the blanketing effect), and it is therefore suggested that the cause of the radar signal loss is probably a combination of a depletion of the available scattering structure, and absorption.

## **Chapter 6**

### **A multiple instrument study of a substorm interval – 21/08/1998**

#### **6.1 Introduction**

In the previous chapter, the response of CUTLASS to a sustained period of intense magnetic activity, in which many substorms occurred in quick succession, was analysed. It was concluded that intense D-region absorption associated with particle precipitation was a self-consistent explanation of the near total loss of the backscattered signal. By way of contrast, the response of CUTLASS to an isolated substorm, which occurred on 21/08/98 will be analysed in this chapter. Again, EISCAT and IRIS data are available from this interval, and will be used in a largely similar way to the previous chapter in the forthcoming analysis.

#### **6.2 The data set from the substorm period**

##### **6.2.1 CUTLASS and IMAGE data**

During the interval being studied in this chapter, CUTLASS was running beam 9 as a high time resolution beam, and is therefore selected as the beam upon which most attention will be focused. Beam 9 LTV data has been plotted along with Z component magnetic perturbations from Tromsø and Sodankyla, and X component Pi2 filtered magnetic perturbations from Kilpisjarvi, using a common time axis running from 2200 UT until 2400 UT on 21/08/98 (Fig.6.1). The start of a substorm expansion phase is marked by a Pi2 pulsation and the onset of magnetic bays, at about 2250 UT. Some 10 minutes or so after the detection of a Pi2 pulsation at Kilpisjarvi, a clear bite out of the CUTLASS LTV data can be seen, which corresponds with the arrival of an absorption enhancement in the field of view of IRIS (Section 6.2.2). It can be seen from the spatial velocity time series (Fig.6.2), that backscatter was being eroding from the north across all the beams, and by 2308 UT the extent of this data loss had peaked, with the region of backscatter having approximately halved. By 2326 UT a substantial recovery in the spatial extent of backscatter returns had occurred, and by 2335 UT, the region of returns had recovered to a level similar to that prior to the substorm onset (Fig. 6.3). CUTLASS power time series through the interval are displayed in Figures 6.4 and 6.5, and are discussed further in section 6.3.2.

##### **6.2.2 IRIS data**

Prior to the onset of a substorm expansion phase at 2250 UT, there was a magnetically quiet period, and IRIS was measuring little absorption. At 2302 UT a region of enhanced absorption arrived in the south west of the field of view, and then spread northward and

# SUPERDARN PARAMETER PLOT

21 Aug 1998

to

22 Aug 1998

Finland: velocity

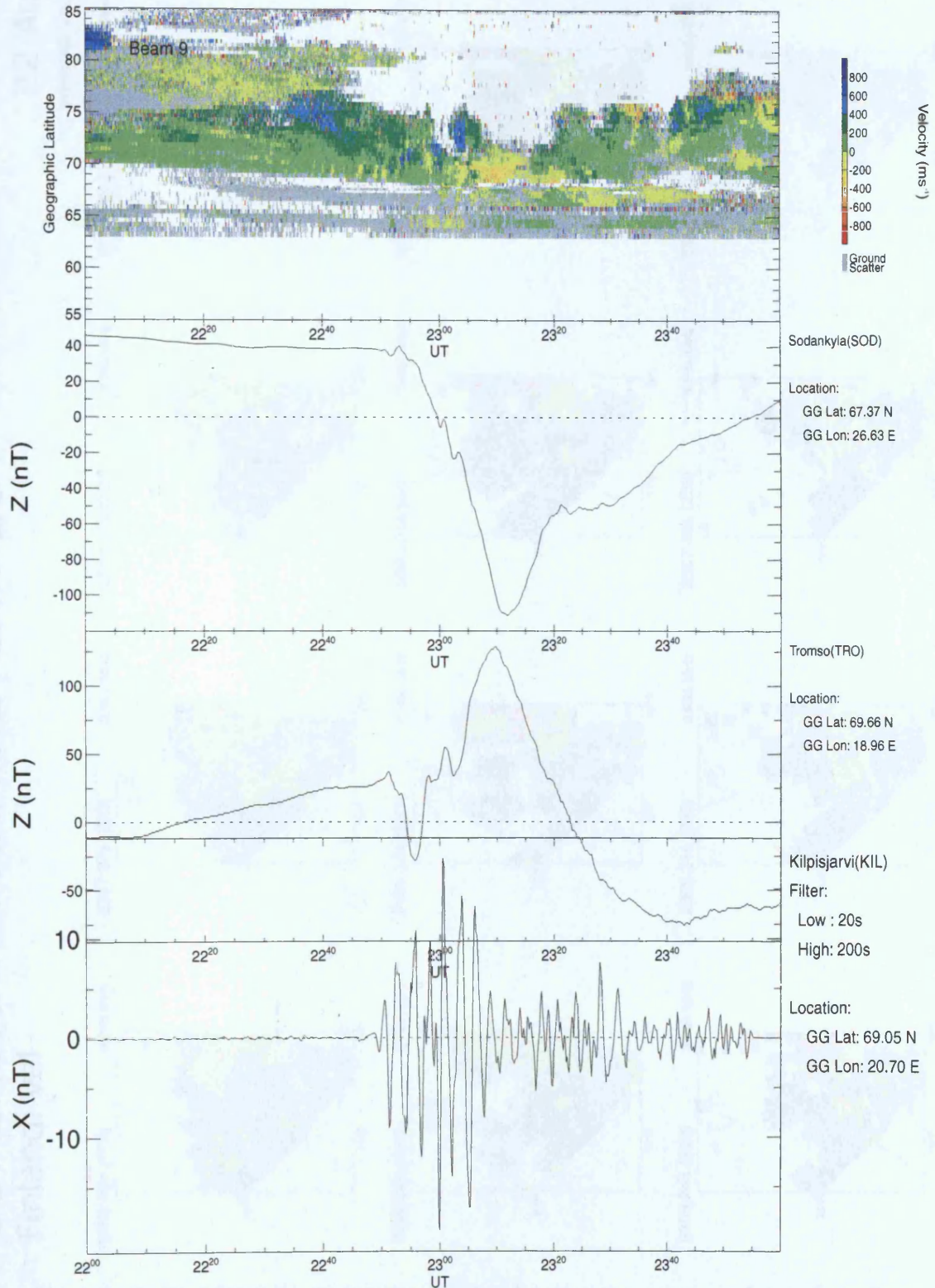


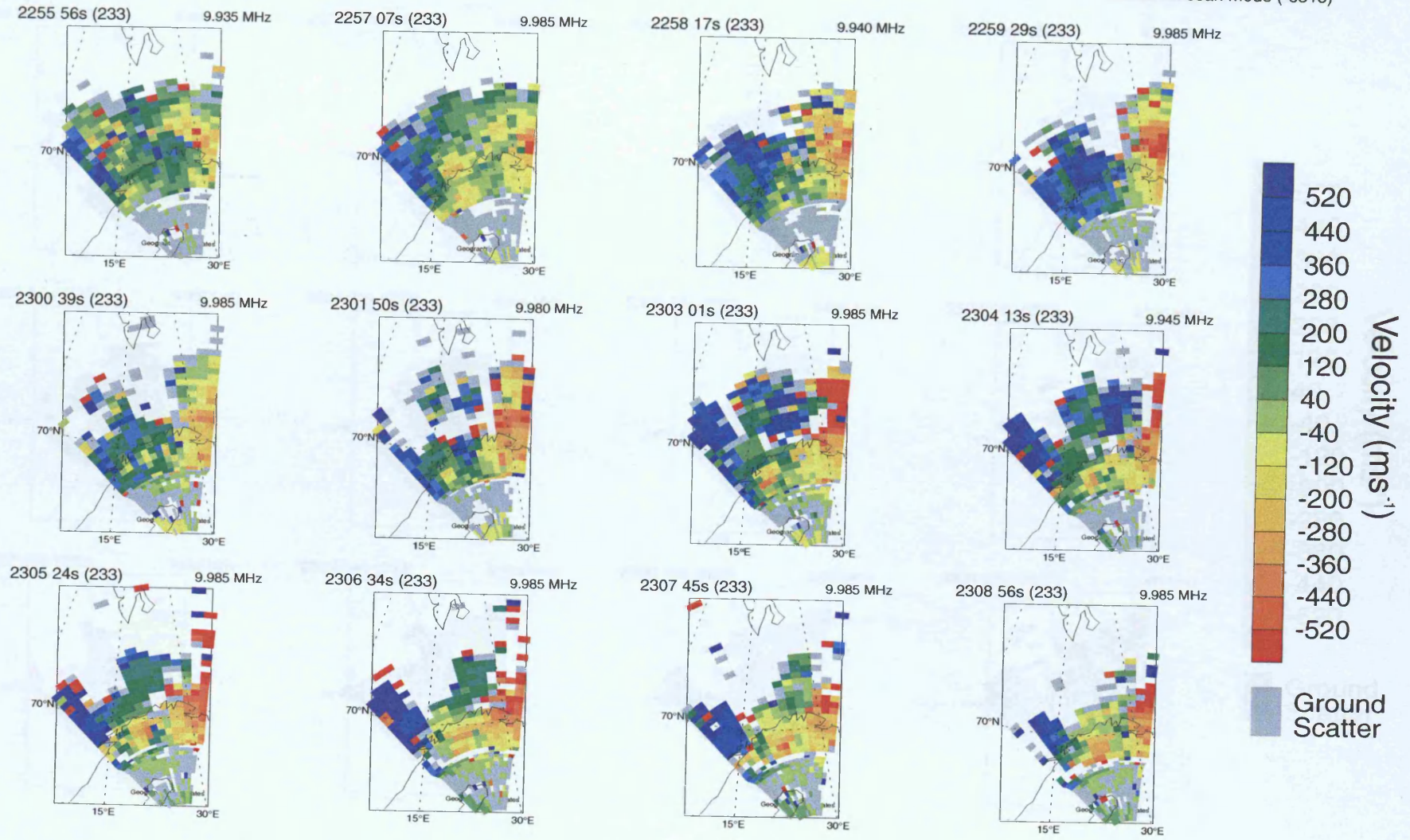
**Fig.6.1.** CUTLASS (LTV) plot, together with Z component magnetic perturbations from Sodankyla and Tromso, and Pi2 filtered magnetic perturbations from Kilpisjarvi. The Z component perturbations suggest that a substorm associated electrojet is located between Sodankyla and Tromso. The substorm has resulted in two clear 'bite outs' of the CUTLASS data, at 2258 UT and 2307 UT.

# SUPERDARN PARAMETER PLOT

## Finland: vel

21 Aug 1998<sup>(233)</sup>  
to  
22 Aug 1998<sup>(234)</sup>  
unknown scan mode (-6315)

Fig.6.2. CUTLASS time series in velocity, showing the erosion of data from the north due to a substorm.



# SUPERDARN PARAMETER PLOT

Finland: vel

21 Aug 1998 <sup>(233)</sup>  
to  
22 Aug 1998 <sup>(234)</sup>  
unknown scan mode (-6315)

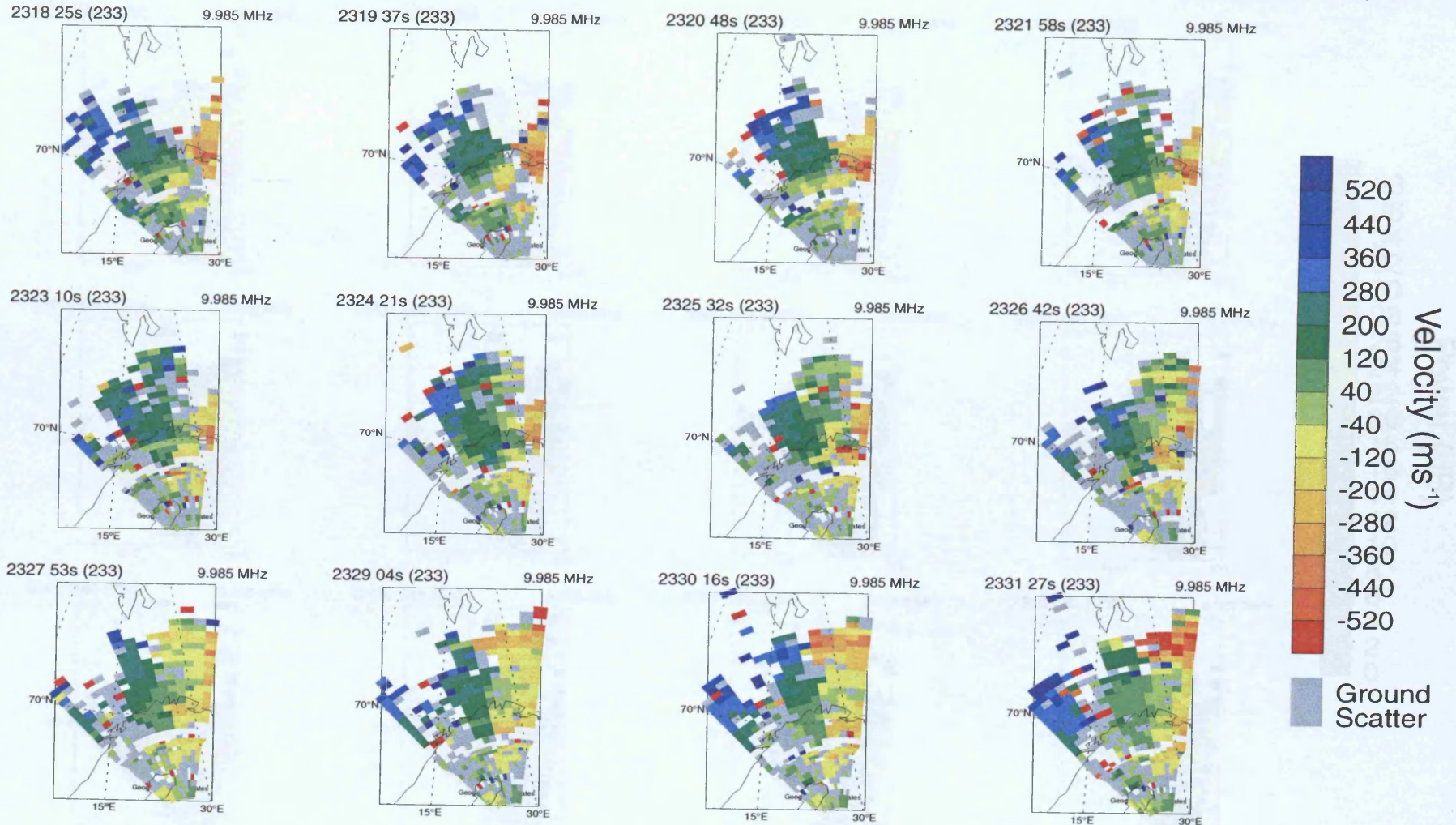


Fig.6.3. CUTLASS time series in velocity, showing the gradual recovery of data following a substorm induced data loss.

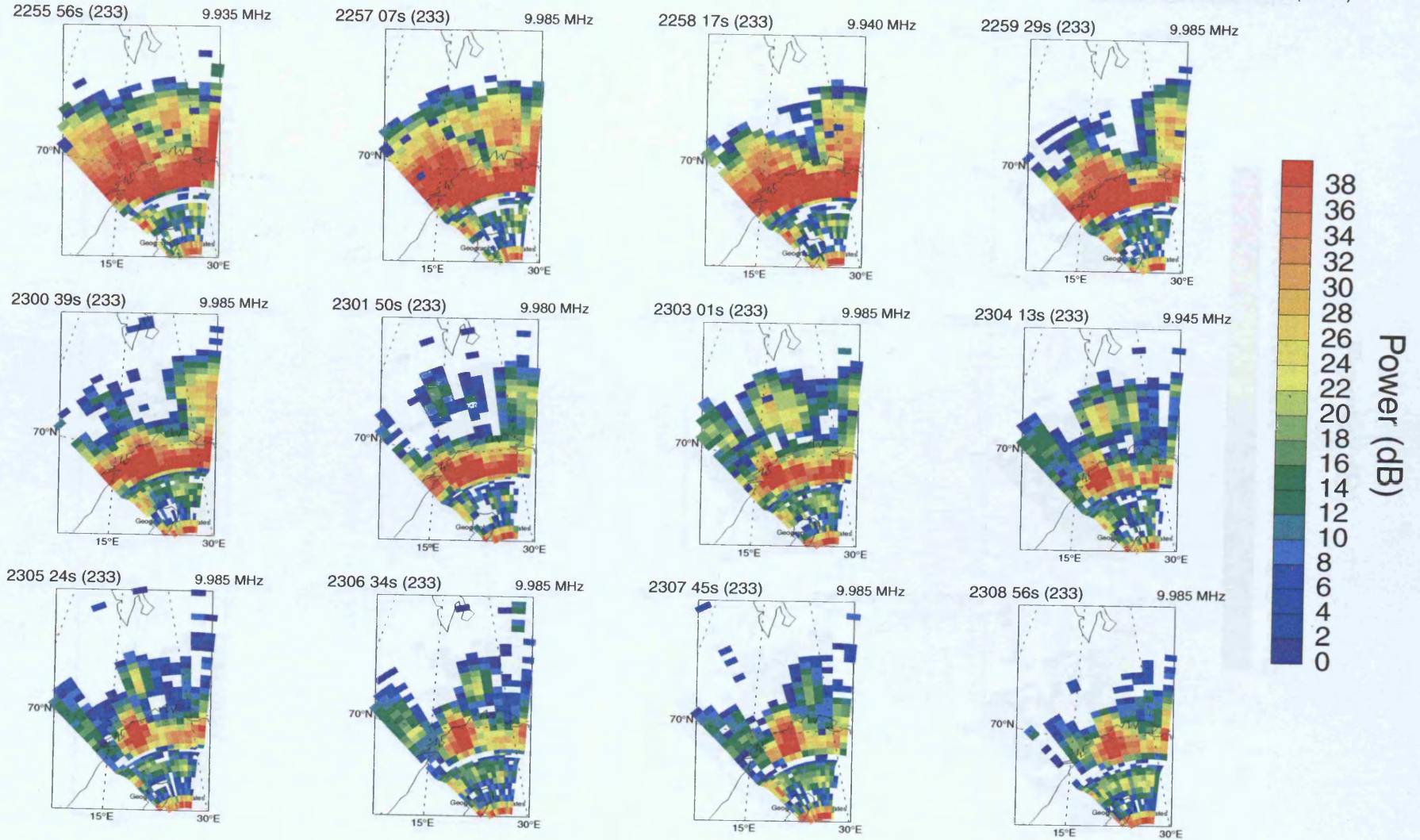
# SUPERDARN PARAMETER PLOT

Finland: pwr\_1

21 Aug 1998 <sup>(233)</sup>  
to  
22 Aug 1998 <sup>(234)</sup>

unknown scan mode (-6315)

Fig.6.4. CUTLASS time series in power, showing the power distribution as the signal faded during the substorm.

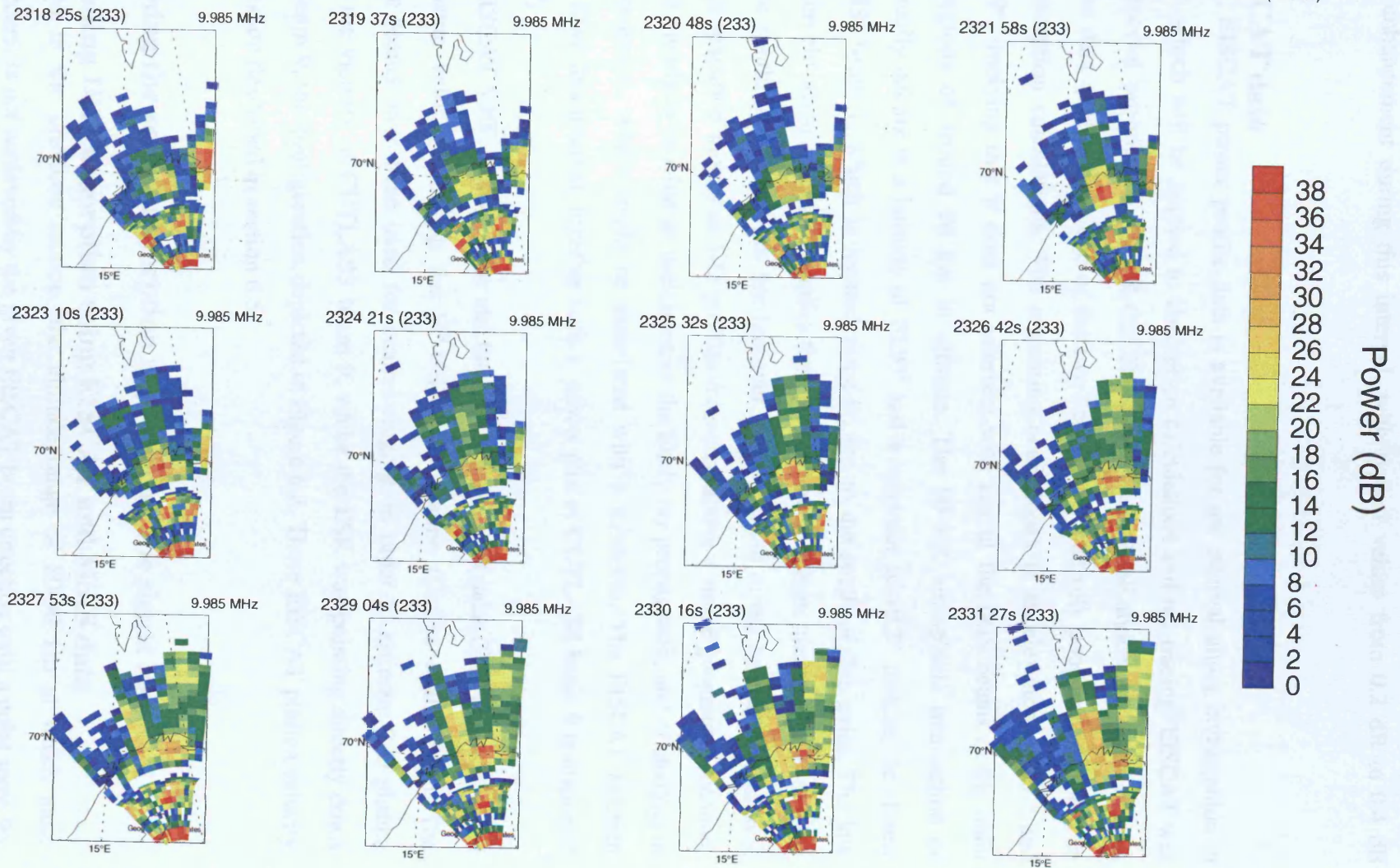


# SUPERDARN PARAMETER PLOT

Hankasalmi: pwr\_1

21 Aug 1998 <sup>(233)</sup>  
to  
22 Aug 1998 <sup>(234)</sup>  
unknown scan mode (-6315)

Fig.6.5. CUTLASS time series in power, showing the power distribution as the signal gradually recovered following a substorm.



eastward across the field of view during the next 6 minutes. Most of the beams witnessed an absorption enhancement during this interval, with typical values from 0.2 dB to 0.4 dB (Fig.6.6).

### **6.2.3 EISCAT data**

Once again, EISCAT power profile data is available for the interval under investigation in this chapter, which will be applied to absorption calculations and ray tracing. EISCAT was running a special programme SP-UK-CSUB, a split beam VHF mode, however, on this occasion, the data quality from one of the two beams was relatively poor and could not be used for absorption calculations. The remaining beam looks at an elevation of 30 ° and azimuth 359°, implying that it does not intersect with any of the IRIS beams in the main absorbing regions of around 90 km in altitude. The 90 km ionospheric intersection of EISCAT actually occurs at a latitude of 70.95° and a longitude of 19.3°, making the closest beam of IRIS, beam 1, which is located some 96 km to the south of this point. The low EISCAT beam elevation angle also implies that profiles are no longer measured over a single location. The resulting 1-D profiles are however, just as useful in the context of analysing CUTLASS propagation modes as 1-D profiles measured above a single geographic location; they are used merely to provide an indication of the likely ray propagation, and of changes in this ray propagation, which might be associated with a substorm. The EISCAT electron density data from this interval, together with a power plot of CUTLASS beam 9 is displayed in Figure 6.7.

Both the EISCAT VHF Tromsø radar and the EISCAT Svalbard radar (ESR) have provided F-region plasma velocities during the SP-UK-CSUB routine (Davies et.al., 2000). The Tromsø split beams have been used for beam-swinging, in order to estimate 2-D plasma velocities in the vicinity of CUTLASS beam 9, whilst the ESR was pointing directly down CUTLASS beam 9, the configuration depicted in Figure 6.8. These EISCAT plasma velocity measurements are described in section 6.5.

## **6.3 Examining the role of absorption in producing the signal loss**

### **6.3.1 Modelling IRIS absorption using EISCAT and MSIS data**

As mentioned in the previous section, the altitude range of 80-90 km at which most absorption occurs, is not achieved by the given EISCAT beam direction until a point some 96 km from IRIS beam 2, the closest of the beams. The vertical path absorption has been calculated following the method detailed in the previous chapter i.e. using the summation (Equation 5.8), and collision frequencies (Equations 5.2 – 5.7), with neutral atmosphere

21 Aug 1998

IRIS Riometer

time\_series

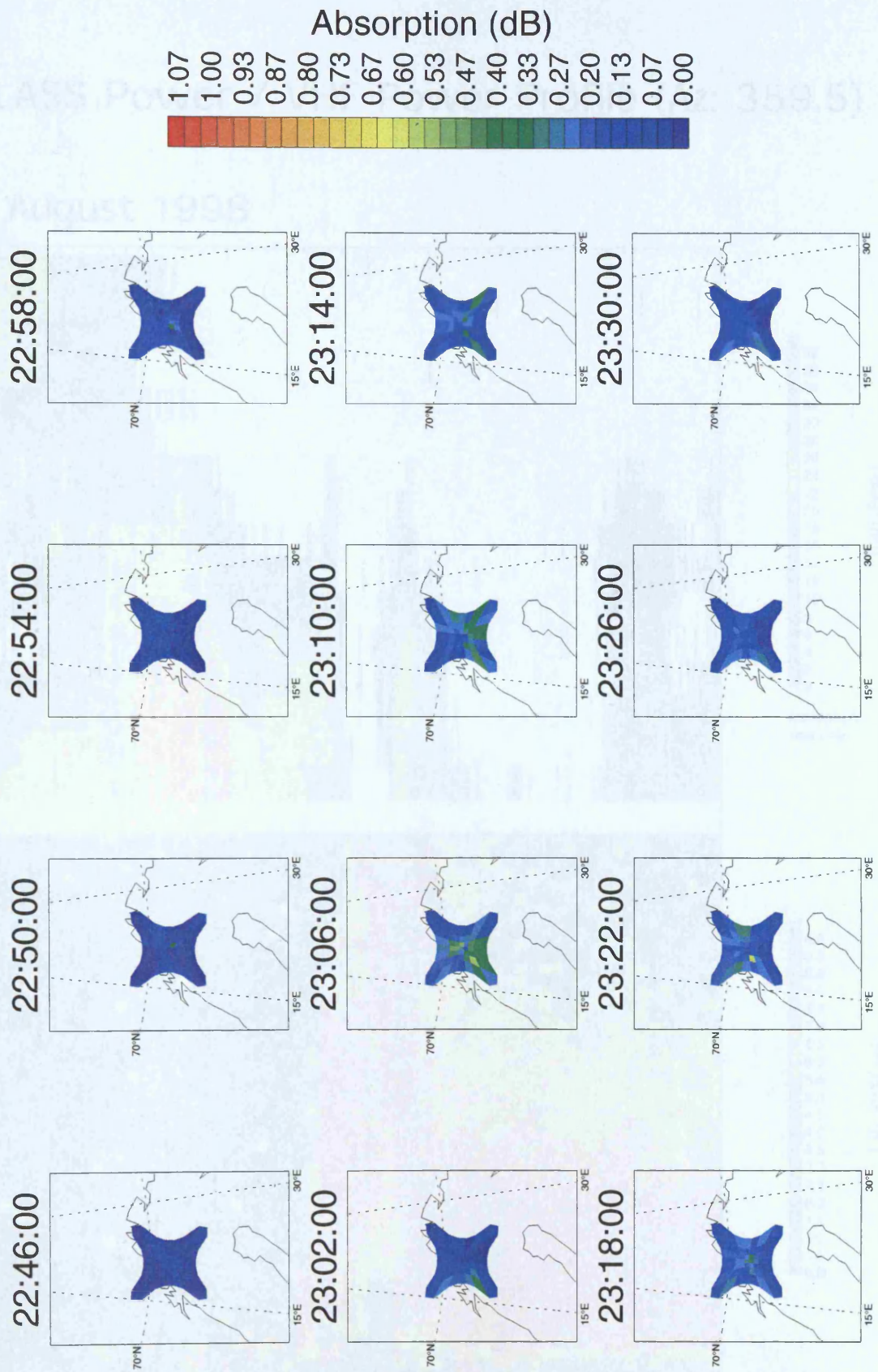
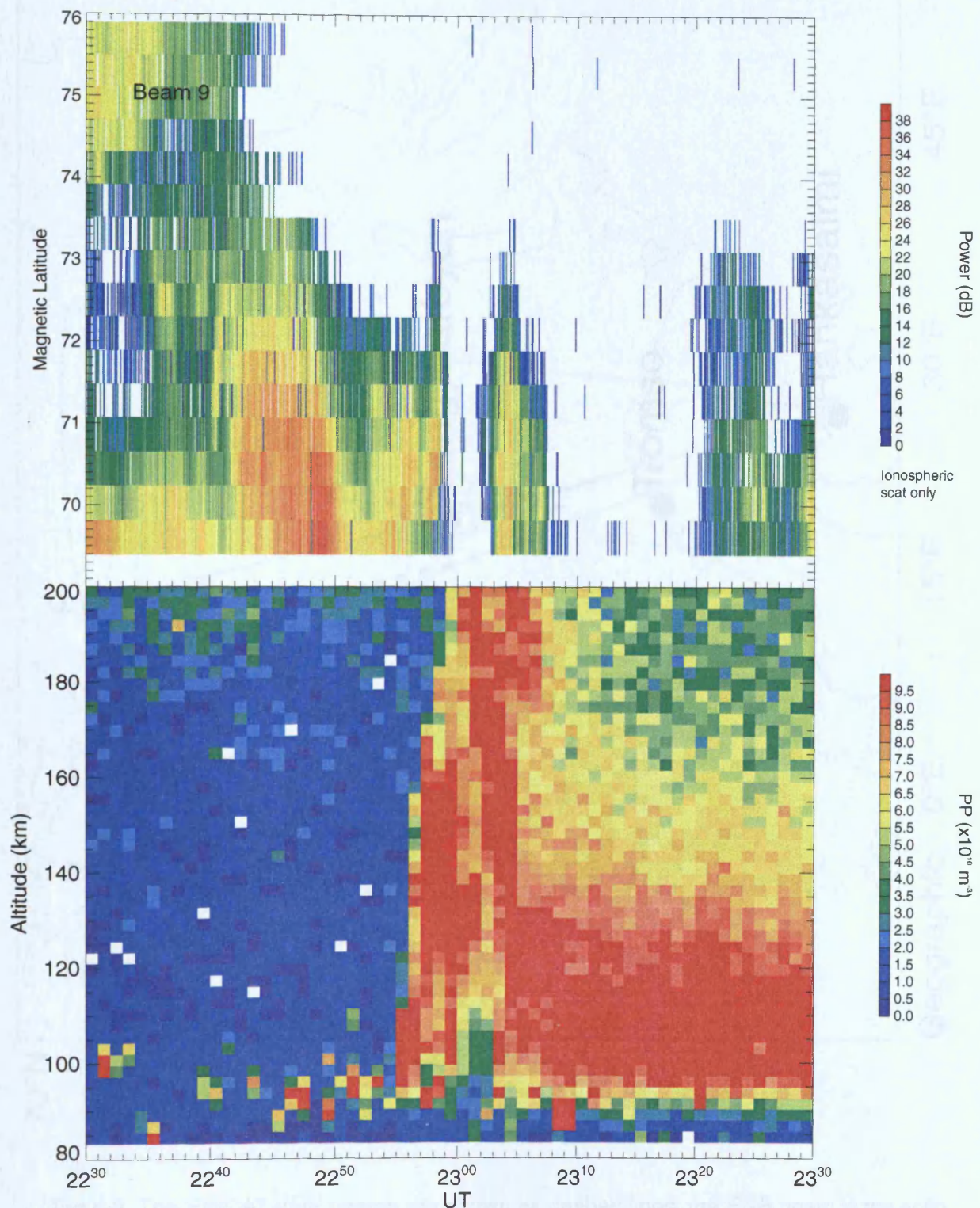


Fig.6.6. IRIS absorption time series, showing an interval of increased activity which is associated with a substorm.

# CUTLASS Power / VHF Power Profile (Az: 359.5)

21 August 1998



**Fig.6.7.** CUTLASS power data and EISCAT electron density data, showing that electron density was greatly enhanced during the substorm interval, and remained so thereafter, especially in the E region.

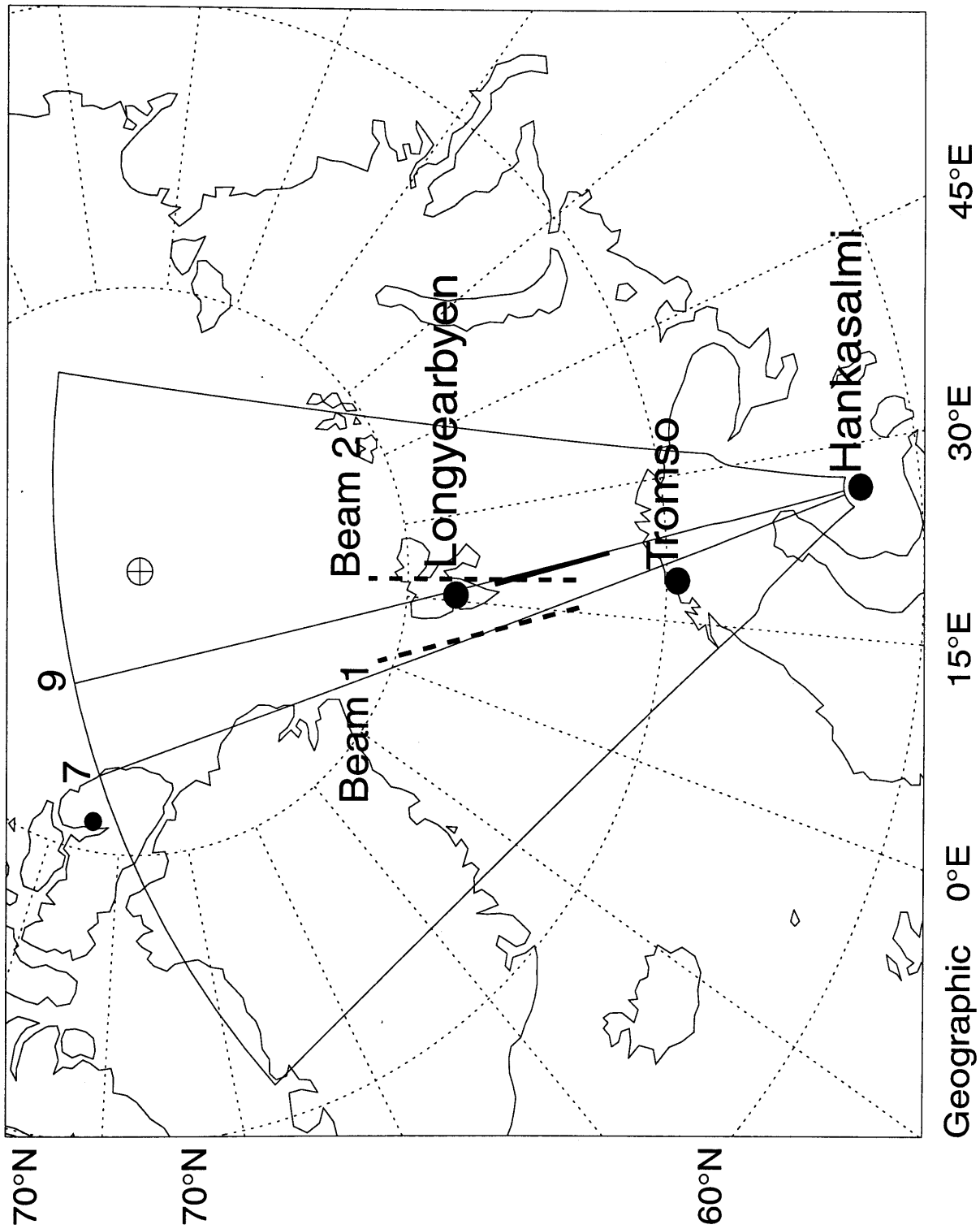


**Fig.6.8.** The EISCAT VHF beams are shown as dashed lines, the ESR beam is the solid line, with beams 7 and 9 of CUTLASS highlighted explicitly (from Davies et al., 2000).

composition and temperature data provided by MSIS. Although the absorption calculation is appropriate for a somewhat different location to the field of view of IRIS, the plot of calculated absorption and absorption measured by beam 2 of IRIS (blue), show impressive similarity (Fig.6.9). Even beam 49 of IRIS, at a range of some 436 km being the most distant beam, is broadly similar to the calculated values (Fig.6.10); the time of the absorption enhancement is slightly later than that observed by beam 1, due to the feature moving from west to east, but the level of absorption is of the same order as the calculated values.

The fact that these modelled and measured absorption values are in broad agreement, despite the consideration of their spatial separation, suggests that the assumption of a uniform absorbing region is not unreasonable, and is therefore the assumption upon which the forthcoming CUTLASS absorption calculations will be based.

### **6.3.2 The absorption experienced by CUTLASS**

With the assumption that the absorbing features are spatially uniform on a scale of order hundreds of kilometres, the IRIS absorption model may now be used, to provide at least an indication of the level of absorption which affected CUTLASS. The details of the calculation will not be repeated here, as they are identical to that described in Section 5.5.1. The CUTLASS absorption has been calculated on the basis of EISCAT profiles from 2248 UT and 2310 UT (Fig.6.11), these having been chosen as representative times from shortly before, and shortly after, the start of the substorm expansion phase. Inspection of the following time series of plasma frequencies leading into the substorm period (Fig.6.12 – 6.13), suggests that the selection of these profiles as typical of pre and post substorm expansion phase onset, is a reasonable choice. The absorption calculation again terminates when the ray has reached the ground range of Tromsø, a distance of 880 km, by which point, the lowest ray elevation angles have not fully penetrated the absorbing layer. The resulting plot of absorption against elevation angle (Fig.6.14), is the result of taking the difference between the absorption calculated for the two representative profiles, in other words, the increase in absorption associated with the substorm activity. The peak increase in absorption is just over 14 dB at an elevation angle of  $5^{\circ}$ , with increases being smaller than 10 dB for elevation angles greater than  $15^{\circ}$  and less than  $3^{\circ}$ . With other things being equal, this level of absorption would suggest a drop in received power of at most 14 dB across the entire region in which the signal was being received, thereby resulting in certain regions in a complete loss of the signal. In fact, the CUTLASS time series in power (Fig.6.4 and Fig.6.5), shows that some regions showed the complete loss of a 30 dB signal, whilst neighbouring regions witnessed little or no power reduction, or even in places saw an increase. Of course, ‘other

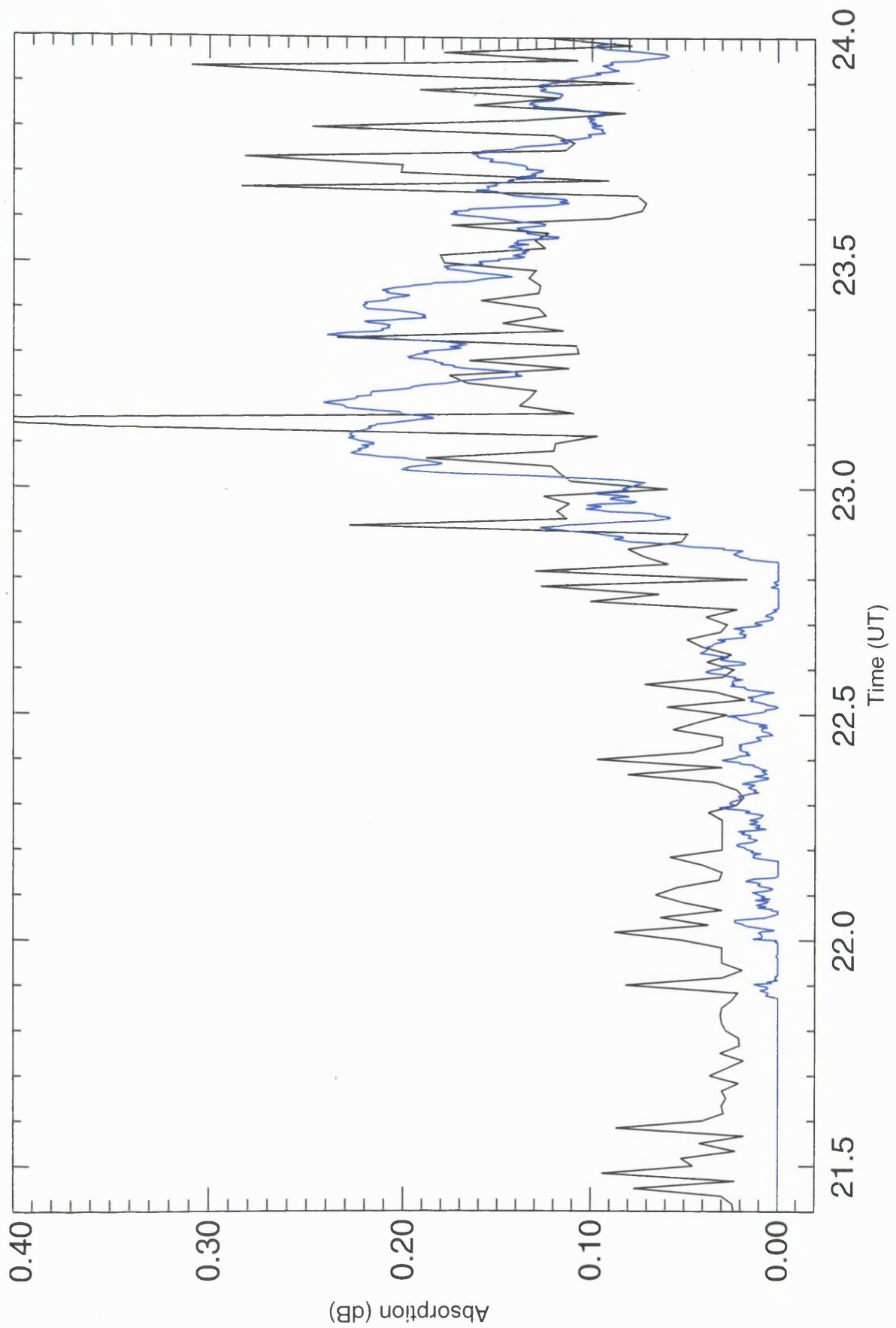


**Fig.6.9.** The absorption measured by IRIS beam 2 (blue) between 2100 UT and 2400 UT on 21/08/98, together with absorption calculated from EISCAT and MSIS data (black).

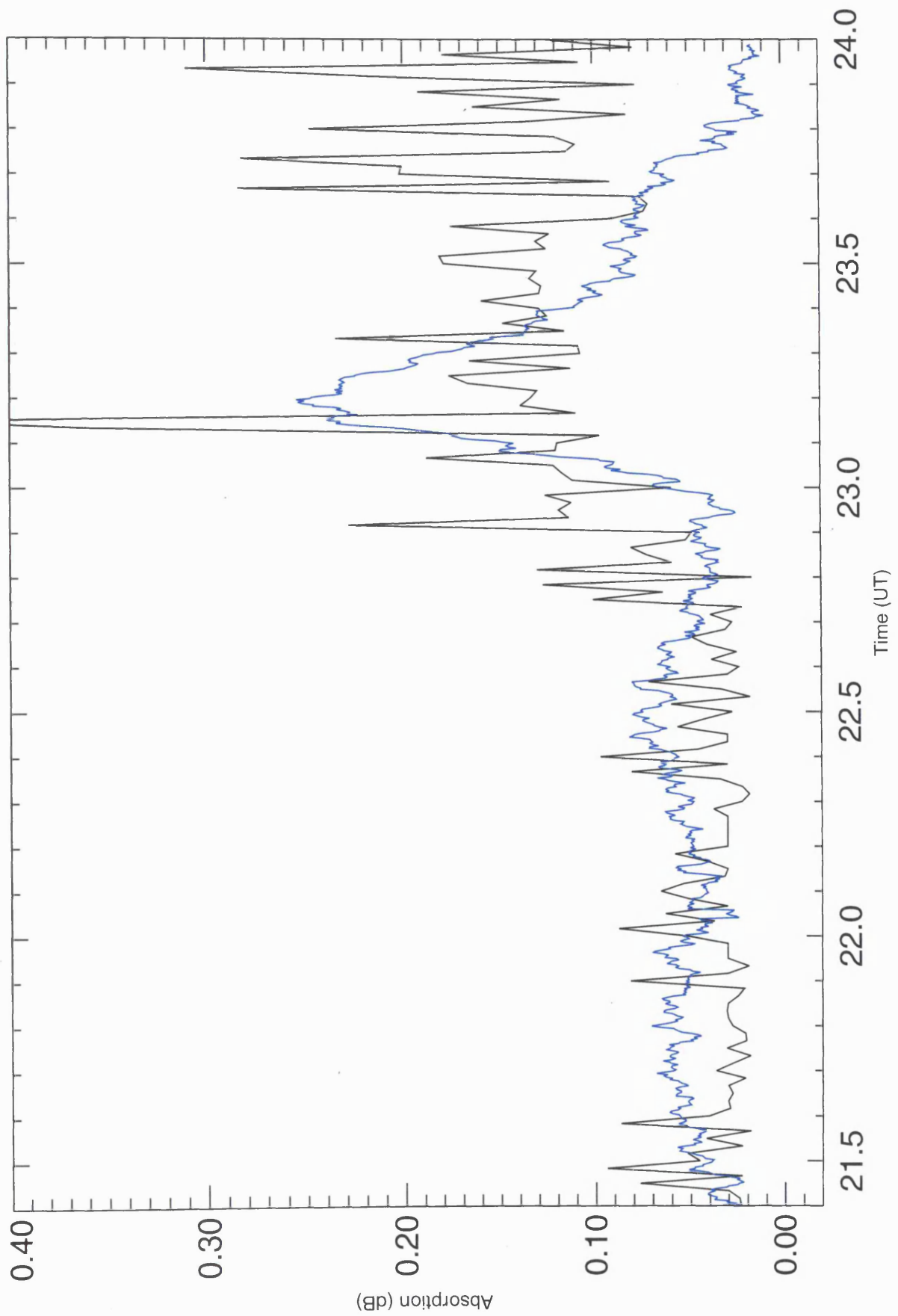


**Fig.6.10.** The absorption measured by beam 49 of IRIS (blue) in the interval 2100 UT until 2400 UT on 21/08/98, together with values calculated from EISCAT and MSIS data (black).

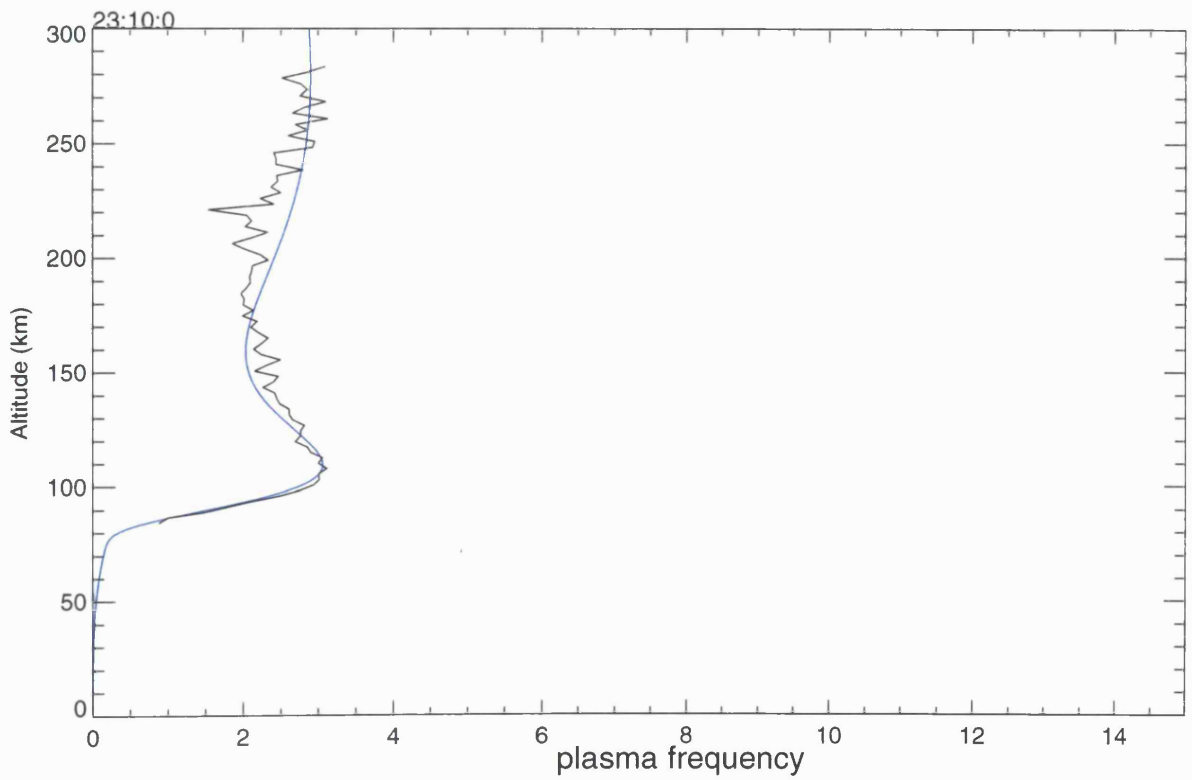
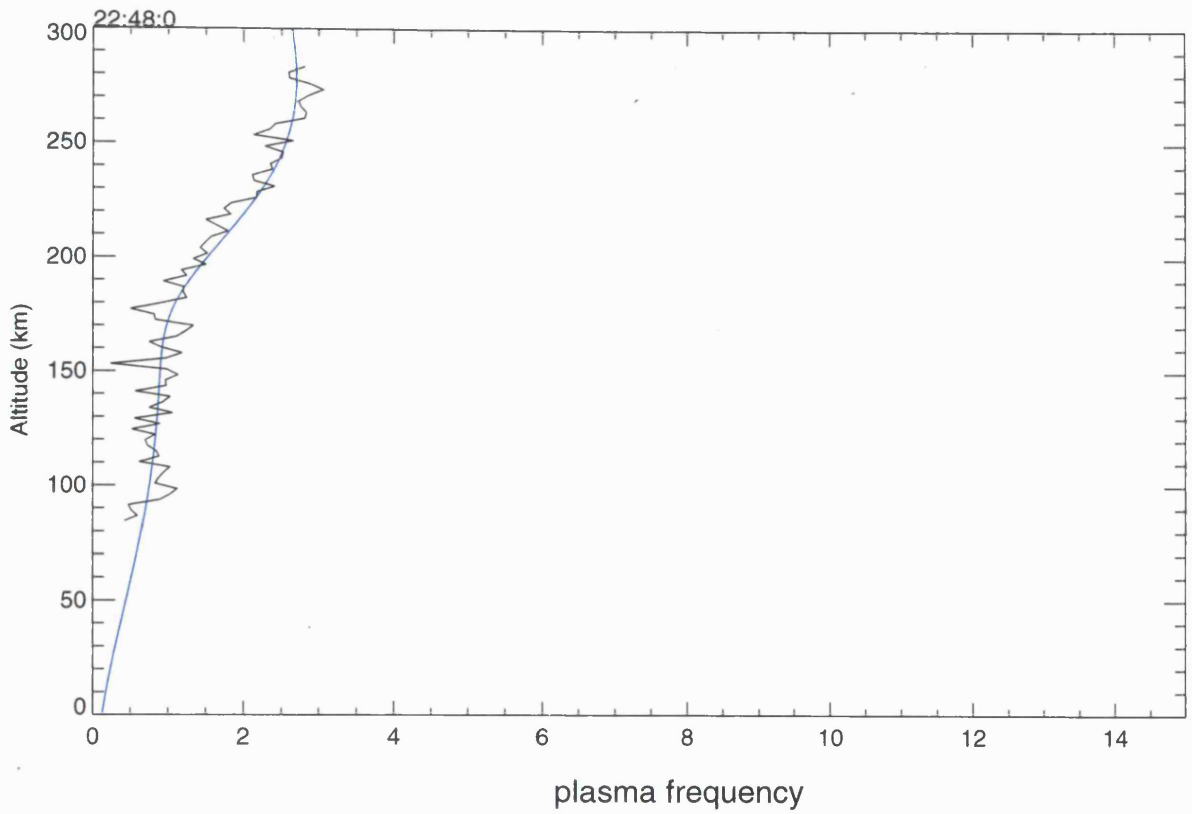


**Fig.6.11.** Plasma frequency derived from EISCAT data, together with double Chapman layer fits to this data. The upper panel, 2248 UT on 21/08/98, is shortly before substorm onset, and the lower panel, 2310 UT on 21/08/98, is shortly after substorm onset.

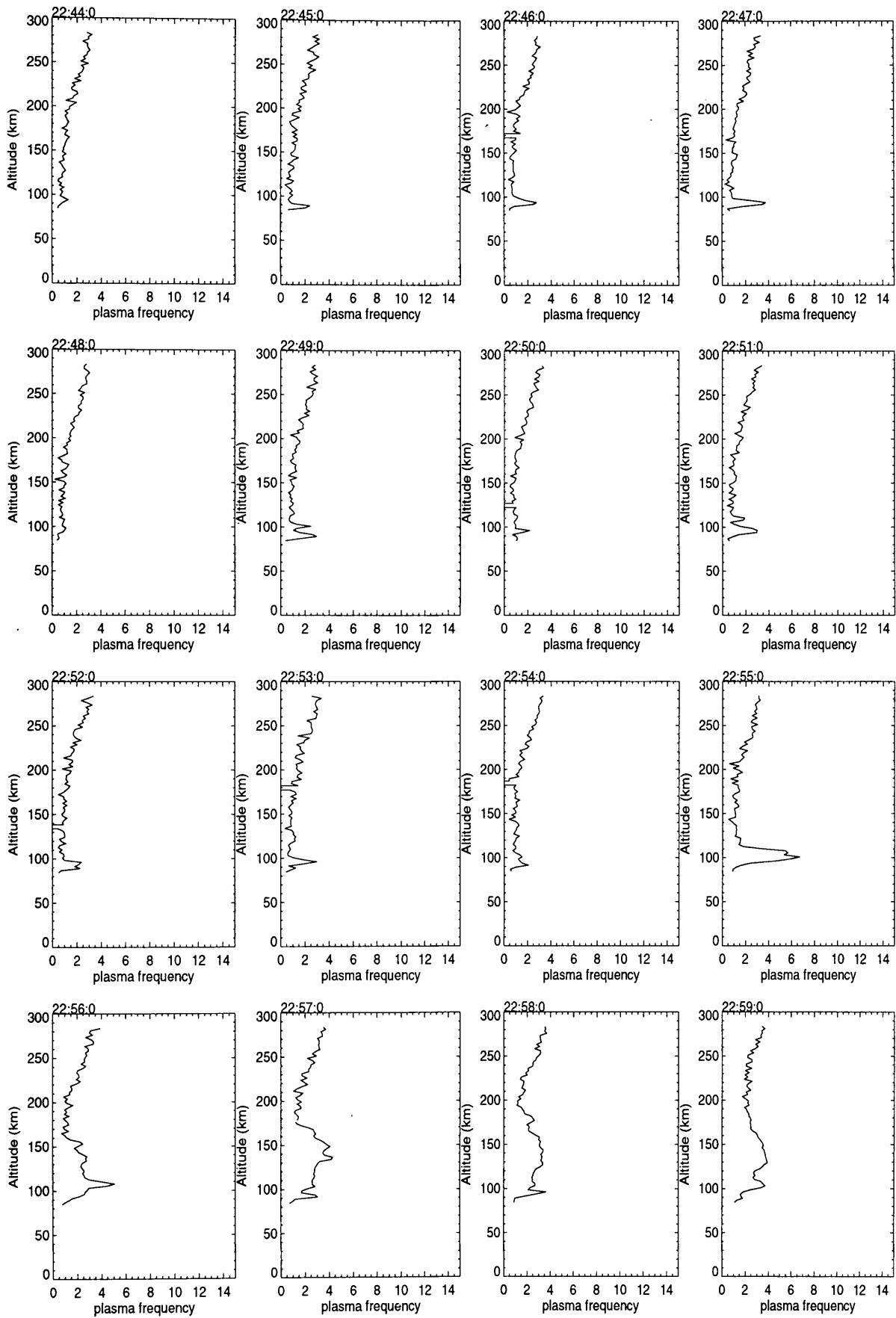


**Fig.6.12.** Time series of EISCAT plasma frequency profiles, measured in MHz. The data covers the interval between 2244 UT and 2259 UT on 21/08/98. The plasma frequency starts to increase after 2254 UT, due to substorm activity.

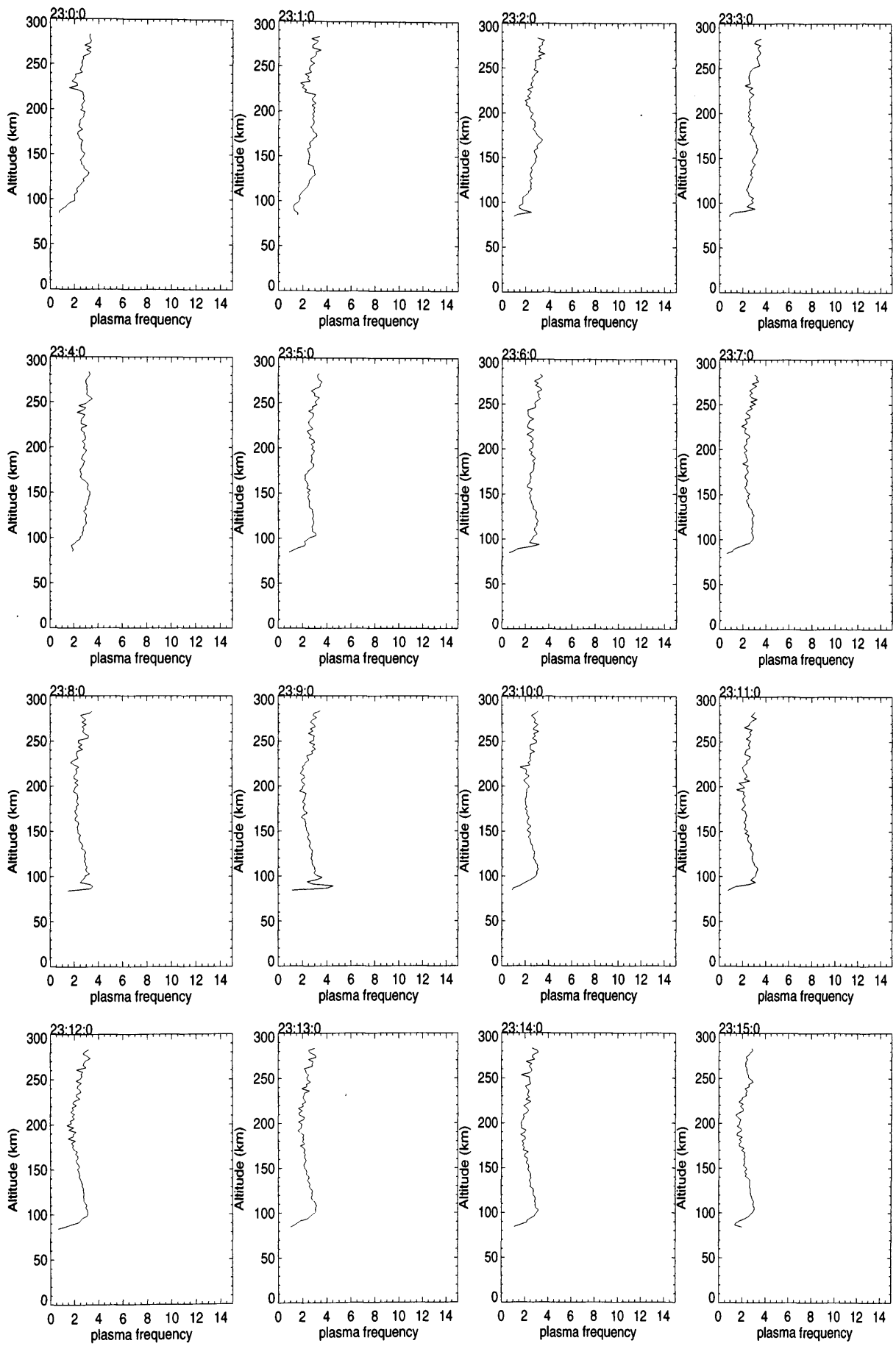


**Fig.6.13.** Time series of EISCAT plasma frequency profiles (MHZ) between 2300 UT and 2315 UT on 21/08/98.

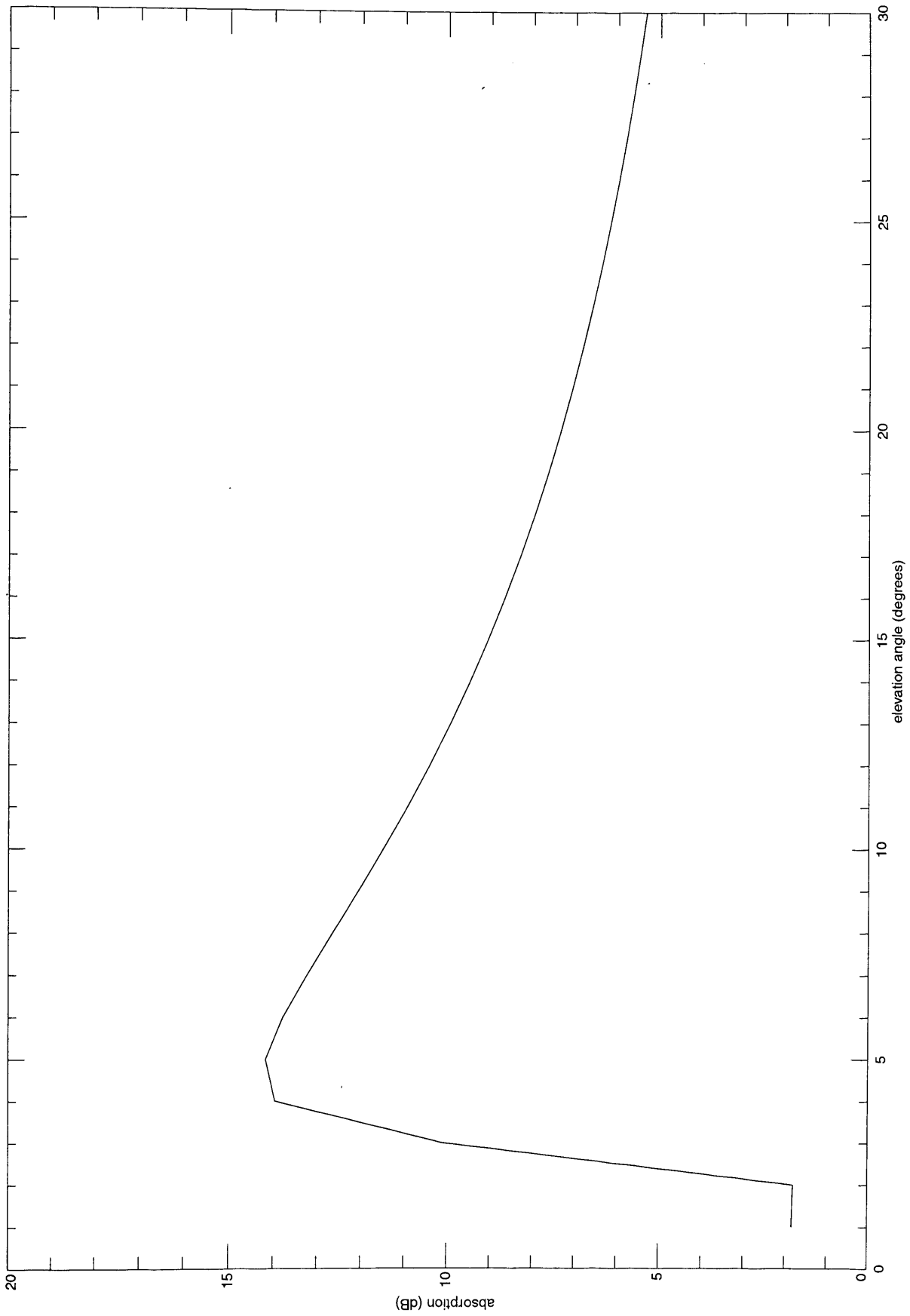


**Fig.6.14.** The increase in CUTLASS absorption associated with the substorm activity. It has been calculated as the difference between the CUTLASS absorption based on EISCAT data from 2248UT on 21/08/98, and CUTLASS absorption based on EISCAT data from 2310 UT on 21/08/98.

things' would not be expected to remain equal in this dynamic system, and it is this lack of consistency between prediction and observation which suggests, that in this case, absorption is not the primary explanation for the HF-radar signal loss.

## **6.4 Examining alterations in radar propagation during the substorm**

### **6.4.1 Ray tracing through EISCAT plasma frequency profiles**

The changes in radar propagation likely to have occurred, as the plasma frequency changed during the substorm interval, will now be examined. Following the same method as the analysis of section 5.5.2, a double Chapman layer fit has been carried out for the EISCAT plasma frequency profiles, at the chosen representative pre and post substorm onset times, of 2248 UT and 2310 UT (Fig.6.11). Jones3D has been used to ray trace through each of these profiles, resulting in the following representative ray paths from pre and post substorm onset (Fig.6.15) and (Fig.6.16). The rays are plotted in elevation angle steps of  $2^\circ$ , and range between  $0^\circ$  and  $50^\circ$ . For elevations of more than  $15^\circ$ , the two ray traces are very similar, showing quasi-linear propagation, terminating in space. The most obvious difference between the ray traces, is that pre-substorm onset, all the rays terminate in space, whereas post-substorm onset, the rays of elevation angle of less than  $15^\circ$ , are reflected earthward. From the perspective of CUTLASS operation, this difference might be very significant. Rays whose direction of propagation is earthward, will be far from satisfying the magnetic field orthogonality condition required for backscatter, and therefore are not candidates for producing backscatter from this region, whereas most of the rays which are heading spaceward will undergo field orthogonal propagation at some point along their path. Clearly, a change in propagation conditions such as this, might be expected to result in alterations to the regions from which a signal is received, and the power distribution of that signal. This idea will be focussed upon in more detail in the next section; since rays which have reflected back towards earth will not give backscatter, the second ray trace (Fig.6.16), suggests that beyond a ground range of about 600 km, there should be an absence of radar returns of elevation angles less than about  $15^\circ$ , with the possible exception of a very low elevation angle mode in the range 600 km to 1000 km. In the next section, radar elevation angle data from the interval will be analysed, looking in particular for evidence of a reduced incidence of elevation angles below about  $15^\circ$  in the period following the substorm expansion phase onset, which if present, would lend support to the ray tracing analysis.

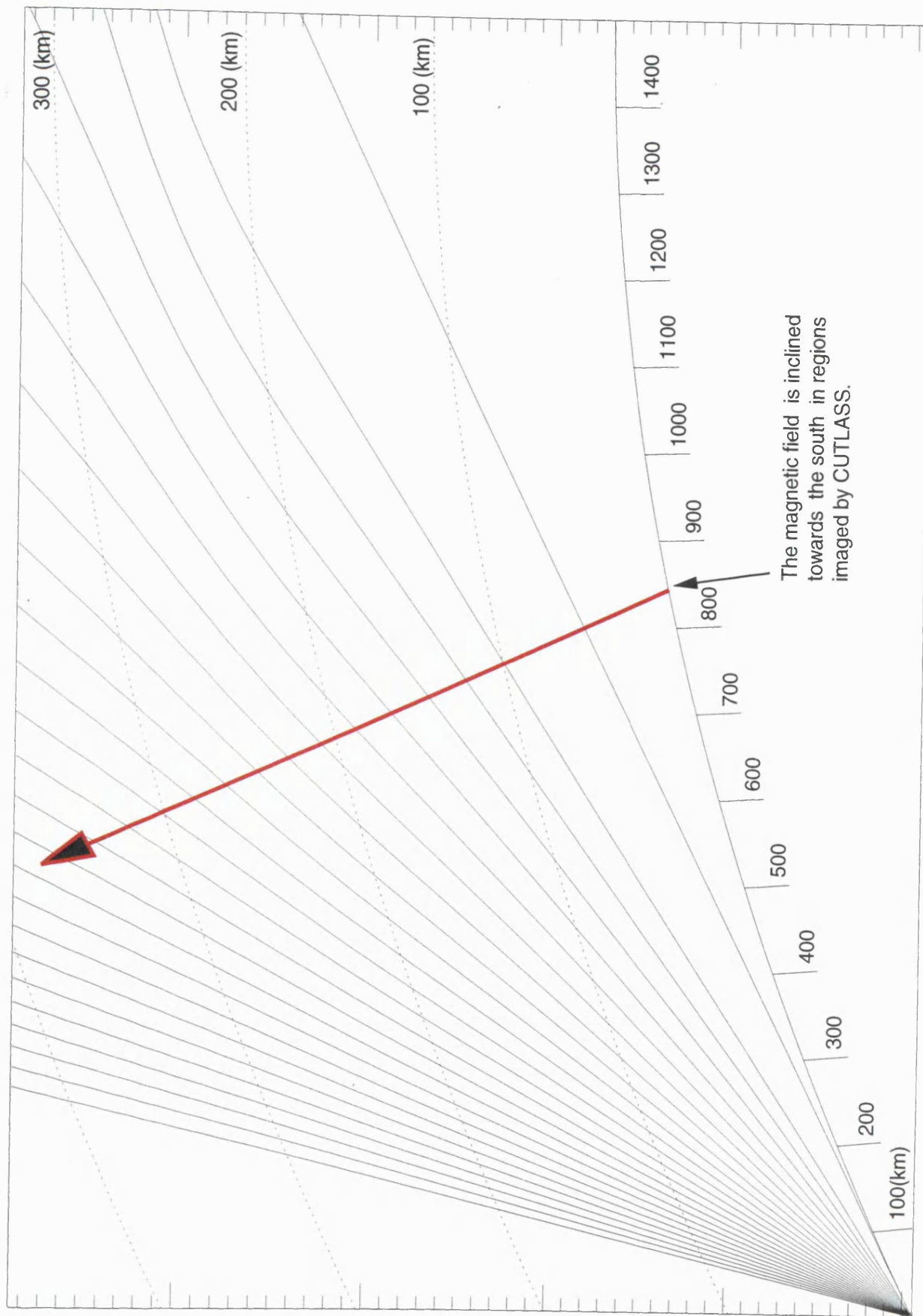


**Fig.6.15.** Ray trace through a 1-D plasma frequency profile, derived from the EISCAT electron density profile of 2248 UT on 21/08/98. The ray frequency is 10 MHz, since it is representative of the propagation mode of CUTLASS.

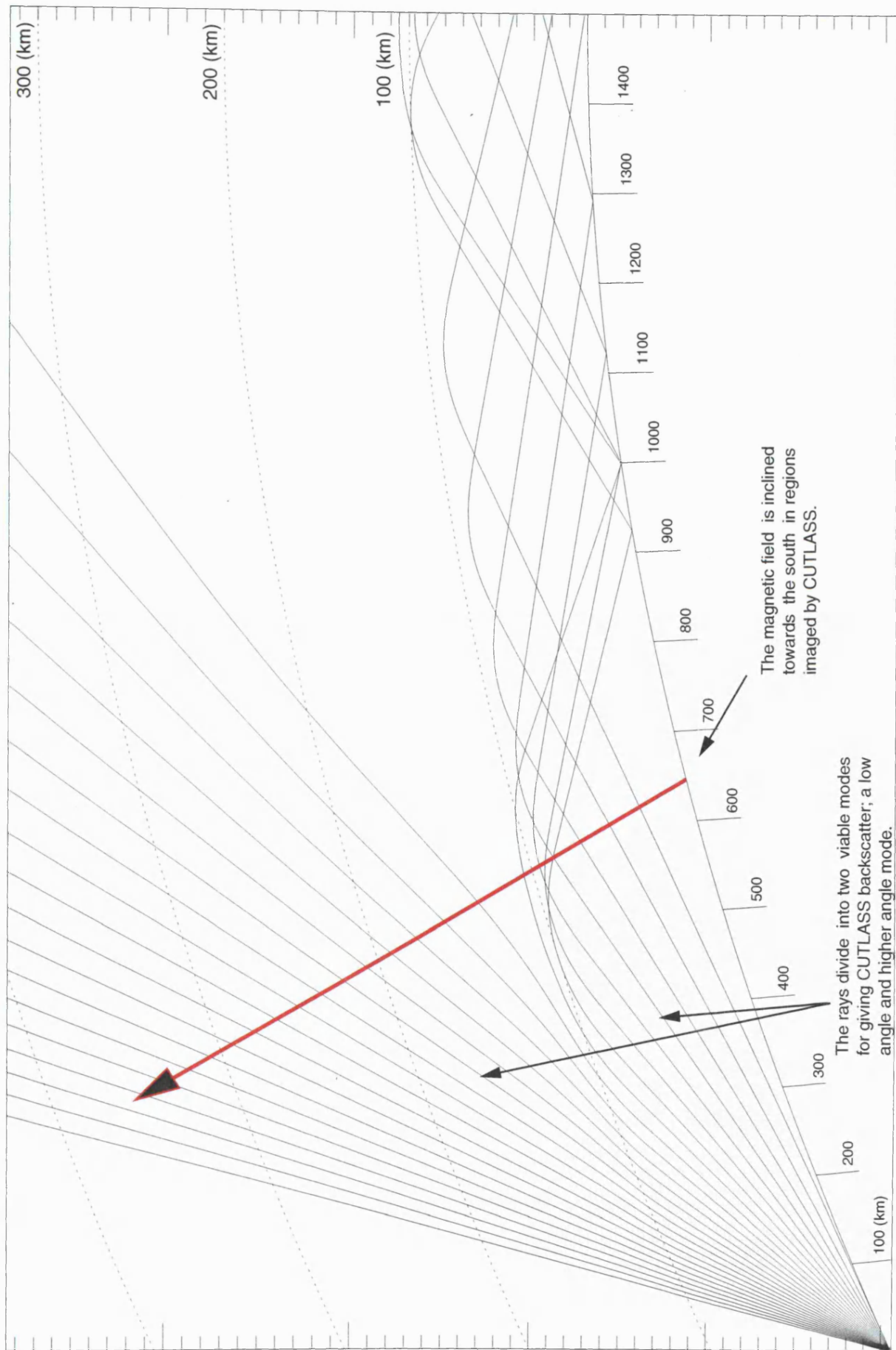


**Fig.6.16.** Ray trace through a 1-D plasma frequency profile, derived from the EISCAT electron density profile of 2310 UT on 21/08/98. The ray frequency is 10 MHz, since it is representative of the propagation mode of CUTLASS.

### 6.4.2 Supporting evidence provided by interferometry

The question which has now been posed is whether the elevation angle data from the interval is consistent with the elevation angles that are suggested by the ray tracings, and in particular, whether any significant changes in the propagation mode can be identified after the substorm onset. It should be noted, that this approach was not possible for the event analysed in chapter 5, due to the near total disappearance of the CUTLASS data after substorm onset, however in this case the data loss is partial, and therefore a more typical example of a substorm associated data loss event. With the ionospheric scatter only flag set, elevation angle data from each scan, beam and range gate, from the half hour preceding and the half hour post substorm expansion phase onset have been plotted on a colour scaled contour map of elevation angle against range, the scale being occurrence frequency per point in the space. The map containing the data from before the substorm onset (Fig.6.17) shows a high occurrence frequency across a broad range of angles between approximately  $7^{\circ}$  and  $25^{\circ}$ , and ranges mainly between 800 km and 2500 km, although there is a thin strip of data from about 400 km also. The map of data from after the substorm onset (Fig.6.18) looks very significantly different to figure 6.17 - occurrences of between  $8^{\circ}$  and  $17^{\circ}$  are virtually absent, having been very common before substorm onset - also a low elevation angle mode ( $<8^{\circ}$ ) has appeared between the ranges of 500 km and 700 km, and the total amount of data received is very much reduced. The fact that such substantial changes have occurred in the elevation angle-space after substorm onset, and in particular the near total loss of angles of between  $8^{\circ}$  and  $17^{\circ}$ , is totally consistent with the ray tracing analysis; in fact, the ray tracing analysis suggests that these elevation angles should not be occurring after substorm onset (except perhaps within a few hundred km of the radar site) due to these rays being unable to reach any backscattering targets in the ionosphere because they reflect at an altitude of around 100 km (Fig. 6.16). The consistency between the CUTLASS elevation angle data and the modelled ray tracing therefore supports the suggestion that the changes in, and losses of, backscatter at substorm onset, were as a consequence largely of altered propagation conditions.

The argument put forward so far has involved looking at all the data recorded by all the beams over an hour, centred on the time of the substorm expansion phase onset; it is also significant however, to look at the way in which the elevation angles behaved over specific scans leading into the active period. A CUTLASS time series in elevation angle, over interval 2247 UT to 2300 UT is presented (Fig.6.19). At the start of the interval, the elevation angles are generally colour-coded green, from  $12^{\circ}$  to  $18^{\circ}$ . By 2252 UT, shortly after the substorm expansion phase onset at 2250, a lot more yellow starts to appear in the more central beams, indicating an increase in elevation angle to more than  $20^{\circ}$ , and in these beams only, a new low

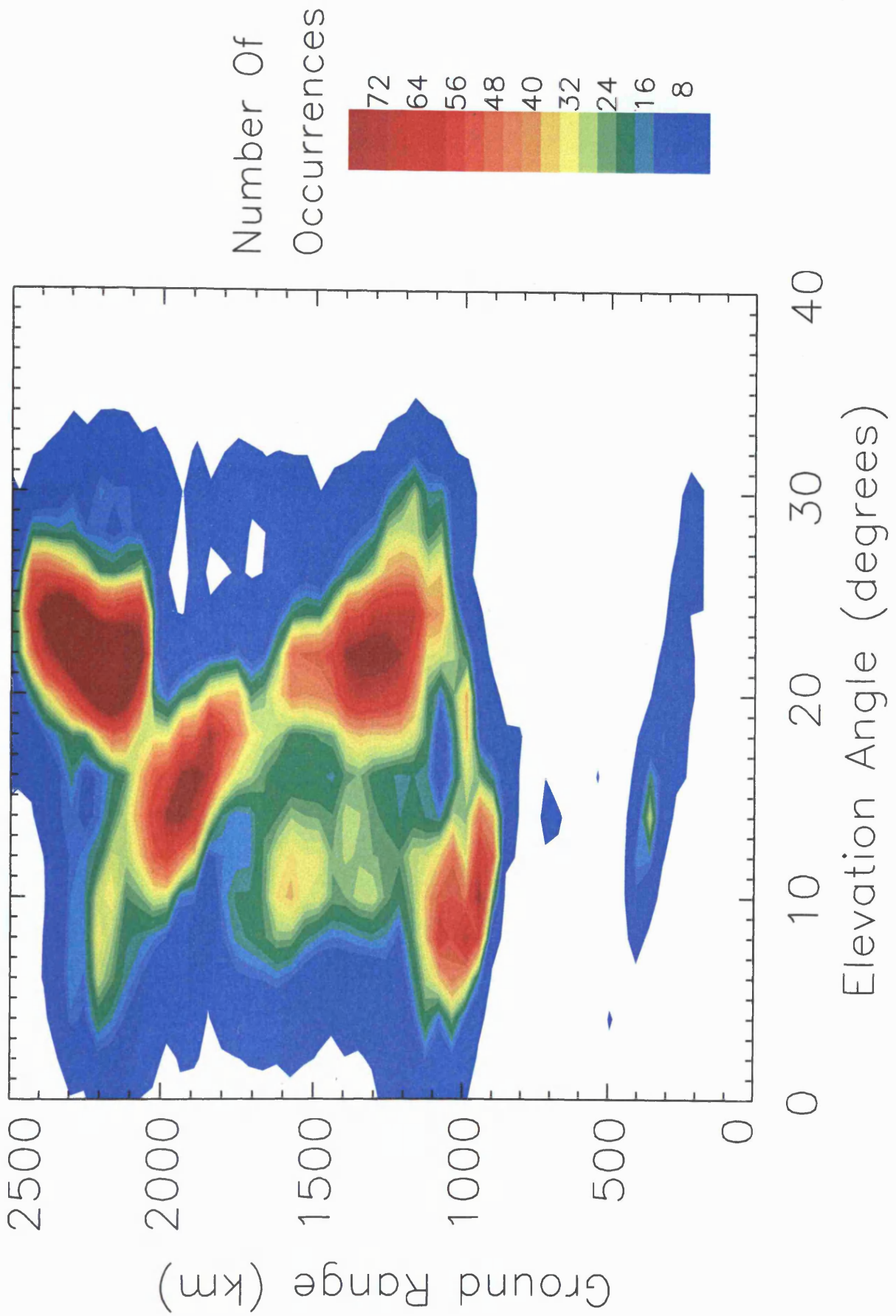


**Fig.6.17.** Elevation angle data from CUTLASS, across all beams and all ranges, in the interval 2220 UT to 2250 UT on 21/08/98. The colour scale is occurrence frequency per per point within the elevation angle - space.

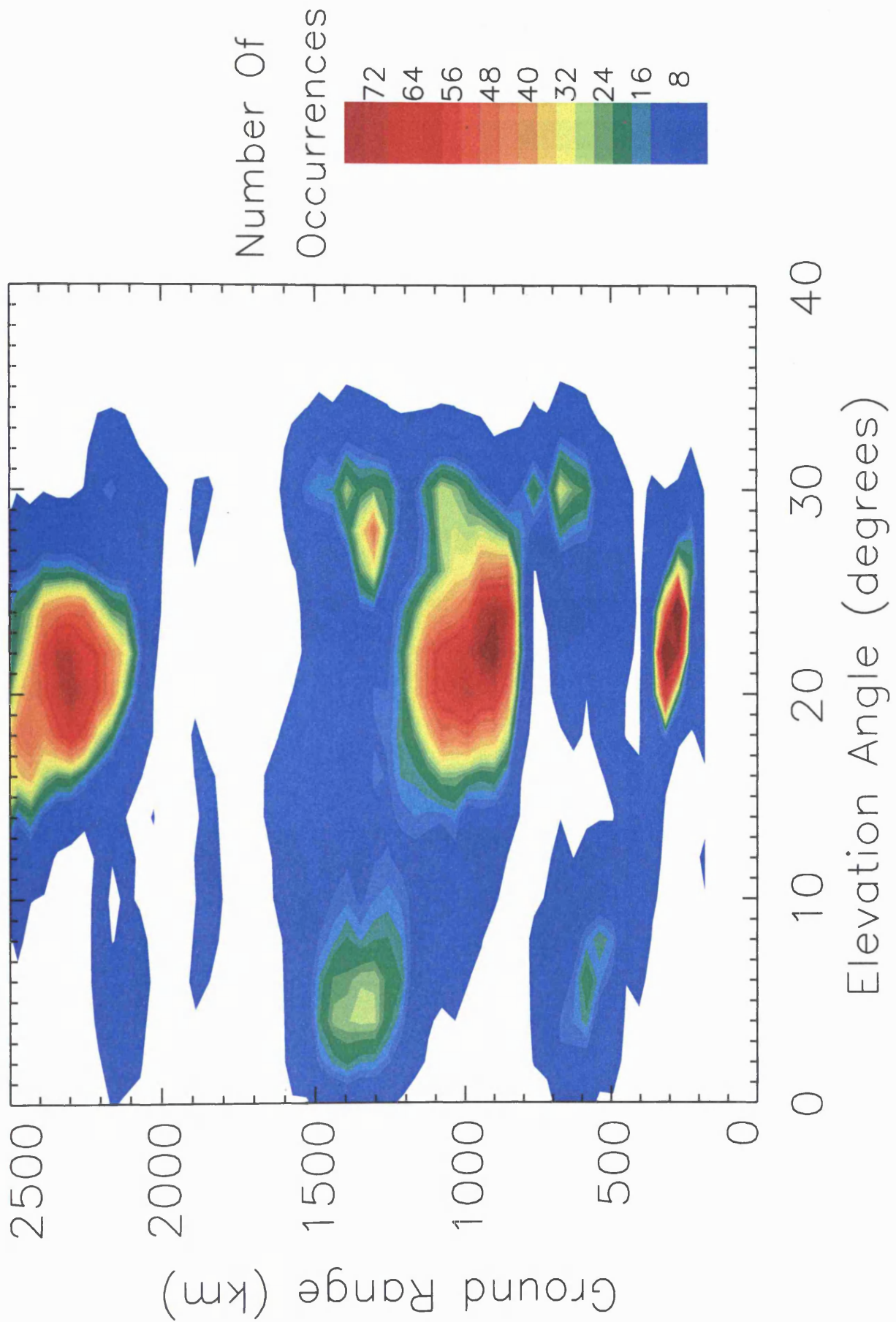


**Fig. 6.18.** Elevation angle data from CUTLASS, across all beams and all ranges, in the interval 2250 UT to 2320 UT on 21/08/98. The colour scale is occurrence frequency per point within the elevation angle - space.

21 Aug 1998 <sup>(233)</sup>  
 to  
 22 Aug 1998 <sup>(234)</sup>  
 unknown scan mode (-6315)

SUPERDARN PARAMETER PLOT  
 Finland: elev (phi0)

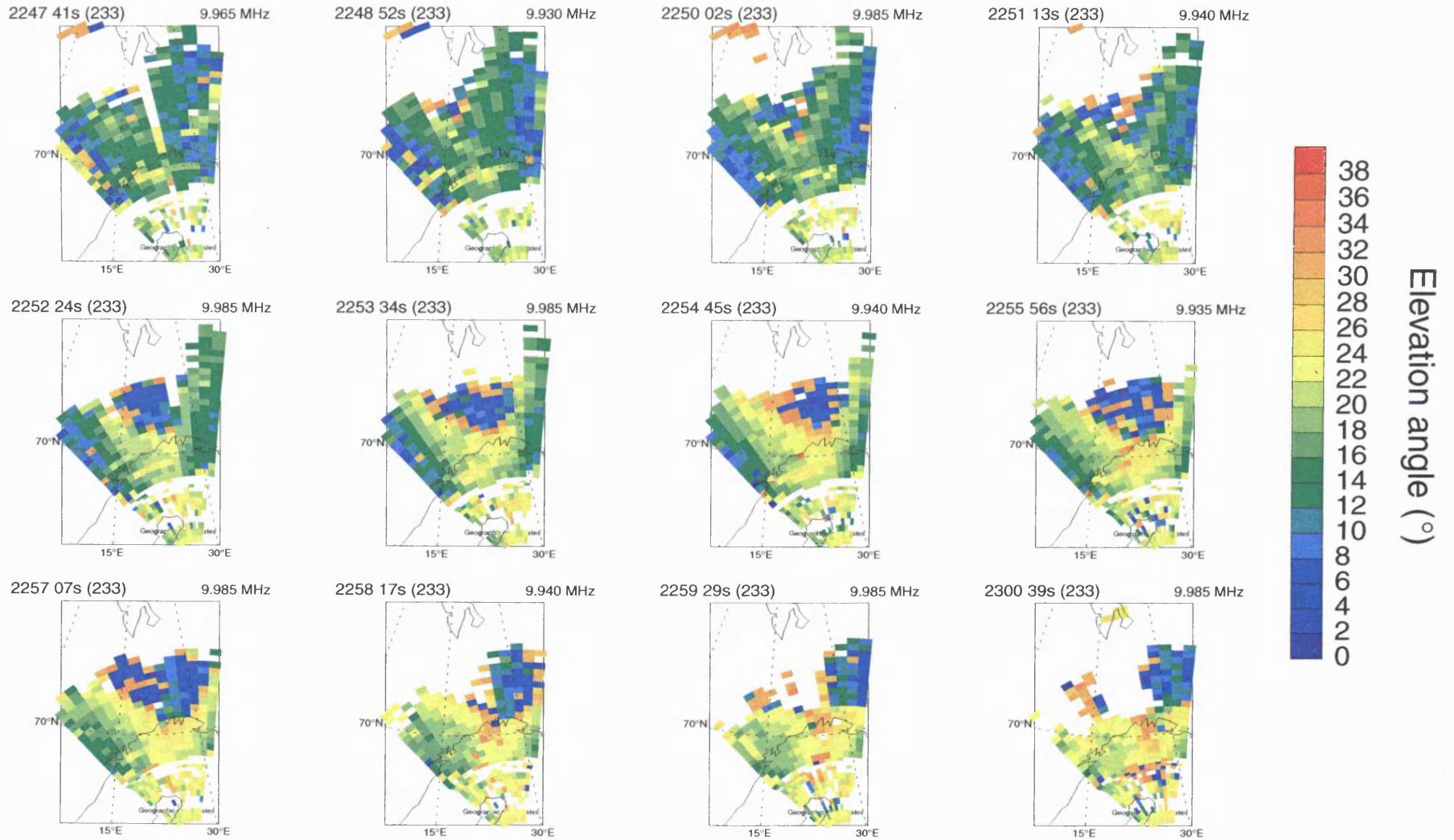


Fig.6.19. Time series of CUTLASS elevation angle data, showing the change in propagation conditions associated with the substorm.

elevation angle mode appears in the northern section, whilst the most easterly and westerly beams remain wholly in the green category. By 2258 UT however, the increase in elevation angle had spread to most of the field of view, and the total area of the returns had reduced. This chain of events is consistent with the previous ray tracing analysis, which suggested that angles below  $15^\circ$  would be lost due to reflection, and that higher angles might then become favoured, or possibly a very low angle mode. These effects can also be viewed on a temporal plot of elevation angle against latitude, which is accompanied by a latitude power plot, in the interval 2245 UT to 2345 UT for the high time resolution CUTLASS beam 9 (Fig.6.20). The mode of propagation is seen to switch at about 2252 UT, with the low elevation angle mode (blue) and higher angle mode (yellow), replacing angles initially in the green category. It is of particular significance to note, that these elevation angle features, also show up on the plot of received power. The (horizontal) dividing line between the blue elevation angle mode and the yellow mode, between 2252 UT and 2255UT, shows up very clearly in the power, as does the sloping feature formed by the vanishing green mode. Of course, different propagation modes, would be expected to have different power regimes, and this data therefore lends further support to the suggestion, that the main influence upon the radar returns during this event was the propagation conditions.

### **6.5 Loss of irregularities by electric field shorting**

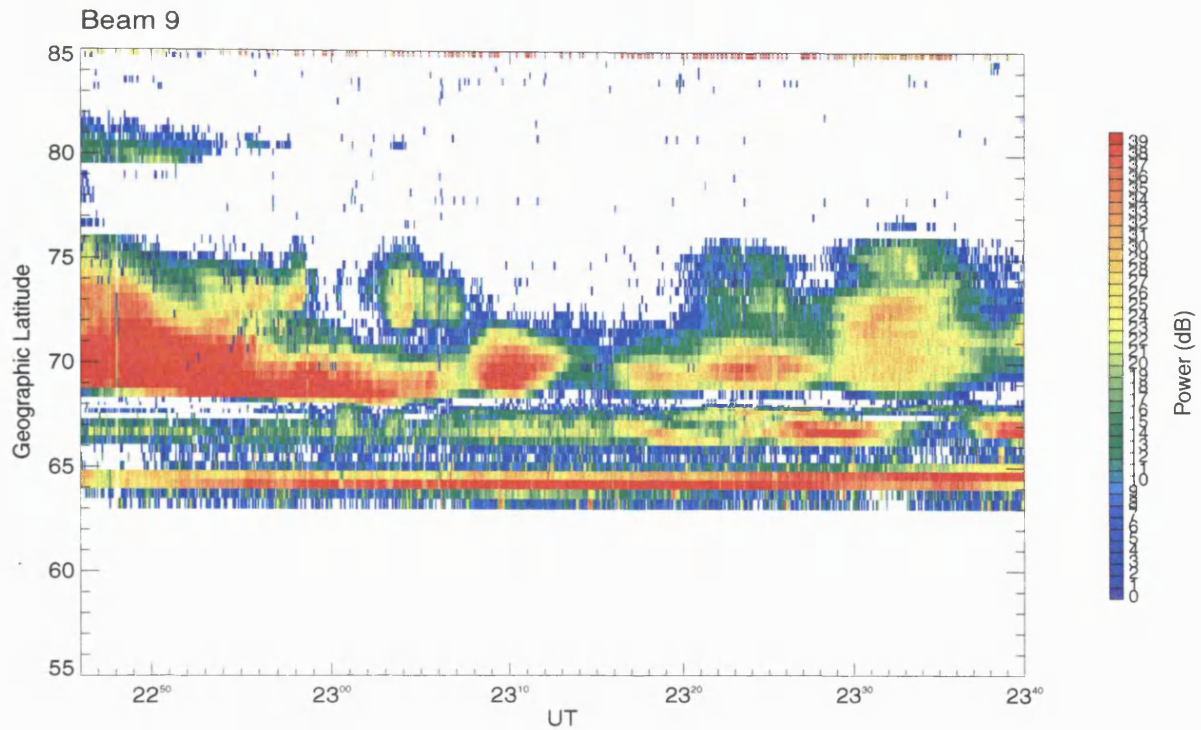
The likelihood that irregularities would have been lost during the substorm interval due to electric field shorting (Section 5.2.2) has so far been neglected, and of course, the level of scattering structure present at any particular time and place cannot be easily assessed. It seems that the best evidence that one can obtain simply, in support of there being an effective depletion in scattering structure, is to show that the electric field strength and radar power have simultaneously reduced in a particular location. The growth rate of any viable instability mechanism would be expected to be dependent upon the applied electric field; for instance, the Farley-Bunemann instability requires a threshold field to achieve a positive growth rate, whilst linear theory of the  $\mathbf{E} \times \mathbf{B}$  instability suggests that the growth rate is proportional to  $\mathbf{E}$  (Section 5.2.2). Of course, if the signal from CUTLASS disappears altogether, then CUTLASS data can no longer be used to provide evidence of electric field suppression in that vicinity. However, on this occasion, we have F-region plasma convection data from both EISCAT (Tromsø) and the ESR, as well as beamsung data from the Tromsø arrangement (Section 6.2.3), which may be easily converted into the convection electric field.

The CUTLASS data from the high time resolution beam 9 shows two distinct bites out of the data, the first being from 2258 UT until 2300 UT, and the second from 2307 UT until

# SUPERDARN PARAMETER PLOT

21 Aug 1998  
to  
22 Aug 1998

Finland: Power



## Finland: Elevation angle

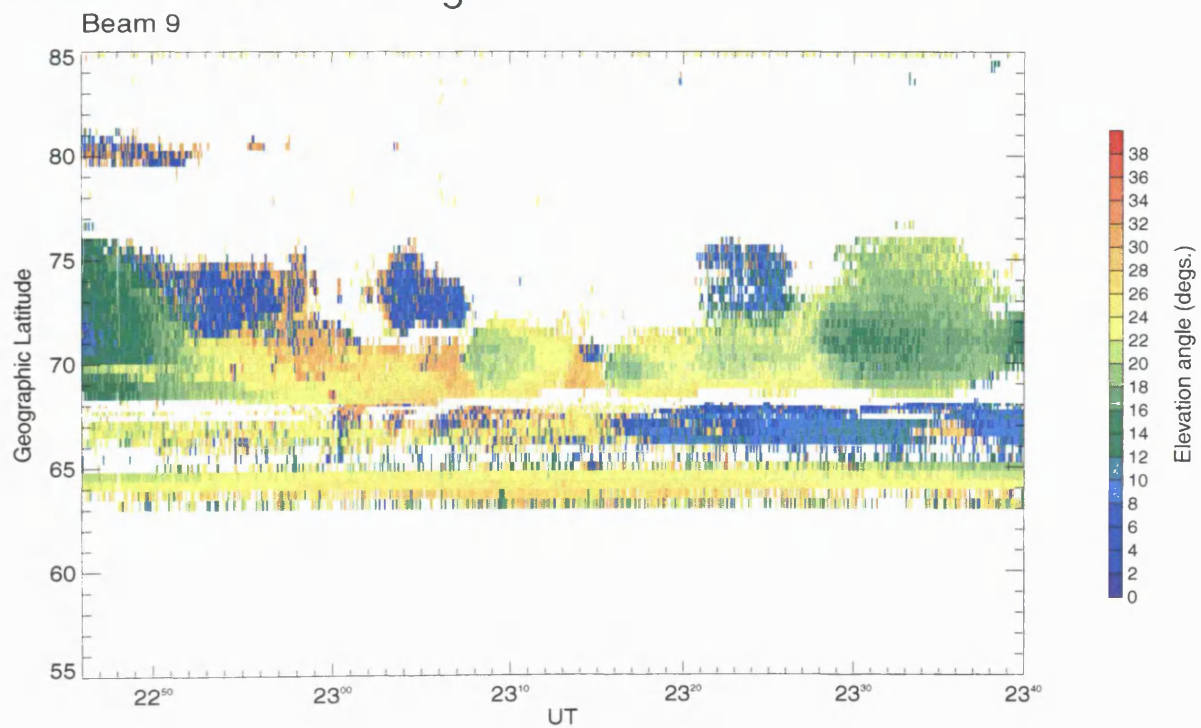


**Fig.6.20.** Power and elevation angle data from CUTLASS beam 9. The propagation conditions can be seen to alter abruptly at 2252 UT as the substorm began. Many of the features in elevation angle can also be clearly identified in the power.

2320 UT (Fig.6.1). The data from CUTLASS beam 9 is reproduced in Figure 6.21, with the beamswung plasma convection velocities overlayed, the ESR line of sight velocity data above, and the derived Hall conductance data underneath; it can be seen from the size of the velocity vectors that the first of these intervals of CUTLASS data loss coincides with a period of electric field suppression in that locality, and is also broadly in agreement with the ESR data which shows lower velocities during this interval. The second interval of CUTLASS data loss is accompanied by far higher convection velocities from both the beamswing and the ESR, indicating a substantial convection electric field, indeed, larger than that in evidence before any CUTLASS data was lost. It may be concluded therefore, that the initial 'bite out' of the data may indeed have been caused by an electric field shorting effect, whilst the second 'bite out' probably was not.

## 6.6 Summary

Using the analysis techniques developed over the last two chapters, it has been possible to gain some quantitative insight into the operational constraints put upon CUTLASS by changes in absorption levels and propagation conditions associated with substorms.

Changes in the extent and power of radar backscatter returns and in the elevation angle space indicate that the process which best explains the behaviour of backscatter returns in the example presented in this chapter is altering propagation conditions. It was concluded that the increased absorption associated with this substorm would not have been sufficient to cause the reductions in power witnessed, and more significantly perhaps, the spatial characteristics of the power loss along each beam are not consistent simply with the presence of a common absorbing region. Ray tracing analysis was applied to representative ionospheres from before and after substorm onset, and it was found that in both instances the elevation angles measured by CUTLASS were consistent with those suggested by the ray tracing. Since the measured angles were consistent with those expected from the ray tracings, and these measured angles were found to alter substantially shortly after substorm onset, the conclusion that the partial loss of radar backscatter was caused, at least in part, by changes of ray propagation is strongly supported by the data. The appearance shortly after substorm onset of a low elevation angle mode, with lower power than the higher elevation mode it replaced, is also consistent with the scenario suggested by the ray tracing (i.e. that after substorm onset, the higher angle rays which had produced backscatter before substorm onset, are reflected back to earth thereby enabling the weaker low elevation angle mode to appear). It is not possible to isolate and separate all of the influences upon radar reception in this large scale

# SP-UK-CSUB

21 August 1998

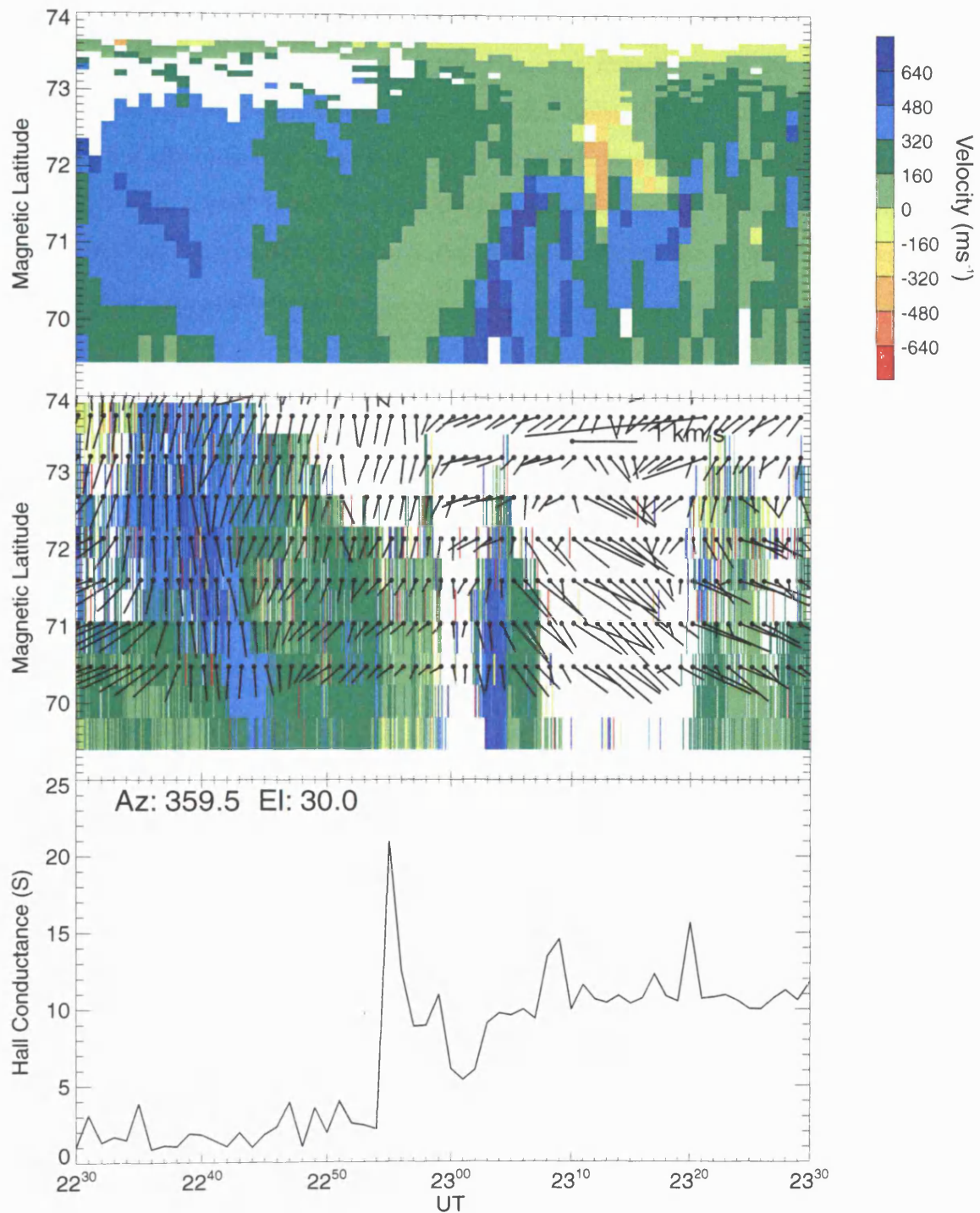


**Fig.6.21.** Data from CUTLASS beam 9 is displayed in the central panel with EISCAT beamswung velocity vectors overlaid. The top panel shows the corresponding ESR velocity data, and the bottom panel is the Hall conductance.

and dynamic environment, and indeed, evidence of electric field suppression during the initial short lived radar dropout has been provided by data from both EISCAT VHF (Tromsø) and the ESR, suggesting that the production of ionospheric irregularities were probably affected by the substorm. These radars also provided evidence that the convection electric field was not suppressed during the second, classical 'bite out', and show that suppression of at least the convection electric field was not prolonged or widespread - it should be noted however, that it is quite possible for irregularity growth rates to reduce even if the convection electric field increases – e.g. the formulation of Vickrey and Kelley (1982, section 2.5).

Despite the obvious difficulties of trying to attribute cause and effect in this complex system, it would appear likely from an overall consideration of the analysis in this chapter that the predominant influence upon radar reception during the substorm interval was the changing radar propagation mode.

## Chapter 7

### An overview of substorm signatures in CUTLASS data

#### 7.1 Introduction

Further examples of substorm signatures in CUTLASS data are presented in this chapter, as well as some basic statistics of the whole set of CUTLASS signal loss events identified. These events number some 15, of which a total of eight are contained in this thesis. Eleven of the events proved to be associated with a clearly defined substorm; the other four events are significantly different to the substorm associated events in that they proved to be localised effects when viewed in CUTLASS spatial data (they were initially selected from LTV data from beam 5 (Section 5.2.2)). The process of selecting the set of events by eye from LTV data led to the discovery that most of the events so selected corresponded with a period of substorm activity; Whilst substorms are a highly variable phenomenon, in terms of location, intensity and duration, and the radar data is likewise variable, the consideration of a number of events does reveal some repeatable behaviours, and allows certain conclusions to be drawn as to what is typical of these radar data drop out events. Such statistics are an interesting quantification of substorm-associated phenomena, and are also useful from the point of view of HF radar operational considerations. In many cases the characteristic features observed, can be explained by analogy with the events covered in depth in chapters five and six. Since there is no EISCAT data available for any of the events presented in this chapter, no further ray tracing or absorption calculations have been attempted. By way of contrast, one of the CUTLASS data loss events which proved not to be associated with any substorm activity has also been included.

#### 7.2 Further CUTLASS case studies

The substorm associated CUTLASS data loss examples presented in this chapter occurred in the spring and summer, being in chronological order 07/05/96, 10/05/96, 24/08/97, 15/04/98, and 29/04/98. The anomalous (non substorm related) event was that of 10/05/96, and is described last, the substorm related events being presented chronologically. IRIS and IMAGE data are again included for all the events.

### **7.2.1 Case study - 07/05/96**

An LTV plot for CUTLASS beam 8, together with IMAGE magnetometer data from Tromsø and Bear Island, for the interval from 2000 UT until 2400 UT on 07/06/96, is depicted in Figure 7.1. The appearance of a 'bite out' of the CUTLASS data just before 21.20 UT, and the simultaneous commencement of magnetic perturbations and Pi2 pulsations is reminiscent of both the example from chapter 1 (Fig.1.9) and the example which was the subject of chapter 6 (Fig.6.1). Again, the bite out is associated with a clearly defined substorm, and IRIS detects a corresponding enhancement of cosmic radio noise absorption (Fig.7.2.). A CUTLASS spatial plot in elevation angle leading through the period of data loss shows the losses to have been widespread (Fig.7.3.); The elevation angles initially are generally between 10° and 14°, however at 2127 UT, a substantial region of a much lower elevation angle mode appears, and this region subsequently expands. The evolution of this elevation angle time series is somewhat reminiscent of the pattern observed in the discussion of the event of 21/08/98 (Section 6.4.2) - i.e. an initial mode giving way to a lower mode, perhaps due to the earthward refraction of the higher mode with increasing plasma frequency - and suggests that the radar propagation mode was affected by the substorm. Evidence from IRIS shows a region of active absorption associated with the substorm in the north and centre of its field of view, with little or no increased absorption indicated in the south of the field of view (Fig.7.2); this suggests that all the rays which initially produced the backscatter (i.e. those of more than 10° in elevation) would have climbed above the altitude of the known region of active absorption (about 85 km in altitude) before having reached the range of 800 km or so at which the absorption was detected by IRIS, indicating that increased absorption may not have been the most significant factor in this event, and in agreement with the conclusions reached for the example of chapter 6. The possibility that irregularities were lost due to electric field shorting effects can never be neglected, however, this example is fairly similar to the one discussed in chapter 6, and its explanation in terms of some combination of the suggested signal loss mechanisms (Section 5.2.2), should perhaps have an emphasis on this being an effect associated with the radar propagation mode.

### **7.2.2 Case study - 24/08/97**

This example again has most of its features in common with the previous cases associated with isolated substorms, the most notable difference being however that the elevation angles start off in a low angle mode, and generally remain in it. A CUTLASS LTV plot together with Pi2 filtered

# SUPERDARN PARAMETER PLOT 7 May 1996

Hankasalmi: vel

normal (ccw) scan mode (127)

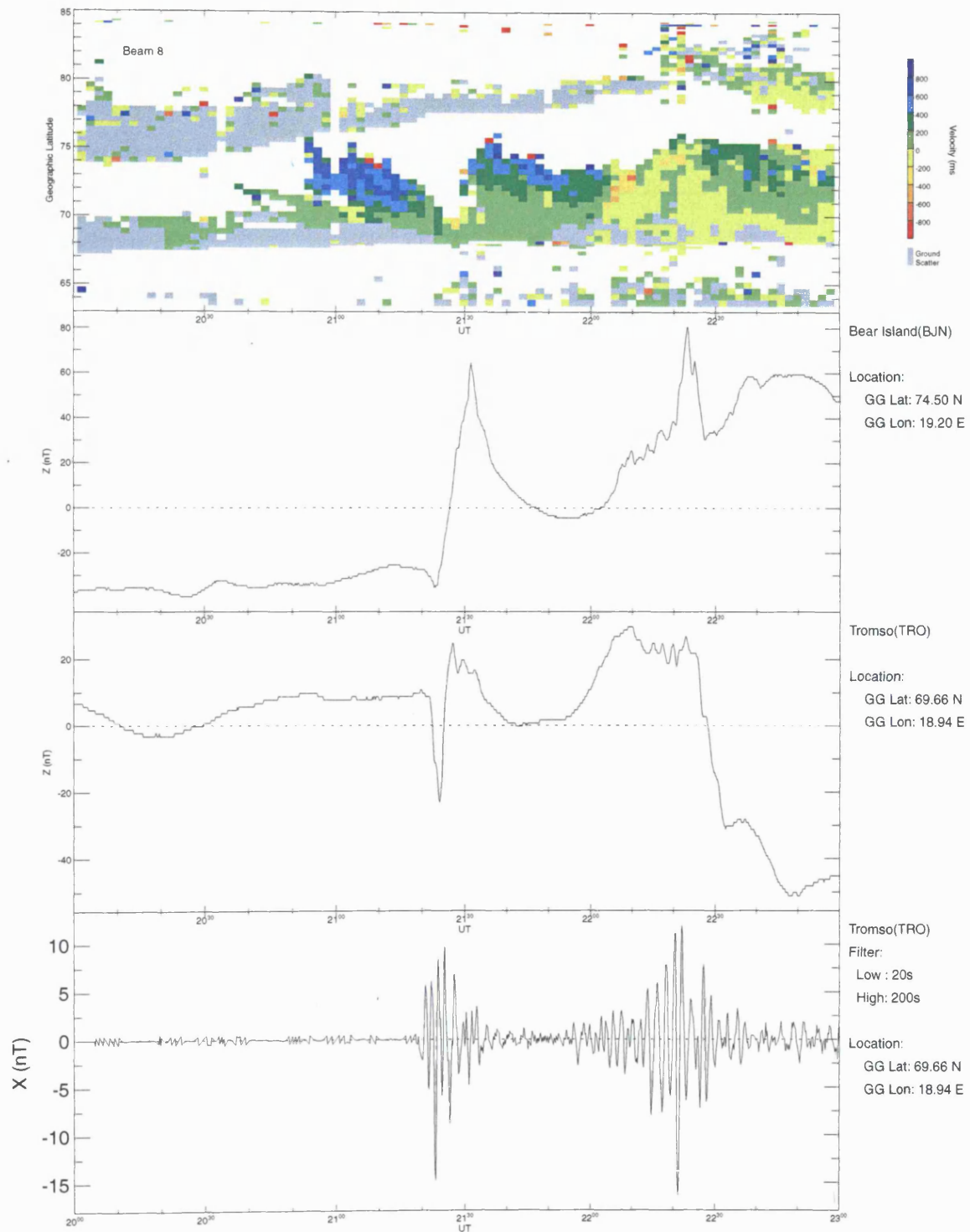


**Fig.7.1.** CUTLASS (LTV) plot, together with Z component magnetic perturbations from Bear Island and Tromso, and Pi2 filtered magnetic perturbations from Tromso. The magnetic perturbations are indicative of a substorm, which also affected the CUTLASS LTV data resulting in a 'bite out'.

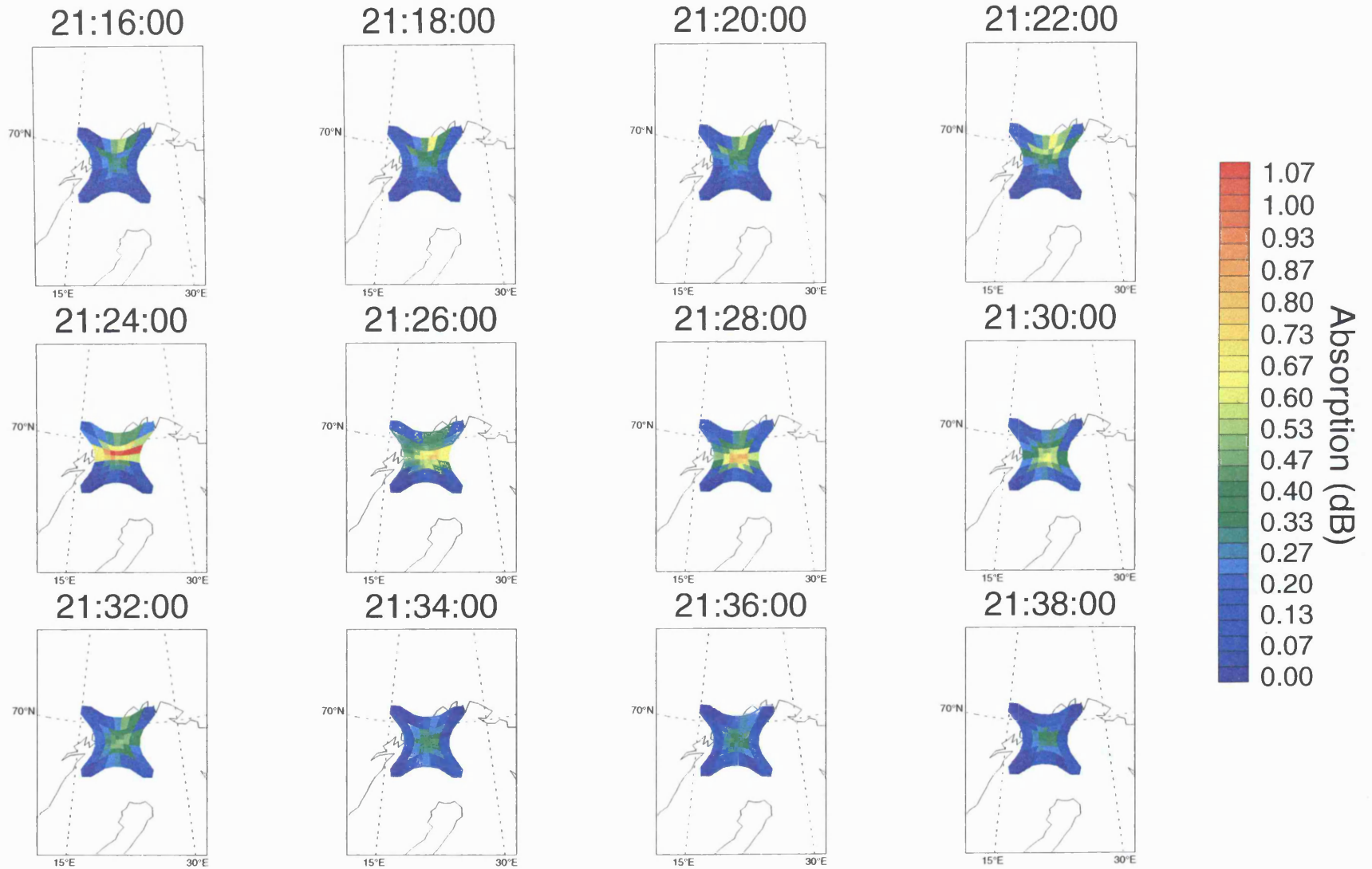
# IRIS Riometer

time\_series

7 May 1996 <sup>(128)</sup>

normal (ccw) scan mode (127)

Fig.7.2. Time series of IRIS absorption data, showing an enhancement shortly after 2120 UT which is associated with a substorm.



# SUPERDARN PARAMETER PLOT

Hankasalmi: elev (phi0)

7 May 1996<sup>(128)</sup>

normal (ccw) scan mode (127)

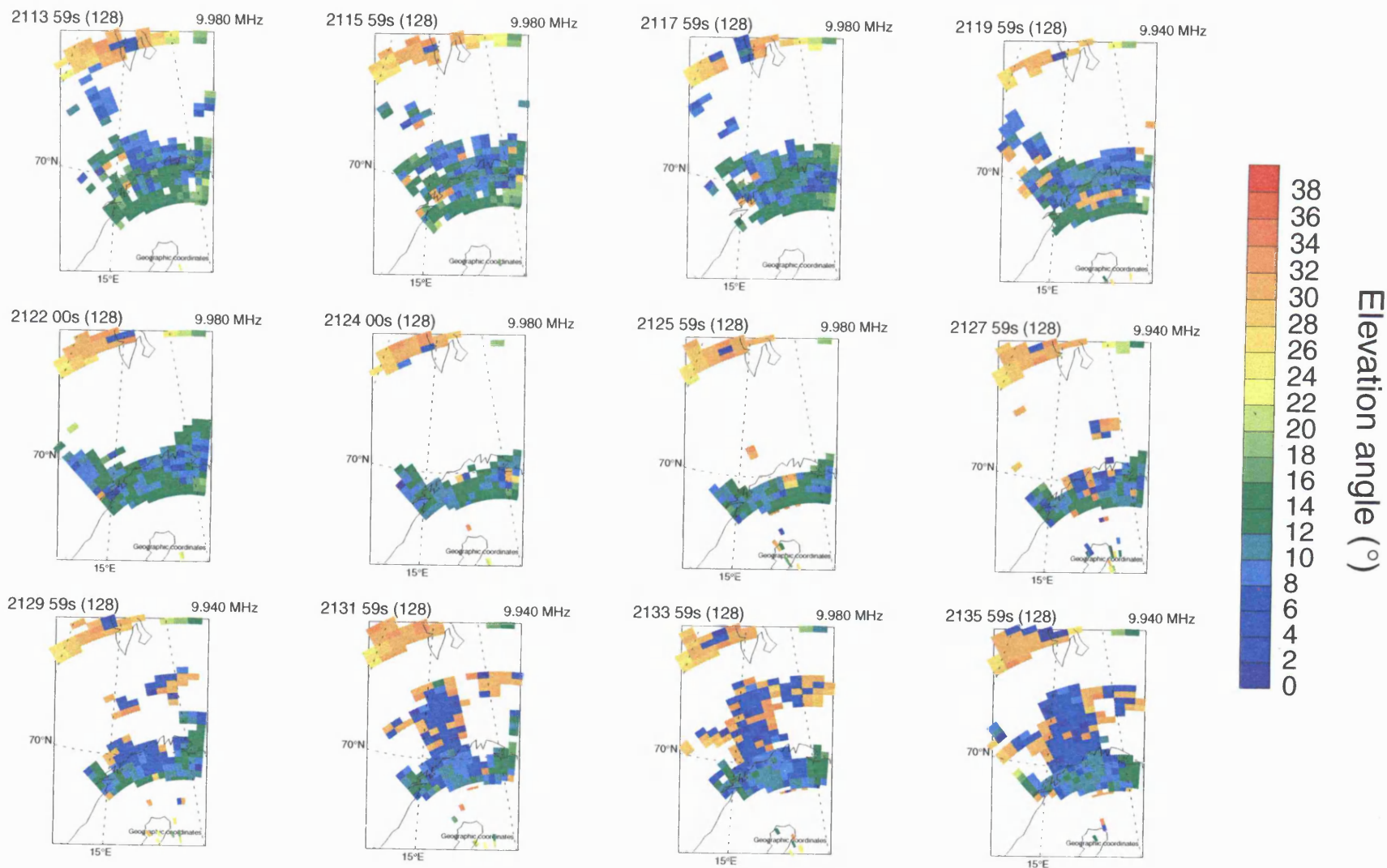


Fig.7.3. CUTLASS elevation angle time series showing that the region of returns receded from the north during the substorm, and then recovered with an increased proportion of the low angle propagation mode.

(from Tromsø) and raw (from Hornsund and Kiruna) magnetic perturbations is displayed in Figure 7.4; The disappearance of CUTLASS data at 2150 UT is accompanied by a Pi2 pulsation, indicative of a substorm. The IRIS data shows a considerable enhancement of cosmic radio noise absorption just before 2150 UT, which then begins to reduce shortly after 2200 UT (Fig.7.5.). The spatial behaviour of CUTLASS data is displayed in an elevation angle time series (Fig.7.6.), which demonstrates that the data loss was widespread and that elevation angles were generally in a low angle mode of less than 10° (although there are still some regions higher than 10°, whilst the large amount of orange colour coding (> 30°) is believed really to be aliased angles of less than 6°). There are several factors which suggest that absorption may be the key mechanism involved in this case - the CUTLASS data initially recedes at the same time as the IRIS absorption increases, and then reappears as the absorption reduces, however, this fact should be noted along with the fact that the low elevation angle mode can indeed reach the region where the enhanced absorption measured by IRIS actually occurred (i.e. below 90 km in altitude), and does so without reaching the altitudes at which refraction would be significant. If the work of chapter 6 is used as an analogy, the ray reflection level would have been close to 95 km for the low angle mode during the substorm (see ray trace fig.6.13), which implies that the low angle mode would not suffer significant refraction until some point after it has suffered absorption.

### **7.2.3 Case study - 15/04/98**

This is another broadly similar example of a CUTLASS data loss event, although again with its own peculiarities; It can be seen that the start of the bite out of the CUTLASS data at 2310 UT and the onset of Pi2 pulsations and magnetic perturbations are virtually simultaneous (Fig.7.7), but unusually the bite shows a degree of symmetry, forming from the northern and southern edges of the data, which is suggestive of a distant common absorbing region (i.e. somewhere close to the radar site). Also notable is the sudden reversal of flow during the bite out period, which indicates altering electrodynamic, presumably associated with the substorm process. The disappearance of the CUTLASS data is seen spatially on an elevation angle time series (Fig.7.8); initially, at 2314 UT, the elevation angles are quite varied, but most commonly in the categories between 14° and 20°. The transition between 2314 UT and 2318 UT is interesting - just as the CUTLASS data starts to rapidly disappear, a substantial region of the low angle propagation mode appears - which is reminiscent of several previous examples, and was explained in terms of the higher angle rays starting to reflect, enabling the lower angle rays to become dominant

# SUPERDARN PARAMETER PLOT<sub>24 Aug 1997</sub>

Finland: vel

normal (ccw) scan mode (150)

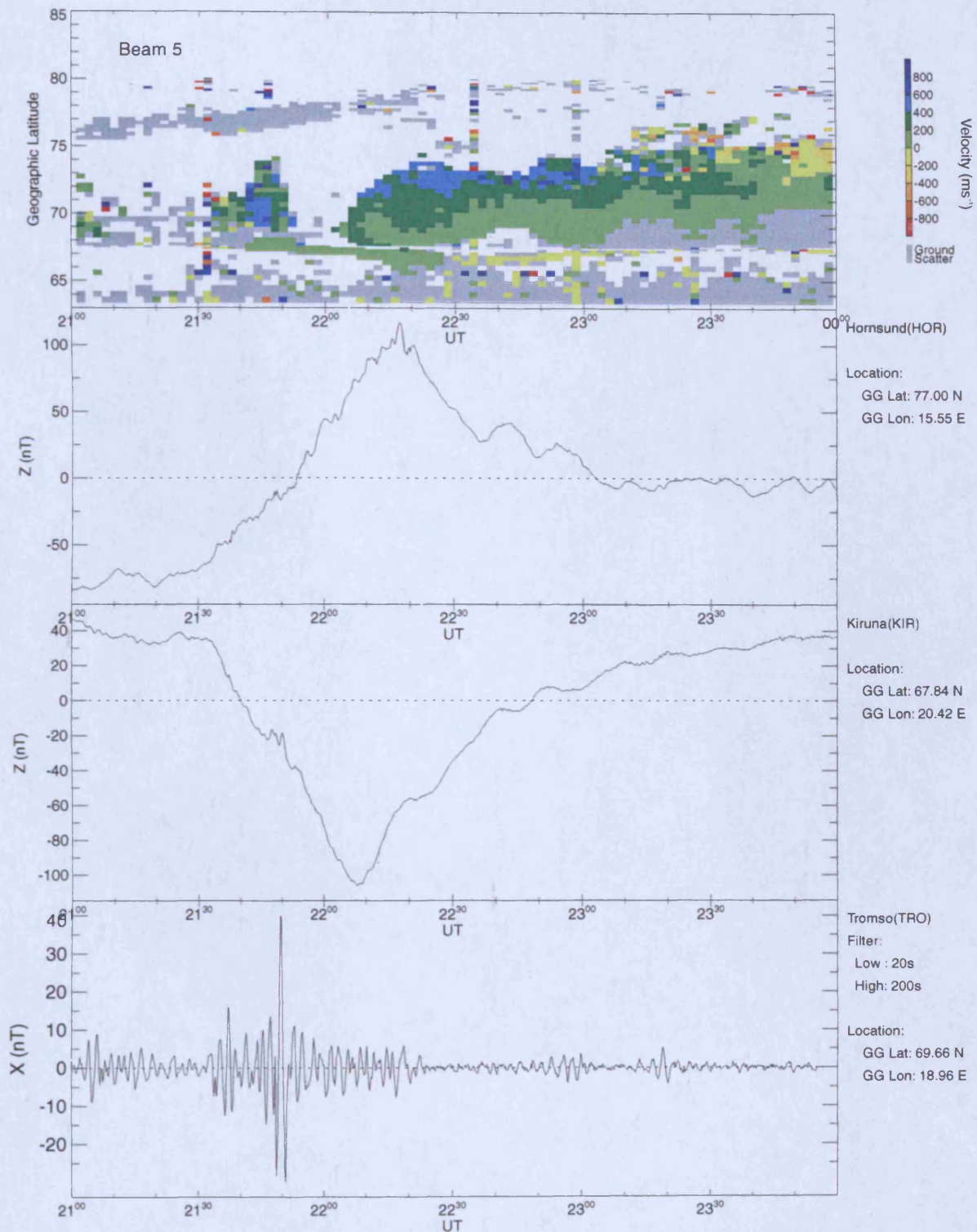


**Fig.7.4.** Data is lost from beam 5 of CUTLASS between approximately 2150 UT and 2205 UT, which is associated with a substorm as evidenced by the Pi2 pulsation at Tromsø. The Z component magnetic pulsations at Hornsund and Kiruna show that an East - West electrojet is situated in the ionosphere between these locations.

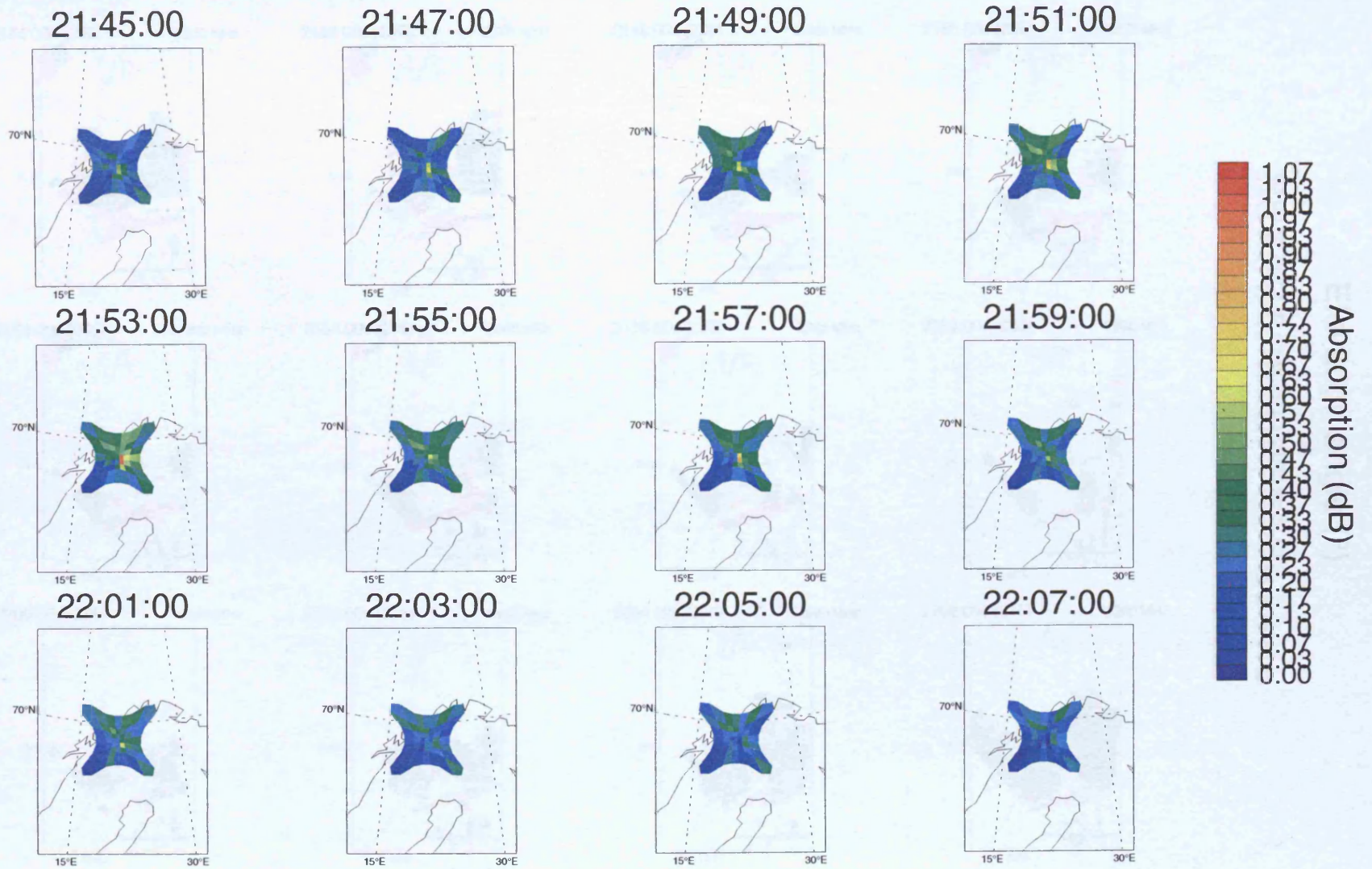
# IRIS Riometer

time\_series

24 Aug 1997 <sup>(236)</sup>

normal (ccw) scan mode (150)

Fig. 7.5. Time series of IRIS absorption data showing a temporary enhancement, which was associated with a substorm.



# SUPERDARN PARAMETER PLOT

Hankasalmi: elev (phi0)

24 Aug 1997<sup>(236)</sup>

normal (ccw) scan mode (150)

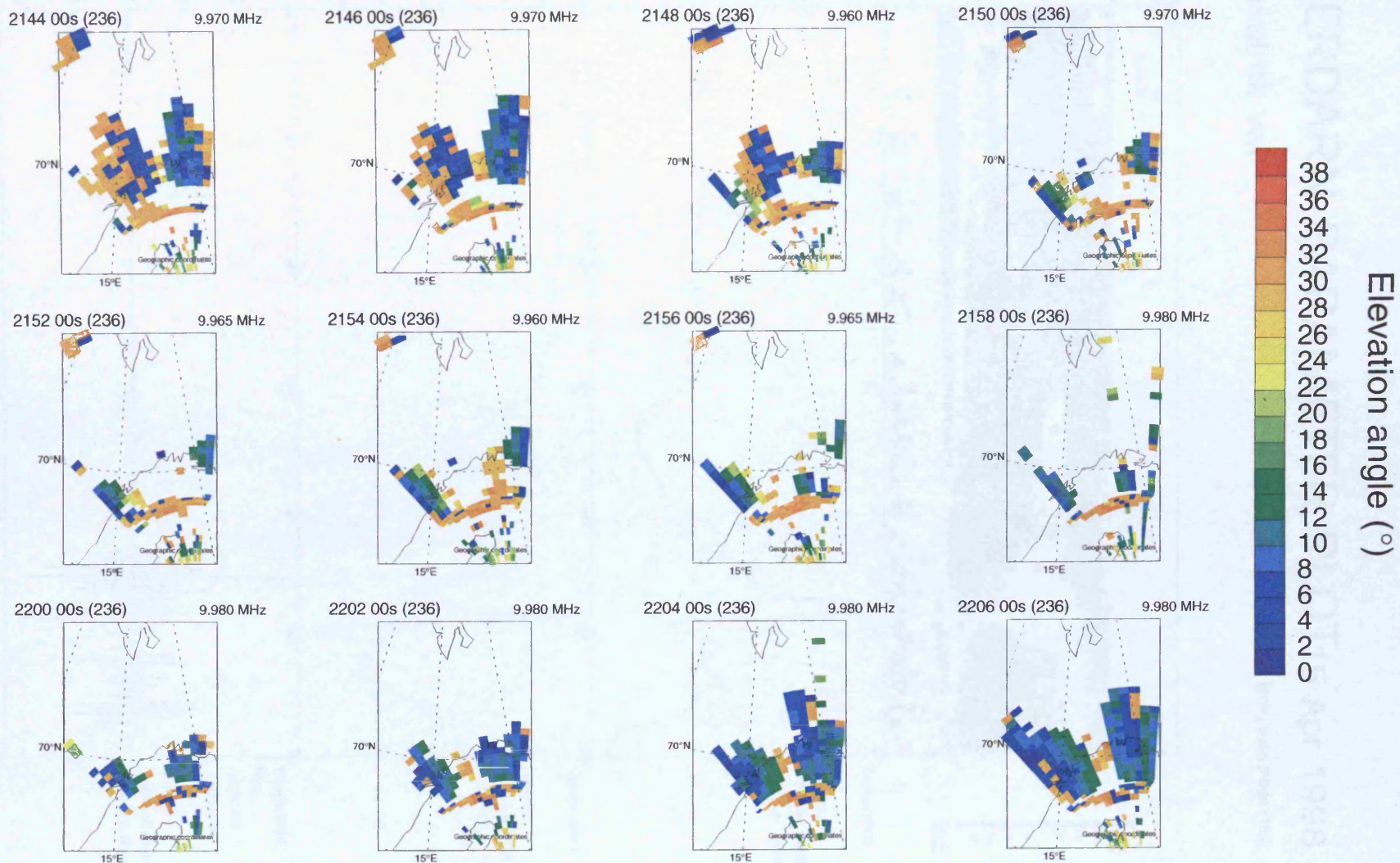
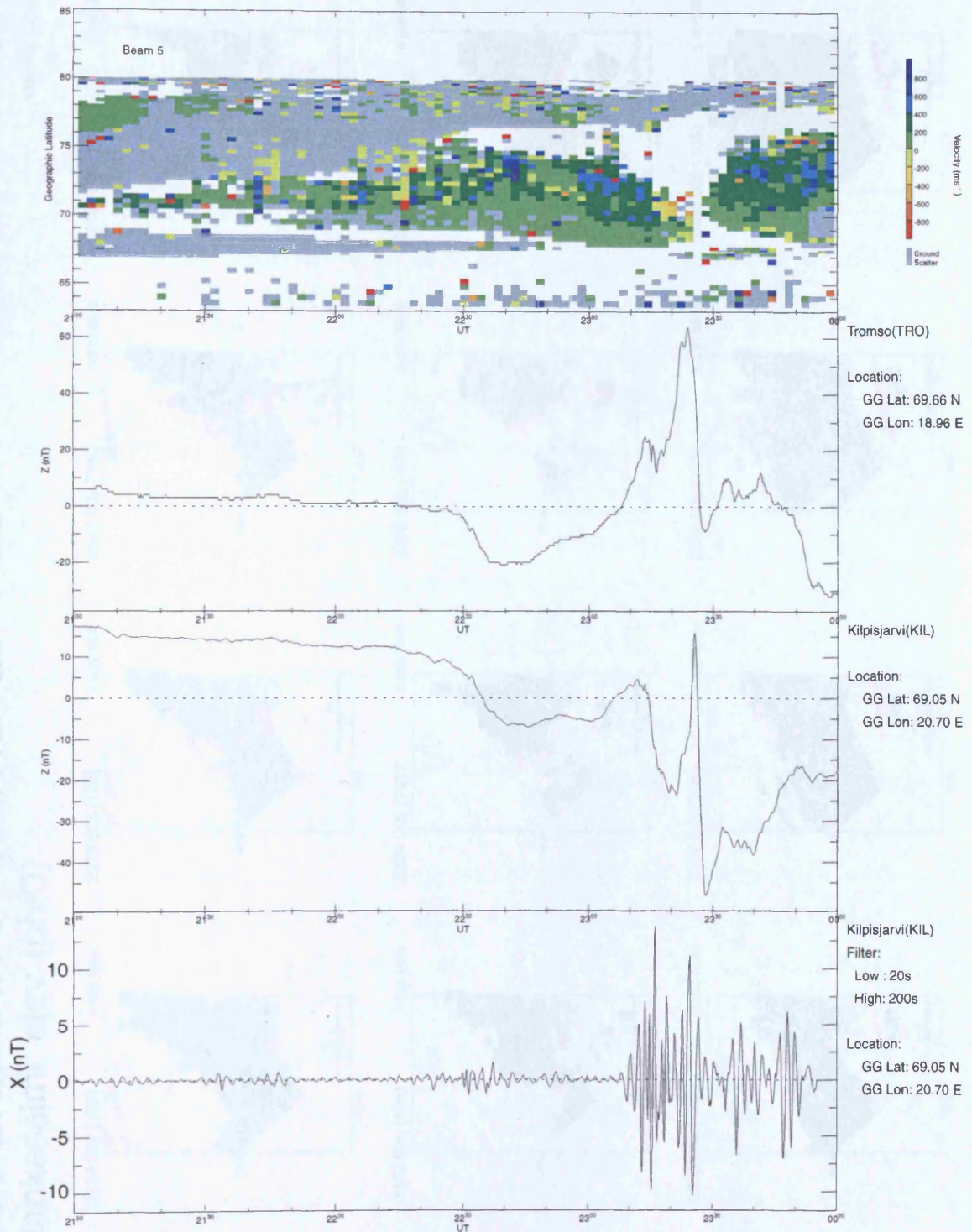


Fig. 7.6. CUTLASS elevation angle time series, showing generally low mode returns throughout, and showing a widespread data loss associated with a substorm.

# SUPERDARN PARAMETER PLOT 15 Apr 1998

Hankasalmi: vel

normal (ccw) scan mode (150)



**Fig.7.7.** CUTLASS (LTV) data from beam 5, together with Z component magnetic perturbations from Tromso and Kilpisjarvi, and Pi2 filtered data from kilpisjarvi. The CUTLASS data loss at shortly after 2310 UT is associated with a substorm.

# SUPERDARN PARAMETER PLOT

## Hankasalmi: elev (phi0)

15 Apr 1998 <sup>(105)</sup>  
 normal (ccw) scan mode (150)

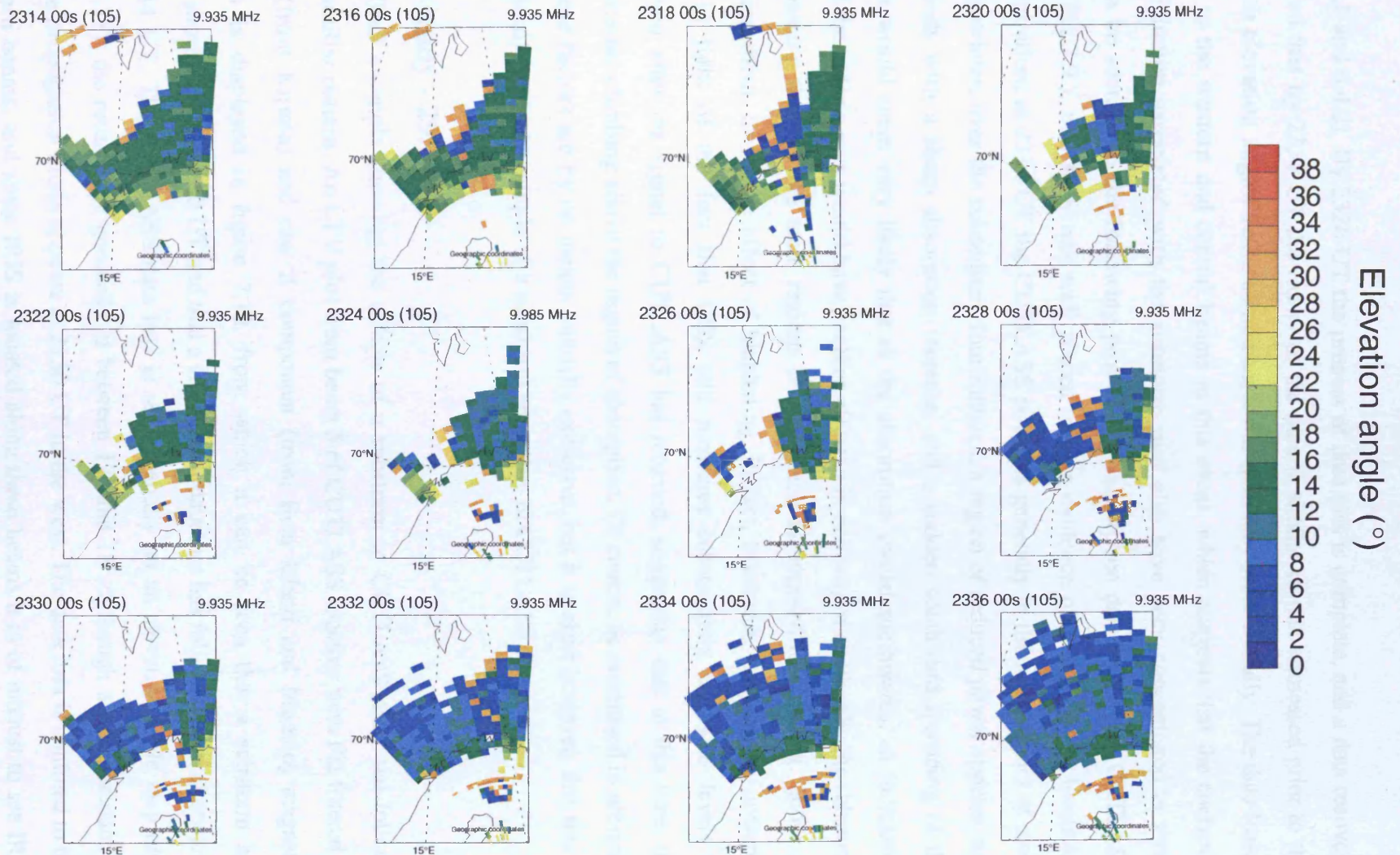


**Fig. 7.8.** CUTLASS elevation angle time series, showing substorm associated data losses confined mainly to the Western beams, and showing the tendency for higher elevation angles to give way to a low mode as the data disappears.

(sections 6.4.1 and 6.4.2). By 2326 UT the process of data loss is complete, and a data recovery commences, so that by 2334 UT the extent of the data is similar to that witnessed prior to the substorm, with elevation angles being somewhat lower than they were initially. The data losses are confined to the western and central beams in this event, which suggests that the energetic particle precipitation associated with the substorm may also have been concentrated in these beams; it can be seen from the following plot of IRIS absorption data overlaying CUTLASS power data (Fig.7.9.), that IRIS was well placed to give evidence of this (possibly localised) particle precipitation; at 2314 UT the CUTLASS power is generally in the red category of more than 27 dB, however, over the subsequent four minutes, a region of reduced power appears, and this corresponds with a sharp absorption increase, and a sudden southward spreading of the absorption. It would seem very likely that as the absorption spread southwards, an increasing proportion of the radar's rays would have become affected in one way or another by the substorm - either by passing through the main regions of absorption as opposed to climbing above or sneaking below them, or by the effect of blanketing. In fact, blanketing may be the favoured explanation in light of the fact that IRIS still measures substantially enhanced levels of absorption even after the signal to CUTLASS has returned, suggesting that at this time, the CUTLASS rays are climbing above the region of absorption. Of course, as mentioned in previous examples, these factors are by no means mutually exclusive, but it is clear however, that this is another essentially typical example of a substorm appearing in CUTLASS data.

#### **7.2.4 Case study - 29/04/98**

This is the final example showing the effects of a substorm in CUTLASS data, and follows largely the familiar pattern. An LTV plot from beam 5 of CUTLASS together with Pi2 filtered X component (from Kiruna) and raw Z component (from Bear Island and Muonio) magnetic perturbations is displayed in figure 7.10, from which it can be seen that a substorm has commenced shortly before 2140 UT and that a CUTLASS data loss has followed soon afterwards at about 2144 UT. The CUTLASS data loss is seen spatially on an elevation angle map time series (Fig.7.11); the returns are generally at between 12° and 18°, although a small amount of the low angle propagation mode appears at 2150 UT in the west. The data loss is confined to the central western beams, and since IRIS is located along these beams it is of interest to see IRIS absorption data overlaying CUTLASS power maps during the event (Fig.7.12); as the absorption gradually increases, between 2138 UT and 2144 UT, the power received by CUTLASS gradually

# IRIS Riometer

15 Apr 1998

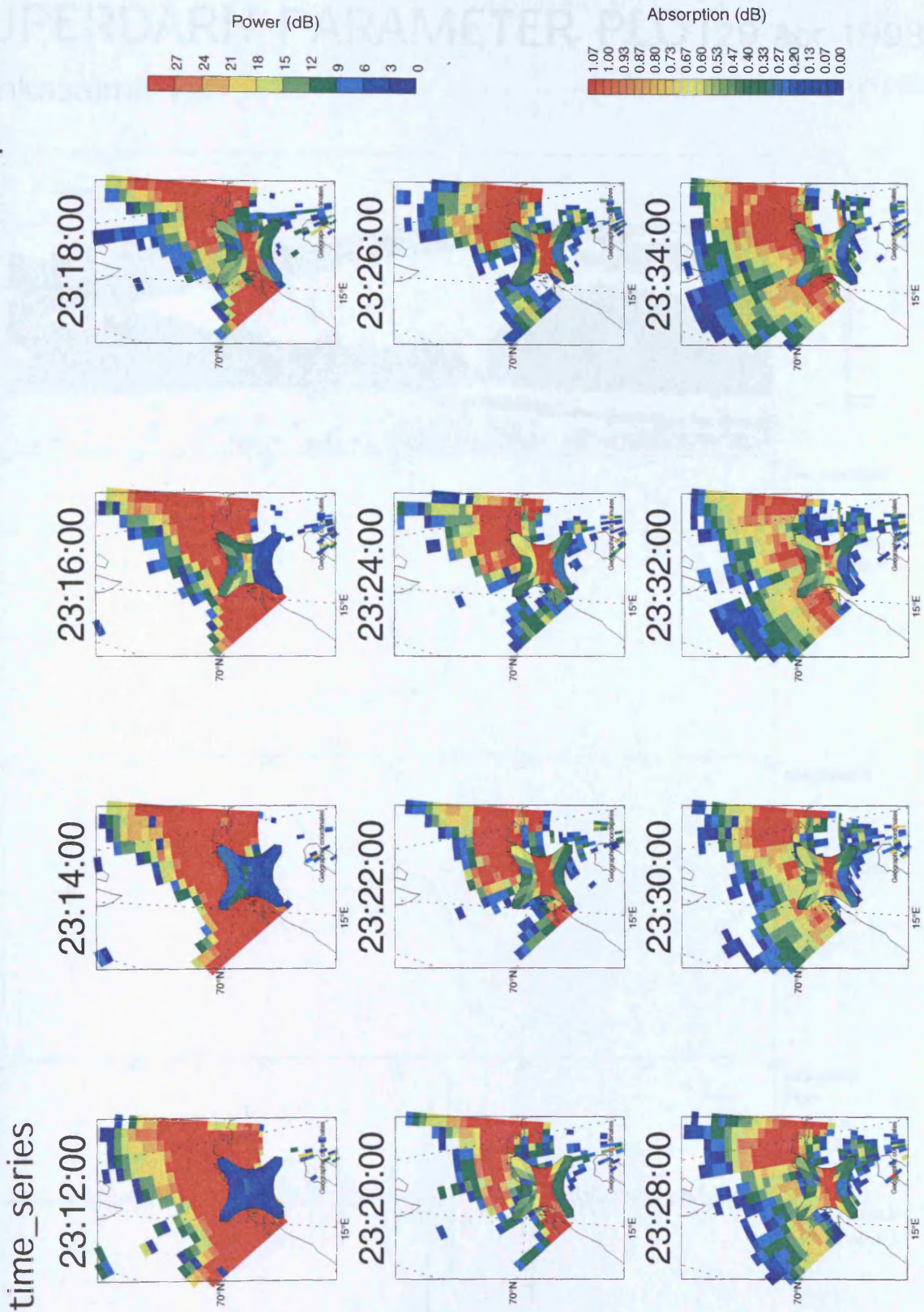


**Fig.7.9.** Time series showing IRIS absorption data overlaying CUTLASS received power. Although the Eastern CUTLASS beams show little change, IRIS is well placed to give evidence of the enhanced absorption associated with a substorm. The enhancement and southward spreading of absorption and associated CUTLASS power reduction and data loss between 2316 UT and 2320 UT is particularly striking.

# SUPERDARN PARAMETER PLOT 29 Apr 1998

Hankasalmi: vel

normal (ccw) scan mode (150)

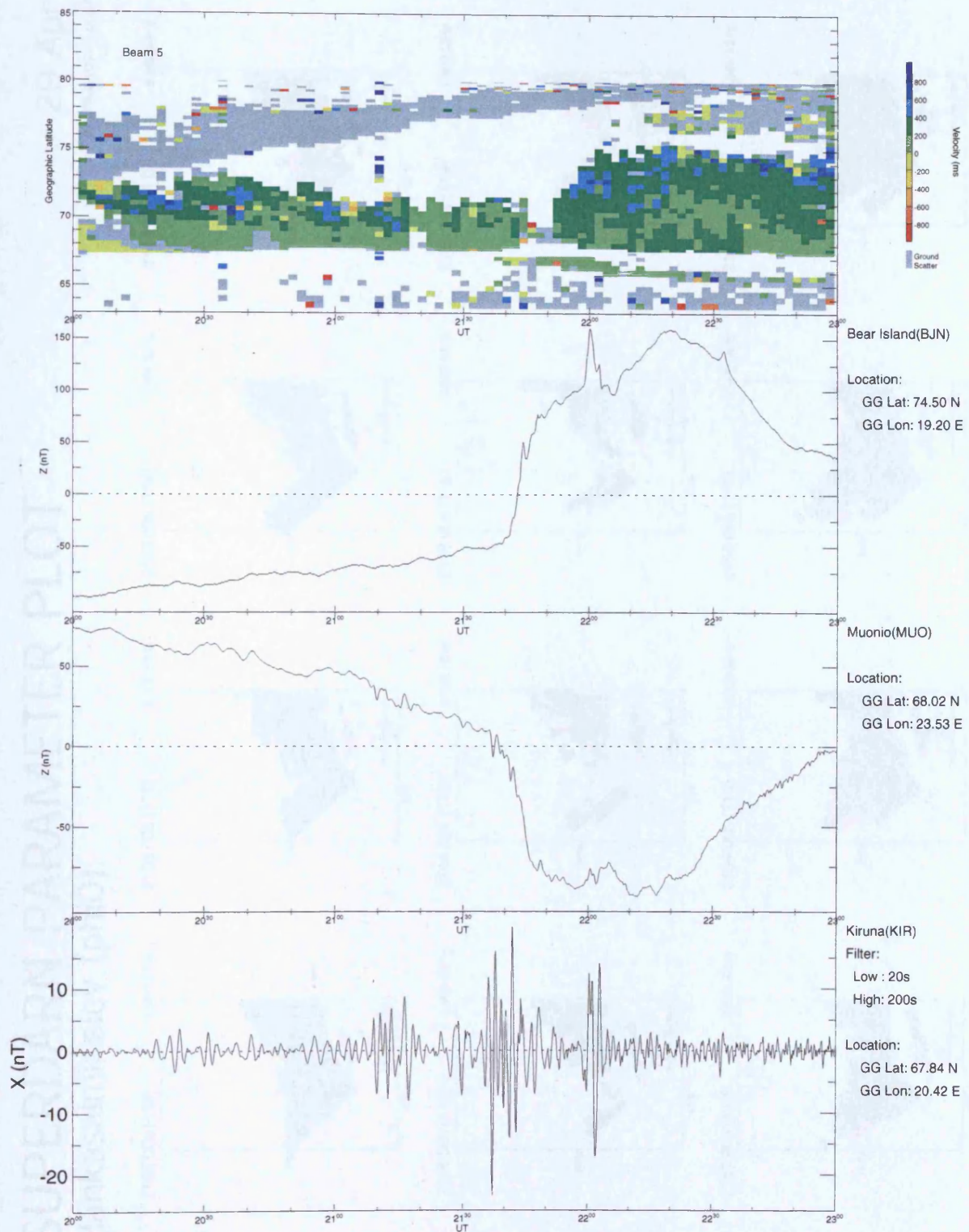


**Fig.7.10.** A substorm associated data loss can be seen in CUTLASS (LTV) data from beam 5. Also displayed are Z component magnetic perturbations from Bear Island and Muonio, which show that an ionospheric electrojet was situated between them, and Pi2 filtered magnetic perturbations from Kiruna indicating a substorm.

# SUPERDARN PARAMETER PLOT

Hankasalmi: elev (phi0)

29 Apr 1998<sup>(119)</sup>

normal (ccw) scan mode (150)

Elevation angle (°)

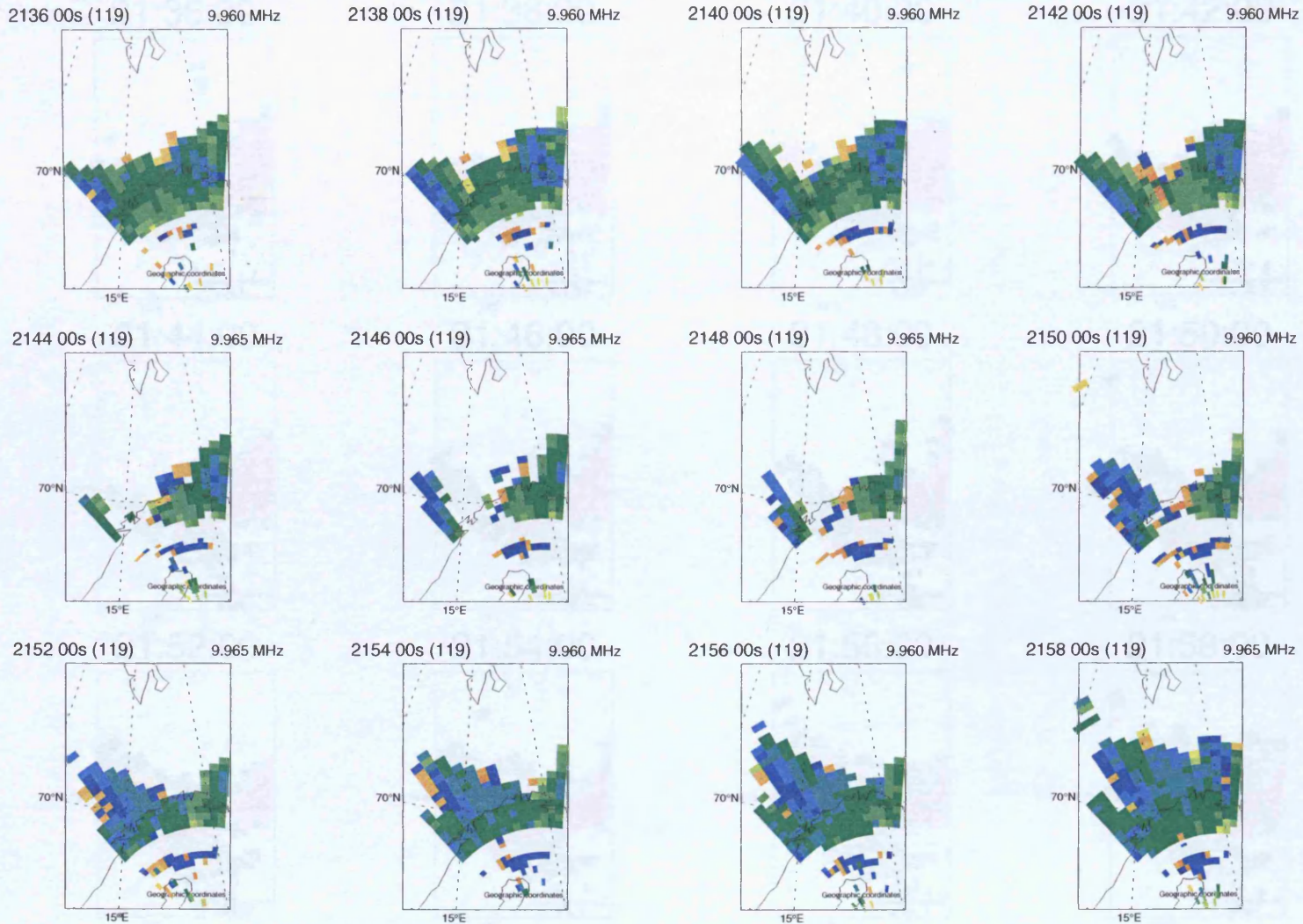
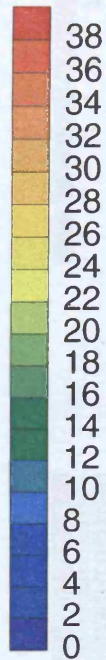
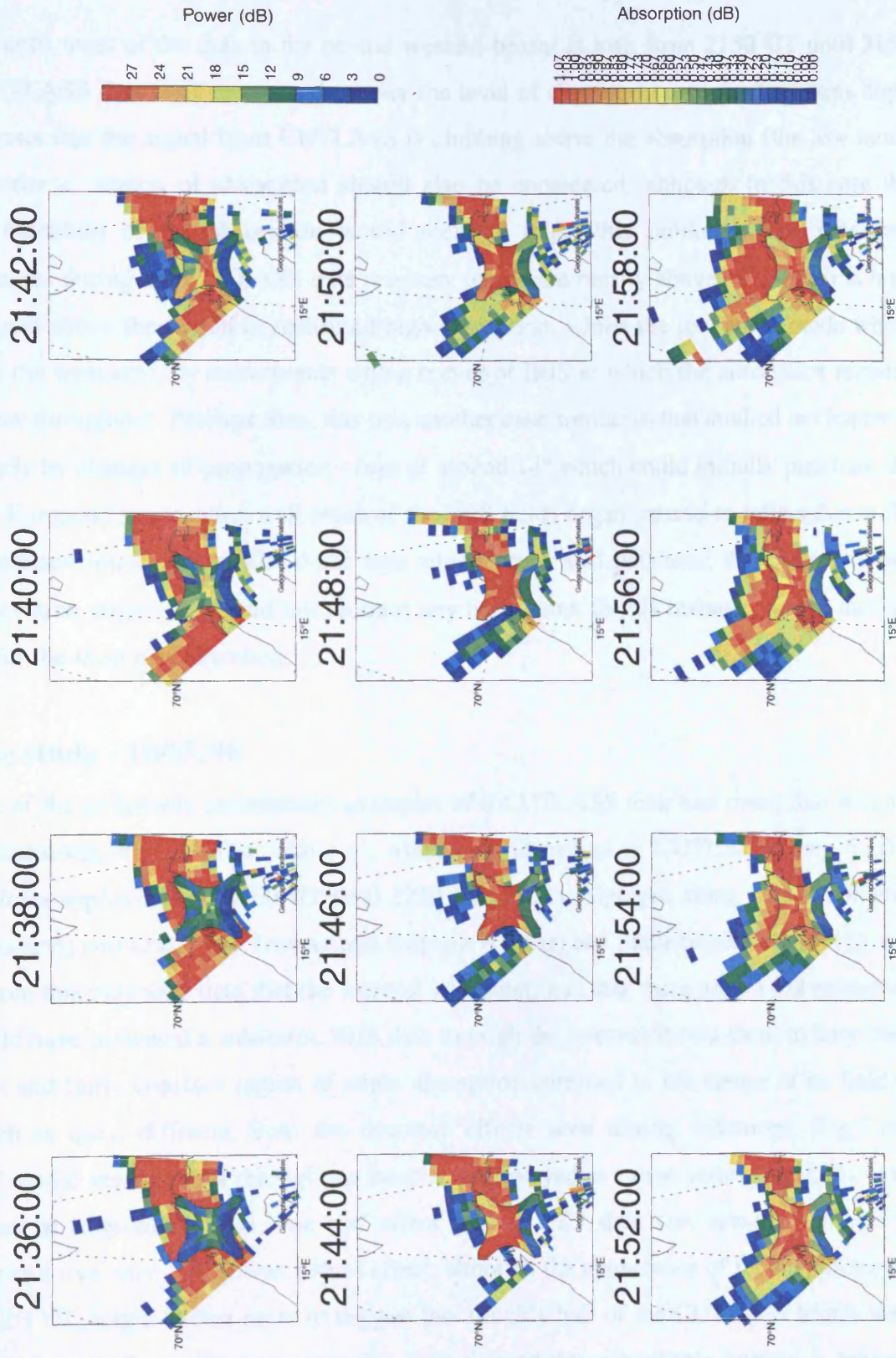


Fig. 7.11. Time series of CUTLASS elevation angle showing the loss and subsequent recovery of data due to a substorm.

# IRIS Riometer

time\_series

29 Apr 1998



**Fig.7.12.** Time series of IRIS absorption data overlaying CUTLASS power data, showing the enhancement and spreading of absorption, and the depletion and subsequent recovery of CUTLASS data associated with a substorm.

diminishes until most of the data in the central western beams is lost; from 2150 UT until 2158 UT, the CUTLASS data fully recovers, however the level of absorption measured remains high, which suggests that the signal from CUTLASS is climbing above the absorption (the low mode sneaking under a region of absorption should also be considered, although in this case the northward extension of the absorption would seem to make this unlikely). The measured elevation angles during the CUTLASS data recovery period are mostly above  $10^\circ$ , which is high enough to pass above the region of measured high absorption, whilst the low angle mode which appeared in the west actually corresponds with a corner of IRIS in which the absorption remains relatively low throughout. Perhaps then, this was another case similar to that studied in chapter 6, caused largely by changes of propagation - rays of around  $14^\circ$  which could initially penetrate the peak of the E region (at a location well south of the IRIS field) began instead to reflect due to the substorm induced ionisation, whilst those rays which could still penetrate the E region peak (perhaps elevation angles  $>20^\circ$ ) did not produce any backscatter in this instance, whilst the low mode was for the most part absorbed.

### **7.2.5 Case study - 10/05/96**

This is one of the (relatively uncommon) examples of a CUTLASS data loss event that was not caused by substorm activity. The 'bite out', which was identified in CUTLASS beam 5 LTV data, lasts from approximately 2200 UT until 2220 UT, and is displayed along with Pi2 filtered (from Kilpisjärvi) and raw (from Tromsø and Kilpisjärvi) magnetic perturbations (Fig.7.13); it is apparent from this magnetic data that the interval was quiet, and that there are no Pi2 pulsations which would have indicated a substorm. IRIS data through the interval shows there to have been a persistent and fairly constant region of slight absorption confined to the centre of its field of view, which is quite different from the dynamic effects seen during substorms (Fig.7.14). CUTLASS spatial velocity data through the interval is displayed in a time series (Fig.7.15), from which it can be inferred that the 'bite out' effect seen in LTV data was actually confined to beams four and five only - i.e. it was a local effect; although the appearance of the map from, for instance 2203 UT, might at first seem to suggest that roughly half of the CUTLASS beams were affected, this is actually an illusion, since the general trend throughout this interval is towards increasing the amount of backscatter received, with only beams four and five having temporarily witnessed data reductions of the type which would stand out to the naked eye in LTV plots. This 'bite out' event then, occurred in an interval in which ionospheric irregularities were becoming

# SUPERDARN PARAMETER PLOT 10 May 1996

Hankasalmi: vel

normal (ccw) scan mode (127)

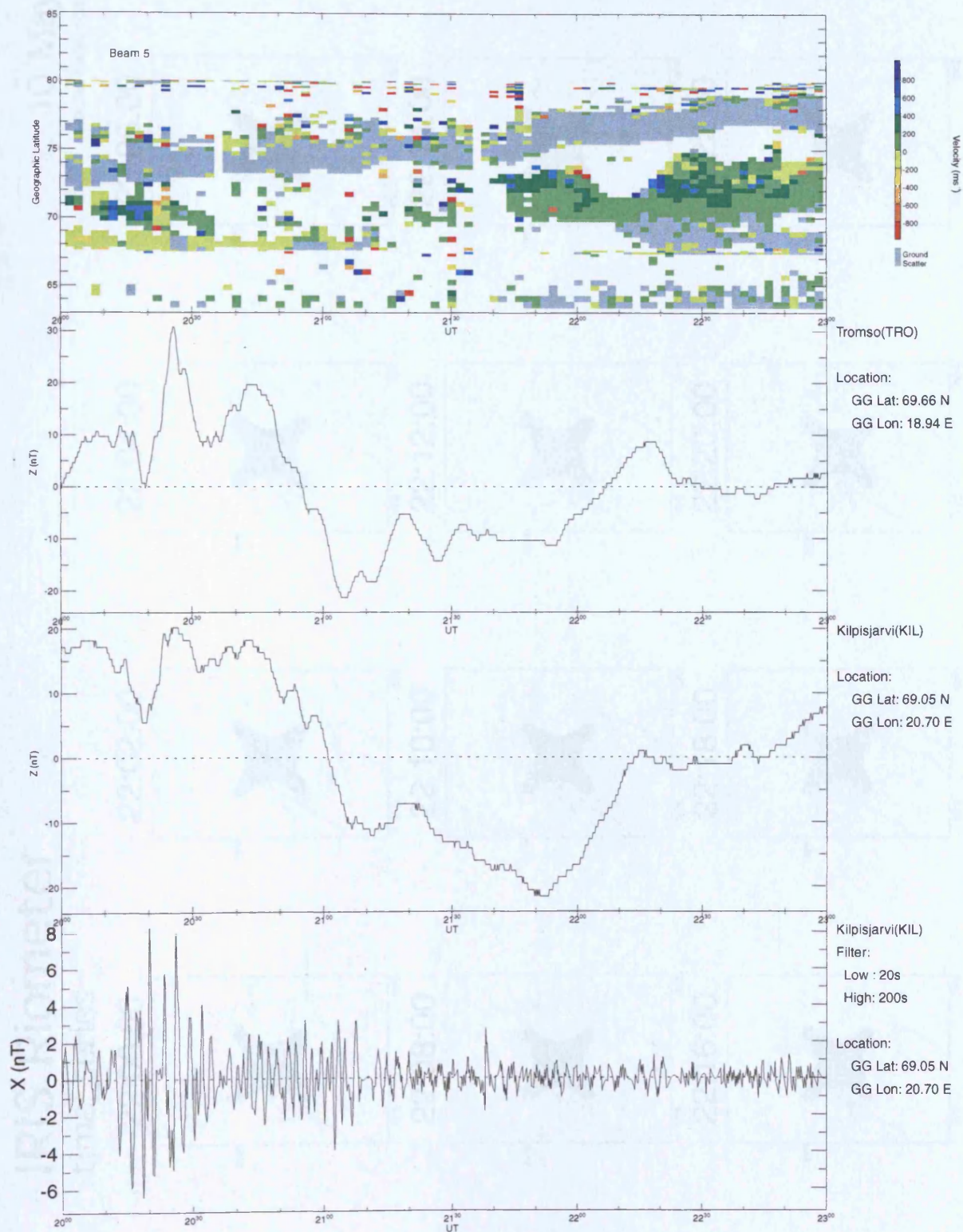


**Fig.7.13.** The retreat or 'bite out' of CUTLASS LTV data observed in beam 5 between 2200 UT and 2220 UT is not associated with a substorm since there is not an associated Pi2 pulsation shortly before this.

# IRIS Riometer

time\_series

10 May 1996 <sup>(131)</sup>

normal (ccw) scan mode (127)

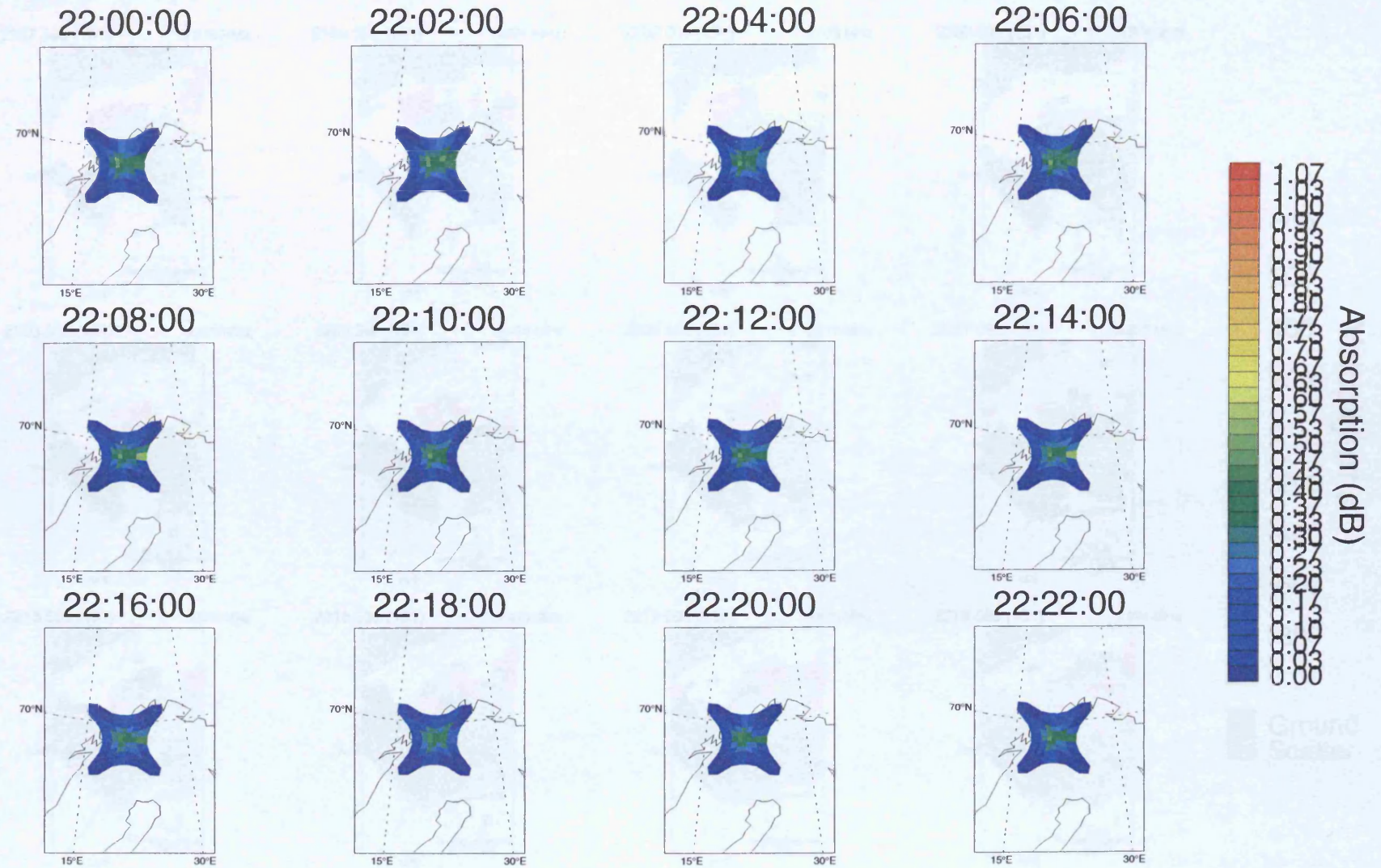


Fig. 7.14. Time series of IRIS data during the interval of CUTLASS data recession. The background level of absorption remains unchanged during this non-substorm interval.

# SUPERDARN PARAMETER PLOT

Hankasalmi: vel

10 May 1996<sup>(131)</sup>  
normal (ccw) scan mode (127)

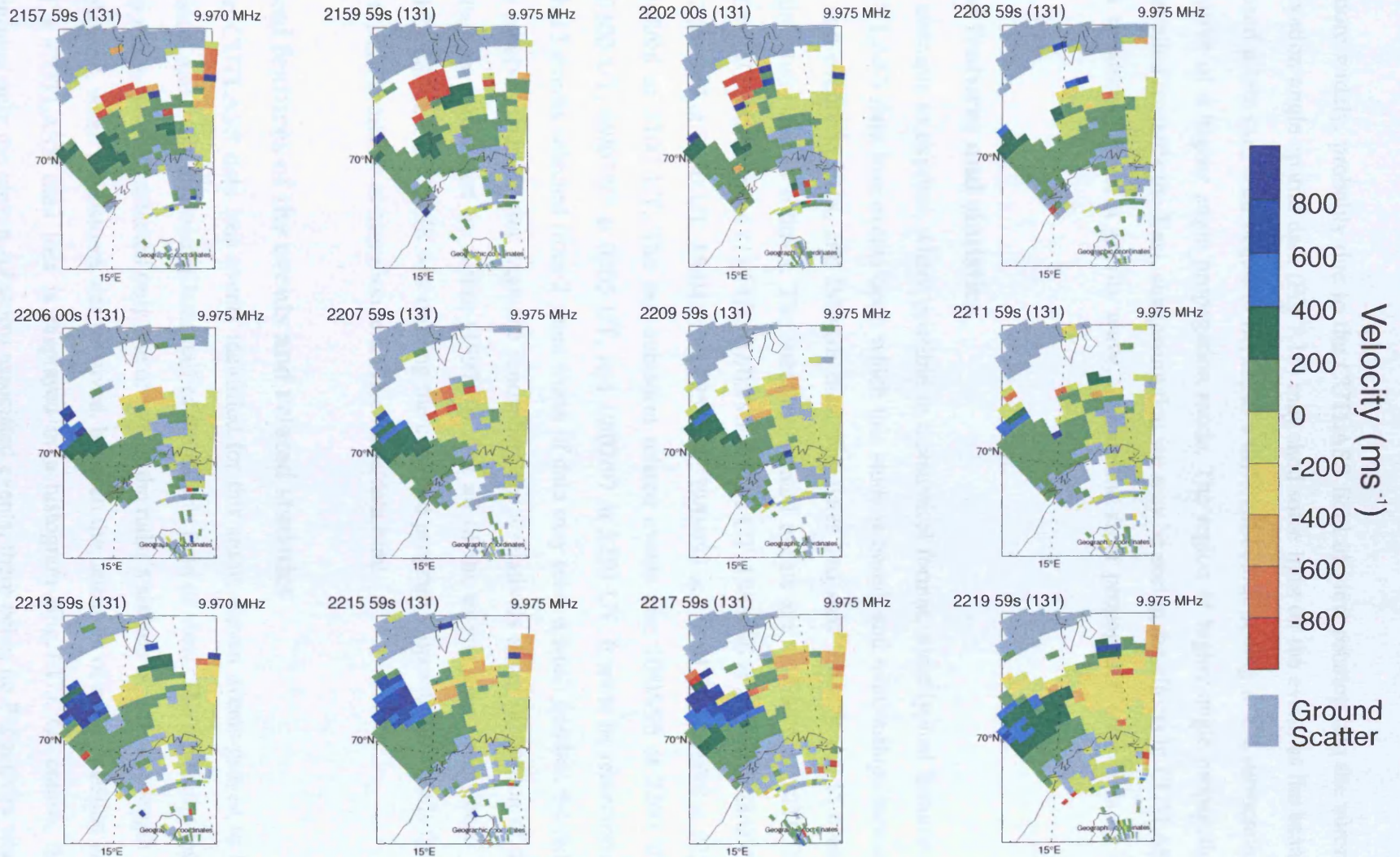


Fig. 7.15. Time series of CUTLASS velocity data during the interval in which a bite out was detected in CUTLASS beam 5 LTV data. The spatial development of the region of returns does not resemble the pattern seen during substorms.

established more widely, probably due to the CUTLASS field of view rotating into the auroral oval. The elevation angle spatial data (Fig.7.16) may shed some light on the event, as the beams which witnessed a bite out, then began to fill in, in a different colour coding to the surrounding beams, indicative of a higher angle propagation mode. The region of higher angle propagation mode then travelled towards the East, suggesting that we may be seeing the effects in CUTLASS data not of a substorm, but of a gravity wave, altering the radar propagation conditions by its passage.

### **7.3 General features and statistics**

This section attempts to express, where possible in a statistical format, some typical features of the set of CUTLASS data loss events upon which this study is based, and relationships between these events and events in IRIS, and IMAGE data. The dates and start times of the 15 events included in the study are as follows. The substorm related events are: 06/08/95 at 2024 UT, 02/05/96 at 2205 UT, 06/05/96 at 2115 UT, 07/05/96 at 2118 UT, 18/06/96 at 2320 UT, 28/06/97 at 0210 UT, 24/08/97 at 2150 UT, 15/04/98 at 2255 UT, 29/04/98 at 2145 UT, 21/08/98 at 2258 UT, and 30/08/98 at 2100 UT. The non-substorm related events are: 10/05/96 at 2200 UT, 13/07/96 at 0300 UT, 09/07/97 at 0205 UT, and 10/07/97 at 2250 UT. It must be remembered that, although 15 events selected from 2 years worth of data may seem a small number, the radar only actually receives backscatter from the ionosphere for a relatively small proportion of the time. This issue is considered by Milan (1997(b)). For all of the events apart from those of 06/08/95 and 21/08/98, CUTLASS was running the common program – operational details from all of the events are available at <http://ion.le.ac.uk/cutlass/data.html> .

#### **7.3.1 Typical features of the events and related statistics**

Of the fifteen CUTLASS data loss events identified for this study, eleven events proved to be substorm related, and these affected at least half of the radar's field of view. The remaining four, non-substorm related events, affected only one or two of the radar's sixteen beams. The length of time which elapsed, when a substorm was involved, between the detection of a Pi2 pulsation and the onset of a CUTLASS data loss is displayed in a histogram (Fig.7.17). Of course, this histogram contains only the eleven substorm associated events, there being no Pi2 activity when a substorm was not involved. The majority of the events occurred within six minutes of a Pi2 pulsation, which is consistent with the idea that the events are due to particle precipitation in the

# SUPERDARN PARAMETER PLOT

## Hankasalmi: elev (phi0)

10 May 1996 <sup>(131)</sup>  
 normal (ccw) scan mode (127)

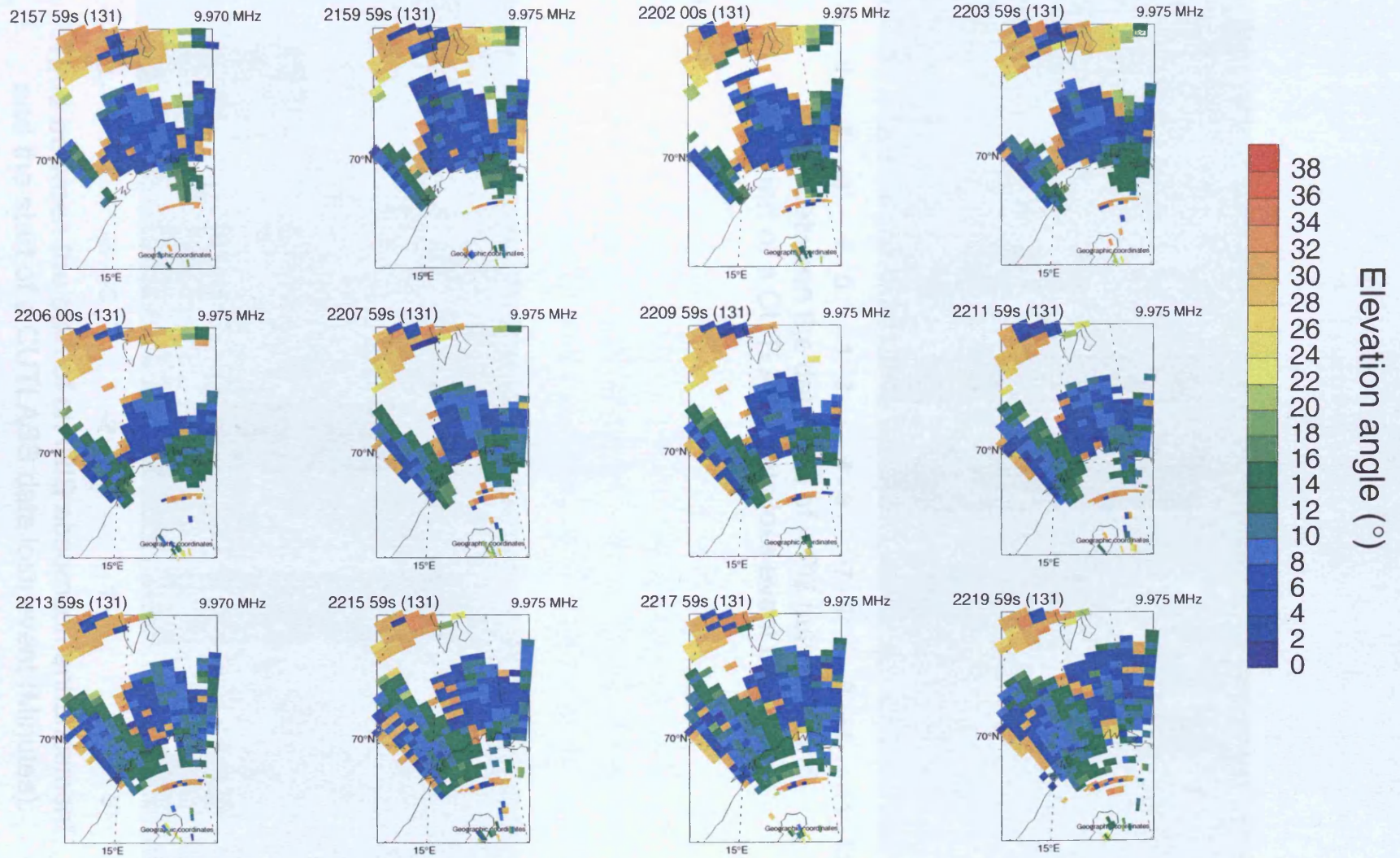


Fig. 7.16. Time series in CUTLASS elevation angle through the interval of interest. In this case, unlike the cases associated with substorms, there are no sudden changes in the propagation mode.

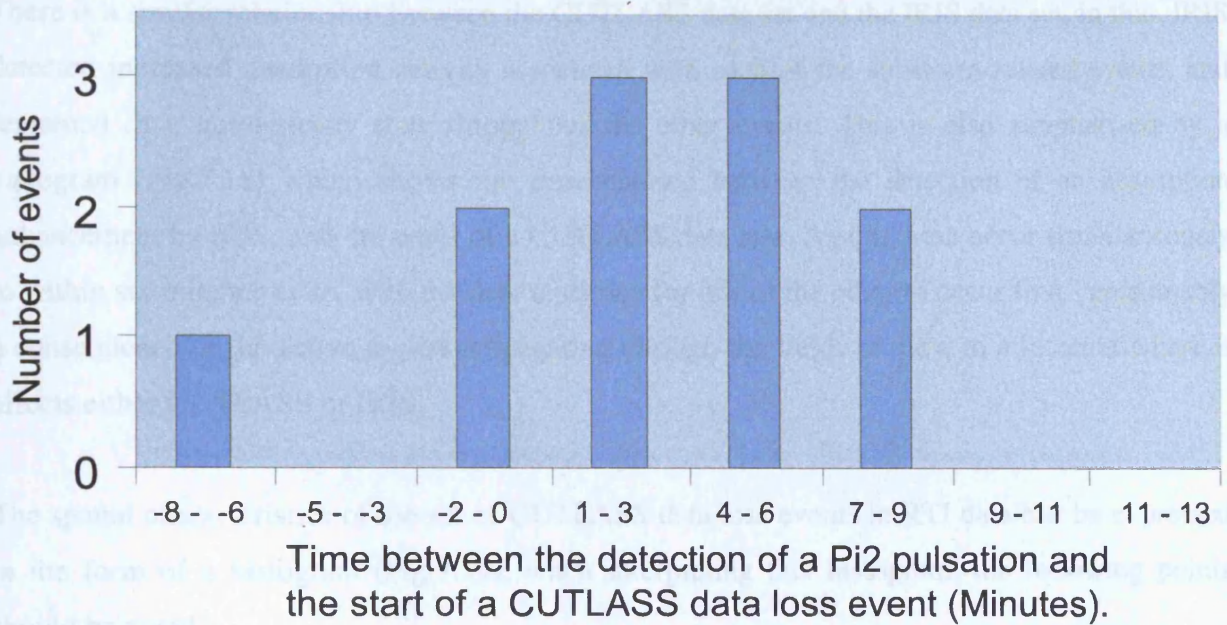


Fig.7.17

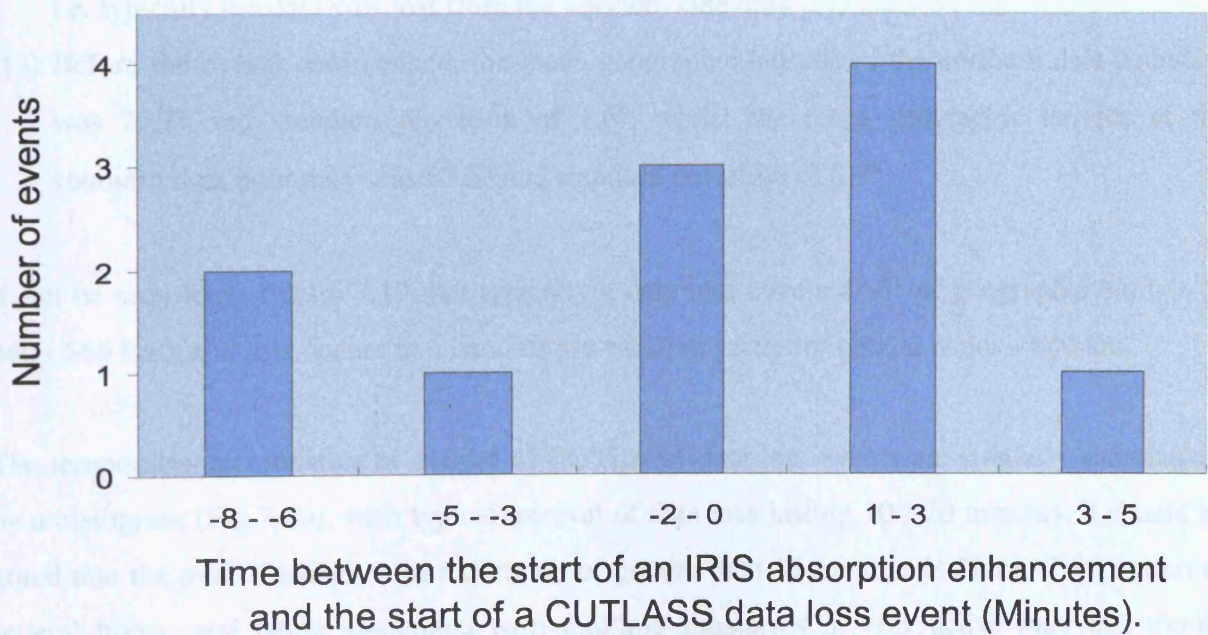


Fig.7.18

substorm expansion phase, with a potential time delay due to expansion of the active region into the radar's field of view.

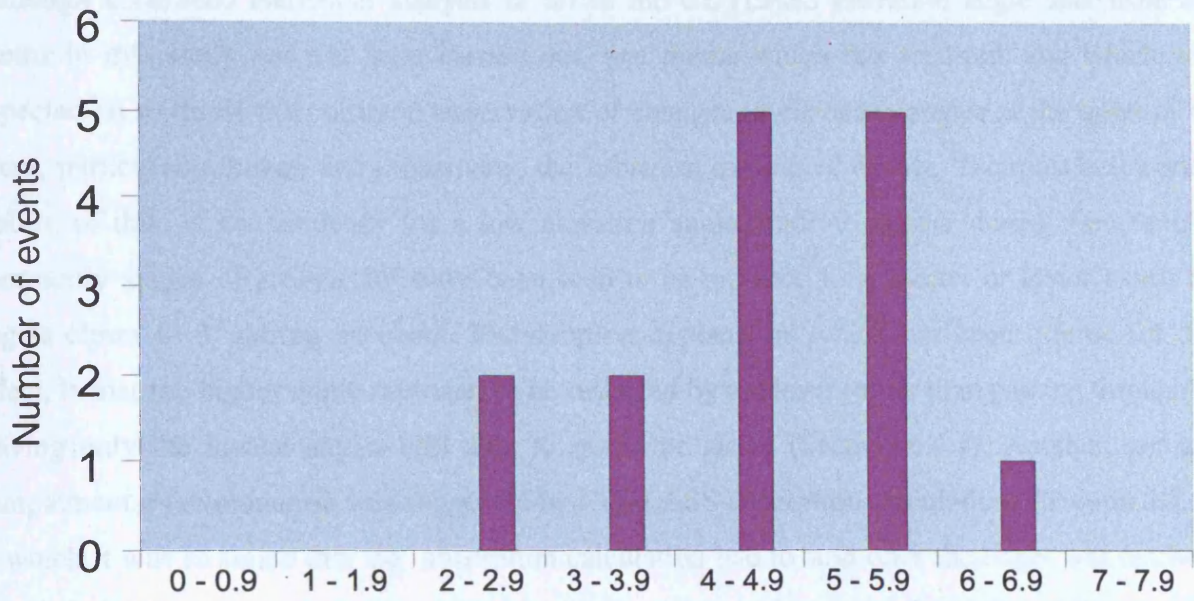
There is a similar relationship between the CUTLASS data set and the IRIS data set, in that, IRIS detected increased absorption activity associated with each of the substorm related events, and remained in a quasi-steady state throughout the other events. This is also summarised by a histogram (Fig.7.18) which shows the time elapsed between the detection of an absorption enhancement by IRIS, and the onset of a CUTLASS data loss. Again, these occur simultaneously to within six minutes or so, with no clear tendency for one or the other to occur first - presumably a consequence of the active region propagating through the fields of view to a location where it affects either CUTLASS or IRIS.

The spatial characteristics of the set of CUTLASS data loss events in RTI data can be expressed in the form of a histogram (Fig.7.19); when interpreting this histogram, the following points should be noted: -

- (1) Of the total set of fifteen events, three events showed data losses extending all the way from the northern boundary to the southern boundary of where the data had initially been.
- (2) Of the remaining twelve events for which the data loss was partial, giving the appearance of a 'bite out' of the data, just one showed any recession of the data from the southern edge, i.e. typically the data was lost from the northern side only.
- (3) Before the events commenced, the mean geographic latitude of the northern data boundary was  $75.7^\circ$  and standard deviation of  $1.6^\circ$ , whilst the mean geographic latitude of the southern data boundary was  $67.6^\circ$  and standard deviation of  $0.9^\circ$ .

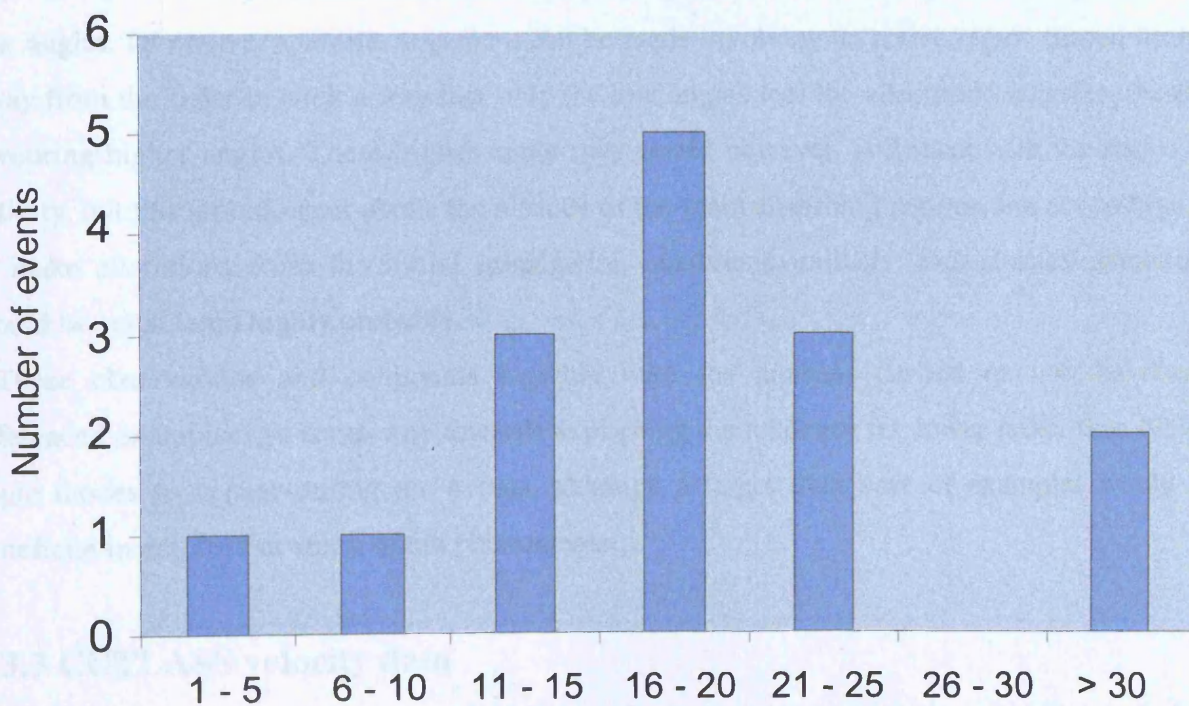
It can be seen from Figure 7.19 that typically a data loss covers  $4^\circ$ - $6^\circ$  of geographic latitude (~ 440 - 660 km), and this occurs in a band of pre-existing scatter of typical width ~ 900 km.

The temporal characteristics of the set of CUTLASS data loss events are similarly summarised by a histogram (Fig.7.20), with typical interval of data loss lasting 10 - 20 minutes. It should be noted that the pair of events with a duration of greater than 30 minutes in fact had a duration of several hours, and being associated with multiple substorms in very active intervals, should probably best be regarded as sequences of conjoined data dropouts – All of the events associated with an isolated substorm had a duration in CUTLASS data of 25 minutes or less.



The spatial extent of CUTLASS data losses in LTV data (Degrees of geographic latitude).

Fig.7.19



The temporal extent of CUTLASS data losses in LTV data (Minutes).

Fig.7.20

### **7.3.2 CUTLASS elevation angle data**

Although a detailed statistical analysis of all of the CUTLASS elevation angle data from the events in this study has not been carried out, one theme which has recurred, and which was expected so to do, is the common observation of changes in elevation angles at the onset of an event, particularly though not exclusively, the substorm associated events. The most noteworthy feature of this, is the tendency for a low elevation angle mode to appear during the events – commonly angles of around  $15^\circ$  have been seen to be replaced to a greater or lesser extent by angles closer to  $3^\circ$  during an event. The simplest explanation which has been offered for this effect, is that the higher angle rays start to be reflected by the layer rather than passing through it, leaving only the lowest angles still able to reach the target (Section 6.4.1). Another, perhaps complementary explanation was suggested by CUTLASS absorption calculations (Section 5.5.1), in which it was assumed that the absorption calculation had to stop once the target was reached, thereby enabling the possibility that low angle rays could reach the target without fully penetrating the absorbing layer. These absorption calculations show a preference for very low angle rays during absorption enhancements, provided that a 1-D ionosphere is used. A more realistic 2-D ionosphere could instead be considered, for instance, an active region of limited extent could be placed close to the radar, with the effect that only the higher angles experienced any increase in absorption due to the low rays passing under the active region, thereby favouring low angles. Of course, a similar argument can be made involving an active region placed further away from the radar in such a way that only the low angles feel the absorption increase, thereby favouring higher angles. These higher angle rays would however, still meet with the region of activity, but this would occur above the altitude of the main absorbing regions, but not so high as to make alterations from the initial propagation conditions unlikely, indeed such alterations would be considered highly probable.

These observations and comments together with the analysis carried out of the above referenced examples, go some way towards explaining the tendency for lower rather than higher angle modes to appear during the events, although a larger data base of examples would be beneficial in any further study of the phenomenon.

### **7.3.3 CUTLASS velocity data**

A feature which has not been stressed until now, is the general increase in variability and often the magnitude, of the large scale plasma velocities measured by CUTLASS during data loss

events. Spatial velocity time series have been examined for all the events in the study, and although a statistical analysis of this data has not been carried out, it is very apparent that the magnitude and variability of the plasma velocities measured in the regions surrounding areas from which data is lost, tends to increase during the events, although regions of suppressed flow are sometimes seen. Of course, as most of the events are associated with substorms, what this really signifies, is that substorms are associated with increased variability of plasma flows and associated large scale electric fields (a fact which has been confirmed by several studies e.g. Yeoman et al. (2000)), and thereby also constitutes typical behaviour of the events in this study.

## **7.4 Summary**

A further five examples of CUTLASS data loss events are described in this chapter, and basic statistics of the whole set of events considered for this study are presented, along with descriptions and possible explanations of behaviours which may be regarded as being typical of the events.

The five CUTLASS data loss events are discussed in relation to the three suggested mechanisms for producing signal losses (Section 5.2.2), and are also compared to the detailed examples which were the subject of chapters five and six; it is concluded that three of the events, those of 07/05/96, 10/05/96 and 29/04/98, were probably due to altering radar propagation conditions, the event of 15/04/98 showed clear evidence of altering radar propagation conditions and of absorption, whilst the event of 24/08/97 appears to be due mainly to absorption. Of the five events, four are associated with the occurrence of a substorm, the event of 10/05/96 being alone in witnessing no substorm activity.

The basic statistics of the whole data set presented, include, the typical length of a data loss event, the typical spatial extent of the data losses, and the typical time lag between the onset of an event in CUTLASS data and a corresponding Pi2 pulsation or absorption enhancement in IRIS. Several other repeatable behaviours associated with the events are also discussed, and explanations offered, for instance into the very common occurrence during the events of a low elevation angle propagation mode.

## Chapter 8

### Summary and Conclusions

#### 8.1 Introduction

The main topics covered in this thesis are radio wave propagation in the ionosphere, radio wave absorption in the ionosphere, and the formation of various ionospheric plasma irregularities. These topics are all related to the main subject of this thesis, which concerns the signatures witnessed in data from an HF coherent backscatter radar (CUTLASS) during magnetospheric substorms. The essential mechanism, which allows substorm occurrences to be detected in HF radar data, is the precipitation of energetic particles into the ionosphere during substorms, whose ionising effects result in changes to the ambient electric field, and also changes in absorption and propagation of the radar beam. Typically, substorms will appear in HF radar data provided that firstly, the substorm activity is within the radar field of view, and secondly that the radar is receiving backscattered returns immediately prior to the substorm activity; a typical signature of substorm activity then appears as a reduction in the spatial extent of the received signal, and sometimes a reduction in backscatter power in the regions where a signal remains. These data losses tend to appear on space-time maps as a 'bite out', and last between ten and thirty minutes or so, although during active periods containing successive substorms the data may be lost completely for several hours. It is assumed, that whenever there is a change in the area where signals are received by the radar it implies a change in the medium in which the radar rays propagate – i.e. the ionosphere. The types of changes in the ionosphere which might be responsible for the loss of the radar signal during substorms fall into three broad categories, essentially the same as the aforementioned main topics of this thesis, namely, changes of radar propagation, changes in the amount of radio wave absorption (either classical or some form of anomalous absorption), and changes in the scattering structures in the ionosphere (the ionospheric plasma irregularities).

The data presented in this thesis consist of several examples of the behaviour of HF radar data during substorms, as well as associated data from an imaging riometer (IRIS), an incoherent scatter radar (EISCAT), and magnetometer chain (IMAGE). The cosmic radio noise absorption measured by IRIS is modelled with the help of electron density profiles from EISCAT, and the high level of accuracy achieved by this model suggested that the model could be used to provide an altitude profile of absorption rate, which can then be used, after various simplifying assumptions, to look at absorption levels along CUTLASS propagation paths. The EISCAT electron density data was also input to a computer ray tracing program (Jones3D), to provide an indication of the likely radar propagation paths during the substorm

activity. The dual techniques of absorption modelling and ray tracing provide the basis for detailed discussions of two of the data loss events (Contained in chapter 5 & 6), with a further six examples presented for which there was no EISCAT data, but which never the less share many of the observable features with the two events which are discussed in detail (Contained in chapters 1 & 7).

There are a number of inherent limitations of the work contained in this thesis. Firstly in terms of data availability, although CUTLASS was running for most of the two year or so period from which the events have been identified, very often the radar actually receives no ionospheric backscatter at all, probably due to there being nothing in the ionosphere from which to scatter. For this reason, we have started with the premise that the radar is initially receiving ionospheric backscatter, and then checked for substorm activity during radar 'bite out' periods, rather than checking every occurrence of a substorm for possible signatures in the radar data. The lack of spatial coverage of other supporting data is also a limitation. Electron density profiles from EISCAT are 1-D, but have been used as the basis for modelling 3-D ray paths and absorption paths, thereby making, a perhaps questionable assumption, as to the spatial uniformity of the medium. Knowledge of the state of the available scattering structures in the ionosphere is a further limitation of the work. This is touched upon in Chapter 6, where we check independent plasma convection data supplied by EISCAT, in order to look for indications of a shorting of the convection electric field, which if present would indicate a likely depletion of the scattering structure. In general however, this factor must be taken as an unknown.

## **8.2 Summary of the events which are examined in detail**

The two substorm associated CUTLASS data loss events which are examined in detail, and are also the best instrumented events, occurred on the 18<sup>th</sup> to 19<sup>th</sup> of June 1996 and the 21<sup>st</sup> of August 1998 respectively. The June event was associated with a very active period of several hours duration in which successive substorms occurred, and the CUTLASS data was, except for some very near ranges, totally lost. The absorption of background cosmic radio noise was found by IRIS to increase sharply during the period, and this absorption was then modelled using electron density data from EISCAT, and particle temperature and collision frequency data from an MSIS empirical model. The agreement between the IRIS data and the model proved to be good, and so the information in the model about the dependence of absorption rate upon altitude was then applied, after making assumptions about spatial uniformity, to CUTLASS rays propagating through the medium at different elevation angles. It was found

that, with other things being equal, the given absorption profile was certainly sufficient to cause the loss of the CUTLASS signal, but in addition to this, the effects of changing radar propagation were considered. By inputting the EISCAT electron density profiles from pre - and post - onset of the active period into the Jones3D computer ray tracing program, an indication of the likely propagation paths of CUTLASS from before and during the data loss period was obtained, and these indicated that the radar would have suffered from so called 'blanketing' during the active period. This means, that rays which could initially penetrate the ionosphere's E region and continue on towards the F region, giving backscatter from here, are instead reflected earthwards in the E region, so that any scatter from other than the closest of ranges would have to be ground scatter or multi-hop scatter, which would certainly have resulted in, (not withstanding the extra absorption caused by multiple ionospheric crossings), a very different pattern of radar returns to be observed once the active period began.

It is concluded therefore, that a combination of absorption and blanketing would have been very effective in causing the radar returns to be lost, which of is course, consistent with the observations. It is also noted that this interval was examined by Milan et al. (1999), who following the work of Tsunoda (1988), were able to show that significant electric shorting through the E region may have also produced a reduction in the irregularity growth rates during the interval of CUTLASS data loss.

The second event which is discussed in detail in the thesis, that of 21<sup>st</sup> August 1998, was associated with an isolated substorm rather than a series of substorms, and the ionising effects of this substorm were less pronounced. Since EISCAT data was again available, the same type of approach involving ray tracing and absorption calculations is used. Absorption calculations are found to be not entirely consistent with both the magnitude of, and spatial distribution of, the observed reductions in CUTLASS power. No doubt some of the change in the signal power and distribution was in fact a consequence of changing absorption, however, the broad agreement found in a comparison between the behaviour of the elevation angles of the received signal and the range of elevation angles which are suggested by the ray tracing analysis indicate that the effects of altering signal propagation conditions during the substorm was likely to have been the dominant factor in this case. The ray tracing suggested that the initial propagation mode would give way during the substorm to either a higher angle mode, or possibly a very low angle mode, and in fact both of these changes were observed in the elevation angle data. Independent measurements of the plasma convection velocity in the region where the CUTLASS data were lost are provided by the EISCAT facility, and have been used to look for evidence of the suppression of the zero order electric field, associated

with a field shorting effect. Evidence of field suppression is found during a fleeting initial data loss, but not during the main data loss event which began several minutes later.

### **8.3 General features associated with CUTLASS data loss events**

This section is a summary of the features which, in both CUTLASS data and supporting instruments, are found to commonly or invariably occur during the identified CUTLASS data loss events, or in other words, typical behaviour. The eight CUTLASS data loss events included in this thesis are a subset of fifteen such events, which were initially selected from the data set because they stood out to the naked eye. Of the fifteen events selected from CUTLASS data, eleven turned out to have begun at the same time, or shortly after, the onset of a substorm, so that the occurrence of Pi2 pulsations, magnetic perturbations, and an associated substorm is typical of CUTLASS data loss events. On each occasion that an event turned out to be substorm related, there were clear effects visible in IRIS absorption data, but when a substorm proved not to be involved then IRIS remained in a quasi steady state. The substorm associated events were of a spatially large scale (affecting at least half the beams) whereas the other events were local (affecting one or two beams). Of the events in which some CUTLASS data remained throughout (which was most of the events), the elevation angle of receipt of the remaining data has been examined, and this suggests that an alteration of radar propagation conditions during substorms is typical. Half of the non substorm associated events also showed propagation changes which were simultaneous with, and in the same beams as, the data losses occurred - perhaps the result of a more localised effect in the ionosphere, such as some sporadic E close to the radar site. Having mentioned that evidence of altered propagation conditions is typical, it should be added, that the most noteworthy feature of this, is the tendency for a low elevation angle mode to appear during the events, which would seem to be somewhat paradoxical since lower angle rays would in general be expected to undergo more absorption than higher angles when passing through a given absorbing layer. The simplest explanation of this effect, is that the higher angle rays begin to be reflected by the layer rather than passing through it, leaving only the lowest angles still able to reach the target. Another explanation however, is provided by CUTLASS absorption calculations, which assume that absorption stops once the target is reached, thereby enabling the possibility that low angle rays can reach the target without fully penetrating the absorbing layer. These absorption calculations show a preference for very low angle rays during absorption enhancements, and therefore may also be important in explaining the phenomenon.

## 8.4 Future work

Apart from the initial example of August 1995, which was shortly after CUTLASS began operation and several months before the installation of the interferometer array, the examples of CUTLASS data losses which form the basis of this study, occurred between June 1996 and August 1998, and numbering fifteen cases, represent fewer than one per month. The events therefore, are fairly rare, and additional examples would enable the phenomena studied to be characterised more fully, and the 'typical' characteristics of the events to be related directly to suitable parameters of the associated substorms. The information presented in this thesis can be directly applied to any future CUTLASS substorm studies. For instance, the new stereo-CUTLASS facility will be able to use two probing frequencies simultaneously, thereby providing significant additional information, which could be used for example, to either verify or contradict the hypothesis that an event was caused by classical absorption. The ray tracing models of CUTLASS propagation, which have so far been based upon 1-D plasma frequency profiles from EISCAT, could be made more accurate by including as well as, or instead of, EISCAT data, the information from an ionosonde chain, thereby forming a 2-D profile by fitting a suitable functional form to the data. These improvements in ray tracing technique could be used in conjunction with stereo-CUTLASS to aid in the design of new experiments. For instance, it may be possible to find a frequency regime for which the anticipated radar propagation at one frequency during an event, would resemble the propagation which had occurred at another frequency prior to the event, thereby effectively cancelling out a propagation change. The existence of a larger data base of CUTLASS substorm studies could be used as the basis for a future statistical study, focussing perhaps on the apparent preference for a low elevation angle mode to appear during substorms. The relationship between measured elevation angles and received power could be tested experimentally, and the results tested against various models, enabling further information to be extracted.

Although the loss of data is generally a negative, in this instance it also provides information, upon the particle precipitation spectrum and its spatial extent during substorms. With a growing understanding of the phenomenon involved in the data loss, we may be able to use it directly as a diagnostic of this particle precipitation, and should also be able to establish which frequency regimes are best able to avoid the problem of data losses during substorms.

## References

- Akasofu, S.I.(1964).** 'The development of the auroral substorm' Planet.Space Sci. 12, 273.
- Anderson, D.N., Decker, D.T. and Valladares, C.E. (1996).** 'Global Theoretical Ionospheric Models (GTIM)' In Solar-Terrestrial Energy Program, Handbook of ionospheric models, Ed. R. W. Schunk.
- Axford W.I. and Hines, C.O. (1961).** 'A unifying theory of high-latitude geophysical phenomena and geomagnetic storms' Can.J.Phys. 39, 1433.
- Baker, K.B., Greenwald, R.A., Walker, A.D.M., Bythrow, P.F., Zanetti, L.J. and T.A. Potemra (1986).** 'A case study of plasma processes in the dayside cleft' J.Geophys.Res. 91, 3130.
- Balsley, B.B. (1969).** 'Some characteristics of non-two-stream irregularities in the equatorial electrojet' J.Geophys. Res. 74, 2333.
- Banks, P.M. (1966).** 'Collision frequency and energy transfer: Ions' Planet. Space Sci. 14, 1105.
- Benyon, W.J.G. and Williams, P.J.S. (1978).** 'Incoherent scatter of radio waves from the ionosphere' Rep. Prog. Phys. 41, 909.
- Brandstatter, J.J. (1959).** 'The theory of propagation of rays in an inhomogenous and anisotropic medium' Stanford research institute, project 2241, final letter report, part 1.
- Browne, S.,Hargreaves, J.K, Honary, F (1995).**'An imaging riometer for ionospheric studies' Electronics and communication engineering journal 7, no.5,209.
- Budden, K.G.(1961).** 'Radio waves in the ionosphere' CUP.

**Budden, K.G and Terry, P.D. (1971).** 'Radio ray tracing in complex space' Proc.Roy.Soc.London A. 321,,275.

**Budden, K.G (1985).** 'The propagation of radio waves' CUP.

**Buneman,O. (1963).** 'Excitation of field aligned sound waves by electron streams'.Phys.Rev.Lett.10, 285.

**Cowley, S.W.H.(1993).**'The Behaviour of Systems in the Space Environment'. Kluwer Academic Publishers, 147.

**Cowley, S.W.H., and Lockwood, M. (1992).** 'Excitation and decay of solar wind-driven flows in the magnetosphere-ionosphere system' Ann. Geophys. 10, 103.

**Davies, K.(1969).**'Ionospheric Radio Waves' Blaisdell Publishing Company, USA.

**Davies, K.(1990).** 'Ionospheric radio' Peter Peregrinus Ltd., London.

**Davies, J.A. (1996).** 'Ion frictional heating in the high-latitude ionosphere' PhD thesis, Leicester University

**Davies, J.A. and Lester, M. (1999).** 'The relationship between electric fields, conductances and currents in the high-latitude ionosphere: a statistical study using EISCAT data' Ann. Geophysicae 17, 43.

**Davies, J.A., Yeoman, T.K., Lester, M. and Milan, S.E. (2000).** 'A comparison of F-region ion velocity observations from the EISCAT Svalbard and VHF radars with irregularity drift velocity measurements from the CUTLASS Finland HF radar' Ann. Geophysicae 18, 589.

**Detrick, D.L., and Rosenberg, T.J. (1990).** 'A phased-array radio wave imager for studies of cosmic radio noise' Radio Sci., 25(4), 325.

**Dungey, J.W.(1961).** 'Interplanetary magnetic field and the auroral zones' Phys.Rev.Lett.6,47.

**Eglitis, P. (1990).** 'Radar studies of small-scale plasma irregularities' Report, Leicester University.

**Eglitis, P. (1994).** 'Radar studies of small-scale E-region plasma irregularities' PhD thesis, Leicester University.

**Fabry C. (1928).** C.R. hebdomadaire Acad. sci., Paris 187, 777.

**Farley, D.T.(1963).**'A plasma instability resulting in field-aligned irregularities in the ionosphere' J.Geophys.Res.68, 6083.

**Farley, D.T. (1985).** 'Theory of equatorial electrojet plasma waves: New developments and current status' J. Atmos. Terr. Phys. 47, 729.

**Fejer, B.G. (1979).**' Ionospheric instabilities and fine structure' J.Atmos. Terr. phys., 41, 895.

**Fejer, B.G. and Kelley, M.C. (1980).** 'Ionospheric irregularities' Rev. Geophys. Space Phys. 18, 401.

**Gosling, J.T., J.R. Asbridge, S.J. Bame and W.C. Feldman (1976).** 'Solar wind speed variations, 1962-1974' J.Geophys. Res. 81, 5061.

**Greenwald, R.A., K.B. Baker, R.A. Hutchins, and C Hanuise. (1985).** 'An HF phased-array radar for studying small-scale structures in the high-latitude ionosphere' Radio. Sci. 20, 63.

**Greenwald, R.A. (1995).**Space science reviews 71,761.

**Haldoupis, C.(1988).** 'A review on radio studies of auroral E-region ionospheric irregularities' Ann.. Geophys. 7, 239.

**Hanuse, (1993).** 'Interpretation of HF radar ionospheric Doppler spectra by collective wave scattering theory' Ann.Geophys. 11, 29.

**Hargreaves, J.K. (1979).** 'The upper atmosphere and solar-terrestrial relations' Von Nostrand Reinhold Publishing Company, New York.

**Hargreaves, J.K. (1992).**'The solar-terrestrial environment' CUP.

**Hazelgrove, J. (1955).** 'Ray theory and a new method of ray tracing' Physics of the ionosphere, Phys. Soc., London, 355.

**Heaviside, O. (1902),**'Telegraphy' Encyclopedia Britannica, 10<sup>th</sup> edition, 33, 215.

**Hedin, A.E. (1991).** 'Extension of the MSIS thermosphere model into the middle and lower atmosphere' J.Geophys.Res. 96, 1159.

**Hines, C.O. (1951a).** 'Wave packets, the Poynting vector and energy flow: Part 1' J.Geophys.Res., 56, 63.

**Hines, C.O. (1951b).** 'Wave packets, the Poynting vector and energy flow: Part 3'. J.Geophys.Res., 56, 207-220.

**Hones, E.W. (1979).** 'Transient phenomena in the magnetotail and their relation to substorms'. Space Sci. Rev., 23, 393.

**Hunsucker, R.D. and Bates, H.F. (1969).** 'Survey of polar and auroral effects on HF propagation' Radio Sci. 4, 347.

**Intriligator, D.S., J.H.Wolfe,D.D.McKibbin,H.R. Collard (1969).**Planet.Space.Sci.17,321.

**Jones, R.M. and Stephenson, J.J.(1975)** 'A versatile three-dimensional ray tracing computer program for radio waves in the ionosphere' OT Report 75-76.US Govt.Printing Office, Washington DC 20402.

**Kelley, M.C.(1989).** 'The Earth's Ionosphere' academic press inc..

**Kelso, J.M.(1964).** 'Radio ray propagation in the ionosphere'. McGraw-Hill Co. Inc., New York.

**Kennelly, A.E.(1902).**'On the elevation of electrically conducting strata of the Earth's atmosphere' Electrical world and engineering 15, 473.

**Keskinen, M.J. and Ossakow, S.L. (1983).** 'Theories of high latitude ionospheric irregularities – a review' Radio Sci. 18, 1077.

**Kivelson, M.G. and Russell C.T. (1995).**'Introduction to space physics' CUP.

**Larmor, J.(1924).**'Why wireless electric rays can bend around the Earth' Phil.Mag.48, 1025.

**Lehtinen, M.S. and Häggström (1987).** 'A new modulation principle for incoherent scatter measurements' Radio Sci. 22, 625.

**Lockwood, M. (1993).** 'Modelling the high-latitude ionosphere for time-varying plasma convection' Proc. I.E.E (H) 140, 91.

**McPherron, R.L., Russell, C.T., and M.P. Aubry (1973).** 'Satellite studies of magnetospheric substorms on August 15, 1968, 9, Phenomenological model for substorms' J.Geophys.Res. 78, 3131.

**Milan, S.E. (1994).** 'Observations of HF radarwaves propagated over high-latitude paths' PhD thesis, University of Leicester.

**Milan, S.E., T.B.Jones, T.R.Robinson, E.C.Thomas and T.K.Yeoman (1997).**  
'Interferometer evidence for the observation of ground backscatter from behind the CUTLASS radars' Ann. Geophys. 15, 29.

**Milan, S.E., T.K. Yeoman, M.Lester, E.C. Thomas and T.B. Jones (1997(b)).** 'Initial backscatter occurrence statistics from the CUTLASS HF radars' Ann.Geophys. 15, 703.

**Milan, S.E., Davies, J.A. and Lester, M. (1999).** 'Coherent HF radar backscatter characteristics associated with auroral forms identified by incoherent radar techniques: A comparison of CUTLASS and EISCAT observations' J. Geophys. Res. 104, 22591.

**Ossakow, S.L. and Chaturvedi, P. K. (1979).** 'Current convective instability in the diffuse aurora' Geophys. Res. Lett. 6, 332.

**Parker, E.N. (1963).** 'Interplanetary dynamical processes' Wiley-Interscience.

**Provan, G. (1998).** 'Coherent scatter radar observations of field line resonances and flux transfer events' PhD thesis, Leicester University.

**Ratcliffe, J.A. (1959).** 'The magneto-ionic theory' CUP.

**Richmond A.D. (1982).** 'Thermospheric dynamics and electrodynamics, Solar-terrestrial physics' D. Reidel Publishing Company, Dordrecht, 523.

**Rishbeth, H. and Garriott, O.K. (1969).** 'Introduction to Ionospheric Physics' Int. Geophys. Ser. 14, Academic Press, New York.

**Register, A and D'Angelo, N. (1970).** 'Type 2 irregularities in the equatorial electrojet' J. Geophys. Res. 75, 3817.

**Samson, J.C., Greenwald, R.A., Ruohoniemi, J.M., Frey, A. and Baker, K.B. (1990).** 'Goose bay radar observations of earth-reflected atmospheric gravity waves in the high-latitude ionosphere' J. Geophys. Res. 95, 7693.

**Schunk, R.W. and A.F. Nagy (1978).** 'Electron temperatures in the F-region of the ionosphere: Theory and observations' Rev. Geophys. Space Phys. 16, 355.

**Schunk, R.W. (1983).** 'The terrestrial ionosphere In Solar-terrestrial physics', D. Reidel publishing company, Dordrecht, 609.

**Storey, J. (2000).** 'Observations in the plasma sheet during substorm activity'. PhD thesis, Leicester University.

**Sudan, R.N., Akinrimisi, J., Farley, D.T. (1973).** 'Generation of small-scale irregularities in the equatorial electrojet' J. Geophys. Res. 78, 240

**Thomson J.J. (1906).** 'Conduction of electricity through gases' CUP.

**Vickrey, J.F. and Kelley, M.C. (1982).** 'The effects of a conducting E layer on classical F region cross-field plasma diffusion' J. Geophys. Res. 87, 4461.

**Villain, J.P., Greenwald, R.A. and Vickrey, J.F. (1984).** 'HF ray tracing at high-latitudes using measured meridional electron density distributions' Radio Sci. 19, 359.

**Villain, J.P., Caudal, G. and Hanuis, C. (1985).** 'A SAFARI-EISCAT comparison between the velocity of F region small-scale irregularities and the ion drift' J. Geophys. Res. 90, 8433.

**Villain, J.P., Greenwald, R.A., Baker, K.B. and J.M. Ruohoniemi (1987).** 'HF radar observations of E region plasma irregularities produced by oblique electron streaming' J. Geophys. Res., 92, 12327.

**Vincent, W.R., Daly, R.F. and Sifford, B.M. (1968).** 'Modelling communication systems. Ionospheric Radio Communications' K. Folkestad, Plenum Press, New York, 321.

**Yeoman, T.K. and Lühr, H. (1997).** 'CUTLASS/IMAGE observations of high-latitude convection features during substorms' Ann. Geophys. 15, 692.

**Yeoman, T.K., J.A. Davies, N.M. Wade, G. Provan and S.E. Milan (2000).** 'Combined CUTLASS, EISCAT and ESR observations of ionospheric plasma flows at the onset of an isolated substorm' Ann. Geophys. 18, 1073.